FLUIDIC AND DIELECTROPHORETIC MANIPULATION OF TIN OXIDE NANOBELTS

A Dissertation
Presented to
The Academic Faculty

by

Surajit Kumar

In Partial Fulfillment
of the Requirements for the Degree
Doctor of Philosophy in Mechanical Engineering

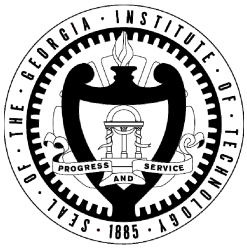

Georgia Institute of Technology
August 2008

FLUIDIC AND DIELECTROPHORETIC MANIPULATION OF TIN OXIDE NANOBELTS

Approved by:

Dr. Peter J. Hesketh, Advisor
School of Mechanical Engineering
Georgia Institute of Technology

Dr. Zhong Lin Wang
School of Material Science and Engineering
Georgia Institute of Technology

Dr. F. Levent Degertekin
School of Mechanical Engineering
Georgia Institute of Technology

Dr. Rosario A. Gerhardt
School of Material Science and Engineering
Georgia Institute of Technology

Dr. Samuel Graham
School of Mechanical Engineering
Georgia Institute of Technology

Dr. Martha A. Gallivan
School of Chemical and Biomolecular Engineering
Georgia Institute of Technology

Date Approved: May 5, 2008

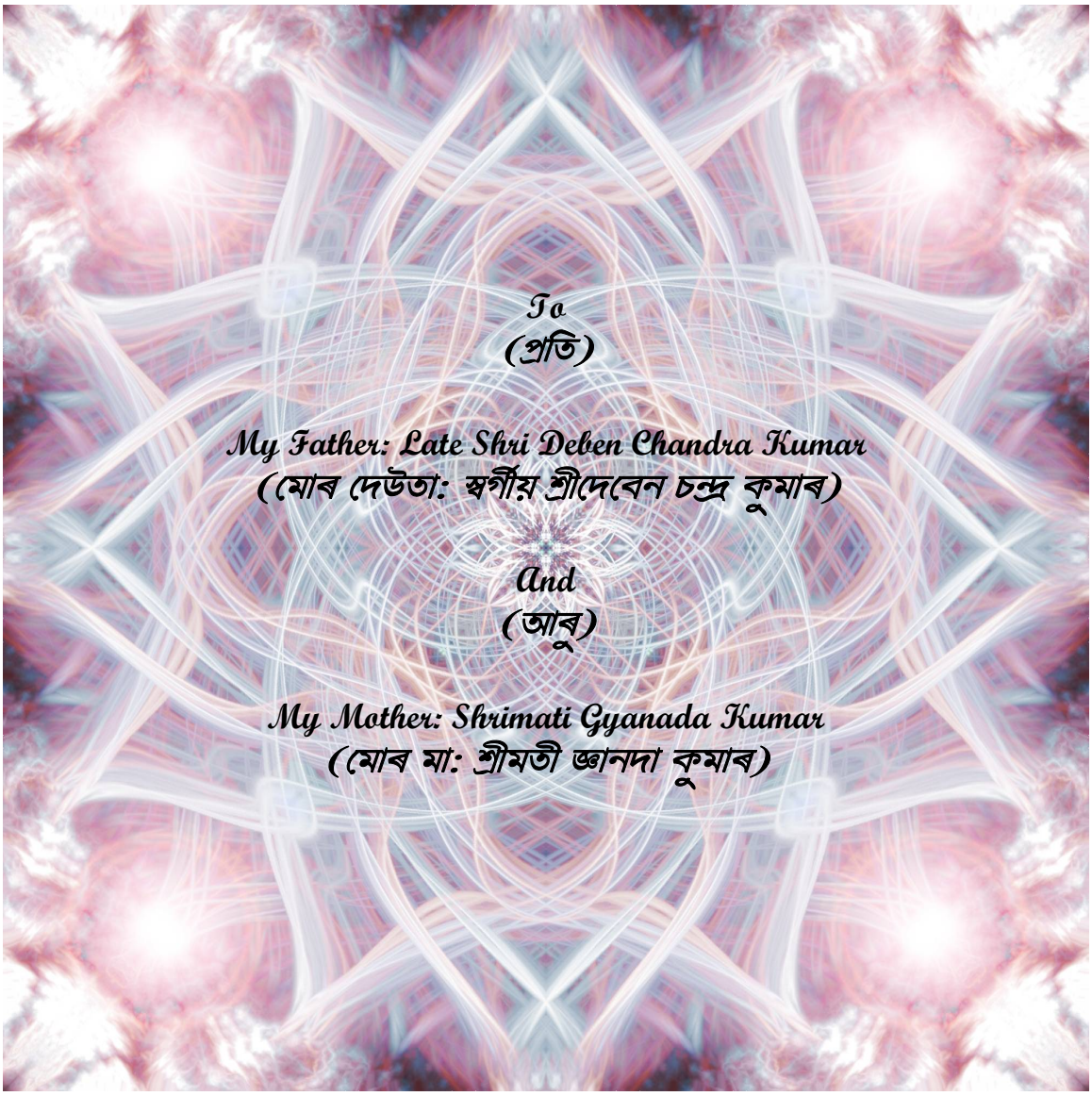
To
(প্রতি)
My Father: Late Shri Deben Chandra Kumar
(মোৰ দেউতা: স্বৰ্গীয় শ্ৰীদেবেন চন্দ্ৰ কুমাৰ)
And
(আৰু)
My Mother: Shrimati Gyanada Kumar
(মোৰ মা: শ্ৰীমতী জ্ঞানদা কুমাৰ)

ACKNOWLEDGEMENTS

First of all, I would like to thank Prof. Peter J. Hesketh for serving as my thesis advisor, for having faith in my abilities, for the many small and big kindnesses, and most importantly for being a great human being. The large amount of academic freedom accorded by him during my PhD program allowed me in deciding my research direction, which was an important factor in the success of my research. I am grateful to my reading committee members - Prof. F. Levent Degertekin, Prof. Samuel Graham, Prof. Zhong Lin Wang, Prof. Rosario A. Gerhardt, and Prof. Martha A. Gallivan for reviewing my work and providing constructive feedback.

Throughout the Ph.D. experience I received help from a number of people. I greatly appreciate the excellent advice on SU-8 patterning for microchannel fabrication from Zhengchun Peng and also for many other help and general discussions related to research. I thank Dr. Heungjoo Shin for his help with the microfabrication of electrodes, and for many useful inputs. I thank Daren Whitelock for writing LabView programs for data acquisition which was found very useful for current and voltage measurements. I thank the efforts of Dr. Arnab Choudhury in the fabrication of the stereolithography parts. I consider myself lucky to be part of a wonderful research group, and thank the present and past members of the MEMS laboratory, with whom I have had interactions on a day to day basis.

Special thanks go to Dr. Xiangyang Kong for making the nanobelt sample, Dr. Yong Ding for conducting some TEM EDX analysis on the nanobelts, and Prof. Wang

for the facilities provided for the nanobelt synthesis. I thank Prof. Gerhardt for providing impedance measurement facilities, and her research group members, especially Dr. Runqing Ou for training me at the beginning on the use of the equipment. Thanks to Prof. Degertekin for letting me use the AFM and the wire bonder, and to his research group members (Guclu Onaran, Rasim Guldiken, Zehra Parlak, and Omkar Karhade) for help with the same. Thanks to Prof. Kenneth Sandhage, and his student Samuel Shian, for supplying the TiO_2 diatoms. Thanks are also due to A. Alec Talin of Sandia National Laboratories for the photoluminescence measurements on tin oxide nanobelt samples. Thanks also to the staff of the Microelectronics Research Center (MiRC) at Georgia Tech for the clean room facilities used for the work.

I wish to acknowledge the financial support of the Nanoscience and Nanotechnology Fellowship Committee of Georgia Institute of Technology for funding for one year through a Nanoscience and Nanotechnology (NaST) Fellowship, and the Georgia Tech Nanoscience/Nanoengineering Research Program for additional financial support. I also extend my thanks to Prof. Gallivan for useful technical discussions and for providing funding for buying a condenser for the inverted optical microscope.

I am also thankful to the George W. Woodruff School of Mechanical Engineering for providing an excellent infrastructure, financial support through several teaching assistantships, and travel grants to present my research work at several national and international conferences.

Finally, I would like to acknowledge my brother and sister for their love and support throughout all these years.

TABLE OF CONTENTS

LIST OF TABLES

LIST OF FIGURES

SUMMARY

Nanobelts are a new class of semiconducting metal oxide nanowires with great potential for nanoscale devices. The present research focuses on the manipulation of SnO_2 nanobelts suspended in ethanol using microfluidics and electric fields. Dielectrophoresis (DEP) was demonstrated for the first time on semiconducting metal oxide nanobelts, which also resulted in the fabrication of a multiple nanobelt device. Detailed and direct real-time observations of the wide variety of nanobelt motions induced by DEP forces were conducted using an innovative setup and an inverted optical microscope. High AC electric fields were generated on a gold microelectrode (~ 20 μm gap) array, patterned on glass substrate, and covered by a ~ 10 μm tall PDMS (polydimethylsiloxane) channel, into which the nanobelt suspension was introduced for performing the DEP experiments. Negative DEP (repulsion) of the nanobelts was observed in the low frequency range (< 100 kHz) of the applied voltage, which caused rigid body motion as well as deformation of the nanobelts. In the high frequency range (~ 1 MHz - 10 MHz), positive DEP (attraction) of the nanobelts was observed. Using a parallel plate electrode arrangement, evidence of electrophoresis was also found for DC and low frequency (Hz) voltages.

The existence of negative DEP effect is unusual considering the fact that if bulk SnO_2 conductivity and permittivity values are used in combination with ethanol properties to calculate the Clausius Mossotti factor using the simple dipole approximation theory; it predicts positive DEP for most of the frequency range experimentally studied.

A fluidic nanobelt alignment technique was studied and used in the fabrication of single nanobelt devices with small electrode gaps. These devices were primarily used for conducting impedance spectroscopy measurements to obtain an estimate of the nanobelt electrical conductivity.

Parametric numerical studies were conducted using COMSOL Multiphysics software package to understand the different aspects of the DEP phenomenon in nanobelts. The DEP induced forces and torques were computed using the Maxwell Stress Tensor (MST) approach. The DEP force on the nanobelt was calculated for a range of nanobelt conductivity values. The simulation results indicate that the experimentally observed behavior can be explained if the nanobelt is modeled as having two components: an electrically conductive interior and a non-conductive outer layer surrounding it. This forms the basis for an explanation of the negative DEP observed in SnO_2 nanobelts suspended in ethanol. It is thought that the nonconductive layer is due to depletion of the charge carriers from the nanobelt surface regions. This is consistent with the fact that surface depletion is a commonly observed phenomenon in SnO_2 and other semiconducting metal oxide materials. The major research contribution of this work is that, since nanostructures have large surface areas, surface dominant properties are important. Considering only bulk electrical properties can predict misleading DEP characteristics.

CHAPTER 1

INTRODUCTION

1.1 MOTIVATION AND PURPOSE OF THE STUDY

Nanobelts [1], are a new class of semiconducting metal oxide nanowires. Nanobelts are formed by oxides such as, SnO_2, ZnO, In_2O_3, $SrTiO_3$, etc. The ribbon-like nanobelts are chemically pure single crystals.[1] They are structurally uniform with clean, sharp, smooth surfaces, and have rectangular cross sections.[1] Nanobelts have great potential as building blocks for nanoscale electronic devices. A few applications of nanobelts have been demonstrated, such as gas sensor using SnO_2 nanobelts [2, 3], and field effect transistors (FET) based on single ZnO and SnO_2 nanobelts [4], etc. There is a growing need for studying methods for manipulating nanobelts for assembly into nanodevices for useful applications. This need is not limited just to nanobelts. Manipulation and assembly is necessary for many other nanostructures, as well. While there are reports of different types of manipulation methods applied in the assembly of nanowires, nanotubes, nanoparticles, etc., there is limited literature on the detailed study of the assembly process, through direct visualization. One of the reasons, is off course the small size of the nanostructures. Real time observation of the assembly process is a challenge.

Keeping the above in mind, the present research focuses on the study of SnO_2 nanobelt assembly and manipulation, combining solution phase processing methods with microfluidics and electric fields. One of the methods is the fluidic alignment of nanobelts

in microchannels. The other method is dielectrophoresis (DEP).[5] DEP is an attractive method of electrical manipulation and assembly of nanostructures. A major focus and contribution of this research is the detailed in-situ visualization and study of the AC dielectrophoresis induced motion of the SnO_2 nanobelts under wide electric field frequency range (Hz to MHz). Application of DC fields revealed presence of fixed or induced charge on the nanobelts. The current literature on the DEP manipulation of long nanostructures like nanowires, are limited to attracting them between electrodes for device fabrication.

The detailed observation of the nanobelt motions, during the AC dielectrophoresis experiments performed on SnO_2 nanobelts suspended in ethanol, revealed unusual DEP characteristics. Explanations are extended for the unusual DEP effects. Numerical simulations are performed to verify the explanations.

While the current research primarily concentrates on SnO_2 nanobelts, the methods and results can be easily extended to other semiconducting nanobelts or nanowires. Ethanol has primarily been used as the suspending media because of its desirable properties. The results of this study will be found useful in analyzing DEP characteristics and estimating DEP force on nanobelts and other nanowires. The observed unusual DEP characteristics in SnO_2 nanobelts are also significant for other oxide nanostructures.

1.2 RESEARCH STATEMENT

The scope of the current work includes the following:

1) Investigation of manipulation and assembly of tin oxide nanobelts using microfluidic alignment and AC dielectrophoresis on microelectrodes.

2) Characterization of the assembled nanobelt devices
3) Impedance spectroscopy measurements to estimate nanobelt electrical properties.
4) Fabrication of a novel microscale experimental setup to enable in-situ visualization and study of nanobelt motions.
5) Detailed experimental investigation of the DEP phenomenon in SnO_2 nanobelts under AC electric fields of wide frequency range (Hz to MHz).
6) Simulation of the DEP phenomenon using COMSOL Multiphysics.

Through this research the following questions will be answered:

1) What are some of the ways to manipulate nanostructures using fluidic and electrical methods, and whether they can be used to make nanodevices?
2) How does electric field frequency affect the DEP force in nanobelts?
3) What types of motions are induced by DEP force in nanobelts?
4) Are there differences in DEP manipulation characteristics of nanostructures compared to larger objects where bulk properties dominate?
5) Do surface dominant properties in nanostructures affect the dielectrophoresis process?
6) How can the DEP force be computed in case the simple dipole approximation method cannot be applied, for example in the case of long objects, like nanowires and nanobelts?

1.3 RESEARCH OBJECTIVES

To answer the research questions the following are the major tasks carried out in the current work:

1) Investigation of microfluidic alignment technique applied to SnO_2 nanobelts in suspension, and application of this technique for the fabrication of single nanobelt devices.
2) Demonstration of manipulation of semiconducting metal oxide nanobelts using AC dielectrophoresis, and application of this method for the trapping of SnO_2 nanobelts between microelectrodes for the fabrication of single and multiple nanobelt based devices.
3) Characterization of the nanobelt devices.
4) Characterize the nature of DEP force according to the signal frequency range by conducting detailed investigation of the DEP phenomenon in SnO_2 nanobelts (suspended in ethanol) under AC electric fields (produced using microelectrodes in microchannels) of wide frequency range (Hz to MHz), for obtaining estimates of the DEP force magnitudes.
5) Conduct direct visualization of single nanobelt motion under the DEP force field, to understand the different types of motions.
6) Perform impedance spectroscopy measurements on the nanobelt devices to investigate the nanobelt electrical properties, and to study the effect of surface interactions of the suspending liquid, if any.
7) Extend an explanation for the unusual negative DEP at low frequency electric fields.
8) Perform multiphysics simulations using COMSOL software to obtain DEP force estimates, compare with the experimental observations, and complement the

available experimental data to gain additional insights on the DEP phenomenon in SnO_2 nanobelts.

1.4 Significance, Limitations, and Assumptions of the Study

While there are many studies on attracting nanostructures between electrodes for device fabrication using DEP, there are very few studies on the direct observation of the dielectrophoresis process in nanowires and such long objects in the literature. In fact there is no study of real time observation of nanobelt DEP. The current research fills that gap. Also, because of the different aspect ratio of the nanobelt cross section (thin and width rectangle) compared with other nanowires, it is of significant interest to study its DEP characteristics. Although the current research focuses mainly on SnO_2 nanobelts, the insights gained from this study can be applied to other nanostructures in general, and to nanowires and nanobelts of functional materials in particular. The realization that the surface dominant properties in nanostructures determine whether the structure will be attracted or repelled in DEP is a major finding. Evidence of electrophoresis has also been found in the oxide nanobelts. This is an important aspect of oxide materials, and it has to be kept in mind in the case of other metal oxide semiconductors.

The quantitative and qualitative nature of the DEP force studied as a function of frequency can have significant utility in other applications of nanostructure manipulation, for example in sorting of nanobelts and nanowires, according to size. The methodology of performing parametric numerical simulations to obtain the DEP forces and torques in the nanobelts can also be extended to other nanostructures.

Some of the limitations and assumptions of the current study are discussed below.

Individual nanobelts from the sample produced in the furnace have a wide size distribution. The width and thickness is different for each nanobelt. The long nanobelts are broken into shorter lengths using ultrasonication. However, it is not possible to get nanobelts of equal lengths in the suspension. Because of the above reasons the liquid suspension of nanobelts used in the DEP experiments also have a size distribution. The individual nanobelts that are observed and studied under DEP force field are different for different experiments. DEP is a size dependent phenomenon. Hence, one has to infer the general characteristic of the DEP study without doing experiments for all sizes and lengths. Some effort was made to measure the size of the nanobelts using AFM after the experiments. However, it is not always possible to do this because the nanobelts which were imaged during the experiments may not be recoverable after the experiments. Moreover, measuring the size using AFM is a time consuming process.

In SnO_2 the electrical conductivity primarily results from the presence of oxygen vacancies, which generate electrons for conduction. However, the oxygen vacancy concentration is not accurately known. This can depend on the processing history of the nanobelt samples, such as whether they have been heated, and in what environment. Hence, a parametric calculation is more useful as opposed to say using the electrical properties of a particular nanobelt sample for the analysis of DEP phenomenon.

For the DEP simulation using Maxwell Stress Tensor approach (MST), it is assumed that quasi-static analysis is valid. One of the limitations of the finite element simulations is that because the mesh elements near the nanobelt have to be defined with fine resolutions (small size), it results in a mesh with large number of elements for the overall domain. This means more computational resources are required for the solution.

Because of this, the length of the nanobelt had to be decreased in the model. The mesh size limitation is severe in the case of modeling a nanobelt with a thin surface layer. All these factors put constraints on the size of the nanobelt that can be simulated. However, even with these constraints, the results that were obtained through the simulations will be able to provide useful insights on the DEP phenomenon of nanobelts and such long nanostructures.

1.5 THESIS OUTLINE

The thesis is divided into 10 chapters:

Chapter 1 describes the motivation and objectives of this research.

Chapter 2 builds the foundation for the development of the current work by providing background information regarding the status of assembly and manipulation of nanostructures. It also introduces several useful concepts relevant to the current research. The information includes fundamentals of electrokinetics, dielectrophoresis, previous research on nanoassembly using dielectrophoresis, etc.

Chapter 3 describes the DEP experiments to trap multiple SnO_2 nanobelts and the characterization of the resulting device. It also describes the DEP experiments for the trapping of TiO_2 diatoms.

Chapter 4 describes the novel experimental setup fabricated to study DEP of single nanobelts in detail, the experimental results, and the unusual characteristics observed.

Chapter 5 reports the fluidic alignment of nanobelts to fabricate single nanobelt devices, so that the electrical properties of the nanobelts can be studied.

Chapter 6 describes the impedance measurements performed on single nanobelts, and liquid ethanol to estimate their electrical conductivities.

Chapter 7 describes the experiments performed to find evidence of charge on the tin oxide nanobelts suspended in ethanol.

Chapter 8 extends possible explanation for the presence of negative DEP in tin oxide nanobelts.

Chapter 9 describes the detailed simulations of the DEP phenomenon in nanobelts using COMSOL Multiphysics software package.

Chapter 10 lists the conclusions reached from the research study, and makes recommendations for future studies.

CHAPTER 2

LITERATURE REVIEW

2.1 ELECTROKINETICS

Because of the advances in semiconductor processing technology, many of those processes have been used for the development of microsystems other than microelectronics. In recent years there have been great interests in the so called fields of Microelectromechanical Systems (MEMS) and "Lab-on-a-Chip" systems. Lab-on-a-Chip refers to microsystems developed for chemical and biological analysis. The objective is to create systems which are able to perform different types of tasks on a microchip. Some of the tasks are manipulation, concentration, separation, and sorting, of different types of bioparticles and biomolecules. One of the popular methods for accomplishing these tasks are electric field based. Electrokinetics is the study of motion of particles and fluids in response to application of electric fields to a suspension of particles. DC or AC fields may be applied. While motion of particles and fluids under DC fields have been studied for 100 years or so [6], the AC counterpart has experienced rapid development only in the past 2 - 3 decades.

For sub-micrometer particles moving in a microsystem, gravity is not a major force to consider. The dominant forces are viscous forces and electrical forces. The application of electrical fields can generate forces on both the particle and the fluid depending on their properties. There are several different types of phenomena included

in the general field of electrokinetics. Some of them are discussed briefly in this section, while the more important concepts are discussed in detail in later sections.

Electroosmosis [6] occurs if there is a gradient in charge density in the fluid. This is generally manifested on the application of DC fields which interacts with the charges in electrical double layers. These motions are not of significance in insulating liquids, where presence of electrical double layer is unlikely.

Electrothermally driven fluid flows [6] occur if there is a temperature gradient in the fluid. The temperature gradient causes the permittivity and/or conductivity to change and an application of AC fields will cause fluid motion.

Forces generated by electrical fields on the particles include electrophoresis and dielectrophoresis.[6] These concepts are discussed in detail in separate sections below, because of their relevance to the current research. Electrophoresis occurs because of the interaction of electrical fields (primarily DC) with the fixed, net charge on suspended particles. DEP occurs because of the induced charges due to non-uniform electric fields. It can occur in AC as well as DC fields. DC dielectrophoresis is less popular because of the possibility of electrolysis.

The major forces on a small particle suspended in a liquid include contributions from electric fields ($\boldsymbol{F}_{dep} + \boldsymbol{F}_{Coulomb}$), fluid drag ($\boldsymbol{F}_{drag}$), and gravity ($\boldsymbol{F}_{buoyancy}$):

$$\boldsymbol{F}_{total} = \boldsymbol{F}_{dep} + \boldsymbol{F}_{Coulomb} + \boldsymbol{F}_{drag} + \boldsymbol{F}_{buoyancy} = \boldsymbol{F}_{external} + \boldsymbol{F}_{drag} \qquad (2\text{-}1)$$

Brownian motion ($\boldsymbol{F}_{Brownian}$) adds a stochastic component to the dynamics of the wire. This is due to the thermal fluctuations at molecular scales in the liquid medium. This induces random forces on the suspended particles.[6] The application of higher electrical fields can make this component less significant. High fields can be generated

by using microelectrodes with smaller gaps and applying high electric potentials. In the case of DEP forces generated on microelectrodes, the DEP force component usually dominates the total force. In such a situation, the buoyancy forces can be neglected for sub-micron particles, because of their small contributions relative to the other forces. However, in general, the relative magnitudes of all the forces have to be considered before making such an approximation.

Fluid drag is an important factor in the motion of sub-micron particles in a fluid medium in microsystems. It has been shown [6] that the velocity (starting from rest) of a particle, of mass *m*, under the influence of externally applied forces ($\boldsymbol{F}_{external}$), at time *t* is given by

$$\boldsymbol{v} = \left(\frac{\boldsymbol{F}_{external}}{D} + \boldsymbol{u} \right)\left(1 - e^{-(D/m)t}\right) = \left(\frac{\boldsymbol{F}_{external}}{D} + \boldsymbol{u} \right)\left(1 - e^{-t/\tau}\right) \tag{2-2}$$

where *D* is the drag coefficient of the particle, and $\boldsymbol{u}$ is the velocity of the fluid in which the particle is entrained. $\tau = \frac{m}{D}$, is a time constant indicative of the period when acceleration is taking place. For $t >> \tau$, the acceleration is zero and the particle moves at the terminal velocity [6]

$$\boldsymbol{v}_t = \frac{\boldsymbol{F}_{external}}{D} + \boldsymbol{u} \tag{2-3}$$

For sub-micron particles, $\tau < 10^{-6}$ sec. It means that for experimental observation times greater that the time constant (τ), the particle will seem to be moving at the terminal velocity, since the acceleration time is too short.[6] Also, if the fluid is stationary ($\boldsymbol{u} = 0$), the particle velocity (terminal) is always proportional to the externally applied force.[6] The reason for this consequence is that for sub-micron particles, the

Reynolds number is very small, and the viscous forces balance the applied forces. Inertial forces are negligible.

2.2 ELECTROPHORESIS

Electrophoresis is a phenomenon that occurs upon the application of an electric field, in which motion of a particle or a nanowire is determined by the magnitude and polarity of the net electrical charge. In the absence of field gradients (uniform electrical field), particles in suspension will move only if they carry a charge.[7] The particles can be charged due to [7]:

a) selective adsorption of ions onto the particles,
b) dissociation of ions from the solid particles,
c) adsorption of dipolar molecules at the surface of the particles, or
d) electron transfer between the solid and liquid phase due to the differences in work functions.

For a suspension of particles, let σ_p be the conductivity of the solid particles, and σ_m be the conductivity of the suspending fluid. On application of a DC field on the suspension of particles, for $\sigma_p > \sigma_m$, usually chains form from an aggregation of the particles between the two electrodes.[8] For $\sigma_p < \sigma_m$, the particles migrate towards one of the electrode.

Electrophoresis was proposed by Feng et al. [8] as the reason for the anomalous electrorheological (ER) behavior in a suspension of ZnO nanowires in silicone oil. Negative ER effect was observed. Electrorheological fluids are suspensions of particles in a liquid medium, whose rheological properties are determined by the application of an

external electric field. The viscosity can change dramatically due to the interactions of the electric fields. The ZnO nanowires migrated towards both electrodes due to the occurrence of electrophoresis induced by the electron transfer among the ZnO nanowires under a DC electric field. Since the conductivity of the ZnO nanowires (ZnO is an n-type semiconductor) is much larger than that of the silicone oil, migration to the electrodes was not expected according to the criteria stated above.

A DC electric field was used on single walled carbon nanotubes (SWNTs) suspended in solvents to align them across the metal electrodes by Kumar et al.[9] In addition to alignment, most of the time, the CNTs moved towards the positive electrode, which indicated the negative charge on the nanotubes.

Experiments on $Mo_6S_3I_6$ nanowires by Ploscaru et al. [10] showed that the bundles are charged when they are dispersed in polar liquids like ethanol and isopropanol. This indicated the potential for separation of the nanowires from impurities, which could be adopted to separate large quantities of material by DC electric field. DEP was also investigated and was found useful in assembling $Mo_6S_3I_6$ nanowires onto metal electrodes (Ni wires covered with 99.95% pure Indium).

2.3 DIELECTRICS

Materials which polarize under the influence of an electric field are known as dielectrics.[6] When an electric field is applied to a dielectric, the bound charges (positive and negative) in the material move small distances in opposite directions and form dipoles. Dielectric materials can be polar or non-polar. Polar dielectrics are

composed of molecules with a permanent dipole, while non-polar dielectric materials are not.

Dielectric constant (permittivity) is a material property which describes how an electric field affects and is affected by the dielectric medium. It depends on the different polarization mechanism allowing the material to polarize in response to the electric field, and effectively reduce the total electric field inside the material. Essentially, permittivity represents the material's ability to transmit (or "permit") an electric field to pass through. The dielectric response of a material usually depends on the frequency of the applied electric field, which indicates that polarization does not respond instantaneously. Because the response takes a finite time after the application of the electric field there is a phase difference. Therefore, it is convenient to define permittivity as a complex function which depends on the frequency of the applied field ω. Hence, the general definition of permittivity is

$$\tilde{\varepsilon}(\omega) = \varepsilon'(\omega) + j\varepsilon''(\omega) \tag{2-4}$$

Dielectrics respond to an applied electric field using different polarization mechanisms: *electronic*, *atomic* (or ionic), *orientational* (or dipolar), and *interfacial* (or space charge) polarization. These polarizations mechanisms [11] are shown in Figure 2.1. Each mechanism has its own characteristic frequency response. The contributions of the different polarization mechanisms to the real part of the permittivity are shown in Figure 2.2.

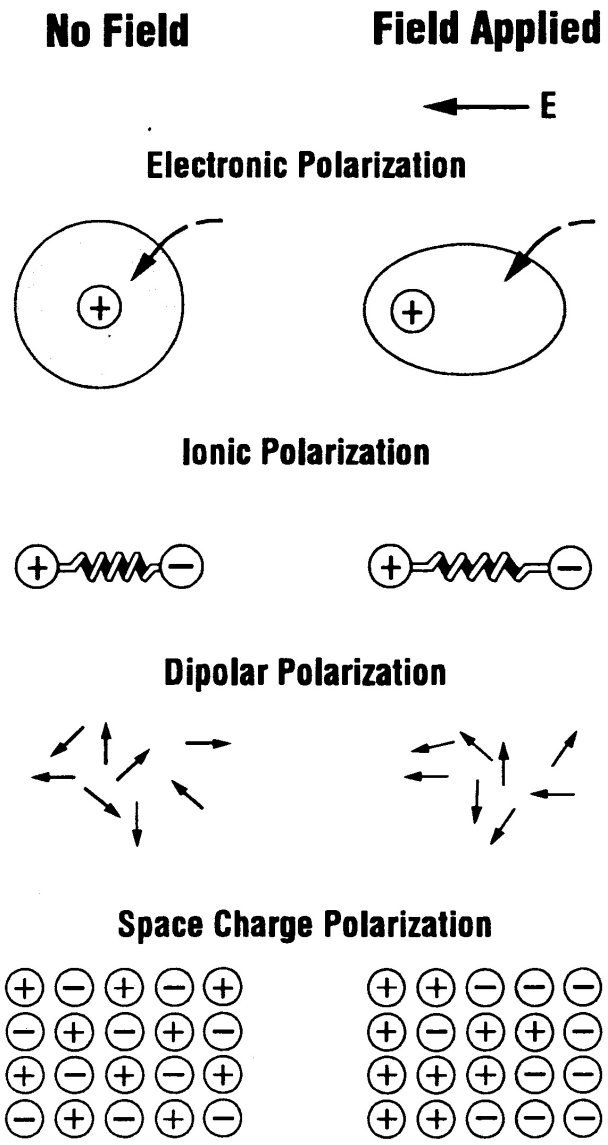

Figure 2.1 Schematic showing the different polarization mechanisms in dielectrics.[11]

During *electronic* polarization, the centre of the electron cloud in an atom moves slightly relative to the centre of the charge on the nucleus, effectively creating a dipole [6]. In ionic solids the positive and negative ions move small distances in opposite directions upon application of an electric field creating dipoles.[6] This is the origin of *atomic* (or ionic) polarization. Polar dielectric materials are composed of molecules

which have permanent dipole moments. On application of an electric field these dipoles orient along the electric field causing an increase in polarization. This is the mechanism for *orientational* polarization.[6]

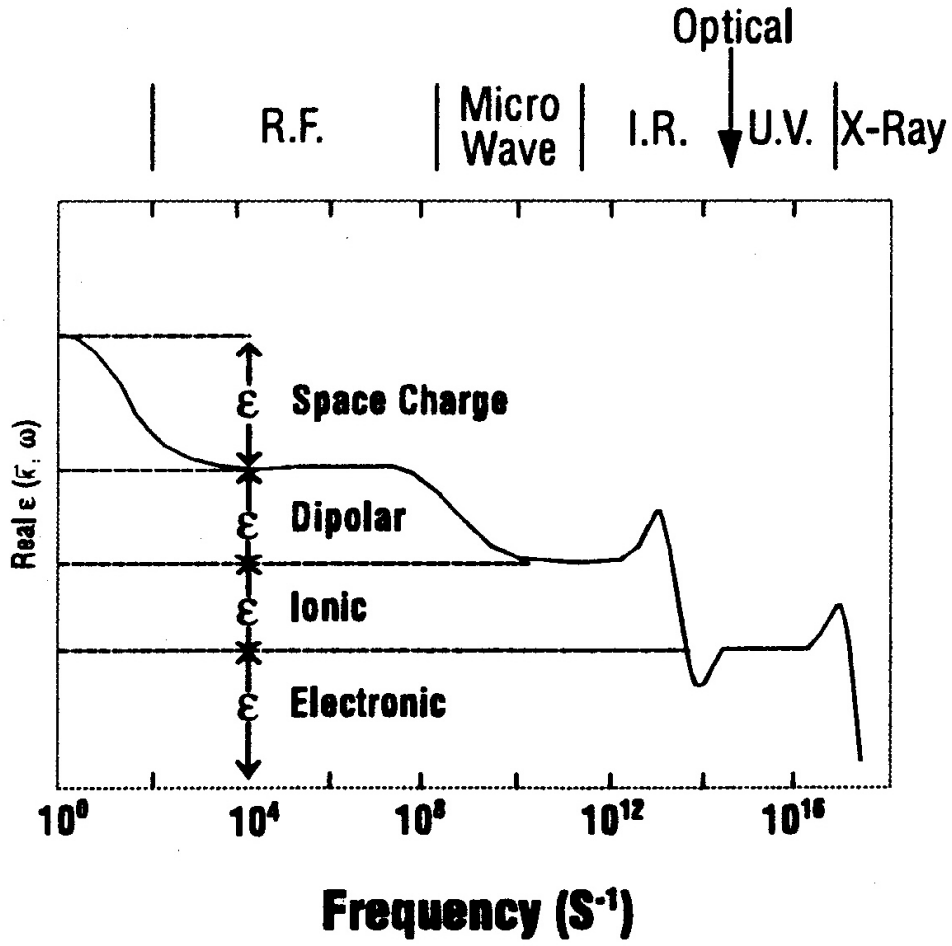

Figure 2.2 Frequency variation of the real part of permittivity showing the contributions from the different polarization mechanisms.[11]

Interfacial (or space charge) polarization mechanism is based on the long-range transport of charges in dielectrics.[6] This type of polarization occurs at locations where there is inhomogeneity in the dielectric properties, e.g., internal interfaces or at surface.[6] Charges get trapped in such locations and it distorts the nearby electric field. For particles suspended in ionic liquids, interfacial polarization occurs via the transport of

ions to the particles surface.[6] Interfacial polarization causes an increase in the charge storage capacity (permittivity) of the dielectric.[6] Interfacial polarization is also known as Maxwell-Wagner polarization. This is the fundamental mechanism involved in dielectrophoresis. It is useful here to go into a little detail on this mechanism. The sole reason for this type of relaxation is the difference in the conductivities and permittivities of the two dielectrics on the two sides of the interface.

Polarization occurs by movement of charge to produce dipoles and it requires a finite time, which is the time required for reaching maximum polarization.[6] This time depends on the polarization mechanism, with a corresponding characteristic time for each mechanism.

2.4 Motion of Uncharged Objects in Uniform Electric Fields

A study of the electrohydrodynamic motion of single conducting particles (spheres or cylinders) in an insulating fluid between horizontal plane-parallel electrodes subjected to a DC voltage was presented by Tobazeon et al.[12] When in contact with the bottom electrode, the particles acquire a charge and, after 'lift-off' proceed to bounce up and down. The laws of particle velocity and the current-voltage relationships were derived for the three possible hydrodynamic regimes of motion (viscous, intermediate and inertial) in the bulk according to the Reynolds number of the particles. The phenomena taking place in the vicinity of the electrodes (field-enhancement and microdischarges between electrode and particle) were analyzed and quantified. The motion of spherical conductive particles under a uniform electric field has also been investigated by Choi et al.[13] They also observed the bouncing motion of particles

between the two electrodes, again due to charging and then discharging when the particle touched the electrode.

Uncharged elongated objects in insulating liquids under uniform fields do not experience net force, but only rotation. In the literature some references have been found which deal with motion of uncharged particles and elongated objects in insulating liquids. The alignment of 200 μm long, 3 μm diameter ceramic fibers of alumina (Al_2O_3) under DC fields has been reported by Itoh et al.[14] The speed of fiber orientation was predicted by the equation of motion based on the polarization model of a prolate ellipsoid. Experiments in CFC-113 insulating liquid showed that the time constant of polarization due to surface conduction is sufficiently small compared to the time scale of the mechanical orientation of the fiber. The field induced polarization of the fiber depends on the ratio of the fiber conductivity (equivalent to its surface conductivity) to the liquid conductivity. The addition of surfactant increases the liquid conductivity, which can affect the polarization. The values of the polarized charge and the force acting on one end of the oriented fibers were estimated using the measurements. Impurity particle motion under DC and AC fields in dielectric liquids have been investigated numerically and experimentally in the literature.[15, 16] Electrostatic alignment processes have also been used in producing composites [17], novel structures [18], and films.[19]

2.5 DIELECTROPHORESIS

Dielectrophoresis (DEP) [5, 20] is defined as the force induced by the polarization processes and the associated motion of a polarizable particle suspended in a fluid medium

under the influence of non-uniform electric fields. In the presence of an externally applied electric field, the particle and the surrounding medium become electrically polarized, and the surface charge can accumulate at the interfaces due to the difference in the dielectric properties of the particle and the fluid medium. The induced motion is determined by the electrical permittivity and conductivity of the particle and the fluid medium. Both alternating current (AC) and/or direct current (DC) electric fields may be employed. There are two different effects associated with DEP: positive DEP (pDEP) and negative DEP (nDEP). Positive DEP occurs when the particle is more polarizable than the medium, causing the particle to be attracted to the maxima of the electric field. The reverse is true for negative DEP.

The DEP forces on an object can be calculated by directly integrating the force distribution due to the induced surface charge over the object, or can be approximated with simpler equations using the dielectrophoretic approximation based on the effective moment method.[5, 20] This approximation is also known as the dipole approximation method. The approximate expressions are derived by assuming that the electric field changes only slightly across the object suspended in the liquid medium. The size of the sphere has to be small relative to a characteristic length scale representing the non-uniformity of the electric fields. In effect it implies that the electric field is approximately uniform across the particle.

In an electric field, a dielectric particle behaves effectively as an electric dipole with an induced dipole moment $\boldsymbol{p}$, which is proportional to the electric field $\boldsymbol{E}$ [21], i.e.,

$$\boldsymbol{p} \propto \boldsymbol{E} \tag{2-5}$$

The constant of proportionality depends on the geometry of the dielectric particle. If the applied frequency is harmonic with angular frequency ω, the relation between the induced dipole moment $\boldsymbol{p}$ and $\boldsymbol{E}$ for a homogeneous spherical particle of radius R can be derived as [6]

$$\boldsymbol{p} = 4\pi\varepsilon_m \tilde{f}_{CM} R^3 \boldsymbol{E} \tag{2-6}$$

To derive this expression, one has to solve for the electric potential inside and outside the sphere, and decompose the potential inside the sphere into components due to an induced electric dipole, and due to the applied electric field. By comparing the potential due to the dipole moment with the standard expression of dipole moment potential, one can deduce the *effective dipole moment* induced in the sphere. The details of the derivation are provided elsewhere.[6] This is the dipole approximation method. The effective dipole moment of the particle depends on the frequency as can be observed from the factor, $\tilde{f}_{CM}$, which is known as the *Clausius-Mossotti factor*.

$$\tilde{f}_{CM} = \left(\frac{\tilde{\varepsilon}_p - \tilde{\varepsilon}_m}{\tilde{\varepsilon}_p + 2\tilde{\varepsilon}_m} \right) \tag{2-7}$$

where $\tilde{\varepsilon}_p = \varepsilon_p - j\frac{\sigma_p}{\omega}$, is the complex permittivity of the particle, and $\tilde{\varepsilon}_m = \varepsilon_m - j\frac{\sigma_m}{\omega}$ is the complex permittivity of the fluid medium. ε_p, and ε_m are the permittivities of the particle and the fluid medium respectively. σ_p, and σ_m are the conductivities of the particle and the fluid medium respectively. The surface conductivity of the particle is also included in σ_p.[21] Analogous expressions have also been derived for ellipsoidal particles, which still require the dipole approximation (the particle dimensions are small relative to the changes in the electric field).

The force on a dipole in a non-uniform electric field is given by

$$\boldsymbol{F} = (\boldsymbol{p} \cdot \nabla)\boldsymbol{E} \tag{2-8}$$

In the case of AC fields, the expression stated here is for the DEP force on a particle in an electric field, the magnitude of which is varying with location, but the phase is constant. In the general case of varying phase one obtains the travelling wave dielectrophoresis force.[6] The *time-averaged* force on the particle subjected to a local electric field $\boldsymbol{E}$ (phasor amplitude) of angular frequency ω is given by

$$\boldsymbol{F}_{dep} = \pi \varepsilon_m R^3 \,\mathrm{Re}\left[\tilde{f}_{CM}\right] \nabla (\boldsymbol{E} \cdot \boldsymbol{E}) \tag{2-9}$$

which simplifies to

$$\boldsymbol{F}_{dep} = \pi \varepsilon_m R^3 \,\mathrm{Re}\left[\tilde{f}_{CM}\right] \nabla |\boldsymbol{E}|^2 = 2\pi \varepsilon_m R^3 \,\mathrm{Re}\left[\tilde{f}_{CM}\right] \nabla |\boldsymbol{E}_{rms}|^2 \tag{2-10}$$

where $\boldsymbol{E}_{rms}$ is the root-mean-square (rms) value of the electric field.

From the force expression, one can note that the frequency dependence of the DEP force is determined by the real part of the Clausius-Mossotti factor, $\mathrm{Re}[\tilde{f}_{CM}]$. It determines both the magnitude and the sign of the DEP force. The value of the $\mathrm{Re}[\tilde{f}_{CM}]$ factor ranges from - 0.5 to + 1.0, and can be calculated from the properties of the medium and the particle. If the value of $\mathrm{Re}[\tilde{f}_{CM}]$ is positive, the particle moves toward higher electric field regions, and is termed positive DEP. If the value of $\mathrm{Re}[\tilde{f}_{CM}]$ is negative, the particle moves toward lower electric field regions, and is termed negative DEP. For a solid homogeneous particle undergoing a single interfacial relaxation process, the characteristic frequency at which the direction of the DEP force changes is known as the crossover frequency or Maxwell-Wagner relaxation frequency. This frequency depends on the conductivity and permittivity of the particle and the suspending medium.

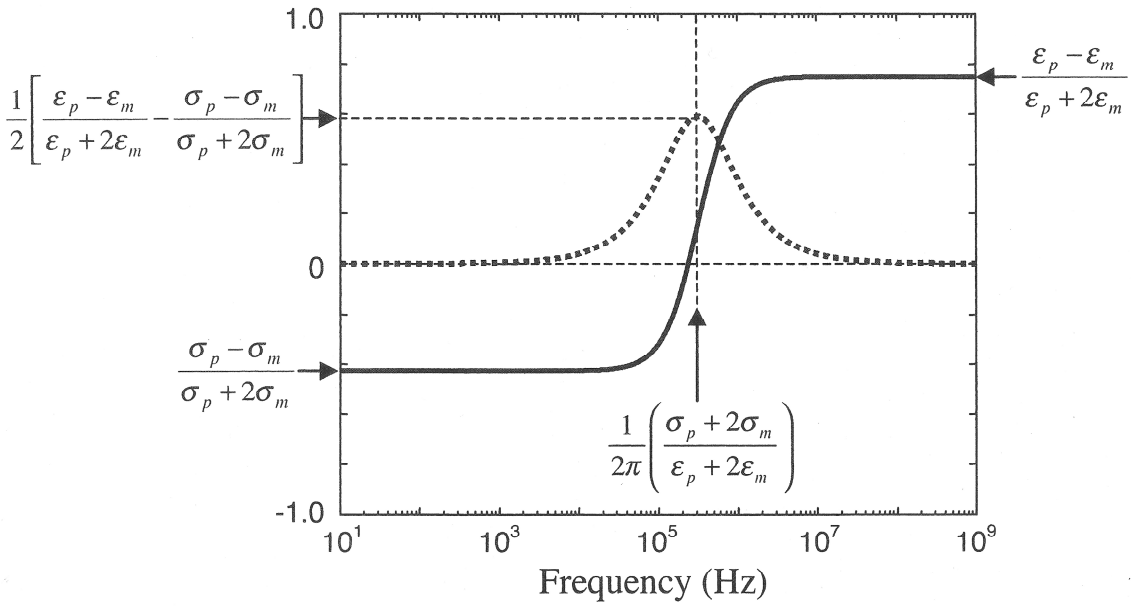

Figure 2.3 Plot showing the real (solid line) and imaginary (dotted line) parts of the Clausius-Mossotti factor as a function of electric field frequency.[6]

Figure 2.3 shows a representative plot of the real and imaginary parts of the Clausius-Mossotti factor. The limiting values at the high and low frequencies of the real part, and the value of the imaginary part at the Maxwell-Wagner relaxation frequency, are indicted in the figure. It is clear that the low frequency limiting value of $\mathrm{Re}\left[\tilde{f}_{CM}\right]$, $\left(\sigma_p-\sigma_m\right)/\left(\sigma_p+2\sigma_m\right)$, depends only on the conductivity, while the high frequency limiting value of $\mathrm{Re}\left[\tilde{f}_{CM}\right]$, $\left(\varepsilon_p-\varepsilon_m\right)/\left(\varepsilon_p+2\varepsilon_m\right)$, depends only on the permittivity of the particle and the suspending liquid.[6] The reason for this can be analyzed qualitatively in the following manner. Dipoles are formed on the application of an electric field. At low frequencies the free charge movement in the particle and the medium is the dominant mechanism for charging the interface.[6] The free charge can move fast and keep up with the changing field direction. At high frequencies the free charges can no longer move with the field direction change, and conductivities become unimportant. At high

frequencies the dominant mechanism for charging the interface is the polarization of the bound charge. This polarization ability is represented by the permittivities.

The Maxwell-Wagner relaxation frequency is also shown in Figure 2.3. At this frequency the imaginary part of the Clausius-Mossotti factor $\mathrm{Im}[\tilde{f}_{CM}]$, reaches a maximum value.[6] Usually, $\mathrm{Im}[\tilde{f}_{CM}]$ values range from - 0.75 to + 0.75.[6]

The analogous expression for the DEP force on a spherical particle in a DC electric field is given by [22],

$$\boldsymbol{F}_{dep} = 2\pi\varepsilon_m R^3 f_{CM} \nabla|\boldsymbol{E}|^2 \tag{2-11}$$

The Clausius-Mossotti factor in the case of DC fields depends only on the particle and medium conductivities, and it does not depend on the permittivities,

$$f_{CM} = \left(\frac{\sigma_p - \sigma_m}{\sigma_p + 2\sigma_m} \right) \tag{2-12}$$

It has to be noted that the above equations are based on classical calculations using bulk material properties. Hence, it may not be quantitatively accurate for nanostructures and molecules. Surface charge and quantum effects are likely to affect the quantitative predictions.[21] However, the equations do give an idea of the variables involved and the possible trends.

2.6 Electrorotation and Traveling Wave Dielectrophoresis

Another effect of AC electric fields on polarizable objects is to orient them with respect to an electric field. The induced dipole moment $\boldsymbol{p}$, of the object interacts with the electric field to produce a torque $\boldsymbol{T}$, given by [21]

$$\boldsymbol{T} = \boldsymbol{p} \times \boldsymbol{E} \tag{2-13}$$

This effect is responsible for the alignment of DNA, nanotubes, nanowires, nanobelts and such thin, long objects in a fluid medium.[21]

If the electric field vector changes its direction with time, the induced dipole also has to change its direction to realign with the field, causing the particle to rotate. This phenomenon is known as electrorotation, which occur in electric fields which have a spatially varying phase.[6] The expressions for the torque generated due to electrorotation on a spherical particle for simple field configurations have been reported in the literature.

Another phenomenon closely related to dielectrophoresis and electrorotation, is traveling wave dielectrophoresis (TWD), in which particle motion is induced by traveling electric fields.[23] This type of field is usually produced using planar multiple-phase traveling wave electrode design.[24] If the electrodes are addressed with a series of sequentially phase-shifted voltages, at an appropriate frequency and medium conductivity, polarizable particles can be levitated above the electrodes under negative DEP force, and the particles will move along the electrode array [25] under the influence of the traveling wave force. The induced dipole moment in the particles interact with the traveling field and it has been shown that the time-averaged traveling wave force [25]

$$\boldsymbol{F}_{twd} \propto \mathrm{Im}[\tilde{f}_{CM}] \tag{2-14}$$

Hence, for a particular particle material and dielectric medium, there is a range of frequencies over which traveling wave dielectrophoresis can occur. At such frequencies two conditions are satisfied: (a) the real component of the Clausius-Mossotti factor is negative providing a negative DEP force to levitate the particle above the electrode, and (b) the imaginary component of the Clausius-Mossotti factor is non-zero so that the

horizontal force component ($\boldsymbol{F}_{twd}$) is of sufficient magnitude to induce motion along a fluid filled channel.

2.7 Shell Model for Dielectrophoresis

In the previous section an expression for the effective dipole moment, and DEP force was derived for a spherical particle. However many occasions, particles can have an outer layer forming a shell structure. Prime examples of this configuration are that of biological cells, which have an outer cell membrane or cell wall. The previous analysis can be extended to the present case with a modified dipole moment, and Clausius-Mossotti factor. Let us consider a particle with a shell structure suspended in a liquid medium as shown in Figure 2.4.

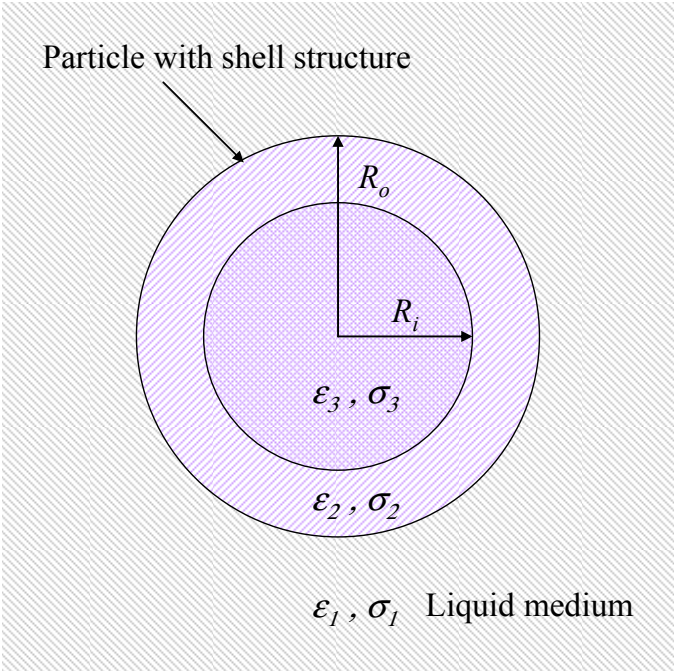

Figure 2.4 Schematic showing a spherical particle with a shell structure suspended in a liquid medium.

Since DEP occurs due to interfacial polarization processes, the presence of two interfaces in the case of the shell structure means that there are two intrinsic relaxation frequencies.[6] For this structure the dipole moment and the DEP force can be calculated using the following expressions.[6]

$$\boldsymbol{p} = 4\pi\varepsilon_1 \tilde{f}_{CM,23} R_o^3 \boldsymbol{E} \tag{2-15}$$

$$\boldsymbol{F_{dep}} = \pi\varepsilon_1 R_o^3 \,\mathrm{Re}\left[\tilde{f}_{CM,23}\right] \nabla \left|\boldsymbol{E}\right|^2 = 2\pi\varepsilon_1 R_o^3 \,\mathrm{Re}\left[\tilde{f}_{CM,23}\right] \nabla \left|\boldsymbol{E_{rms}}\right|^2 \tag{2-16}$$

The modified Clausius-Mossotti factor to use in these expressions is

$$\tilde{f}_{CM,23} = \left(\frac{\tilde{\varepsilon}_{23} - \tilde{\varepsilon}_1}{\tilde{\varepsilon}_{23} + 2\tilde{\varepsilon}_1} \right) \tag{2-17}$$

where, $\tilde{\varepsilon}_{23}$ is the effective complex permittivity of the particle with the shell structure

$$\tilde{\varepsilon}_{23} = \tilde{\varepsilon}_2 \left[\frac{\gamma^3 + 2\left(\frac{\tilde{\varepsilon}_3 - \tilde{\varepsilon}_2}{\tilde{\varepsilon}_3 + 2\tilde{\varepsilon}_2} \right)}{\gamma^3 - \left(\frac{\tilde{\varepsilon}_3 - \tilde{\varepsilon}_2}{\tilde{\varepsilon}_3 + 2\tilde{\varepsilon}_2} \right)} \right] \tag{2-18}$$

and, ε_1, σ_1, and $\tilde{\varepsilon}_1 = \left(\varepsilon_1 - j\frac{\sigma_1}{\omega} \right)$ are the particle permittivity, conductivity, and complex permittivity, of the inner sphere, respectively; ε_2, σ_2, and $\tilde{\varepsilon}_2 = \left(\varepsilon_2 - j\frac{\sigma_2}{\omega} \right)$ are the permittivity, conductivity, and complex permittivity of the outer shell, respectively; and ε_3, σ_3, and $\tilde{\varepsilon}_3 = \left(\varepsilon_3 - j\frac{\sigma_3}{\omega} \right)$ are the medium permittivity, conductivity, and complex permittivity of the liquid medium, respectively. $\gamma = \frac{R_o}{R_i}$ is the ratio of the outer radius to the inner radius of the spheres which make up the shell structure. The above procedure can be extended to multiple shelled structures.[6]

2.8 PEARL CHAIN FORMATION

Pearl chain formation phenomenon was originally observed in biological materials as a result of their response to electric fields.[5] This phenomenon refers to the end-to-end attachment of particles resulting in a formation similar to that of a chain of pearls. It is a common site in DEP experiments on biological cells. Pearl chains form because of the electrostatic interactions among the particles under an electric field. Van der Waals forces also contribute to the total force when the particles come together.[6] The electrostatic interaction force is very weak and it decays as r^{-5}, where r is the distance between the particles.[26] Hence, pearl chain can form only when the particles come very close to each other, and can be neglected when the particles are separated by large distances.

The mechanism of this process can be understood from the fact that particles acquire induced dipole moments under an electric field. When two particles are very close to each, the positive charge of one dipole interacts with the negative charge of the other dipole. Hence, they experience an attractive force which results in the particles getting attached to each other. This phenomenon is illustrated in Figure 2.5.

The situation when particles of different DEP characteristics are present in the same suspension is illustrated in Figure 2.6. Particles of same DEP characteristics align along the applied electric field direction, forming long chains.[6] On the other hand, particles of opposite DEP characteristics form chains, with the pDEP and nDEP particles alternating in the chain.[6] The chain aligns perpendicular to the applied field direction.[6] The details of this phenomenon has been discussed by Morgan et al. [6] by analyzing the computed electric field distributions. The field distribution generated

around the particles determines what particle arrangements and chain orientations will form stable configurations. It turns out that the arrangements of the type shown in Figure 2.6 are stable.

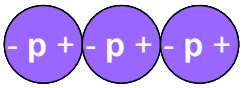

Figure 2.5 Schematic showing the simplified mechanism of pearl chain formation due to the interaction of the separated charge of the induced dipoles (p).

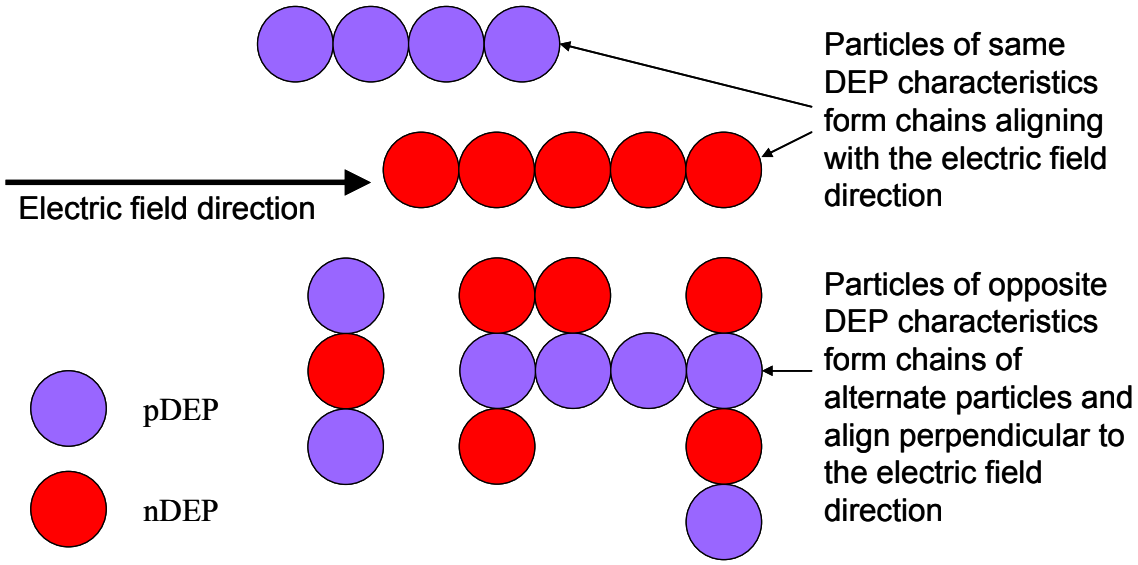

Figure 2.6 Schematic showing pearl chain formation when particles with different DEP characteristics (pDEP and nDEP) are present in a suspension.

While pearl chain formation in biological cells is frequently reported in the literature, nanoparticle pearl chain arrangements have also been demonstrated (Figure 2.7) through DEP of gold nanoparticles on microelectrode gaps.[27] It was possible to pass currents through the assembled nanoparticle chain, which showed ohmic behavior. Passing currents above a threshold value resulted in local melting of the particles. During the experiments, short circuit currents, generated when the chains bridged the electrode gaps, created problems in assembly, because it caused melting.

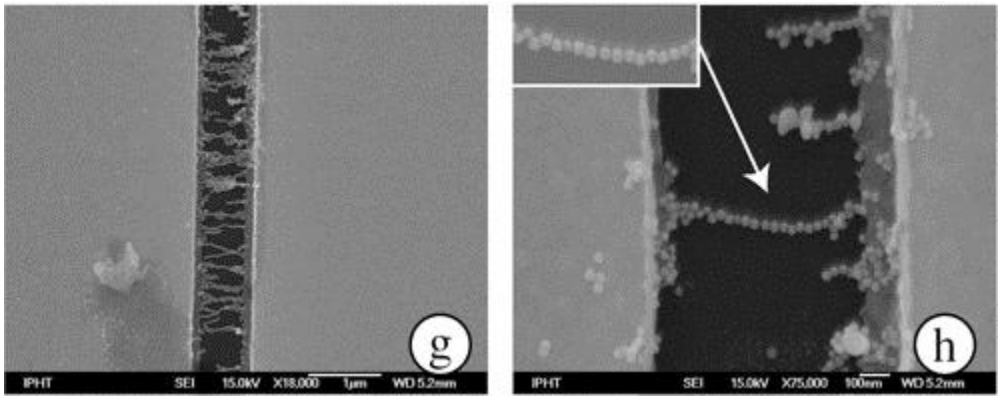

Figure 2.7 Gold nanoparticles forming a pearl chain after AC dielectrophoresis experiments on 1 μm gap electrodes, resulting in gold nanowires bridging the gap.[27]

2.9 Simple Models for Dielectrophoresis of Long Objects

The dipole approximation calculations on dielectrophoresis apply only to spherical and ellipsoidal particles. In general, the dipole approximation does not apply to long objects like nanobelts and nanowires, since the different locations of the long object are under the influence of different electric fields, and hence the DEP force expressions cannot be used for quantitative information on long objects. However, the Clausius-Mossotti factor can provide useful qualitative information to some extent on whether positive or negative DEP will occur in certain material and fluid combinations, and in predicting the trends as a function of frequency.

A simple model has been used for DEP of long objects. They are mostly related to nanowires and nanotubes. The model tries to extend the dipole moment approximation used for ellipsoidal particle, resulting in a DEP force expression for a long object to be of the form [28]

$$\boldsymbol{F}_{dep} = \frac{1}{4}\upsilon(3\varepsilon_m \,\mathrm{Re}[\tilde{K}])\nabla|\boldsymbol{E}|^2 = \frac{1}{2}\upsilon(3\varepsilon_m \,\mathrm{Re}[\tilde{K}])\nabla|\boldsymbol{E}_{rms}|^2 \qquad (2\text{-}19)$$

where υ is the particle volume, $\widetilde{K}$ is the frequency dependent factor equivalent to the Clausius-Mossotti factor, which depends on the shape of the particle. The general expression for $\widetilde{K}$ is given by

$$\widetilde{K}_\alpha = \frac{\widetilde{\varepsilon}_p - \widetilde{\varepsilon}_m}{3\left[\widetilde{\varepsilon}_m + (\widetilde{\varepsilon}_p - \widetilde{\varepsilon}_m)L_\alpha\right]},\ \alpha = x, y, \text{or } z \tag{2-20}$$

where L_α is known as the Lorentz depolarization factor, which depends on the particle orientation relative to the electric field direction.[6] The three L_α components represent the contributions of the polarization of the particle along the three principal axes (of the ellipsoid) due to its interaction with the electric field for a particular orientation. For an ellipsoid, the three $\widetilde{K}_\alpha$ values indicate three distinct Maxwell Wagner relaxation processes, and correspondingly three different relaxation times.[29] The $\widetilde{K}_\alpha$ values depend on the shape anisotropy of the particle. In the case of an isotropic spherical particle, $L_x = L_y = L_z = 1/3$. So, the polarizations along all the three directions are equal, and the previously derived DEP force expression for a sphere is recovered.

For cylindrical particles the polarization depends on their orientation with respect to the electric field. Let us analyze the special case in which a cylindrical nanowire is aligned along the x axis, between electrodes. In such a situation the polarization components along the radial directions can be neglected since these components are much less than the polarization along the wire direction. Hence, the depolarization factors $L_x \to 0$, and, $L_y = L_z \to 1$.[6] For this special situation which may be found useful in nanowire assembly, the Lorentz depolarization factor becomes.

$$\widetilde{K}_x = \frac{\widetilde{\varepsilon}_p - \widetilde{\varepsilon}_m}{3\widetilde{\varepsilon}_m}, \tag{2-21}$$

The $\widetilde{K}_y$, and $\widetilde{K}_z$ components are of no significance, because only the x component of the polarization is the dominant one, in the particular situation considered. The particle volume for a long cylinder is

$$\upsilon = \pi r^2 l \tag{2-22}$$

where r is the radius of the cylinder, and l is the length of the cylinder. Hence, the DEP force on a cylinder with the major axis aligned along the field direction, is given by

$$\boldsymbol{F}_{dep,x} = \frac{1}{4}\pi r^2 l \varepsilon_m \,\mathrm{Re}\left(\frac{\widetilde{\varepsilon}_p - \widetilde{\varepsilon}_m}{\widetilde{\varepsilon}_m}\right)\nabla\left|\boldsymbol{E}\right|^2 = \frac{1}{2}\pi r^2 l \varepsilon_m \,\mathrm{Re}\left(\frac{\widetilde{\varepsilon}_p - \widetilde{\varepsilon}_m}{\widetilde{\varepsilon}_m}\right)\nabla\left|\boldsymbol{E}_{rms}\right|^2 \tag{2-23}$$

The high frequency limit of the DEP force depends on the permittivity mismatch, while the low frequency limit depends on the conductivity mismatch between the particle and the fluid.[30]

$$\omega \to 0, \;\; \mathrm{Re}\left[\widetilde{f}_{CM}\right] \to \frac{(\sigma_p - \sigma_m)}{\sigma_m} \tag{2-24}$$

$$\omega \to \infty, \;\; \mathrm{Re}\left[\widetilde{f}_{CM}\right] \to \frac{(\varepsilon_p - \varepsilon_m)}{\varepsilon_m} \tag{2-25}$$

Hence, low fluid conductivity can cause large forces at low frequencies. This is in contrast with the different frequency limits in the case of spherical particles (Figure 2.3).

The above model was used for estimating the DEP force magnitudes for the dielectrophoretic alignment of gold nanowires [30], and gallium nitride nanowires.[31] However, their utility of this model is limited, because the force expression is valid only for one special case. If the location and orientation of the cylinder changes, the model is invalid. Also, this model is unlikely to be useful for calculating DEP forces in the case of

nanobelts, because of their unique shape and aspect ratio. For accurate quantitative information, a full electrostatics calculation has to be performed. One such method is the Maxwell Stress Tensor (MST) methodology.[22, 32]

2.10 MAXWELL STRESS TENSOR (MST) METHODOLOGY

It has been shown in the literature that the total force on a volume *V*, of dielectric inside an electromagnetic field can be calculated by integrating the so called Maxwell Stress Tensor (MST) of the electromagnetic field [32] over the surface area *S*, of the volume. This tensor is defined as,

$$\boldsymbol{\sigma}^{MST} = \tilde{\varepsilon}\left(\boldsymbol{EE} - \frac{1}{2}(\boldsymbol{E}.\boldsymbol{E})\boldsymbol{I} \right) + \tilde{\mu}\left(\boldsymbol{HH} - \frac{1}{2}(\boldsymbol{H}.\boldsymbol{H})\boldsymbol{I} \right) \tag{2-26}$$

where $\tilde{\varepsilon}$ is the complex electrical permittivity, $\tilde{\mu}$ is the complex magnetic permeability, $\boldsymbol{E}$ is the electric field, $\boldsymbol{H}$ is the magnetic field, $\boldsymbol{I}$ is the unit tensor, and the product of two vectors without a dot denotes the dyadic product.[32] In Einstein notation it can be written as

$$\sigma_{i,j}^{MST} = \tilde{\varepsilon}\left(E_i E_j - \frac{1}{2}E^2\delta_{i,j} \right) + \tilde{\mu}\left(H_i H_j - \frac{1}{2}H^2\delta_{i,j} \right) \tag{2-27}$$

where $\delta_{i,j}$ is the Kronecker delta.

Hence, the force on the volume of dielectric can be written as

$$\boldsymbol{F} = \oint_S \boldsymbol{\sigma}^{MST}.\boldsymbol{n}\, dS \tag{2-28}$$

where *S* represents the surface enclosing the particle, and $\boldsymbol{n}$ is the unit vector normal to the surface of the volume pointing into the region.

In the case of DEP, the magnetic fields can be neglected using the near field approximation [32], since in DEP, the frequency is typically low and the wavelength of the electromagnetic field is much larger compared to the DEP setup. Hence, the tensor reduces to

$$\boldsymbol{\sigma}^{MST} = \tilde{\varepsilon}\left(\boldsymbol{EE} - \frac{1}{2}(\boldsymbol{E}.\boldsymbol{E})\boldsymbol{I} \right) \tag{2-29}$$

For AC fields, it has been shown that the time averaged stress tensor is given by [32]

$$\left\langle \boldsymbol{\sigma}^{MST} \right\rangle = \frac{1}{4}\mathrm{Re}[\tilde{\varepsilon}]\left(\boldsymbol{EE'} + \boldsymbol{E'E} - |\boldsymbol{E}|^2 \boldsymbol{I} \right) \tag{2-30}$$

For DEP force evaluation, the surface for integration is the interface between the particle and the medium, and the electrical field used in the stress tensor is calculated using the fluid medium properties. Hence,

$$\left\langle \boldsymbol{\sigma}^{MST} \right\rangle = \frac{1}{4}\mathrm{Re}[\tilde{\varepsilon}_m]\left(\boldsymbol{EE'} + \boldsymbol{E'E} - |\boldsymbol{E}|^2 \boldsymbol{I} \right) = \frac{1}{4}\varepsilon_m \left(\boldsymbol{EE'} + \boldsymbol{E'E} - |\boldsymbol{E}|^2 \boldsymbol{I} \right) \tag{2-31}$$

and, the time averaged DEP force and torque on the particle can be obtained by performing the following integrations on the particle outer surface

$$\boldsymbol{F}_{dep} = \oint_S \left\langle \boldsymbol{\sigma}^{MST} \right\rangle . \boldsymbol{n}\, dS \tag{2-32}$$

$$\boldsymbol{T}_{dep} = \oint_S \boldsymbol{r} \times \left\langle \boldsymbol{\sigma}^{MST} \right\rangle . \boldsymbol{n}\, dS \tag{2-33}$$

where $\boldsymbol{r}$ is a vector connecting the axis of interest, about which the torque is evaluated, to the particle surface. These integrations can be easily performed numerically in finite element packages for arbitrary particle shapes.

2.11 DIELECTROPHORETIC ASSEMBLY AND MANIPULATION

The DEP effect is independent of the charge on the particle.[5] Neutral particles are subject to this effect, and therefore DEP is more versatile in its applications for manipulating live cells, macromolecules, nanostructures, etc. DEP has traditionally been used for manipulating cells and other objects of size in the micrometer range (1 - 1000 μm) [5]. A review of cell manipulation using DEP has been provided by Voldman.[33] Only recently has DEP been used to study, manipulate and separate nanometer scale objects such as latex spheres, viruses, nanowires, carbon nanotubes, macromolecules, etc.[21] One of the reasons for this is the recent advances in fabrication of micro and nanoelectrodes. Since the DEP force on an object is generated by gradients in the electric fields, as the electrode size and spacing is reduced, the fields (proportional to the inverse of the gap) and the gradients go up dramatically. Hence, microfabricated electrodes are very popular in the field of DEP research and applications. The force fields in microelectrode structures and the dynamics of sub-micrometer particles in such structures have been reviewed in the literature by Morgan, and Green.[6] An excellent review of the applications of DEP in nanotechnology and future possibilities has been presented by Burke.[21] The rest of this section reviews a few important early studies on the applications of DEP for assembly and manipulation of nanowires, carbon nanotubes, and such long objects.

AC dielectrophoretic alignment and assembly of metallic (Au) nanowires (35 to 350 nm diameter, and up to 8 μm long) was demonstrated by Smith et al. [34] on electrically isolated electrodes. Field strengths of up to 10^7 V/m, and frequencies from 20 Hz to 20 kHz were applied for attracting the nanowires. A silicon nitride layer of 500 nm

thickness was deposited over the electrodes so that the shorting of the electrodes could be prevented, once the highly conductive Au nanowires aligned between the electrodes.[34] Positive trapping (Figure 2.8) of the Au nanowires was found between the electrodes for frequencies above 200 Hz, with the effectiveness increasing with higher frequencies. Iso-propyl alcohol (IPA) was the dielectric medium used during the DEP assembly process.

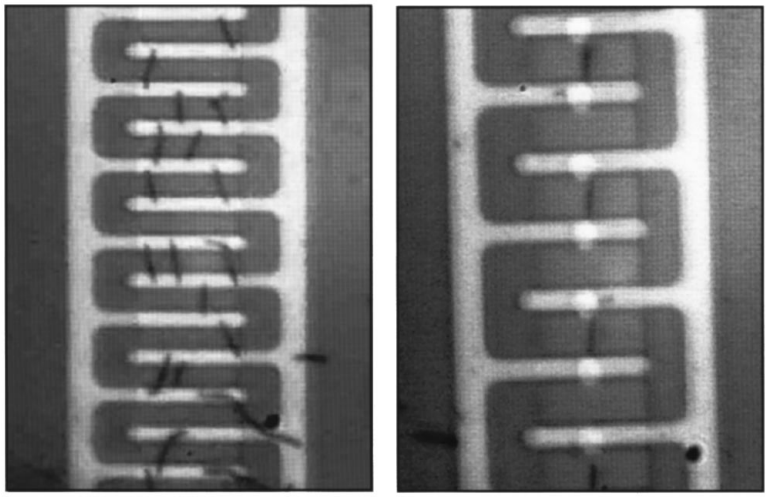

Figure 2.8 Au nanowires (dark lines) aligned using (a) 30 V_{rms}, 1 kHz signal between electrically isolated electrodes beneath silicon nitride layer, and (b) 20 V_{rms}, 1 kHz signal to the same electrodes, but with additional electrode pads on top of the nitride layer.[34]

Yamamoto et al. [35] performed DEP studies on multi-walled carbon nanotubes (MWNTs) of lengths between 1 and 5 μm, using Al electrodes with 400 μm gaps, field strengths of 2×10^5 V/m, and iso-propyl alcohol (IPA) as the dielectric medium. They observed alignment and attraction of the nanotubes to the electrodes (pDEP) for AC frequencies between 10 Hz and 10 MHz. The degree of alignment of the nanotubes increased with increasing frequency, and increasing nanotube lengths. They also found that the alignment was more effective with AC dielectrophoresis compared to DC

dielectrophoresis.[36] Similar studies were carried out on single walled carbon nanotubes (SWNTs) by Chen et al.[37] The SWNTs were dispersed in ethanol, and electric fields of 5×10^6 V/m strength in the frequency range 500 Hz to 5 MHz was applied. The DEP was positive for all the frequencies studied. The SWNTs were found to be oriented more strongly at higher frequencies. They found no effect of DC electric fields on the alignment.

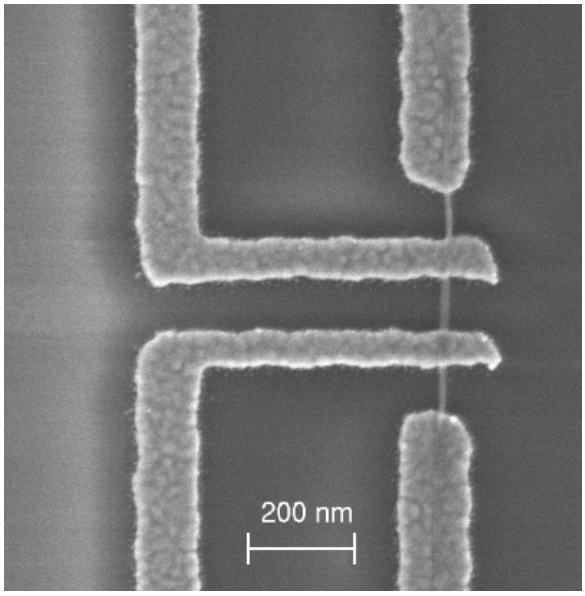

Figure 2.9 SEM image of a single 9 nm diameter SWNT bundle trapped on four Au electrodes. AC field was applied between the upper right and lower right electrodes.[38]

Single walled carbon nanotube bundles were suspended in N, N-dimethylformamide (DMF) and attracted between nanoelectrodes (~ 100 nm gap) (Figure 2.9) with an applied AC voltage of 1 V_{rms}.[38] Good alignment between the electrode was observed at frequencies above 1 kHz. Because of the presence of –COOH functional groups on acid-treated nanotubes, the selection of the electrode material was found to affect the DEP manipulation process.[38] The nanotubes formed electrical contacts with

Ag electrodes in the presence of the suspension, while similar contacts did not form with Au electrodes. The reason for this is thought to be the strong affinity of the –COOH groups on the acid-treated nanotubes to Ag surfaces. As a result, a single or just a few nanotubes got trapped on Ag electrode gaps, while most of the time, multiple nanotubes got trapped on Au electrode gaps.[38]

DEP manipulation of nanotubes using very small electrode gaps have been studied by Chung et al. [39], who demonstrated the assembly of single walled carbon nanotubes (SWNTs) between 20 nm gap electrodes. The electrode tip radius had a strong influence on the assembly and alignment of the nanotubes. In another study, SWNTs suspended in aqueous medium were attracted between nanoelectrodes with gaps ranging from 20 - 80 nm using [40] AC voltages between 0.5 - 2.5 V_{pp} of 5 MHz for 1 - 30 seconds.

A multi walled carbon nanotube (MWNT) based gas sensor has been fabricated using DEP.[41] MWNTs were dispersed in ethanol and trapped and concentrated at an interdigitated microelectrode gap under the action of a positive DEP force. After the DEP process, the ethanol was evaporated and the microelectrode retaining the MWNTs was exposed to ammonia (NH_3) gas.

To the best of my knowledge, the earliest reported work on manipulation of semiconducting nanowires using DEP was done by Duan et al.[42] However, it was DC dielectrophoresis, which was used to align and electrically contact InP nanowires of 30 nm diameter to Ni/In/Au contact electrodes. The electrode gap separation was about 25 μm and the electric field strength between the electrodes was ~ 10^7 V/m. Chlorobenzene was used as the solvent medium, so that electrolysis was not an issue, since high DC

voltages (50 - 100 V) were used in the DEP process. They were able to align InP nanowires into a cross-bar topology using a layer-by-layer application of the alignment process.

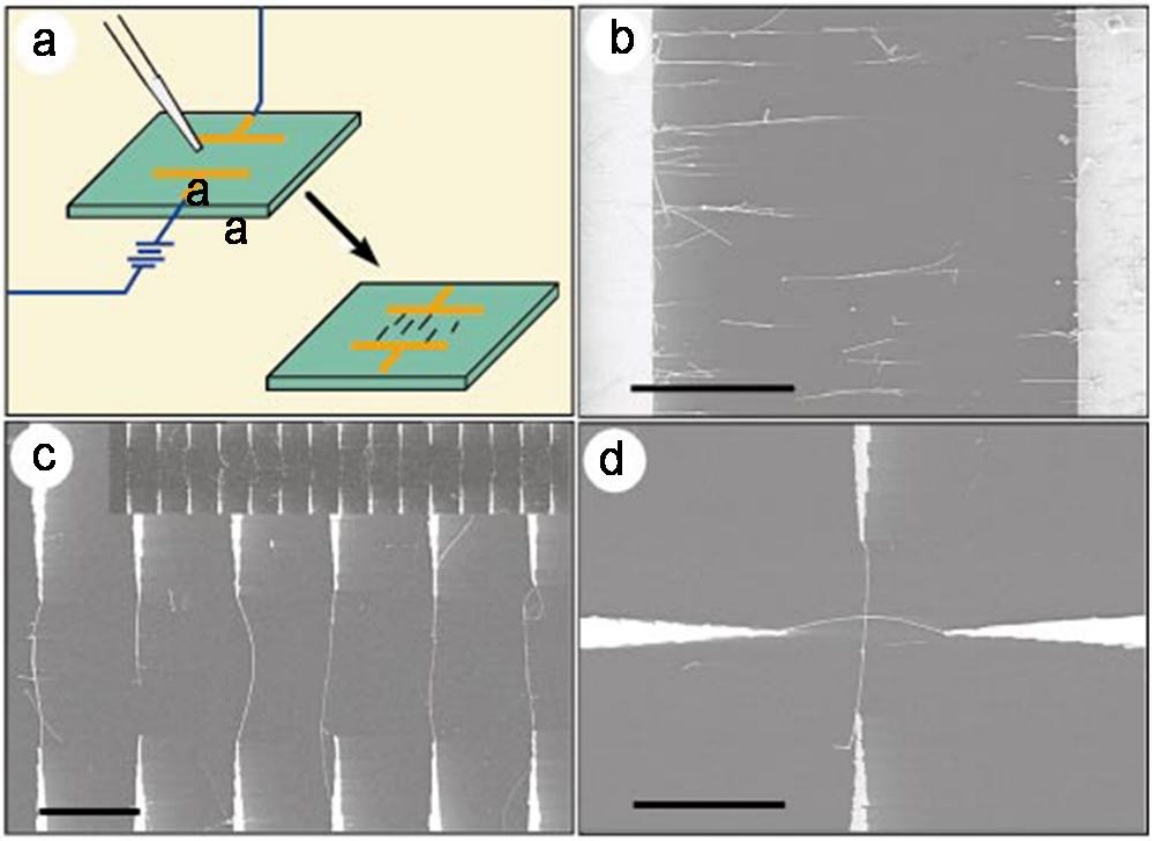

Figure 2.10 Assembly of InP nanowires, (a) schematic view of the alignment process, (b) nanowires aligned between two parallel electrodes, (c) parallel array of nanowires, and d) orthogonal nanowire junction obtained using layer-by-layer alignment with the electric field in two assembly steps. The scale bars in (b) - (d), are 10 μm in length.[42]

In recent years there have been many more reports on the assembly of nanowires, nanotubes, and other types of nanowire structures using AC dielectrophoresis. It has been used for the assembly of SnO_2 nanobelts in ethanol [43], ZnO nanowires in ethanol [44], and nickel silicate (NiSi) nanowires (Figure 2.11) in ethanol.[45]

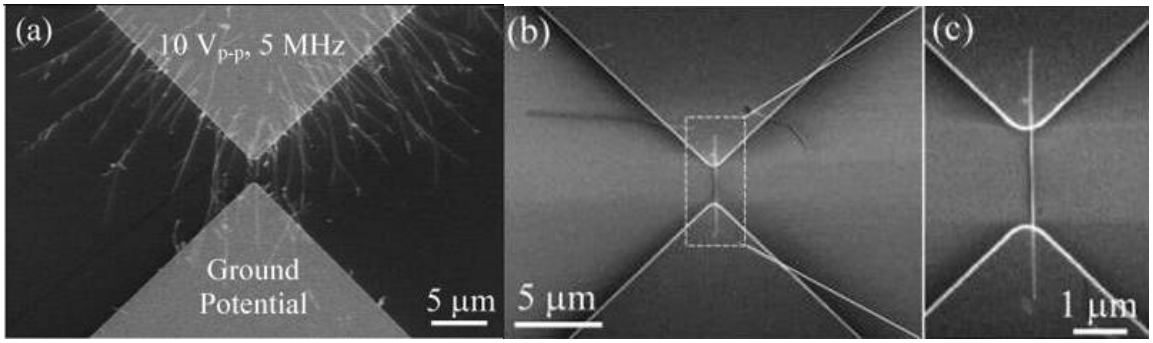

Figure 2.11 NiSi nanowires aligned using dielectrophoresis on Pt electrodes, (a) multiple nanowires, (b) single nanowire, and (c) magnified view of the single nanowire.[45]

2.12 REAL TIME STUDY OF NANOWIRE DIELECTROPHORESIS

As described in section 2.11, several research groups have demonstrated the manipulation and assembly of nanowires, carbon nanotubes, etc., utilizing DEP. However, most of these reports are limited to attracting the nanostructures between electrodes for device fabrication, including our report [43] on SnO_2 nanobelts. Very few publications exist in the literature on the direct observation and visualization of the DEP process applied to nanowires and such long objects. Recently, there have been some reports in this direction.

Fan et al. [46] studied the real time motion of Au nanowires of 300 nm nominal diameter and lengths between 10 and 15 μm under the action of AC dielectrophoretic forces, using concentric circular electrodes. The advantage of using circular electrodes is that the electric field distribution (Figure 2.12) is identical in most radial paths. The electric field and its gradient are both along the radial direction. Experiments can be performed in almost any radial section between the electrode gap, and the results will be the identical. However circular electrodes are of not much use in real applications.

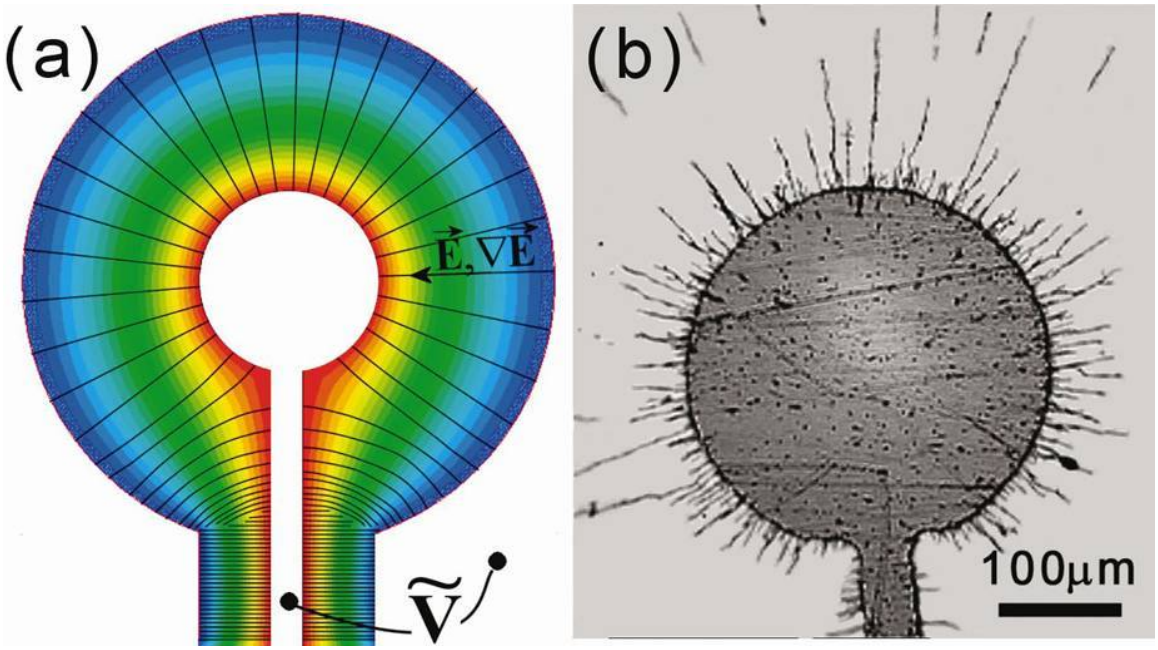

Figure 2.12 (a) Electric field distribution (black lines) and electric potential (color contour) between concentric Au electrodes (in white), and (b) Au nanowires attached to the inner electrode (in gray) after DEP experiments.[46]

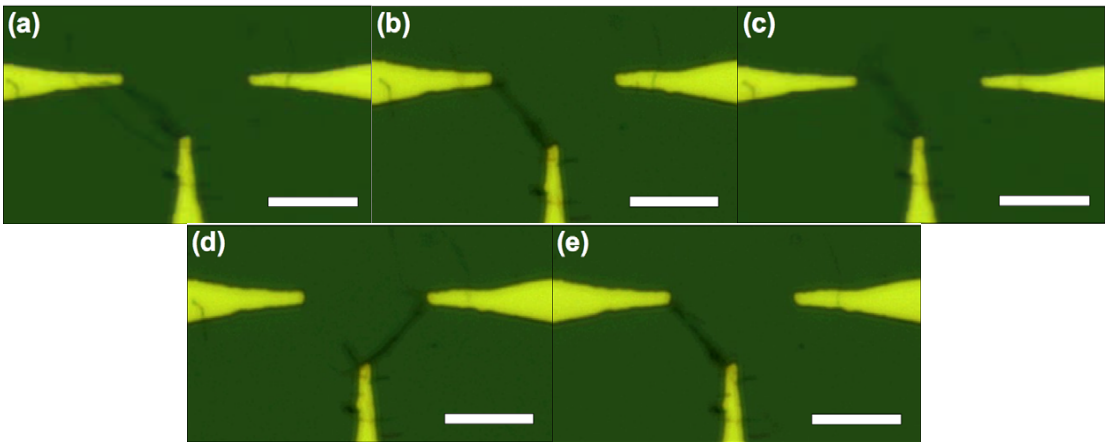

Figure 2.13 Images showing reconfiguration of Si nanowires between electrodes by modulating the relative phase between the three electrodes. The scale bar is 15 μm.[47]

P-type silicon nanowires suspended in benzyl alcohol was used to demonstrate assembly, reconfiguration, and disassembly between gold electrodes (Figure 2.13) by Wissner-Gross.[47] The real time observation of the changing configuration was

performed using an optical microscope. The change in the configuration of a nanowire bundle was performed by using 'source' and 'drain' electrodes with opposite phase and a 'latch' electrode with variable phase.[47] A similar but more rudimentary study on silver and gold nanowires was performed by Papadakos et al. [48] in water and ethanol medium.

Hammers et al. [49], and Marcus et al. [50] performed real time detection of nanowire bridging events. The experiments were performed in aqueous media using gold nanowires (diameters ~ 50 - 250 nm), silicon nanowires (diameter ~ 50 nm), and carbon nanofibres (diameter ~ 70 nm).

As can be inferred from the limited literature, there is a need for more detailed real time observation of nanowires and similar long nanostructures under dielectrophoretic force fields. The current research is an effort in this direction. AC dielectrophoresis experiments on SnO_2 nanobelts suspended in ethanol are performed to observe the wide variety of nanobelt motions, induced by the DEP forces. Estimates of the relative DEP force magnitude as a function of the applied signal frequency is also made. Unusual DEP effects are observed. Measurement of the material properties of the nanobelts and numerical simulations provide insights to explain these effects.

2.13 Fluid Flow Alignment of Long Objects

Assembly of nanowires and other nanostructures usually requires manipulation in liquid suspension. One of the methods reported in the literature is that of fluid flow alignment [51] of nanowires on chemically patterned substrates. The principle is simple. A suspension of nanowires is allowed to flow along microfluidic channels. The drag

force of the liquid allows the nanowires to be aligned straight along the channel while in suspension, and eventually fall on to the substrate surface and get attracted to the chemically patterned positions with orientations along the channel. Some devices have also been made using this method.[51] Recently this technique was used for the alignment of carbon nanotubes [52, 53], and for the fabrication of carbon nanotube field-effect transistors.[54]

Single monolayer (SAM) patterning was used for the assembly of single walled carbon nanotubes (SWNTs), during which the nanotubes aligned over the molecular patterns through chemical interactions.[55] However, there was no need of fluidic alignment. The substrate was simply dipped in the solution of carbon nanotubes.

Mahajan et al. [56] created 2D parallel arrays of aligned lipid micro- and nanotubules with controlled separations using fluidic alignment and dewetting inside microfluidic channels on a glass substrate. The pattern was then used as a template to synthesize silica thin films.

CHAPTER 3

DIELECTROPHORESIS OF MULTIPLE TIN OXIDE NANOBELTS AND TITANIUM DIOXIDE DIATOMS

Using castellated electrodes with multiple electrode gaps, positive and negative dielectrophoresis (DEP) was demonstrated for the first time on semiconducting oxide nanobelts. This effect was then used for the fabrication of a nanodevice, which consisted of SnO_2 nanobelts attached to castellated gold electrodes, defined on a glass substrate, and covered by a microchannel. The SnO_2 nanobelts were suspended in ethanol and introduced into the microchannel. AC voltage signals with variable frequencies were applied between the electrodes (minimum electrode gap ~ 20 μm). In the low frequency range (10 Hz - 1 kHz), repulsion between the nanobelts and the electrodes occurred, while attraction was observed in the high frequency range (1 - 10 MHz),. Once the nanobelts touched the electrodes, those that were sufficiently long bridged the electrode gaps. The device was characterized and can potentially be used as a nanosensor. Some additional DEP experiments were also performed on SnO_2 nanobelts suspended in kerosene, SnO_2 microparticles suspended in kerosene and ethanol respectively, and TiO_2 diatoms suspended in ethanol.

3.1 EXPERIMENTAL

The DEP manipulation of nanobelts was carried out using arrays of castellated microelectrodes defined on Pyrex glass. The microelectrode array was covered with a

microchannel so that the nanobelt suspension could be pumped through it. Some experiments were conducted on an alternate arrangement in which an SU-8 photoresist defined space acted as a reservoir for the nanobelt suspension. A glass coverslip was used to close this space after putting the suspension over the electrode.

3.1.1 Fabrication of Microelectrodes

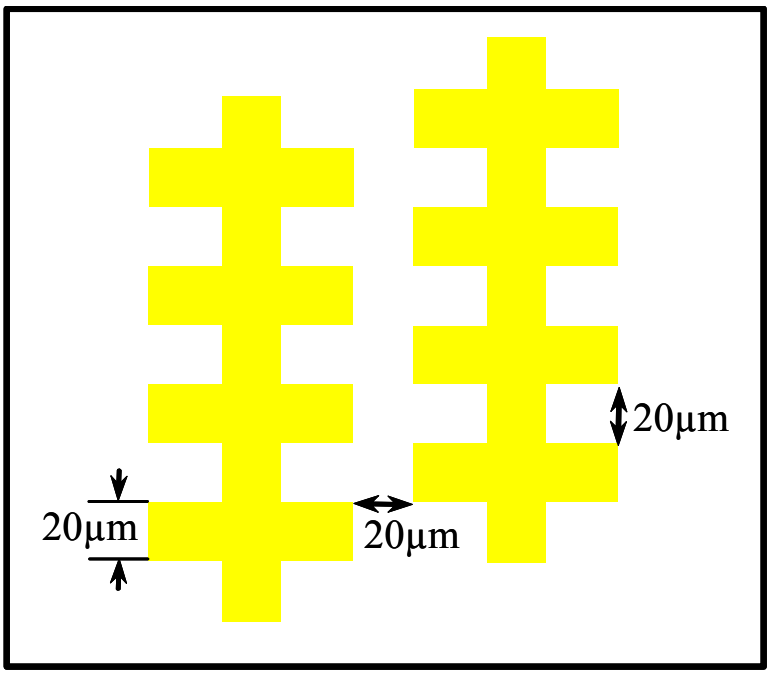

Figure 3.1 Castellated structure of the DEP microelectrodes.

Fabrication of the microelectrodes was carried out on 1 mm thick Pyrex glass substrates (*G.M. Associates Inc.*, Oakland, CA, USA). The transparent substrate allowed visualization of the nanobelt manipulation from the bottom side using an inverted microscope. The substrates were cleaned to improve adhesion using a base clean solution (5:1:1 solution of DI / NH_4OH / H_2O_2), and then treated with O_2 plasma for 15 minutes in an RIE system (*Plasma-Therm Inc.*). The Ti/Au electrode was patterned on the wafer using standard lithographic techniques and lift-off process. First, the pattern was defined

in negative acting NR5-8000 photoresist (*Futurrex Inc.*, Franklin, NJ, USA). After treating the wafer with oxygen plasma for 3 - 5 minutes, a 300 Å thick Titanium (Ti) layer and a 2500 Å thick Gold (Au) layers were deposited using an electron beam evaporator system. The sample was then dipped in acetone for about 10 minutes to remove the photoresist, making the microelectrodes ready for use. The pattern of the electrodes is castellated in nature as shown in Figure 3.1. The fabrication process flow is summarized in Figure 3.2, which also includes the SLA microchannel integration.

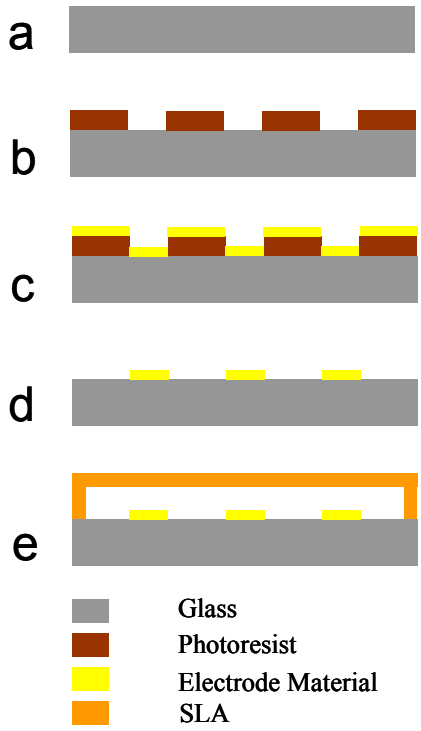

Figure 3.2 Schematic diagram of the process flow (steps (a) to (e)) used in the fabrication of the DEP device.

3.1.2 Fabrication of SLA Microchannel

Stereolithography (SLA) is a rapid prototyping technique [57] that can be used for making parts of complicated geometry. The advantages of SLA process are the rapid

fabrication and design flexibility. The microchannel, with a channel depth of about 150 μm, has an inlet and an outlet (see Figure 3.3 (a) and (b)) so that the nanobelt suspension can be pumped through it. The SLA microchannel fabrication was performed using a 3D Systems Viper 1500 (*3D Systems Corporation*, Valencia, CA, USA) machine. Stereolithography resin Vantico SL 5510 (*Huntsman Advanced Materials,* Salt Lake City, UT, USA) was used. The fabrication process involves the curing of the resin layer by layer using a computer controlled laser. The fabricated parts are then cleaned in iso-propyl alcohol (IPA) and cured in an ultra violet (UV) oven for 90 minutes. The details of the process are described in section 5.1.1, although that section considers a different configuration.

3.1.3 Assembly of Microelectrodes and SLA Parts

The SLA microchannel and the Pyrex substrate, which had microelectrodes defined on it, were carefully aligned and bonded with epoxy (Loctite Extra Time, *Henkel Consumer Adhesives*, Avon, OH, USA) to assemble the DEP device. Electrical connections were made using gold wires and conductive epoxy (Loctite 3880, *Henkel Consumer Adhesives*, Avon, OH, USA). A layer of epoxy (Loctite Extra Time) was then coated on the wire bonds to prevent them from breaking off. Figure 3.3 (a) and (b) show the assembled DEP device. The width and length of the SLA microchannel are ~ 1 cm and ~ 2 cm respectively. Connections were established with the two independent electrode arrays on the same device. They are marked as E_1 and E_2 in Figure 3.3(a).

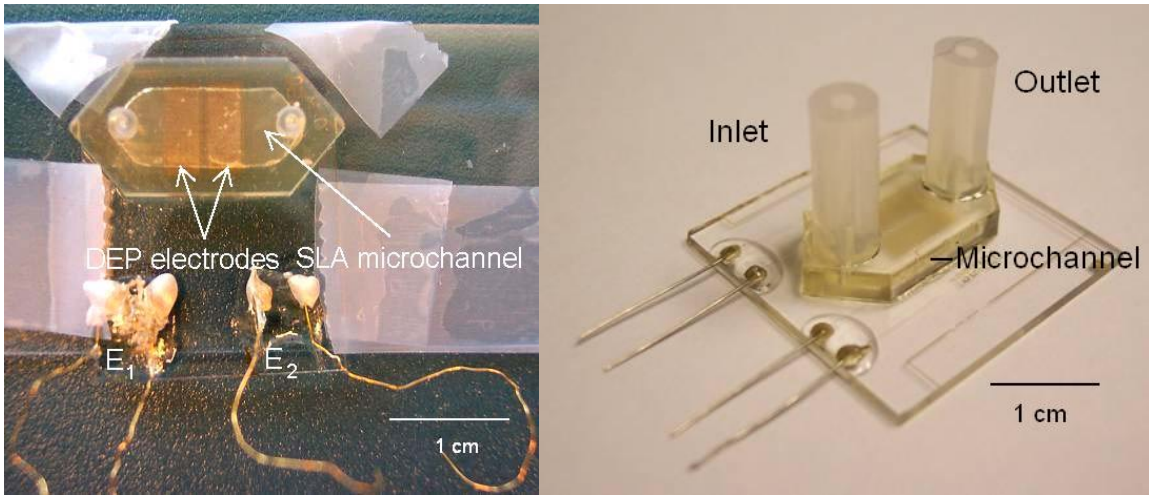

(a) (b)

Figure 3.3 DEP Experimental Arrangement 1 showing (a) top view of the SLA microchannel and the electrodes under it, and (b) the fluidic connections viewed from an angle.

3.1.4 Alternate Arrangement Using SU-8 Patterning

An alternate DEP experimental arrangement 2 (Figure 3.4(a) and (b)) was made by patterning SU-8 layer on top of the DEP electrodes to form the measurement cell. To fabricate the cell, a 40 μm thick layer of SU-8 2050 (*MicroChem* Corp., Newton, MA, USA) was coated on the glass substrate on which the microelectrodes were already defined. The SU-8 was then patterned using photolithography to define the measurement cell. Experiments with SnO_2 microparticles (~ 1 μm diameter) and also some SnO_2 nanobelts were performed on this arrangement. The suspension was made in kerosene and ethanol respectively. A droplet of suspension was put into the cell and a glass cover slip placed over it. The liquid surface tension ensured that the glass coverslip was firmly in place over the cell. AC voltage was applied and its effect observed.

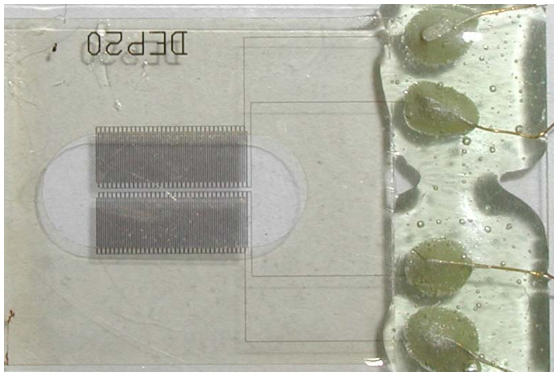

(a)

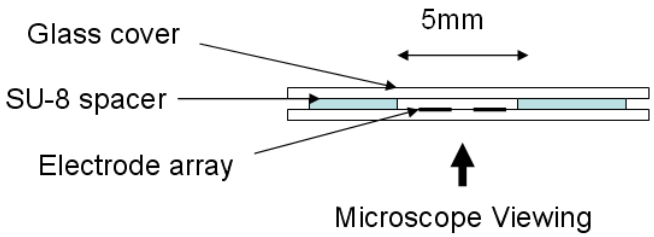

(b)

Figure 3.4 DEP Experimental Arrangement 2 showing (a) electrode array with 40 μm SU-8 layer to define measurement cell, and (b) schematic diagram indicating the experimental set up for observing the nanobelt motion over the electrodes.

3.1.5 SnO_2 Nanobelt Samples

SnO_2 nanobelt samples were made using the thermal evaporation (PVD) method outlined in [1, 58]. It is a process in which condensed powder source material is vaporized at an elevated temperature in a tube furnace and the resultant vapor is condensed under controlled conditions (temperature, pressure, atmosphere, substrate, etc.) to form the desired product. Argon (Ar) carrier gas enters the alumina tube in the furnace (50 cm long, 4 cm diameter), and is pumped out by a rotary pump. The source material is loaded on an alumina boat and positioned at the center of the tube. Several alumina plates (60 mm × 10 mm) were placed downstream, one behind the other, inside the alumina tube, which acted as substrates for collecting the growth products. At a pressure of 200 - 600 torr, thermal evaporation of SnO powder (purity 99.9 %, melting

point 1080 °C, *Alfa Aesar*, Ward Hill, MA, USA) was carried out at ~ 1050 °C for 2 hours, under an Ar carrier gas flow of 50 SCCM. The substrate temperature was carefully controlled during the deposition. The same nanostructure can also be made at 1350 °C from SnO_2 powder (purity 99.9 %, melting point 1630 °C).[58]

The chemical composition of the nanobelts is of the form SnO_{2-x}, where x = 0 - 0.2, which was determined using EDS measurements.[59] This is thought to be evidence of oxygen vacancies, which are responsible for the n type semiconducting properties of SnO_2.[59] The nanobelts have a rutile structure with lattice constants a = 4.732 Å and c = 3.184 Å, which is the same as in the case of bulk SnO_2 material structure.[59] The individual SnO_2 nanobelt crystals grow along the [101] crystal direction and the surfaces enclosing them are the $\pm(010)$ and $\pm(10\bar{1})$ crystallographic planes.[1, 58] The nanobelt product obtained from the furnace is in the form of agglomerates, with the individual nanobelts intertwined with one another. Figure 3.5 shows an SEM picture of raw SnO_2 nanobelt sample. Nanobelts have a rectangle like cross section with typical widths of 30 - 300 nm, width-to-thickness ratios of 5 to 10, and lengths of up to a few mm's.[1] Nanobelts wider than 300 nm are also encountered in the samples, sometimes. The size range is determined by the growth conditions.[1, 58] The figure shows that in addition to nanobelts, the sample also contains other structures, such as nanodisks.[58] Moreover, one can notice that the size of the nanobelts is not very uniform. There is a size distribution of the nanobelts in any sample.

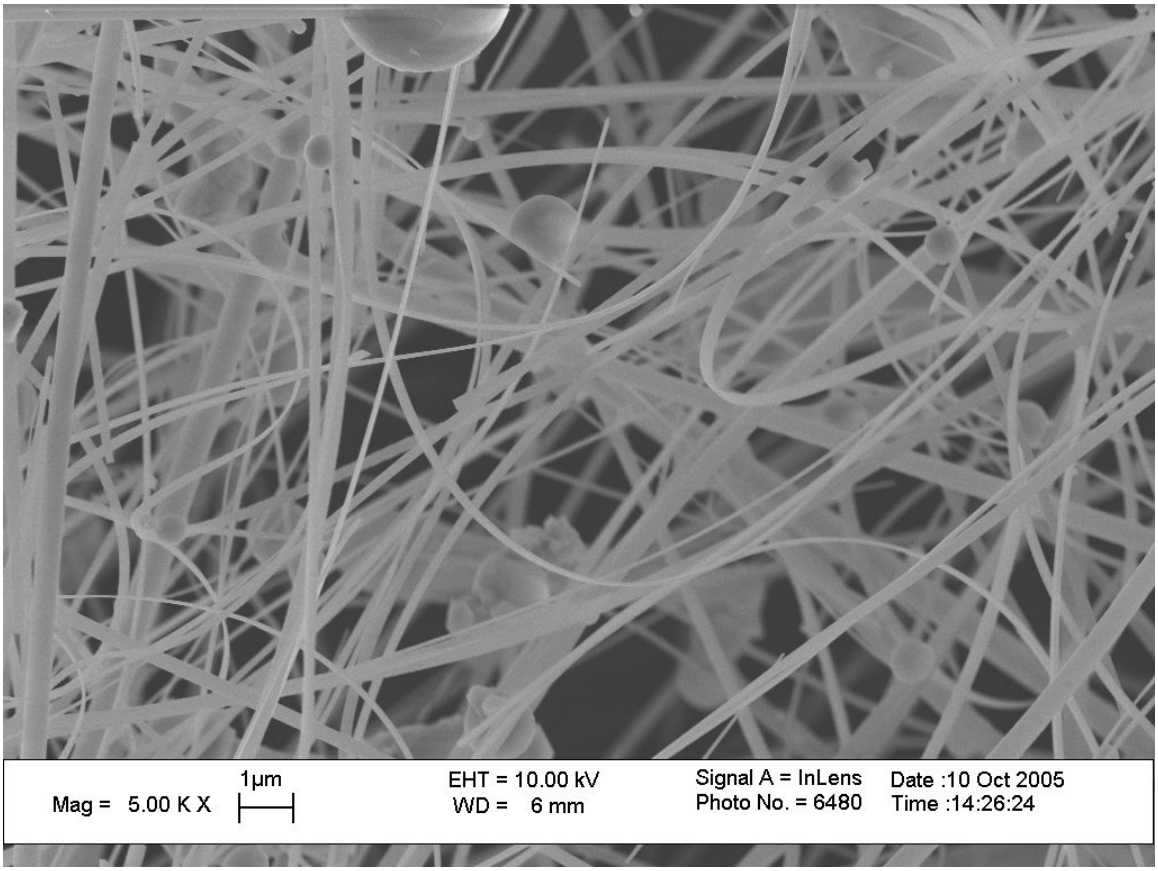

Figure 3.5 SEM image of raw SnO_2 nanobelt sample (agglomerates).

The individual nanobelts can be very long (up to a few mm's in length) which are intertwined with other long nanobelts. In order to use the nanobelts in a device, it is necessary to separate the agglomerates into individual nanobelts. Hence, ultrasonication of the nanobelt agglomerates was carried out in ethanol (and in a few cases, in kerosene) to produce a nanobelt suspension. Ultrasonication, which is a standard method of suspending the nanobelts in liquids, causes the long nanobelts to break up into smaller lengths.

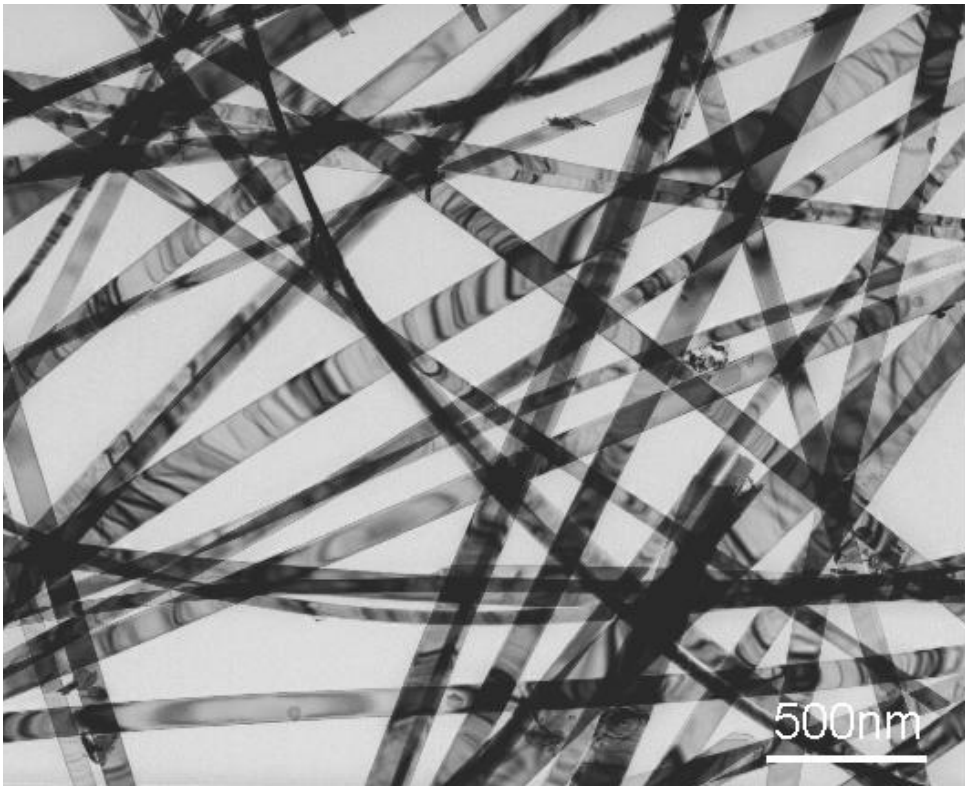

Figure 3.6 TEM images of an as synthesized SnO_2 nanobelt sample (agglomerates).[58]

Figure 3.6 shows a typical TEM image of SnO_2 nanobelts. Since the nanobelts are under stress and deformation, it shows up in the TEM image as the bright and dark fringes on the nanobelts.

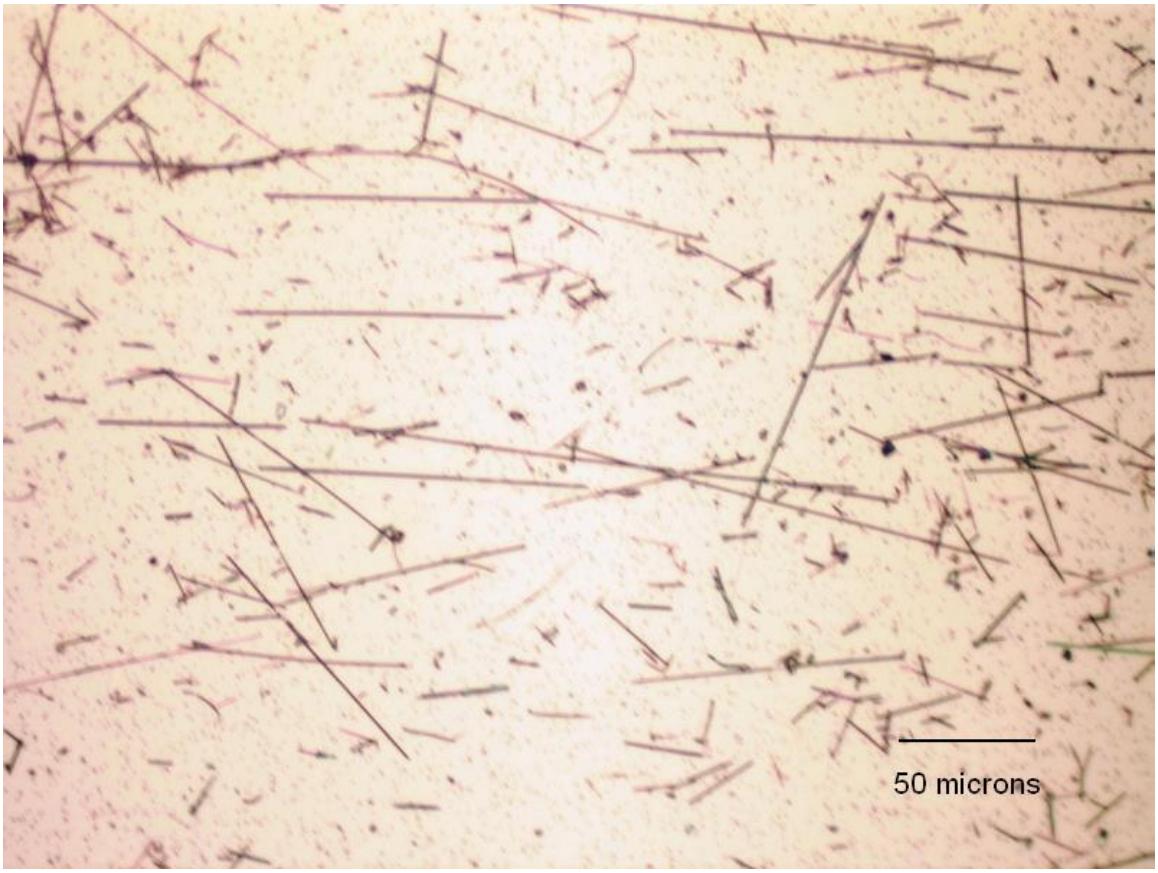

Figure 3.7 Optical microscope image of SnO_2 nanobelts dispersed on Au/Si substrate. The lengths of the nanobelts vary depending on the sonication time.

Figure 3.7 shows an image of SnO_2 nanobelts dispersed on Au/Si substrate (gold layer on top of silicon). The ethanol was evaporated and the sample observed under an optical microscope. The length distribution of the nanobelts depends on the sonication time used to break up the initially long nanobelts. In the photograph, both short and long nanobelts are visible. The nanobelts used in the tests had a width in the range of 100 - 300 nm, so that they could be observed under an optical microscope as dark lines. Figure 3.8 shows an atomic force microscope (AFM) measurement to obtain the nanobelt thickness. The measurement indicates the thickness to be ~ 65 nm and the width to be ~ 500 nm. However, the typical thickness of the nanobelts is 30 - 40 nm. SEM imaging of

the nanobelt samples used in the DEP experiments was also used to confirm the widths of the nanobelts.

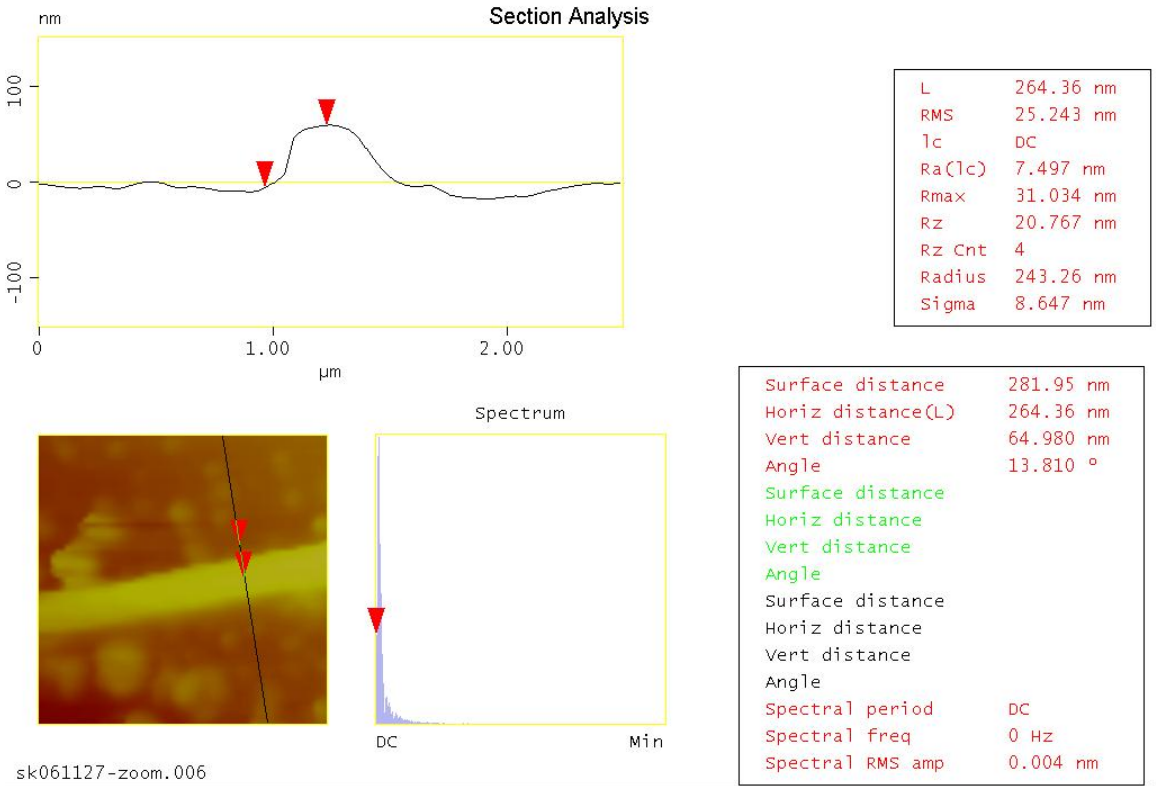

Figure 3.8 Picture showing AFM imaging of an SnO_2 nanobelt on glass substrate.

3.1.6 Experimental Setup and Testing

Flexible Tygon tubings of 1.02 mm ID were attached to the inlet and outlet of the DEP device. A 20 ml syringe was filled with the nanobelt suspension and used with a syringe pump to pump the nanobelt suspension through the SLA microchannel at a controlled flow rate (0.05 - 0.10 ml/min). Once the suspension started flowing, an AC voltage of 10 V_{peak} was applied between the electrodes using a Synthesized Function Generator (*Stanford Research Systems Inc.*, Sunnyvale, CA, USA). The signal frequency was varied from 10 Hz to 10 MHz and the effect on the nanobelts was observed. During

the experiment the flow time was monitored so that the number of nanobelts bridging the electrode gaps could be controlled. The nanobelts could be seen as dark lines through the Nikon Eclipse TE2000-S (*Nikon Instruments Inc.*, Melville, NY, USA) inverted microscope. Digital images were taken using a computer controlled imaging software, MetaMorph® Imaging System (*Universal Imaging Corporation*, Downingtown, PA, USA), which enabled automated image capture and analysis from a digital CCD camera attached to the microscope.

After the DEP experiment, the ethanol in the device was evaporated by drying. The application of DC voltages between the electrodes caused currents to flow through the nanobelts between the electrodes. It shows that the electrical contacts between the gold electrodes and the SnO_2 nanobelts did take place, although it might not be the best possible contact without metal deposition over the nanobelts. Various tests were performed using the DEP device to characterize it, which involved measurements of current, voltage, and impedance. The effect of changes in temperature and lighting conditions was also studied.

LabVIEW software (*National Instruments Corporation*, Austin, TX, USA) was used for data acquisition. For current and voltage measurements, a Keithley 195A Digital Multimeter (*Keithley Instruments, Inc.* Cleveland, OH, USA) was used in combination with Tektronix PS2520G Programmable Power Supply (*Tektronix, Inc*. Beaverton, OR, USA). The LabVIEW software could also scan the applied voltage at a predetermined scan rate and record the current.

As a source of visible light, a Model 180 - Standard 150 Watt Illuminator (*Dolan-Jenner Industries, Inc.*, Lawrence, MA, USA) with a quartz halogen lamp was used. For

UV light, a Blak-Ray Model B-100A (*Blak-Ray Inc.*, San Gabriel, CA, USA) which emits UV radiation at 365 nm wavelength, was used.

For impedance measurements Solartron SI 1260 Impedance/Gain-Phase Analyzer (*Solartron Analytical*, Farnborough, UK) was used in combination with Solartron 1296 Dielectric Interface. The range of the frequency sweep was 0.01 Hz to 10 MHz.

Measurements were performed in ambient under different lighting conditions - no light, visible light, and UV light exposures. The effect of temperature was studied under inert conditions, by flowing dry nitrogen through the DEP microchannel, with an electrical strip heater (*Watlow Electric Manufacturing Company*, St. Louis, MO, USA) was attached to the Pyrex glass substrate (bottom of the DEP device). A variable DC current source was attached to the heater to control the temperature of the device.

Some DEP experiments were also performed on TiO_2 diatoms. In those experiments the SLA microchannel was not used. Only the bare electrodes were used. The diatoms are much larger than the nanobelts. Hence, they readily came close to the electrode surface due to sedimentation, and the visualization was much easier.

3.2 Results and Discussion

3.2.1 Dielectrophoresis of SnO_2 Nanobelts

Figure 3.9 shows the DEP electrodes as observed under the inverted microscope. The electric field is generated between the alternating branches. As explained in the experimental section, the SnO_2 nanobelt suspension was introduced into the microchannel, and the nanobelts manipulated using AC voltages with different

frequencies. The voltage applied was 10 V_{peak}, which is quite low compared to other DEP studies [34, 42].

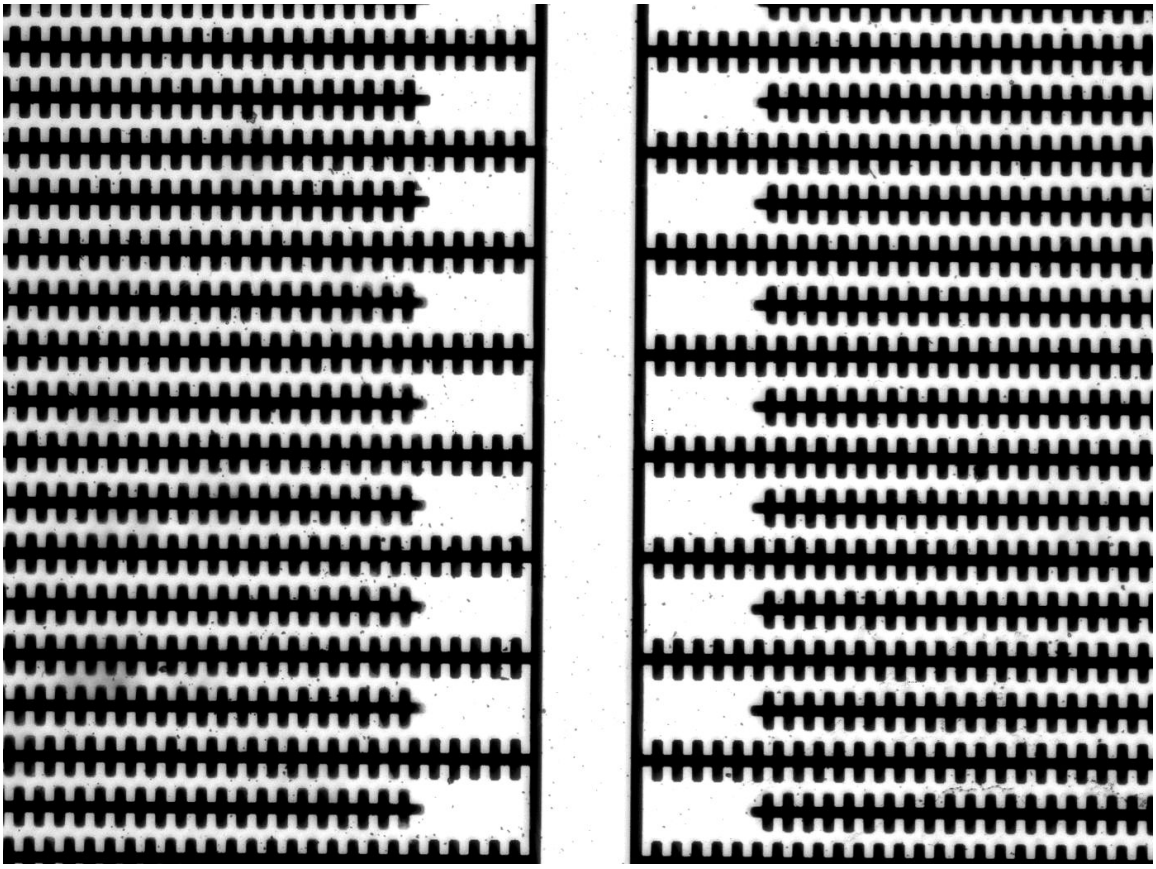

Figure 3.9 An optical microscope photograph of the DEP electrode arrays, showing two separate arrays and the electrode structure (dark). The electric field is established between the alternating branches (dark). The white background is the glass substrate. The electrode gap is ~ 20 μm.

It was observed that in the 10 Hz - 1 kHz (low) frequency range, repulsion of the nanobelts from the electrodes occurred, which demonstrates negative DEP. The nanobelts were seen vibrating in the gaps between the electrodes such that the ends of the nanobelts were away from the electrodes (aligned perpendicular to a line connecting the gaps). In the 1 - 10 MHz (high) frequency range, the nanobelts were attracted between the electrodes (positive DEP). The reason for the alignment under low voltage is

possibly the long lengths of the nanobelts (see Figure 3.7). In Chapter 9 the finite element simulations indicated that the major portion of the total DEP force is concentrated at the ends of the nanobelt that is close to the electrode. Hence, this acts as a torque generating mechanism. Longer nanobelts will be easier to rotate with the same force magnitude applied to the nanobelt end(s), compared to a shorter nanobelt. In a similar study on carbon nanotubes (MWNTs) [35], it was found that longer nanotubes were attracted and aligned more easily than shorter ones.

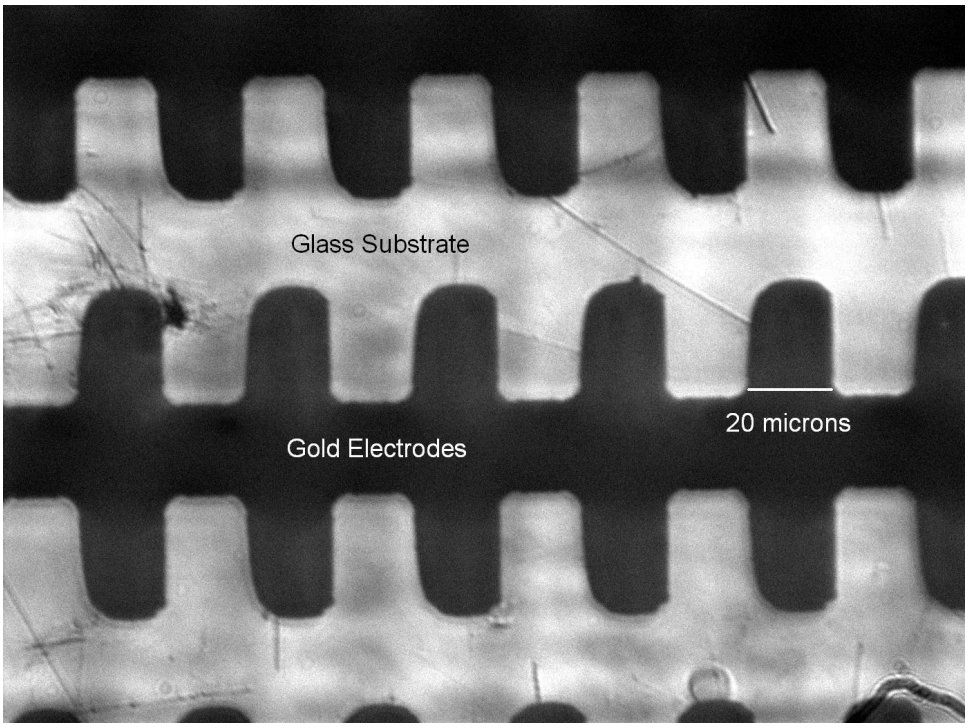

Figure 3.10 SnO_2 nanobelts bridging DEP electrode gaps during positive dielectrophoresis. Shorter nanobelts are sticking out from the electrodes due to the action of the DEP forces.

Attraction of the nanobelts between the electrodes caused the nanobelts to touch the electrodes. Once the nanobelts made contact with the electrodes, they remained stuck there. Figure 3.10 shows the situation during positive DEP. The longer nanobelts bridged the electrode gaps and were not affected further by the AC field. However, the

short nanobelts which could not bridge the electrode gaps are seen to be sticking out in the direction of the maximum field gradient. As flow of the suspension continued, the number of nanobelts between the gaps increased with time. This was verified later from the I-V characteristics of the devices. Devices in which more flow time was allowed showed higher current levels. It was also observed that if the flow was stopped, the manipulation was still possible, since the fluid (ethanol) was inside the microchannel, suspending the nanobelts. In fact that provides insight into a possible way of making nanodevices. Microelectrodes can be fabricated and a drop of nanobelt suspension applied on the electrodes. Application of AC voltage will allow the nanobelts to make contacts with the electrodes.

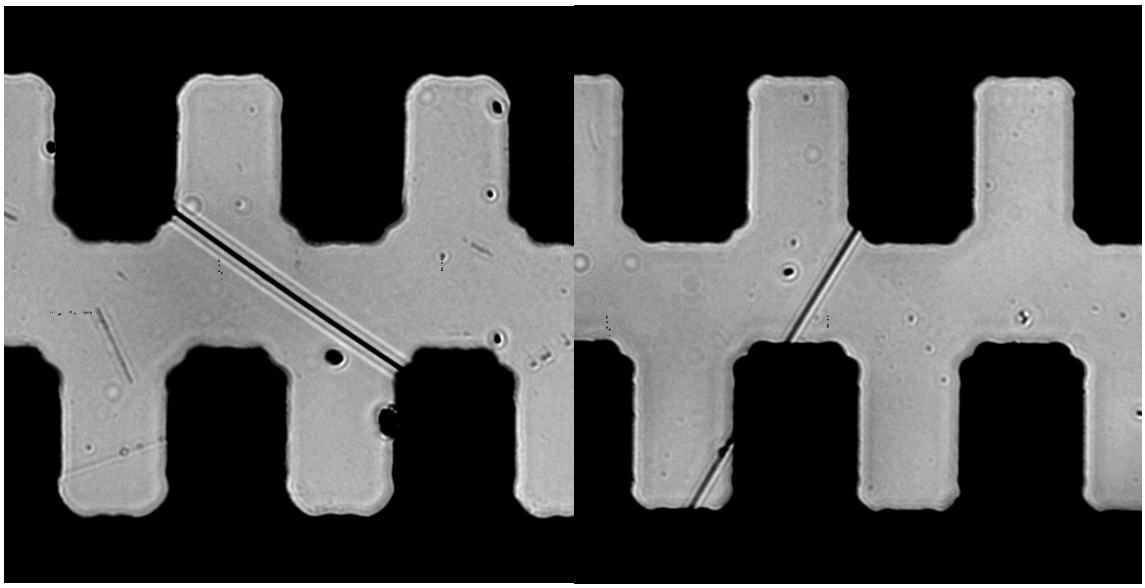

(a) (b)

Figure 3.11 Optical microscope images showing long SnO_2 nanobelts of large widths between (a) two non-adjacent, and (b) two adjacent castellated Au electrodes (dark regions). The electrode gaps are ~ 20 μm.

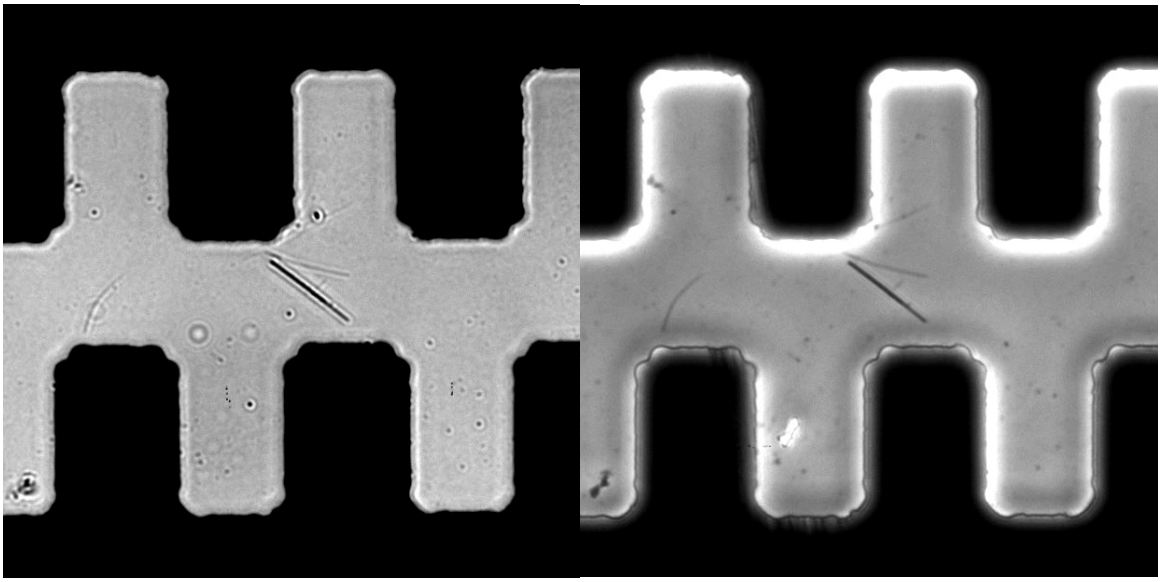

(a) (b)

Figure 3.12 Optical microscope images showing a short SnO_2 nanobelt of large width between castellated electrodes (dark regions), (a) under normal optical imaging, and (b) the same nanobelt under optical phase contrast imaging. The electrode gaps are ~ 20 μm.

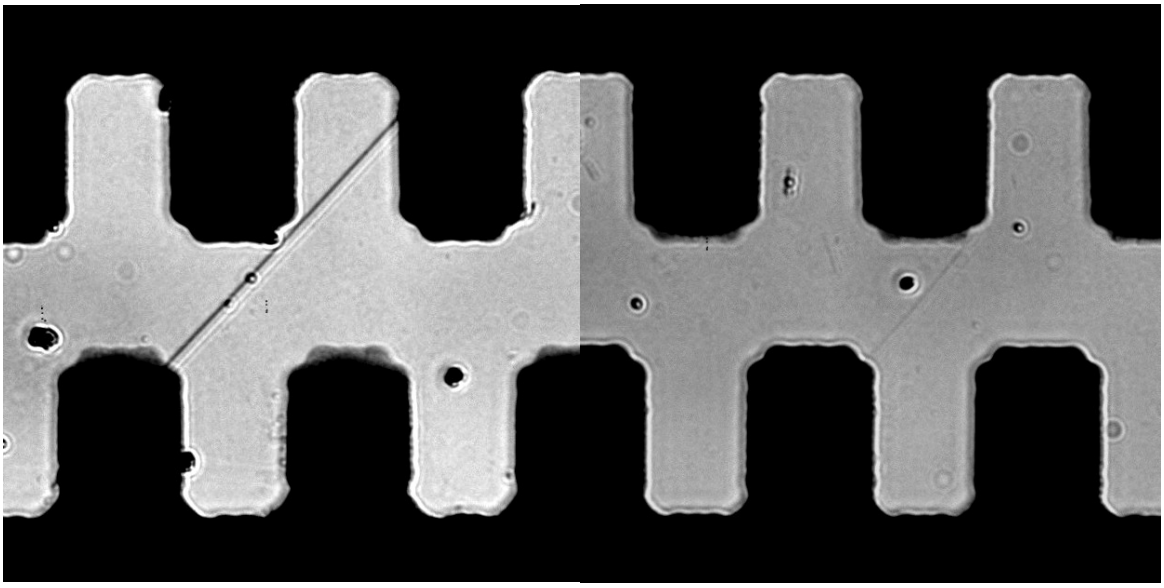

(a) (b)

Figure 3.13 Optical microscope images showing (a) a long SnO_2 nanobelt of medium width between two non-adjacent castellated electrodes (dark regions), and (b) an SnO_2 nanobelt of narrow width between two adjacent electrodes. The electrode gaps are ~ 20 μm.

Figure 3.11, Figure 3.12, and Figure 3.13 show some typical optical microscope images of the nanobelts after DEP experiments. The microscope is capable of capturing images of wide and narrow nanobelts, with proper lighting and digital contrast adjustments.

3.2.2 Dielectrophoresis of SnO_2 Microparticles

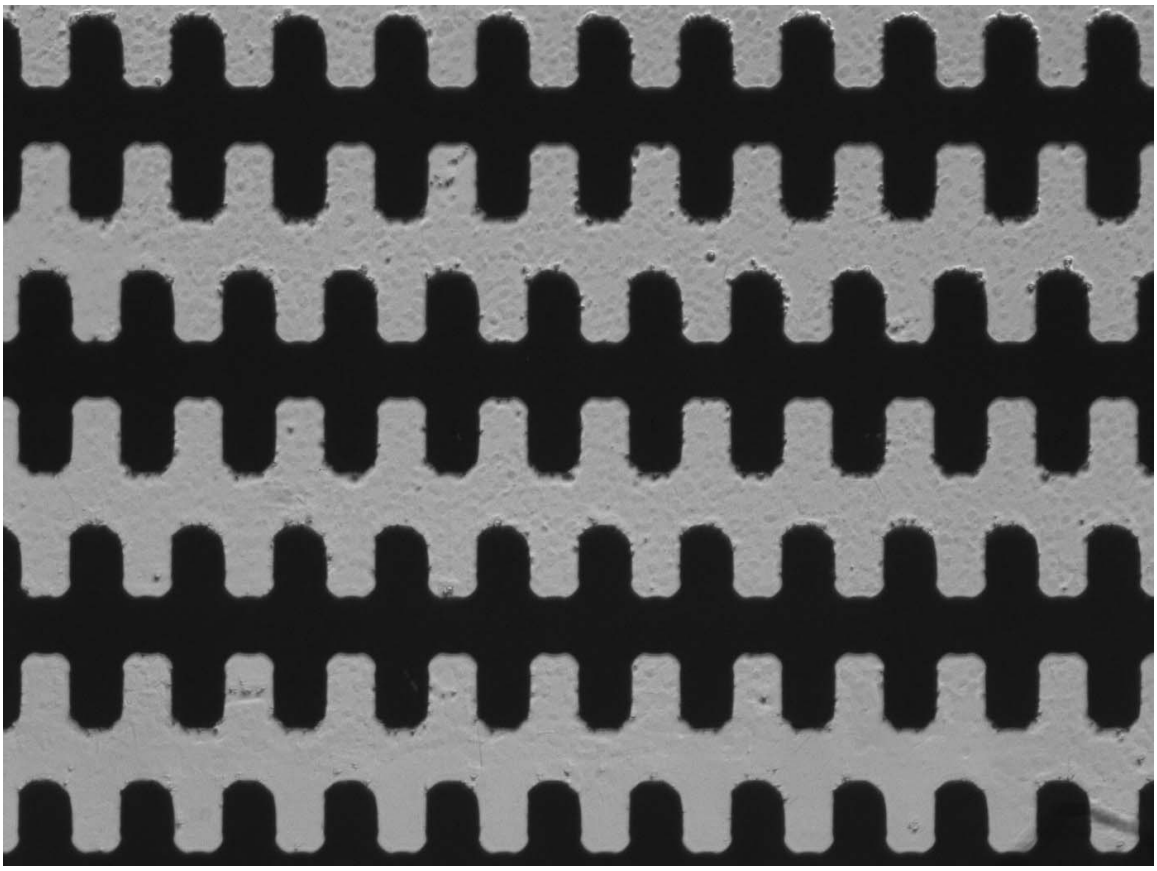

Figure 3.14 SnO_2 microparticles in ethanol attracted to the electrodes (dark regions) on application of a high frequency (1 MHz, 10 V_{peak} AC) electric field. The electrode gaps are ~ 20 μm.

Some DEP tests were performed on SnO_2 microparticles (*Alfa Aesar*, Ward Hill, MA, USA) of about 1 μm diameter, suspended in either ethanol or kerosene. Experiments using either liquid media indicated that at high frequencies the

microparticles collected at the edges of the microelectrodes, indicating attractive forces. Figure 3.14 shows a typical result using ethanol as the suspending medium. At very low frequencies (~ 1 Hz), the microparticles could be observed jumping between the electrode gaps, which is probably an indication of the presence of charge on the microparticles, and hence electrophoretic phenomenon. Dielectrophoretic forces allow movement in only one direction according to field gradients, irrespective of the polarity change in the electrodes due to AC signals. The jumping motion would indicate that the electrophoretic effect is dominating at the very low frequencies. As the frequency increased, movement ceased. This can be explained from the fact that when the electrophoretic force changes rapidly in time because of the changing field direction, the particles cannot keep up with this change due to inertia effects. This results in zero average electrophoretic force, and hence the jumping motion is not observed at higher frequencies.

3.2.3 Nanobelt Dielectrophoresis in Kerosene

Figure 3.15 shows an image of SnO_2 nanobelts attracted between the castellated electrodes when kerosene was used as the suspending medium for the DEP experiments. For SnO_2 nanobelts in kerosene, the DEP behavior appeared to be qualitatively similar to that with ethanol. However, the force magnitude seemed to be lower. This is expected because the relative permittivity of kerosene is about 1.8 as opposed to 24 for ethanol. Also, the frequency range corresponding to positive DEP seemed wider with kerosene compared to that with ethanol. The repulsive forces were seen only at very low frequencies (~ 10 Hz). Because of the low force magnitudes, it was not possible to see the effect clearly in the case of kerosene. The attractive forces could be inferred, after the

DEP experiments, from the fact that the nanobelts got trapped between the electrodes As far as the Clausius Mossotti (CM) factor is concerned the lower permittivity of kerosene is expected to affect the DEP characteristics at high frequencies. A simple analysis with the dipole approximation shows that the frequency corresponding to a change in sign (crossover) of the CM factor is higher than the highest frequency (10 MHz) used in the DEP tests. At frequencies below the crossover frequency the electrical conductivities of the particle and the liquid medium determine the DEP characteristics. Because of the small sizes of nanobelts it can be expected that if surface dominant properties of the nanobelt affect the DEP characteristics, they should be important in both the liquids.

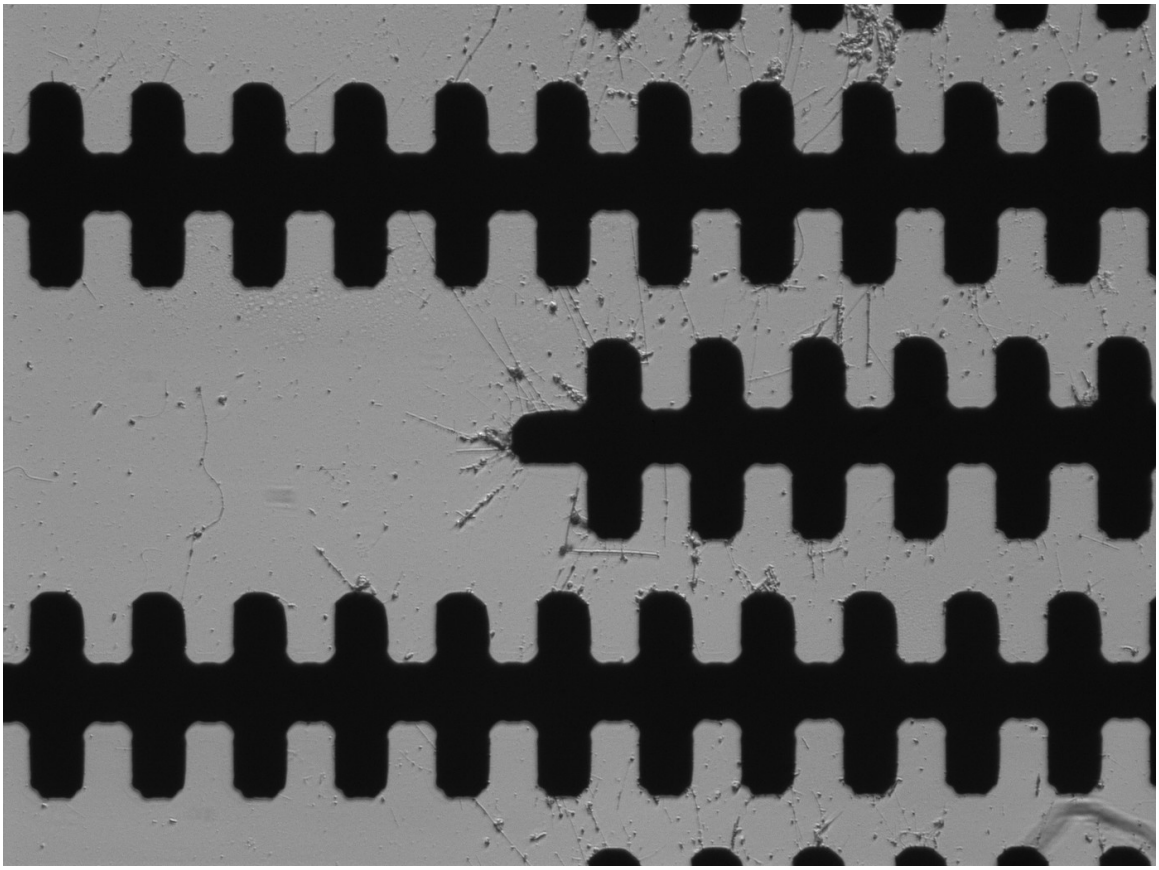

Figure 3.15 Optical microscope image showing SnO_2 nanobelts collected between electrodes (dark regions) at high frequency (1 MHz, 10 V_{peak} AC) electric field in kerosene medium. The electrode gaps are ~ 20 μm.

3.2.4 I-V Curves

In the DEP device, there were two sets of dielectrophoretic electrode arrays E_1 and E_2 (see Figure 3.3(a)). Potential could be applied independently to each of them, although both are inside the same microchannel. In one of the electrode arrays (E_1), the number of trapped nanobelts was smaller than in the other electrode array (E_2). This could be deduced from the current levels in the I-V curves, which showed orders of magnitude difference for each electrode array. This was also confirmed from impedance measurements, and optical imaging.

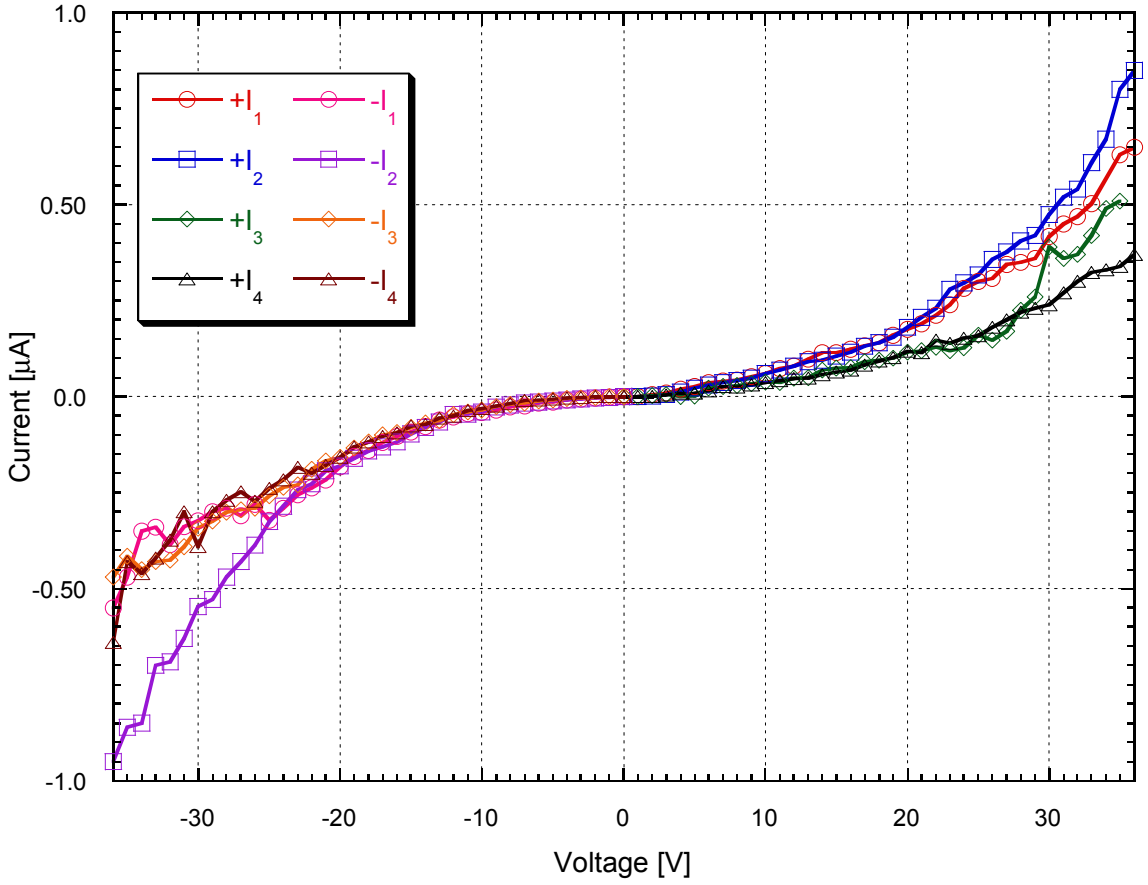

Figure 3.16 I-V characteristics of SnO_2 nanobelts bridging the DEP electrode gaps (electrode array E_1, which has few nanobelts).

Figure 3.16 and Figure 3.17 show the I-V curves for the DEP electrode arrays E_1 and E_2, respectively. The I-V characteristics are quite different in the two cases. In the case of E_1, the curves are nonlinear and close to exponential, indicating non-ohmic contacts, which are expected for metal (Au) semiconductor (SnO_2) junctions. However, the I-V curves for E_2 are close to linear. A possible explanation for this behavior is that because of the varying levels of contact of the large numbers of nanobelts involved in E_2, the non-ohmic behavior of the individual nanobelts averages out and gives an almost linear curve. The forward and reverse bias characteristics are similar in both cases. However, some non-linearity is still visible in the low voltage range (Figure 3.17).

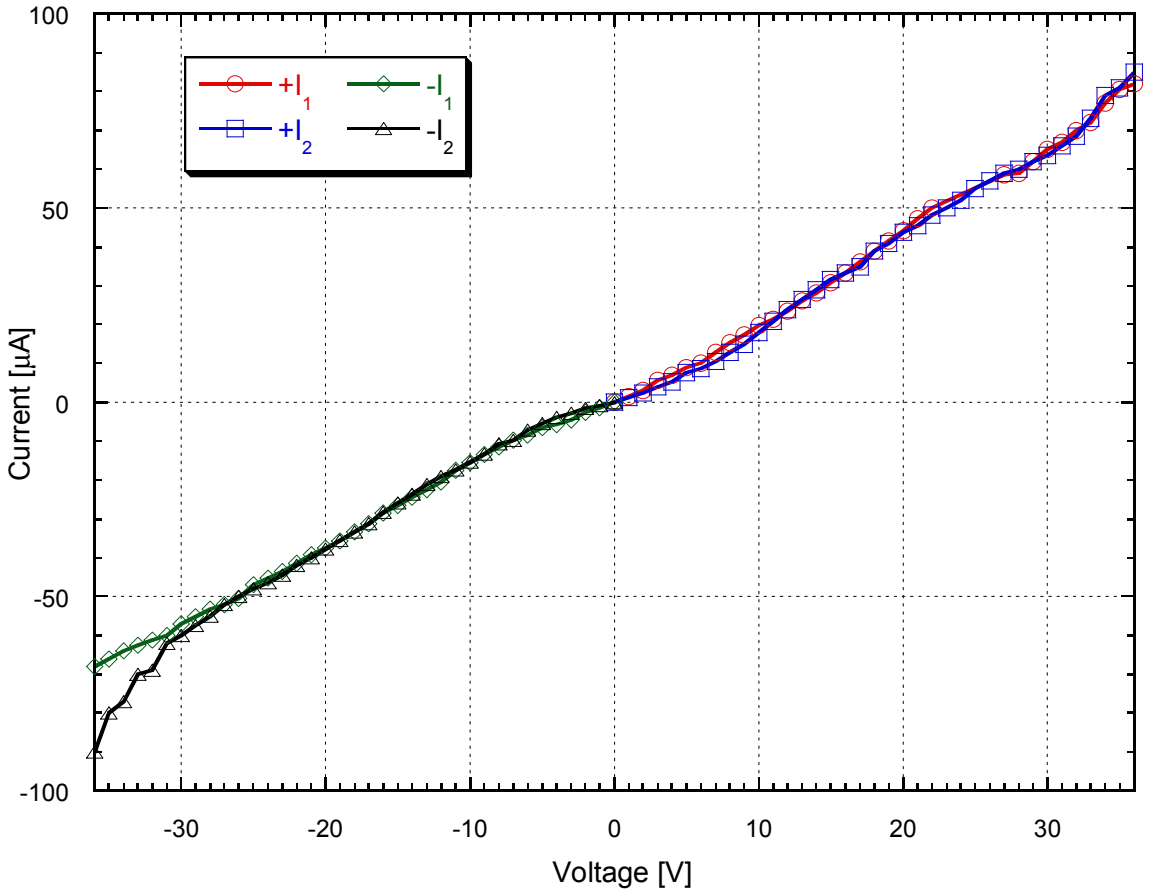

Figure 3.17 I-V characteristics of SnO_2 nanobelts bridging the DEP electrode gaps (electrode array E_2, which has a large number of nanobelts).

3.2.5 Effect of Temperature Change

The effect of temperature change on the nanobelt device was studied in an inert dry nitrogen atmosphere. During the measurements nitrogen was flowing through the SLA microchannel. As mentioned in the experimental section, an electrical strip heater (*Watlow Electric Manufacturing Company*, St. Louis, MO, USA) was attached on the Pyrex glass substrate (bottom of the DEP device) to heat it. The current flowing through the nanobelt device (electrode array E_1) at a bias of 10 V DC was monitored with time. The current flowing through the device increased as the strip heater current was raised. The current in the device changed from a low level steady state value, sharply to finally reach a higher level steady state value, showing that the temperature of the device and hence, the nanobelts was changing during the transient period. The approximate temperature values for the steady state conditions were measured using a K type thermocouple (*Omega Engineering, Inc.*, Stamford, CT, USA) attached on the top surface of the Pyrex glass surface. Since the thermocouple size is quite large (diameter ~ 0.5 mm) the temperatures should be considered approximate.

The semiconducting nature of the nanobelts is clear from the current versus temperature plot shown in Figure 3.18. The steady state current through the nanobelt, I_s has an exponential relationship with the substrate temperature, T given by the fit

$$I_s[nA] = 8.7704\times10^{-7}[nA]\cdot\exp(0.052396\cdot T[K]) \qquad (3\text{-}1)$$

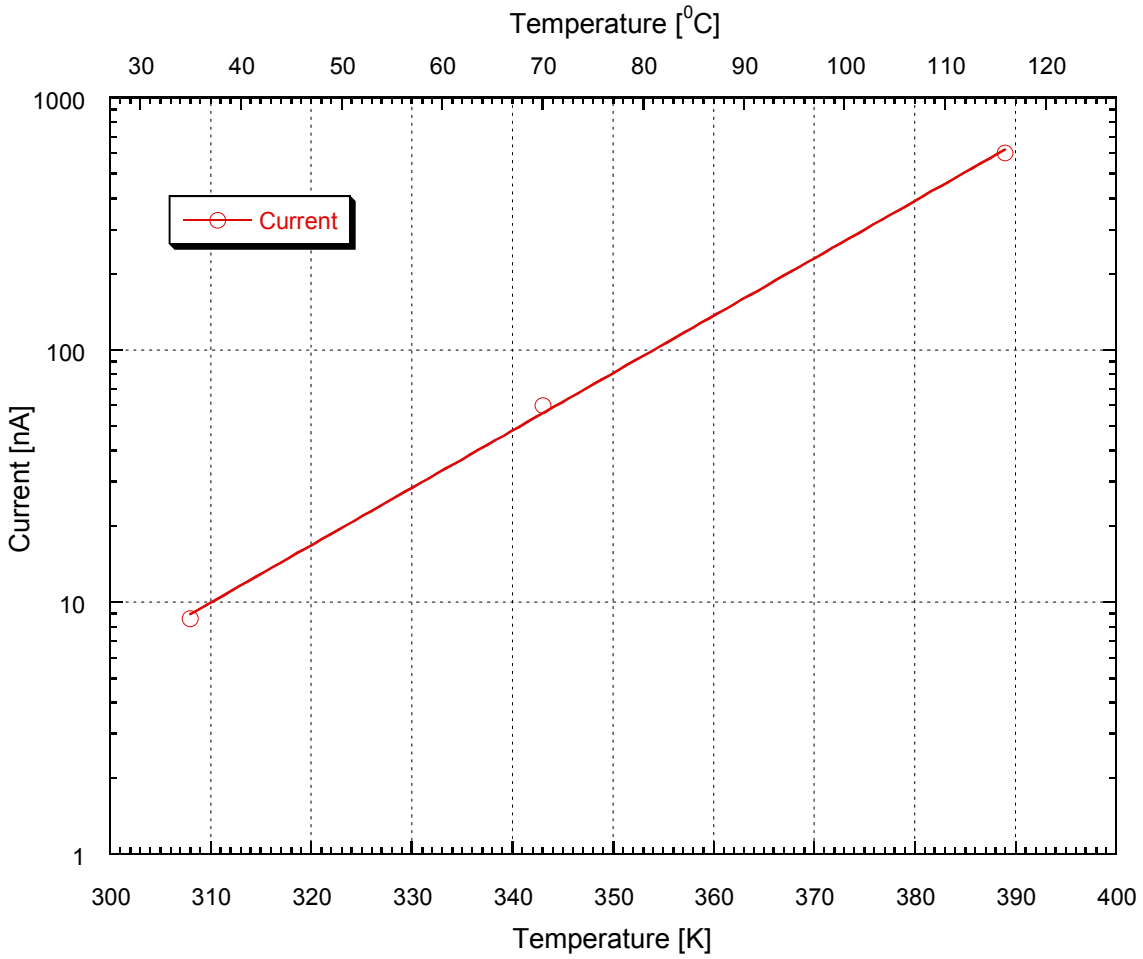

Figure 3.18 Log plot showing the effect of temperature change on the steady state current flowing through the nanobelt device (electrode array E_1).

3.2.6 Effect of Visible and UV Light Illumination

To verify the semiconducting nature of the nanobelts, the trapped SnO_2 nanobelts were exposed to UV light, and the current flowing between the electrodes was monitored under atmospheric conditions. Out of curiosity, visible light exposure was also performed. Change in current (conductivity) flowing through the nanobelts was observed in both the cases. Figure 3.19 shows a plot of the current through the DEP device (electrode array E_1) as a function of time, with periodic visible light and UV light exposures. The response to visible light was faster than the response to the UV light.

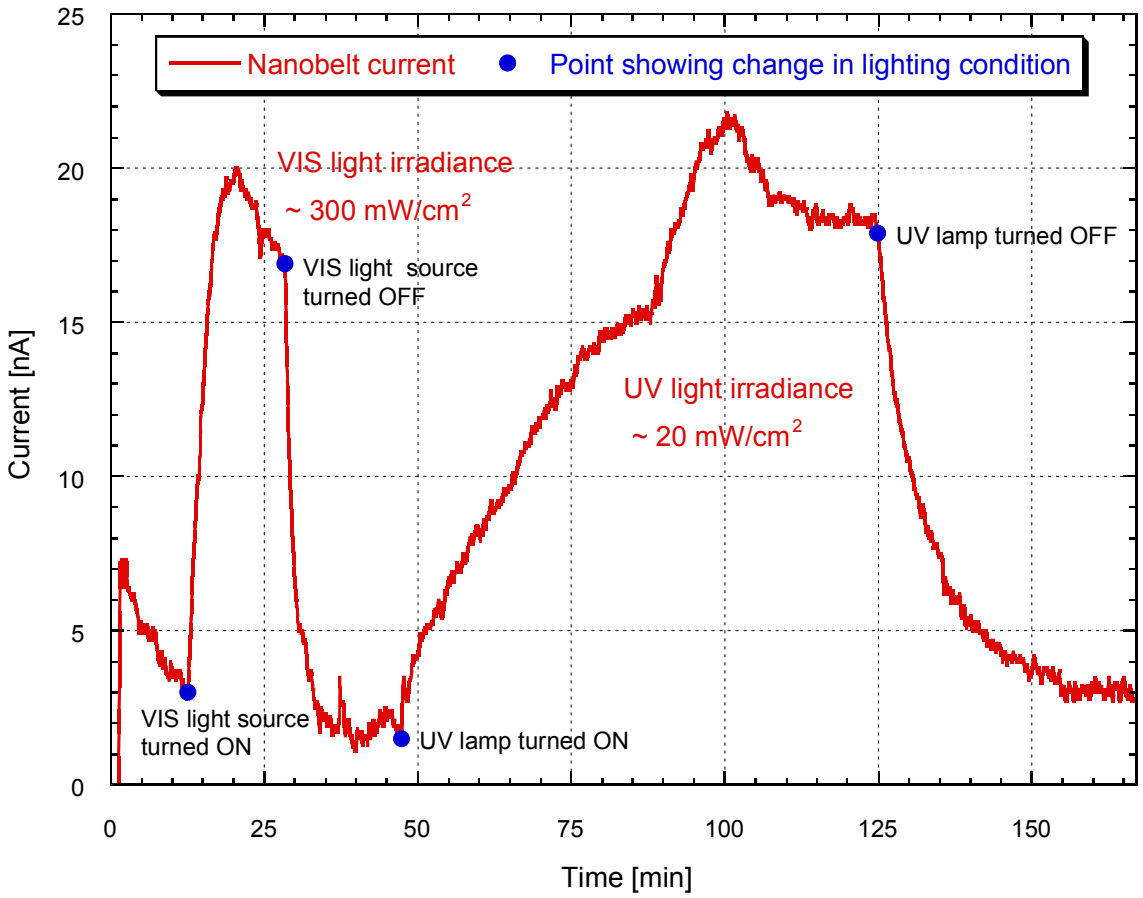

Figure 3.19 Plot showing the effect of visible and UV light on the SnO_2 nanobelts between the DEP electrodes (electrode array E_1) under a bias of 10 V DC. The orders of magnitude of the light irradiance are indicated in the plot.

The nanobelts have a depletion layer due to the absorbed oxygen on the surface of the nanowires.[60] The UV photons interacting with the semiconducting oxide is likely to cause two distinct processes.[61] One is the removal of adsorbed oxygen species (O^{2-}, O_2^-, and O_2) releasing the surface-bound electrons in the depletion zone causing conduction to increase.[61] The other effect is to increase the density of charge carriers by excitation of electrons (photogeneration of electron-hole pairs) from the valence band into the conduction band [61], as well as from the defect states (if any) to the conduction bands. Hence, the conductivity increase on UV light exposure is due to both

photogeneration of electron-hole pairs as well as doping by UV light induced surface desorption of adsorbed molecules.[61] In the case of visible light band defect states are likely to play the major role, since the bulk SnO_2 is a wide band gap (E_g = 3.6 eV at 300 K) material.

Since the experiments were performed in ambient atmosphere, surface adsorption and desorption of molecules are possible. The slow response can be attributed to the interaction of free electrons and adsorbed molecules during light exposures. On stopping the light exposure, regeneration of the depletion layer takes place slowly due to adsorption of the molecules.

Impedance measurements also demonstrated the effect of light exposure. Impedance measurements in ambient conditions were performed on the SnO_2 nanobelts by exposing the DEP trapped SnO_2 nanobelts with a probe light source and a UV lamp (refer to the experimental section 3.1.6). The average irradiance of the light falling on the SLA microchannel, which covers the DEP electrodes, was estimated using a Model 5200 PowerMax™ laser power meter with a PM3 Probe (*Molectron Corporation*, Sunnyvale, CA, USA, currently *Coherent Inc., Santa Clara*, CA, USA) for the probe light source. For the UV lamp the average irradiance was estimated from its specifications. The actual irradiance of light reaching the nanobelts under the SLA microchannel will be considerably less that the values measured on top of the microchannel. The irradiance from the probe light is considerably higher than that of the UV lamp, since the probe light emits photons in a wide range of wavelengths, while the UV source is almost monochromatic.

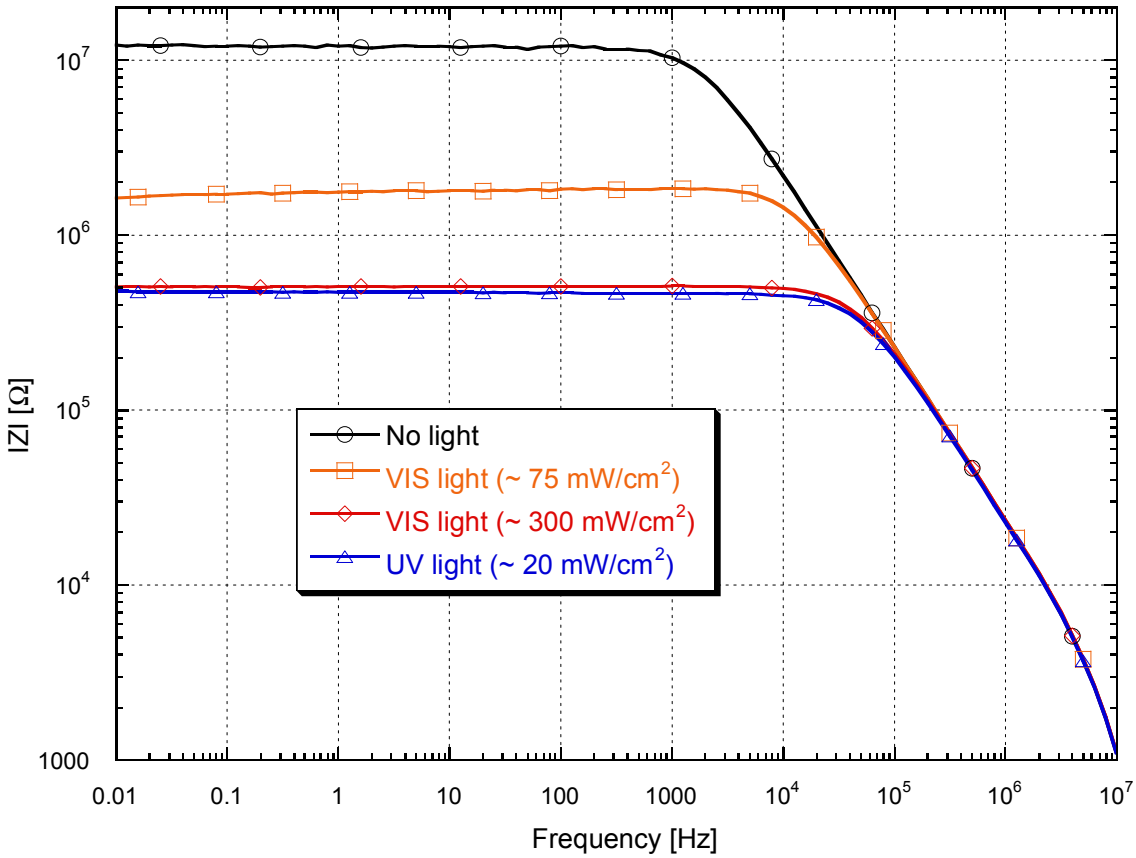

Figure 3.20 Bode plot showing frequency response of the impedance of SnO_2 nanobelts in the DEP device (electrode array E_2). The approximate values of the average irradiance of light falling on the SLA microchannel, which covers the DEP electrodes, are indicated in the plot.

The impedance decreased when the SnO_2 nanobelts were exposed to visible and UV light. Figure 3.20 shows the impedance magnitude (|Z|) as a function of frequency (Bode plots) for the E_2 electrode array. The effect of light can be noted. The curve with the highest impedance corresponds to the situation when the nanobelts were not exposed to any external light source. The exposure of predominantly visible (VIS) light from the probe light decreased the impedance. Increasing the irradiance of the visible light from the probe light caused further decrease in the impedance. UV light also caused a decreased in the impedance. It can be noted that the irradiance of the UV light falling on

the sample is quite low compared to the visible light, but the impedance response is comparable. Hence, the relative response of the SnO_2 nanobelts to UV light is much stronger compared to visible light. This is expected because the UV photons have higher photon energy. The flat portion of the Bode plot in the low frequency range indicates the value of the resistance of the sample under study. The light exposure caused an order of magnitude decrease in the resistance of the device.

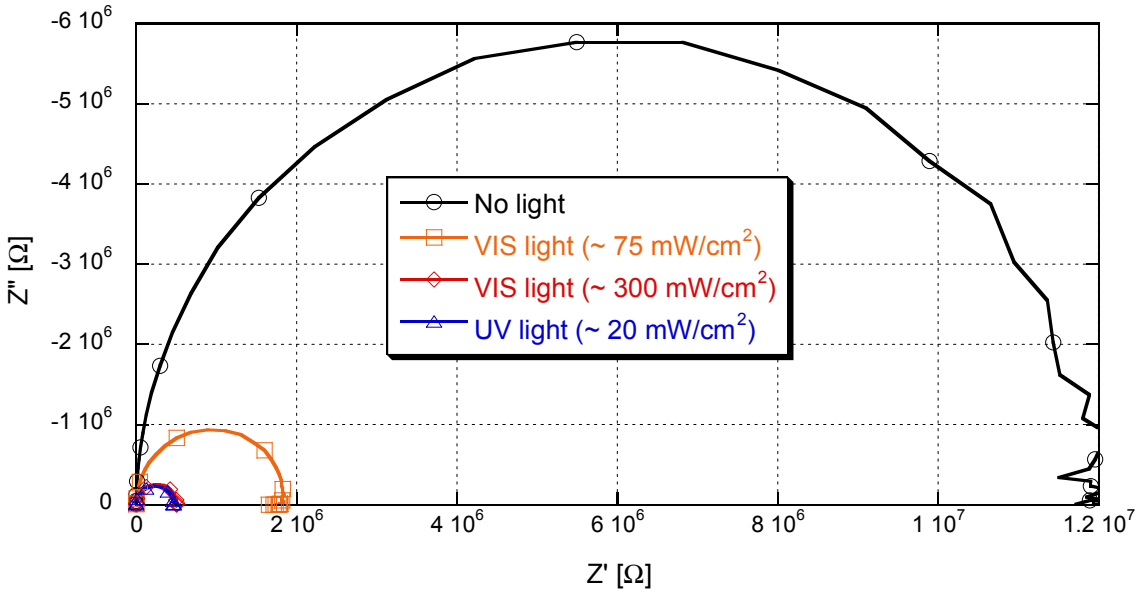

Figure 3.21 Complex impedance plot showing the impedance measured on the SnO_2 nanobelt DEP device (electrode array E_2). The frequency increases counter-clockwise on the semicircles. The approximate values of the average irradiance of light falling on the SLA microchannel, which covers the DEP electrodes, are indicated in the plot.

The corresponding complex impedance plot is shown in Figure 3.21 for the E_2 electrode array. The plot shows a single semi-circle in each case, which implies resistance-capacitance parallel equivalent circuit. The decreasing diameters of the semi-circles in the plot, demonstrates the decrease in resistance of the device upon the exposure of light. In fact, the diameter represents the resistance of the device.

3.2.7 Photoluminescence

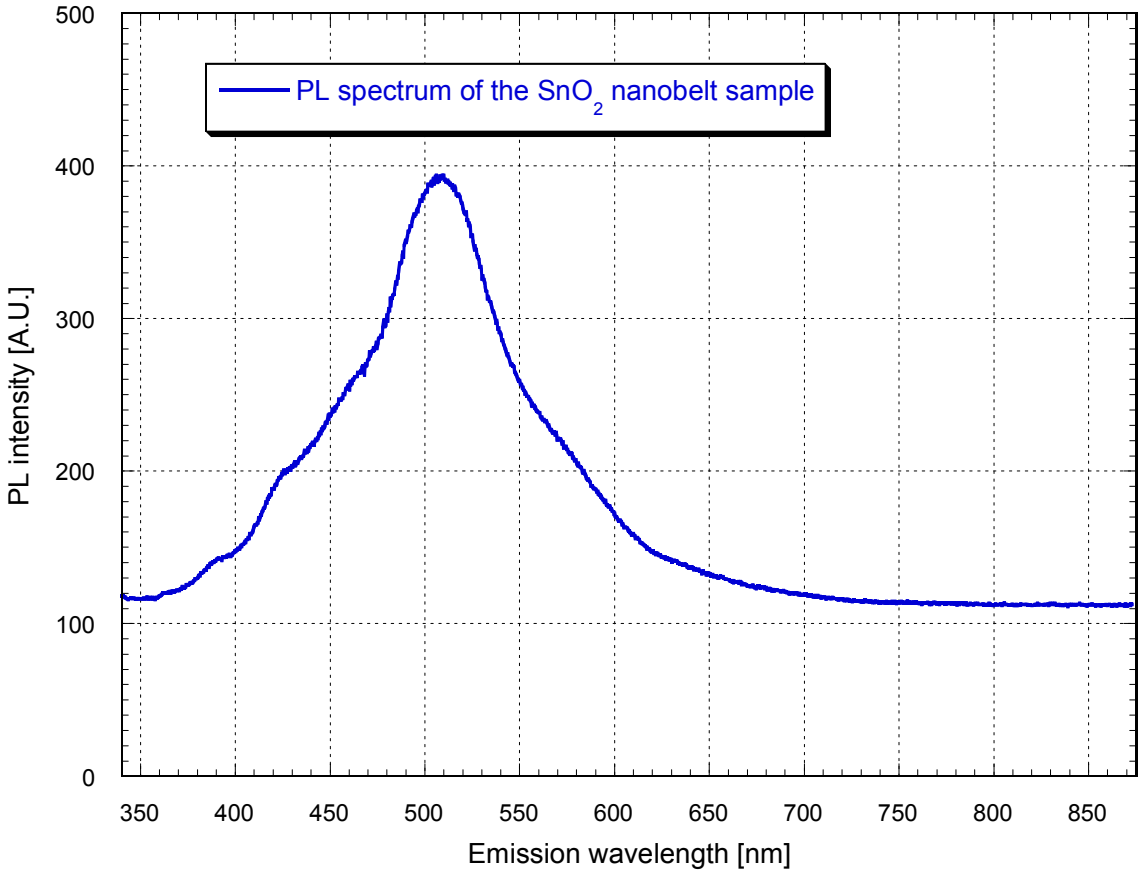

Figure 3.22 Photoluminescence (PL) spectrum of the SnO_2 nanobelt sample.

To understand the reason for the visible light response in SnO_2 nanobelts, photoluminescence (PL) measurements were performed. Pressed mats of SnO_2 nanobelt samples at room temperature were used for the experiment, which showed the presence of visible photoluminescence. Figure 3.22 shows the photoluminescence spectra. The existence of visible light effect is unusual since bulk SnO_2 is a wide band gap semiconductor (E_g = 3.6 eV at 300 K for bulk SnO_2). The probable reason for the visible light response in the SnO_2 nanobelts is the presence of defect states. This seems to be supported also by the presence of visible photoluminescence in SnO_2 nanobelts, which is

generally believed to stem from defects such as tin interstitials, dangling bonds, or oxygen vacancies.[62]

TEM EDX analysis of individual SnO_2 nanobelts was performed to verify its composition. Figure 3.23 shows the spectrum. Within the detection limit of the EDX, the sample contains tin and oxygen only. The Cu shown in the spectrum comes from the TEM grid.

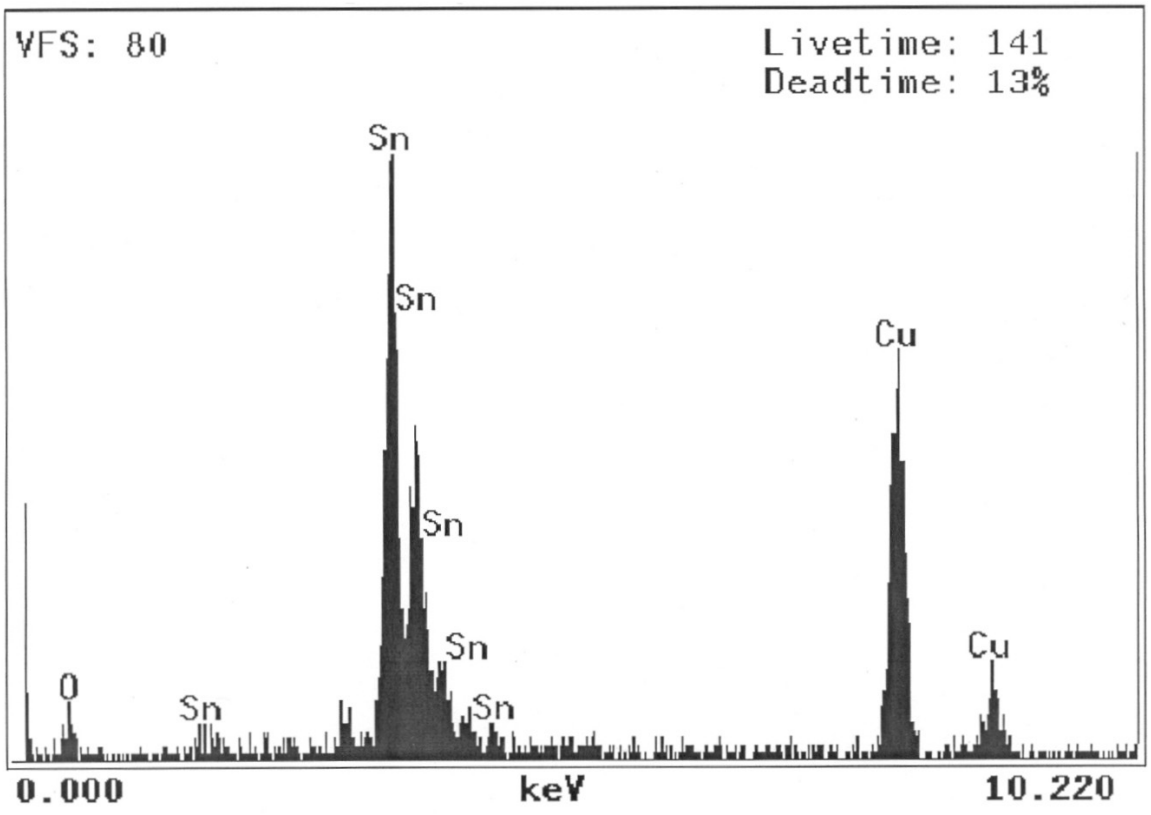

Figure 3.23 TEM EDX spectrum of a single SnO_2 nanobelt on a Cu grid.

3.2.8 Dielectrophoresis of TiO_2 Diatoms

DEP was also demonstrated on TiO_2 diatoms suspended in ethanol. The TiO_2 diatoms were prepared and supplied by Prof. Kenneth H. Sandhage's research group at the Material Science and Engineering Department at Georgia Tech.

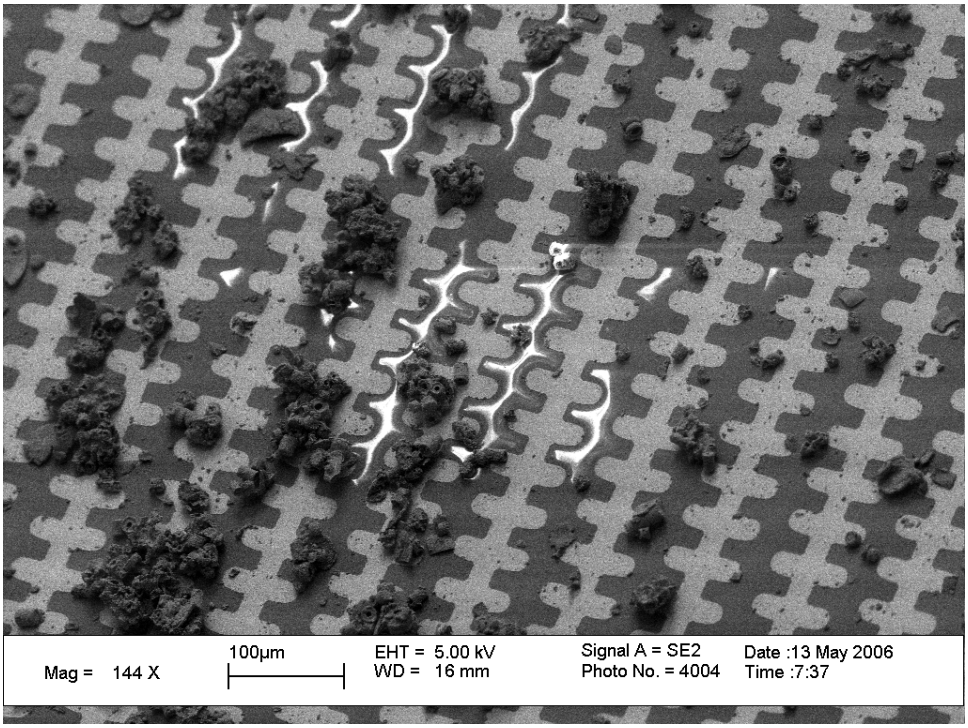

(a)

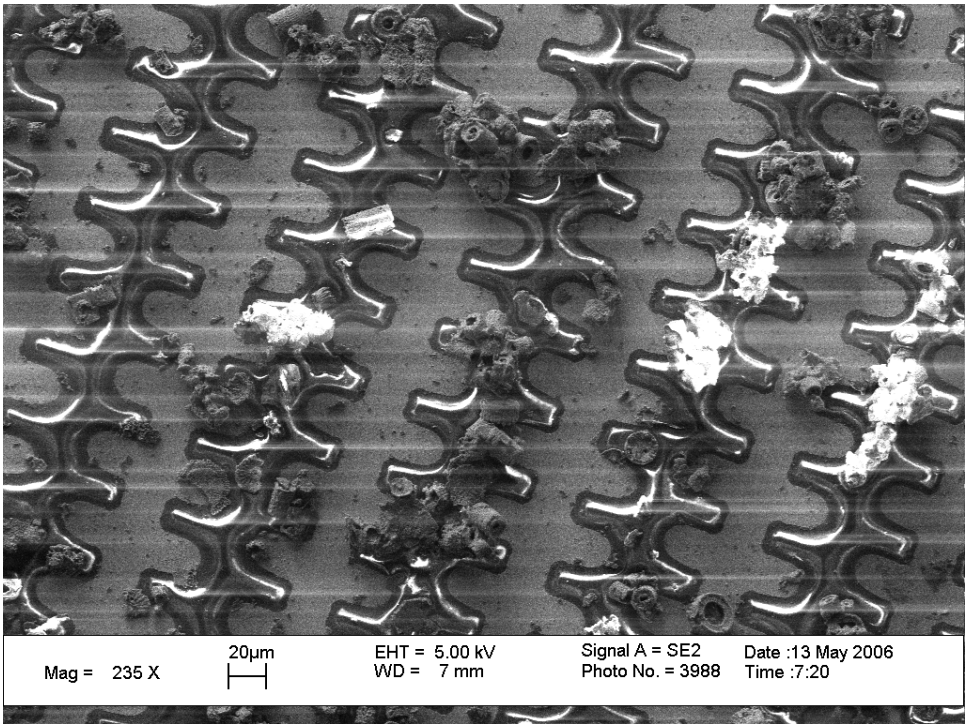

(b)

Figure 3.24 SEM image of TiO_2 diatoms attracted between castellated electrodes after DEP experiments (Sample T09). The light areas are the electrodes.

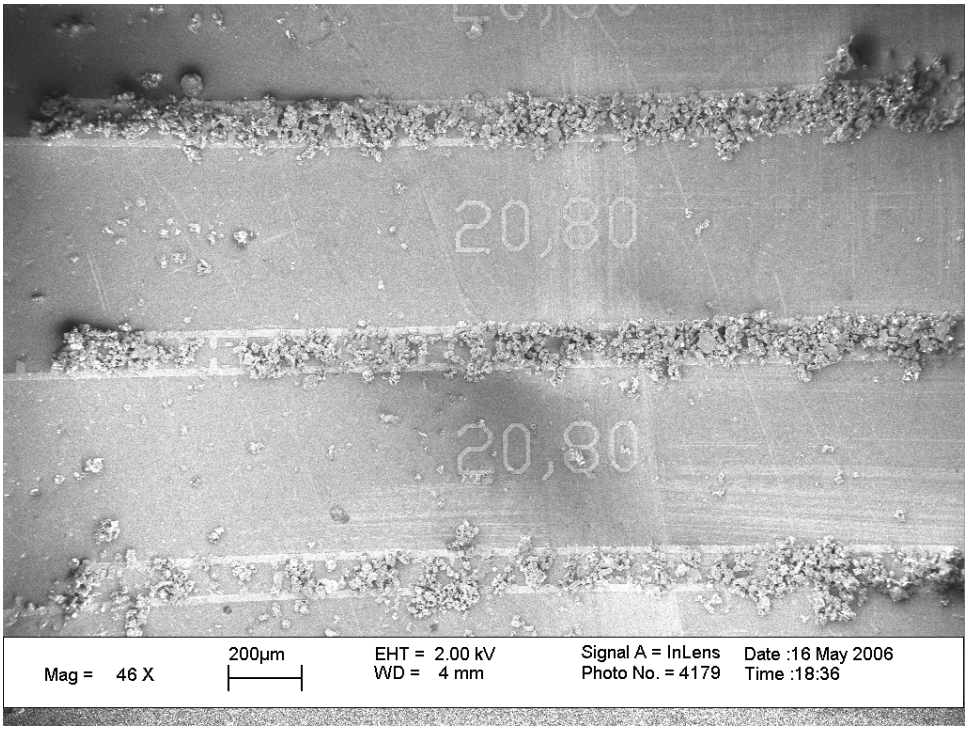

(a)

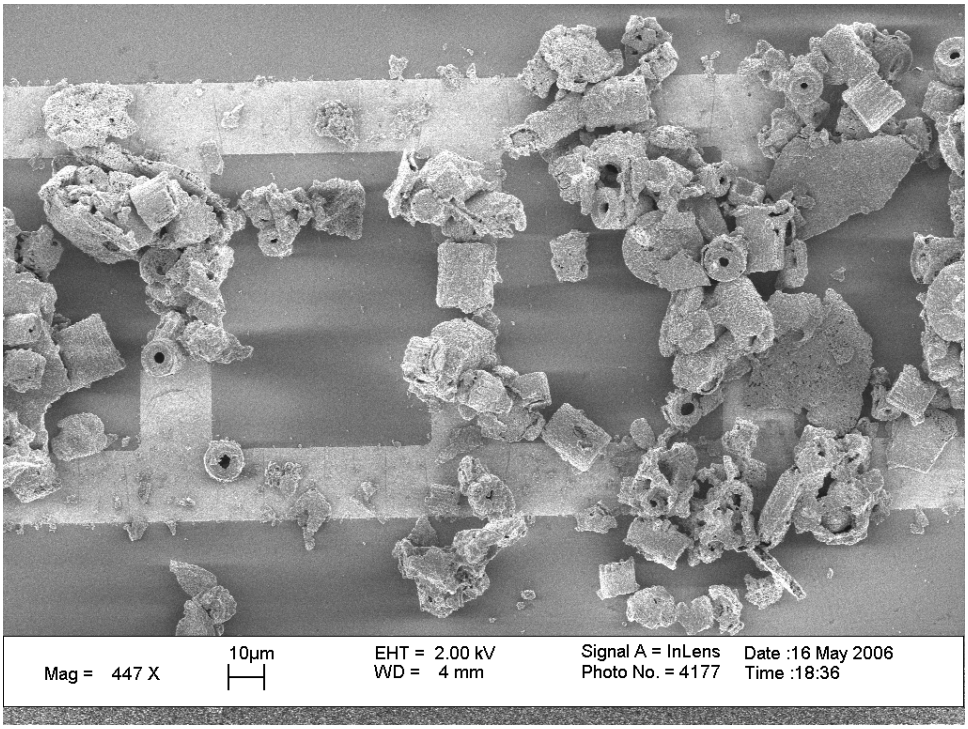

(b)

Figure 3.25 SEM image of TiO_2 diatoms attracted between castellated electrodes after DEP experiments (Sample T10). The light areas are the electrodes.

The details of the process used for preparing the diatoms can be found in the published literature.[63] The diatoms were attracted between the electrodes by applying 50 V_{peak}, 50 kHz AC signal. Large signals were required because the diatoms are very large in dimension (~ 10 μm). From the electrode surface the diatom will appear very tall. The electric field gradient (hence DEP force) falls rapidly as the vertical distance from the electrode surface increase. So, the DEP force generated using small voltages could not move the diatoms. As the SEM images (Figure 3.24 and Figure 3.25) show, the DEP experiments caused preferential arrangement of the diatom frustules between the electrodes. However, the electrode gaps (~ 20 μm) are larger than the typical length of a diatom frustule (~ 10 μm). Hence, most of the frustules bridged the electrode gap via agglomeration. The alignment of single frustules between the electrodes was not seen because of their short lengths. Decreasing the spacing between the electrodes, and lowering the concentration of the diatom frustules in the liquid suspension used for the DEP trapping, are likely to improve the situation.

Efforts were made to use the trapped diatoms to sense ethanol vapor at high temperatures. Figure 3.26 shows the current through the diatoms for different temperatures. Higher currents flowed through the diatoms for higher temperatures. However, preliminary tests did not show any response of resistance (conductivity) change when ethanol of different concentrations (in a carrier gas) was flowed over the substrate.

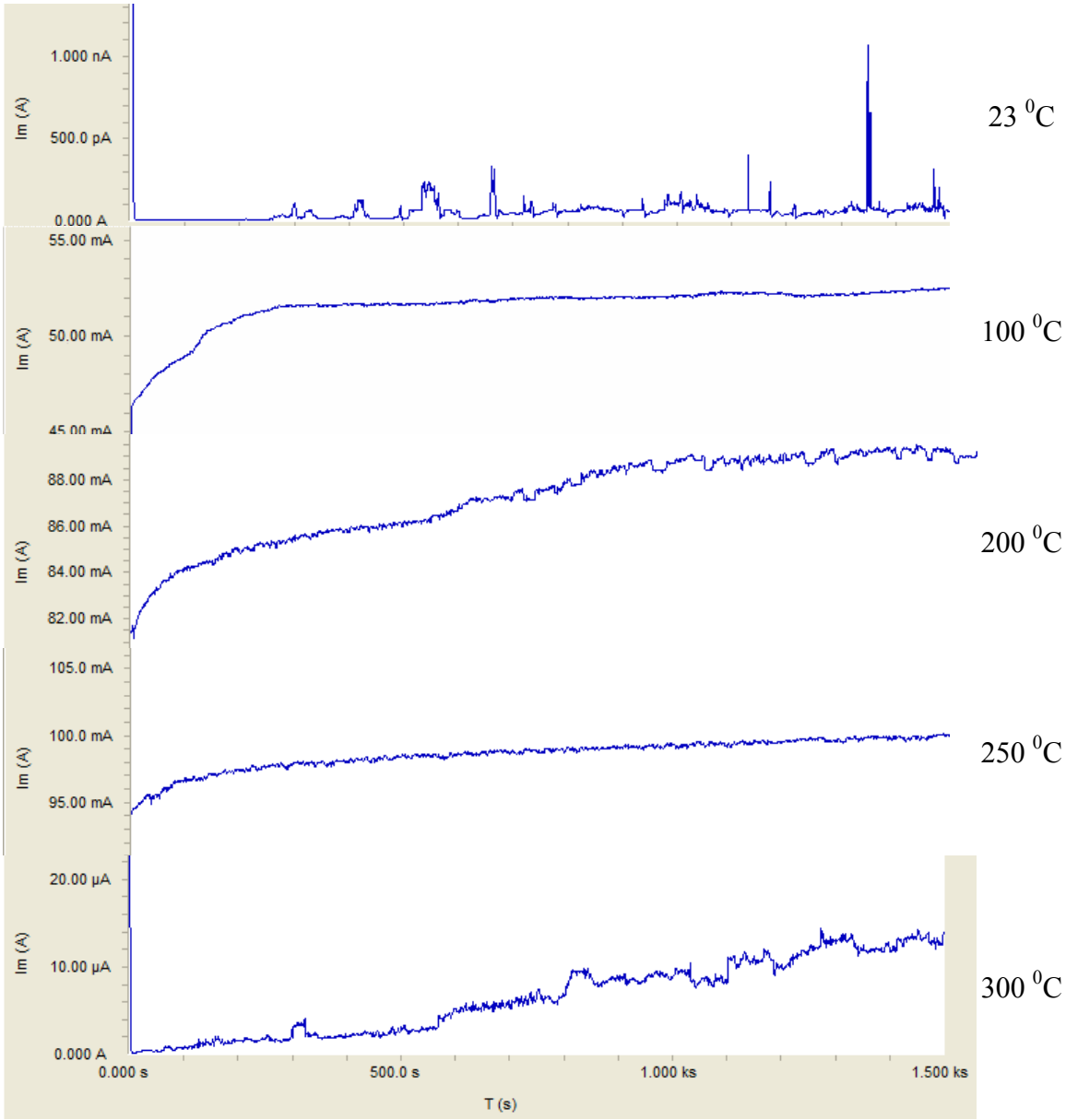

Figure 3.26 Current through the diatoms (trapped using DEP) for different temperatures (Sample T10: Electrode A).

3.3 SUMMARY OF RESULTS

For the first time positive and negative dielectrophoresis on metal oxide semiconductor material based nanobelts/nanowires was demonstrated using AC electric fields. 10 V_{peak} AC was used between the DEP electrodes (electrode gap ~ 20 µm) with variable frequencies. In the low frequency range (10 Hz - 1 kHz) negative DEP occurred,

while in the high frequency range (1 - 10 MHz) positive DEP was observed. DEP was also demonstrated on TiO_2 diatoms to trap them between electrodes.

The dielectrophoretic manipulation of the SnO_2 nanobelts resulted in a nanodevice. Several characterization methods were used to study it. Metal oxides are commonly used for detecting flammable and toxic gases, including organophosphorus compounds [64] (e.g. nerve agents), halogenated hydrocarbons, CO, NO_2, NH_3, CH_4, H_2, H_2S, alcohols, O_2, and ozone. The sensing mechanism is based on a surface oxidation-reduction (redox) process that changes the concentration of oxygen vacancies in the metal oxide and thus alters its electrical conductance.[65] Because, only the surface layer is affected by the reaction, the sensitivity of a metal oxide sensor increases with decreasing thickness, motivating the development of thin film metal oxide sensors with the use of MEMS technologies.[66] Since the thickness of SnO_2 nanobelts is small compared to polycrystalline thin films, and nanobelts are single crystals, it is possible that the device with the trapped nanobelts can be used as a gas sensor. Monitoring the current or conductance through a nanobelt device will allow the detection of gases. Nanosensors have the potential to provide higher sensitivity and rapid response time on very small sample volumes, with the added benefits of low power and small size.

CHAPTER 4

DIELECTROPHORESIS OF SINGLE TIN OXIDE NANOBELTS

Chapter 3 described the experiments on dielectrophoresis (DEP) of multiple nanobelts and provided a general sense of the frequency dependence. However, the experimental setup was not appropriate for detailed observations of the nanobelt motion. The major reason was that the SLA channel height (~ 150 μm) was very large compared to the electrode dimensions and the fact that DEP forces fall rapidly above the electrodes. Also, because of the large liquid space above the electrodes the nanobelts could move around more freely, and hence, it was difficult to focus the optical microscope image. To overcome these difficulties a new experimental setup was designed and used for closer and detailed characterization of the DEP process in nanobelts. This is the subject of this chapter.

Direct observation of the dielectrophoretic manipulation process of nanowires and such long objects is quite rare in the literature. In this chapter the results of AC dielectrophoresis experiments on single SnO_2 nanobelts suspended in ethanol are reported. Detailed and direct observations of the wide variety of nanobelt motions, induced by DEP forces, were made under a wide frequency range. These observations also allowed an approximate estimation of the relative DEP force magnitudes as a function of the frequency of the applied electrical signal. Estimation of the absolute DEP force magnitudes will require detailed simulations. It is difficult to get such quantities experimentally because the electric field changes with position between the electrodes,

and also because nanobelts are not point objects but extended long entities. Some simulation results are discussed in a separate chapter. The trends observed in the experimental data will be found useful for comparison with the simulated results qualitatively.

4.1 EXPERIMENTAL

The DEP manipulation of single nanobelts was carried out on linear arrays of Au microelectrodes, defined on Pyrex glass substrates using standard microfabrication processes. The microelectrode array was covered with a shallow (10 μm tall, 100 μm wide) PDMS (polydimethylsiloxane) microchannel so that the nanobelt suspension could be introduced through it. The cross section of the inlet and exit of the channel was ~ 250 μm square. The microchannels were fabricated using replica molding of PDMS on SU-8 negative resist pattern, created using multiple photolithography and alignment steps.

4.1.1 Fabrication of Microchannel Mold Using SU-8

AutoCAD (*Autodesk, Inc.* San Rafael, CA, USA) was used to design 2 photomasks for making the microchannel mold with proper dimensions. The entrance region has a 250 μm width, and the central region of the channel has a 100 μm width. Figure 4.1 shows a schematic of the PDMS microchannel.

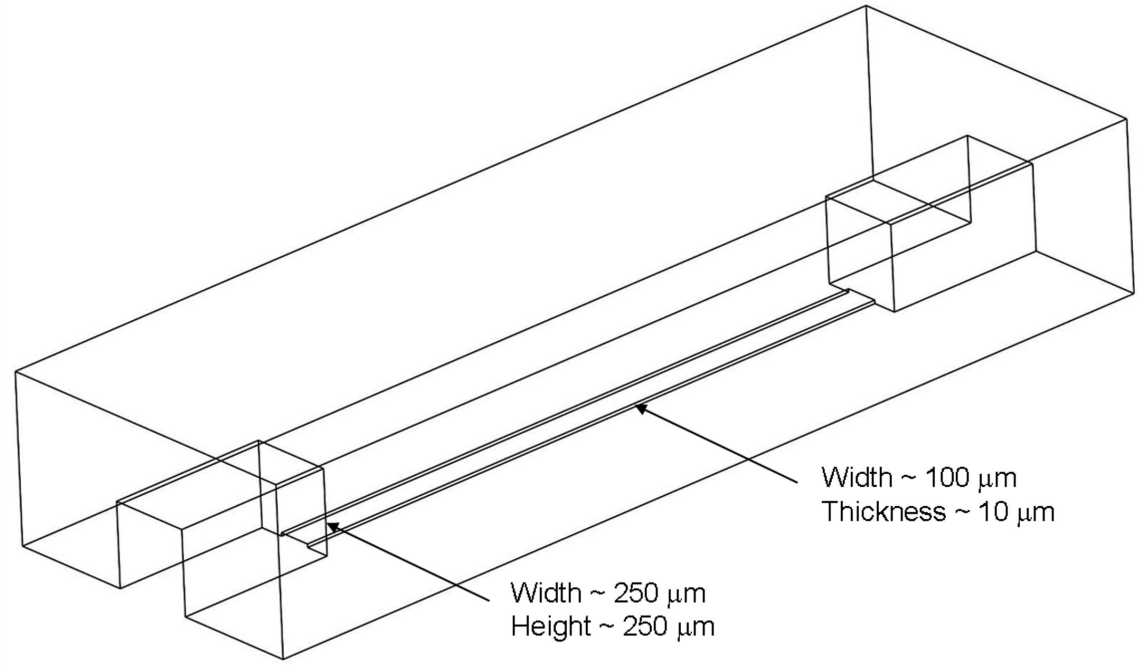

Figure 4.1 Schematic of the PDMS microchannel fabricated using replica molding of SU-8 mold.

The process for making the SU-8 mold is outlined below:

1) Spin SU-8 2010 (*MicroChem* Corp., Newton, MA, USA) at 3000 rpm, 500 rpm/s for a total of 40 s to obtain ~ 10 μm thickness on a silicon wafer.
2) Perform soft bake at 95 °C using a horizontal air flow oven (*Sheldon Manufacturing Inc.*, Cornelius, OR, USA) with the programmed temperature profile shown in Figure 4.2.
3) Use Photomask 1 and expose UV radiation (365 nm wavelength) for a total of 160 mJ/cm^2.
4) Perform post exposure hard bake at 95 °C using the oven temperature profile shown in Figure 4.3.
5) Develop in SU-8 developer (*MicroChem* Corp., Newton, MA, USA) for ~ 5 min.

6) Rinse with iso-propyl alcohol, and dry the substrate.
7) Spin SU-8 2075 (*MicroChem* Corp., Newton, MA, USA) at 800 rpm, 400 rpm/s for a total of 40 s to obtain ~ 250 μm thickness over the substrate with the first layer.
8) Perform soft bake at 95 °C using the oven temperature profile shown in Figure 4.4.
9) Align using Photomask 2 and expose UV radiation (365 nm wavelength) for a total of 700 mJ/cm^2
10) Perform post exposure hard bake at 95 °C using the oven temperature profile shown in Figure 4.5
11) Develop in SU-8 developer (*MicroChem* Corp., Newton, MA, USA) for ~ 60 min.
12) Rinse with iso-propyl alcohol, and dry the substrate.

The soft bake and hard bake procedures are important steps in the SU-8 patterning process. The heating and cooling of the wafer using the programmed oven temperature profiles was performed to ensure that cracks do not develop after the baking process. While baking the wafer in the oven, it is necessary to make the oven surface on which the wafer is placed precisely horizontal. A level was used to ensure this. The reason for this requirement is that if the surface is not horizontal, the uncured SU-8 structures will gradually flow on the wafer surface during the long baking process. This will create a channel mold with one of the ends of the microchannel master thicker/thinner that the other end, causing the fabrication of an unusable microchannel after the PDMS molding process.

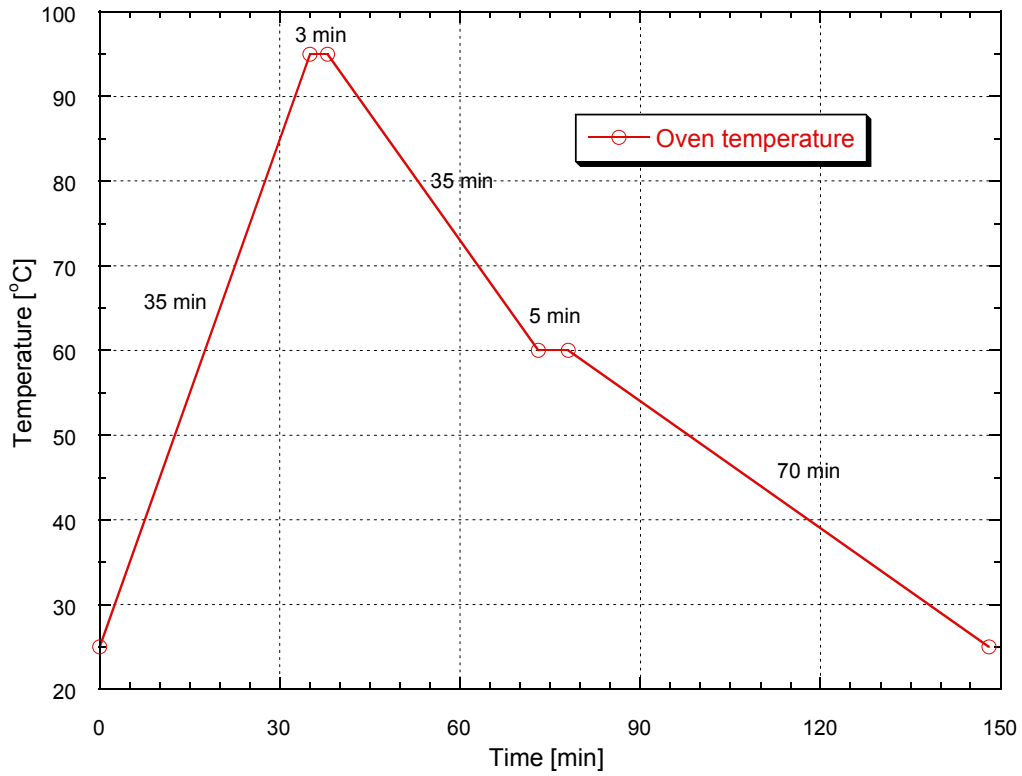

Figure 4.2 Temperature profile of oven used for soft bake of SU-8 2010.

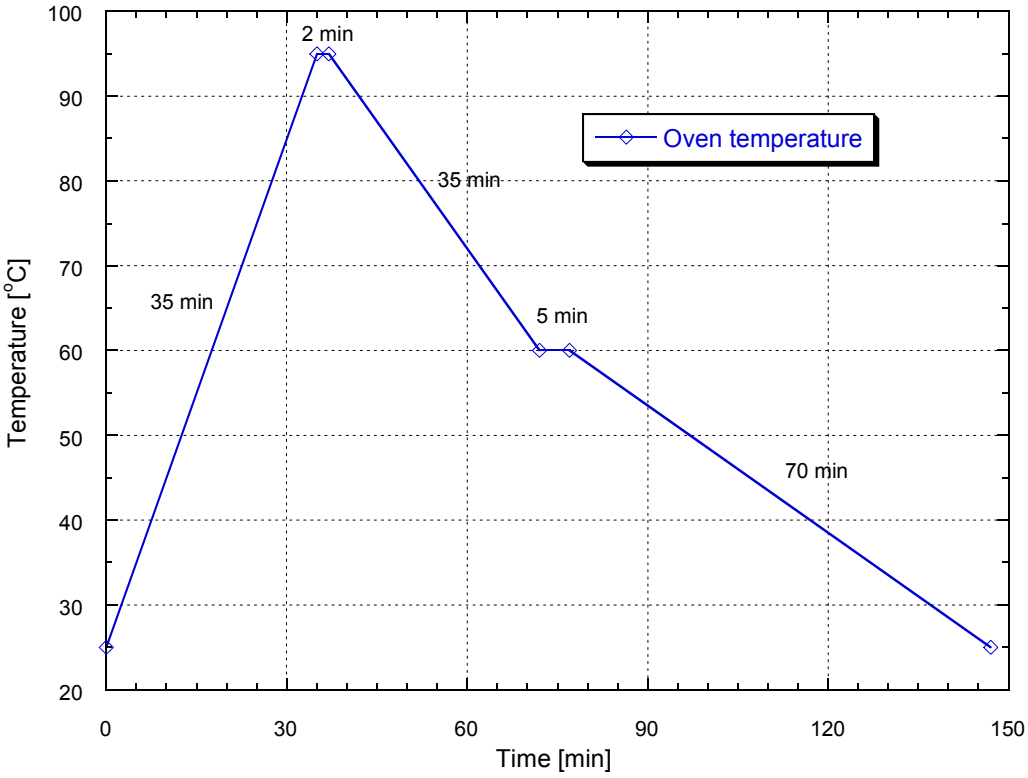

Figure 4.3 Temperature profile of oven used for hard bake of SU-8 2010.

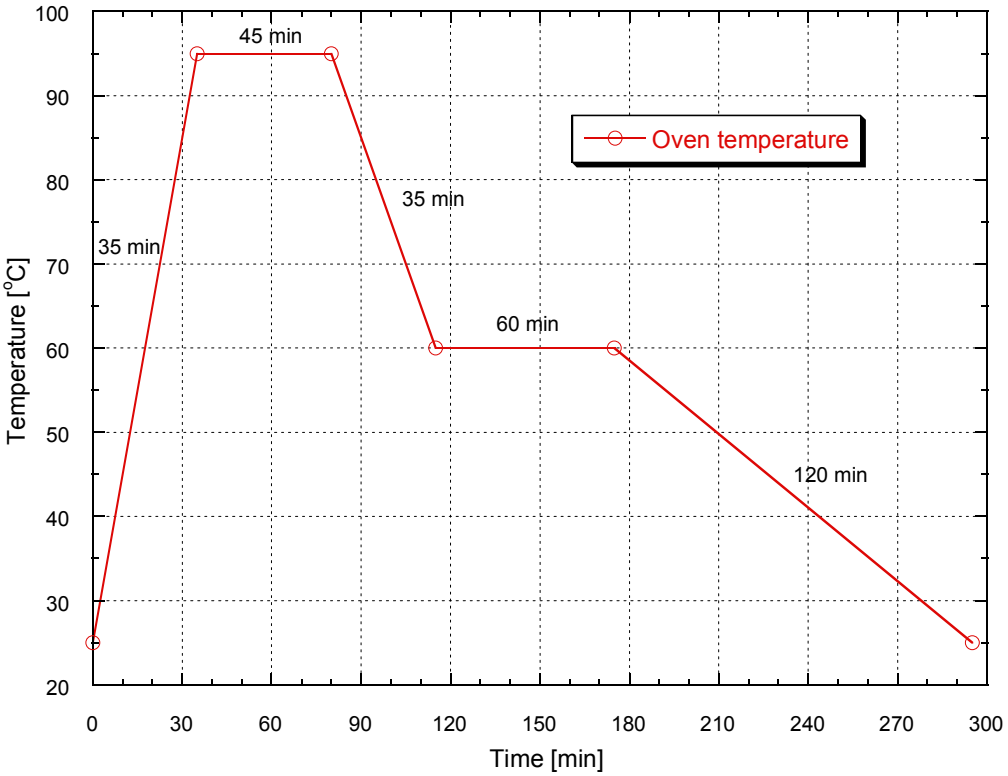

Figure 4.4 Temperature profile of oven used for soft bake of SU-8 2075.

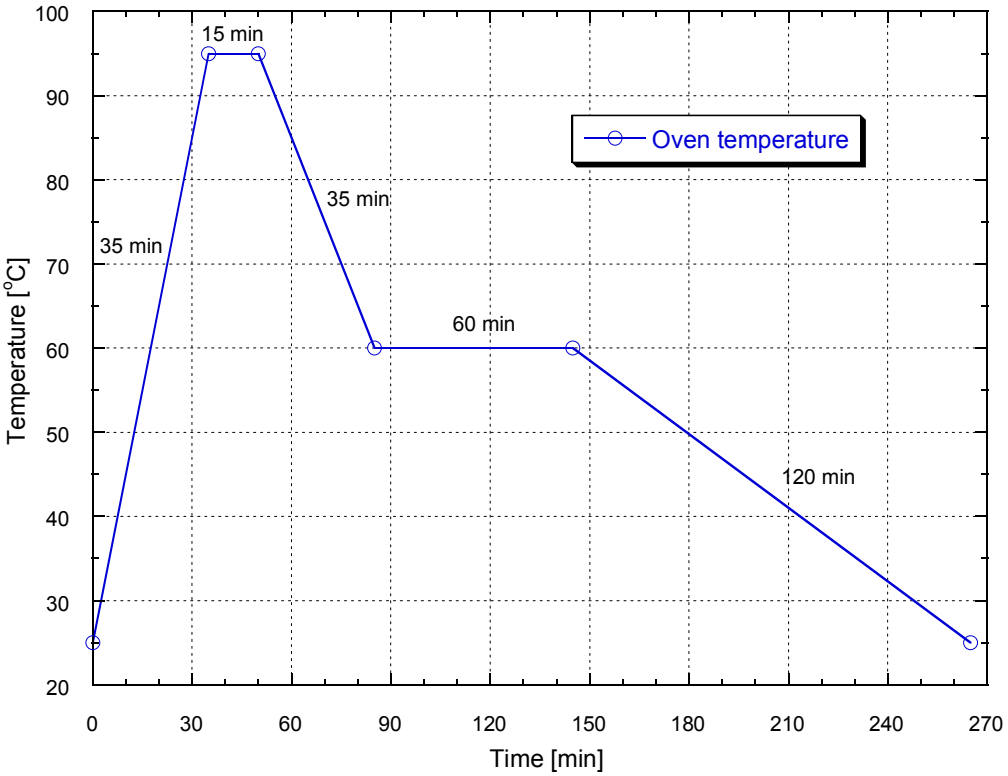

Figure 4.5 Temperature profile of oven used for hard bake of SU-8 2075.

Figure 4.6 shows the SU-8 mold used for the PDMS molding of microchannels. It can be used multiple times for molding if the PDMS layer is carefully peeled off after curing so that the small SU-8 structures on the mold are not damaged.

4.1.2 PDMS Replica Molding of Microchannel

Polydimethylsiloxane (PDMS) is the most widely used silicon-based organic polymer. The chemical formula for PDMS is $(CH_3)_3SiO[SiO(CH_3)_2]_nSi(CH_3)_3$, where n is the number of repeating monomer $[SiO(CH_3)_2]$ units. PDMS is a soft polymer that has attractive physical properties, in addition to low cost. Its desirable physical properties include elasticity, conformality, optical transparency, etc. Devices made of PDMS can be integrated with other components, since PDMS conforms to materials like silicon or glass easily. It is possible to make reversible and irreversible seals taking advantage of its conformal property. It is non-toxic to biological agents, such as proteins, and it is gas permeable. Because PDMS is transparent to visible and UV light, many optical detection methods can be applied on devices made from PDMS. It is generally inert, non-toxic and non-flammable. It is used in microfluidics because of these desirable properties. It is a good elastomer because the bonds between the silicon atom and the two oxygen atoms attached to it are very flexible. This flexibility enabled multiple replications of SLA molds and leak-free binding of the PDMS structure to the glass electrode chip used for the DEP experiments. Additionally, its transparency makes inspection of the nanobelts feasible. Because a very shallow channel (~ 10 μm deep) was necessary for the nanobelt DEP experiments, PDMS was chosen, keeping in view its ease of fabrication and its good conformality property.

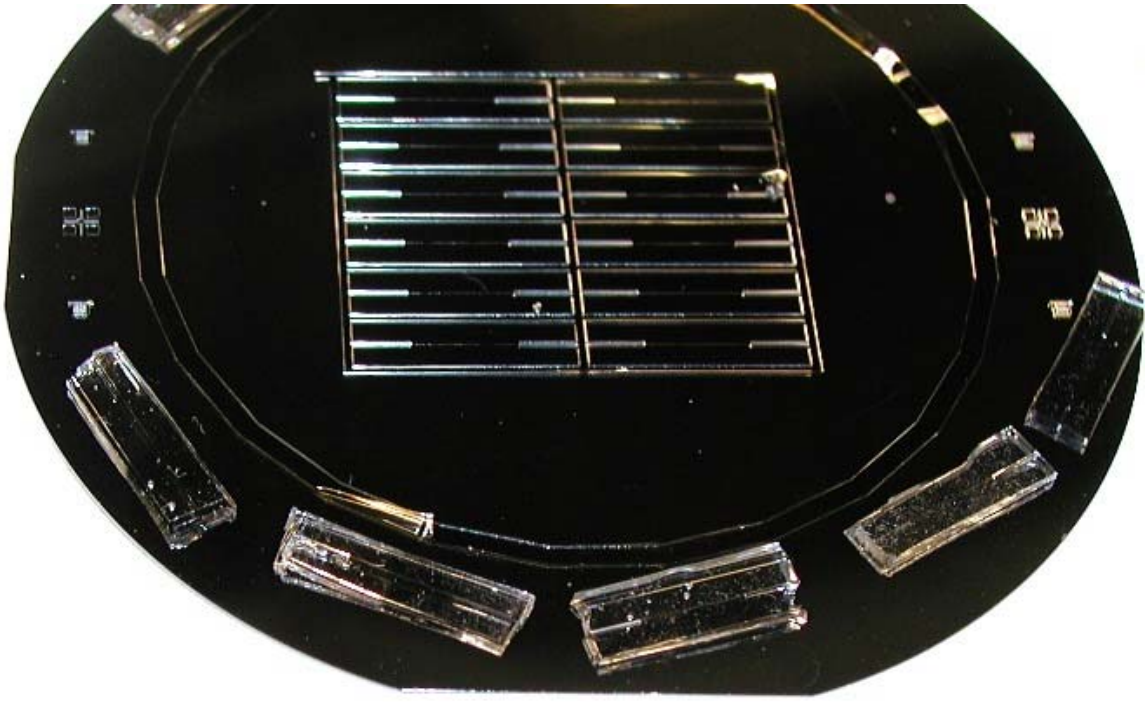

Figure 4.6 SU-8 mold structures (centre) and cut PDMS microchannels (on the wafer periphery).

PDMS (polydimethylsiloxane) polymer was prepared by adding the curing agent to the base with 10 parts base to 1 parts agent by weight. The pre-polymer components are Sylgard® 184 Silicone Elastomer base and Sylgard® 184 Silicone curing agent (*Dow Corning Corporation*, Midland, MI). After mixing them carefully, the mixture was degassed in a vacuum chamber for 30 minutes. The PDMS was then poured into the SU-8 mold to create the microchannel. Finally, the PDMS was thermally cured by placing the mold with the PDMS in an oven at 80 °C for 2 hours. After the curing process, the PDMS layer on the mold was carefully peeled off from the mold. The peeled PDMS layer was then cut carefully to obtain individual pieces (see the periphery of wafer in Figure 4.6), which contains the microchannels.

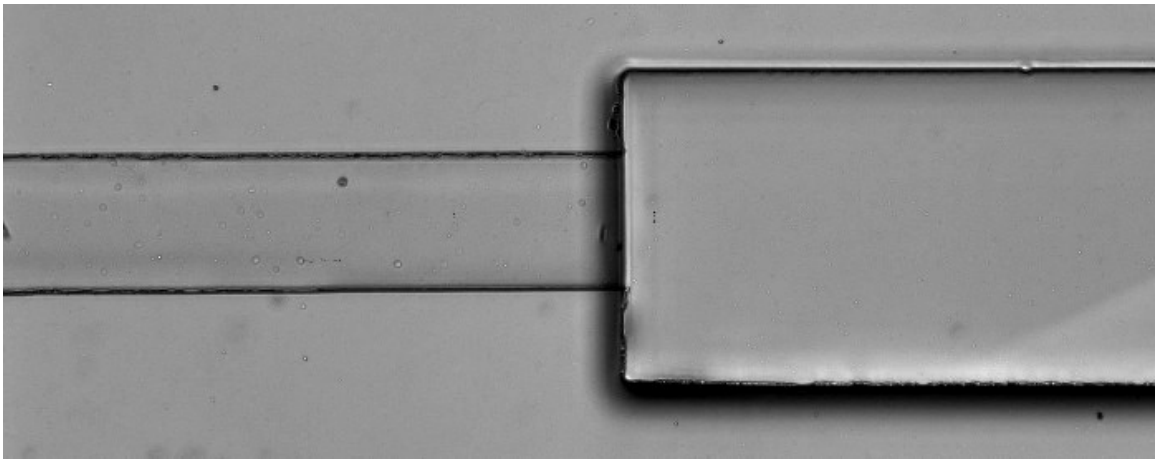

Figure 4.7 Optical microscope image showing the outline of the 100 μm wide test area (left), and the 250 μm wide entrance (right) of the PDMS channel.

4.1.3 Microelectrode Fabrication

Fabrication of the DEP electrodes was carried out on a 500 μm thick Pyrex glass wafer (*G.M. Associates Inc.*, Oakland, CA, USA). The transparent substrate allowed visualization of the nanobelt manipulation from the bottom side using an inverted optical microscope. The Ti/Au (20 nm/250 nm) electrode was patterned on the wafer using standard lithographic techniques and lift-off process. The fabrication steps are: a) start with glass substrate, b) pattern formation after photolithography, c) metal (Ti/Au) deposition, and d) lift-off using a solvent. The details of the process are provided in section 3.1.1.

The electrode pattern is shown in Figure 4.8, which consists of two linear arrays of triangular electrodes (minimum electrode gap ~ 20 μm.) facing each other. The array of microelectrodes is connected to bond pads through wider Au lines. Electrical connections to the bond pads were made using gold wires and conductive silver epoxy (Loctite 3880, *Henkel Consumer Adhesives*, Avon, OH, USA) for easy handling and measurements. A layer of epoxy (Loctite Extra Time) was then coated on the wire bonds

to prevent them from breaking off. Wire bonding is not appropriate because it would require the use of a package, which will interfere with the use of the microfluidic channels and fluidic connections.

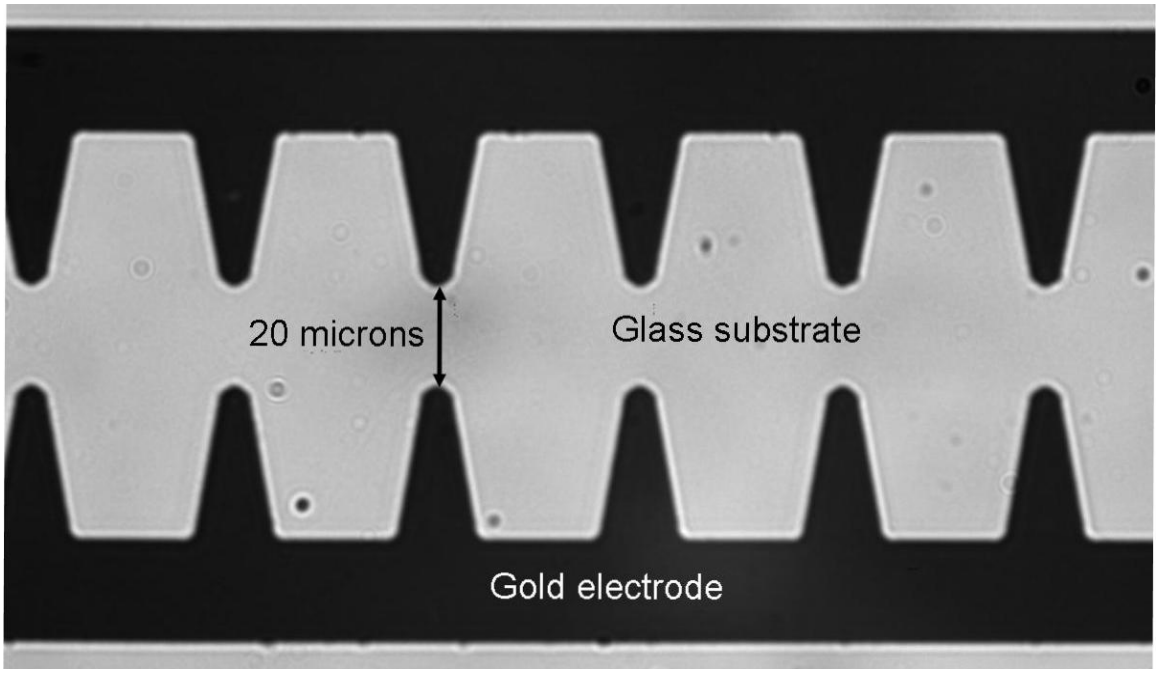

Figure 4.8. Gold microelectrodes fabricated on glass substrate, for performing DEP experiments on single SnO_2 nanobelts.

4.1.4 SnO_2 Nanobelt Sample

SnO_2 nanobelt samples were made and suspended in ethanol as described in section 3.1.5 of Chapter 3.

4.1.5 Experimental Setup and Testing

The PDMS microchannel was aligned and attached over the gold microelectrode array (Figure 4.8), forming the liquid chamber for DEP experiments. Polyimide-coated flexible fused silica capillary tubing of OD ~ 250 μm, and ID ~ 100 μm (*Polymicro Technologies LLC*, Phoenix, AZ) was used to connect a glass syringe to the PDMS

channel. The syringe was fitted with a luer lock to CE column adapter (*InnovaQuartz, Inc.*, Phoenix, AZ) so that the capillary tube has a leak free connection with the syringe. Figure 4.10 shows the connection of the capillary tube with the syringe. The 250 μm diameter capillary tubes were connected to the inlet and exit (~ 250 μm square cross section) of the PDMS channel. Figure 4.11 shows the configuration. One of the syringes was filled with SnO_2 suspension in ethanol, and the other was filled with just ethanol. By pressing the first syringe, SnO_2 suspension was introduced into the PDMS channel inlet. By pressing the other syringe connected to the exit, one could slow down the nanobelts coming from the inlet side, giving better control of the location of the nanobelts to be studied.

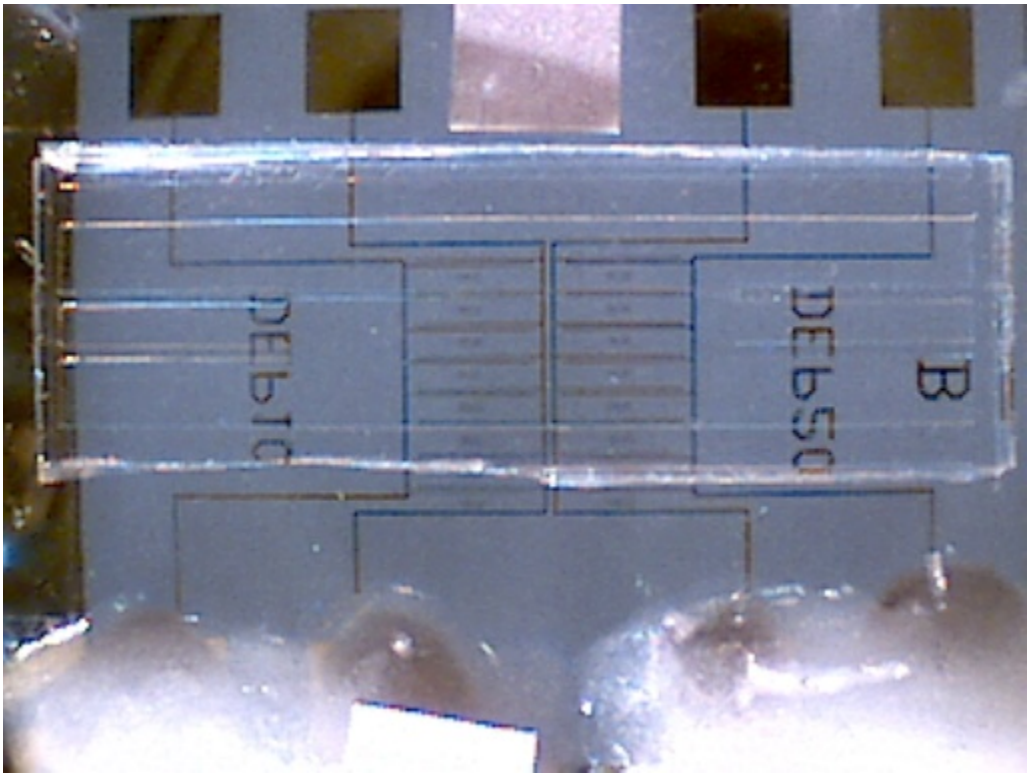

Figure 4.9 PDMS microchannel attached over the linear electrode array.

Figure 4.10 Capillary tubing attached to a syringe fitted with a luer lock to CE column adapter.

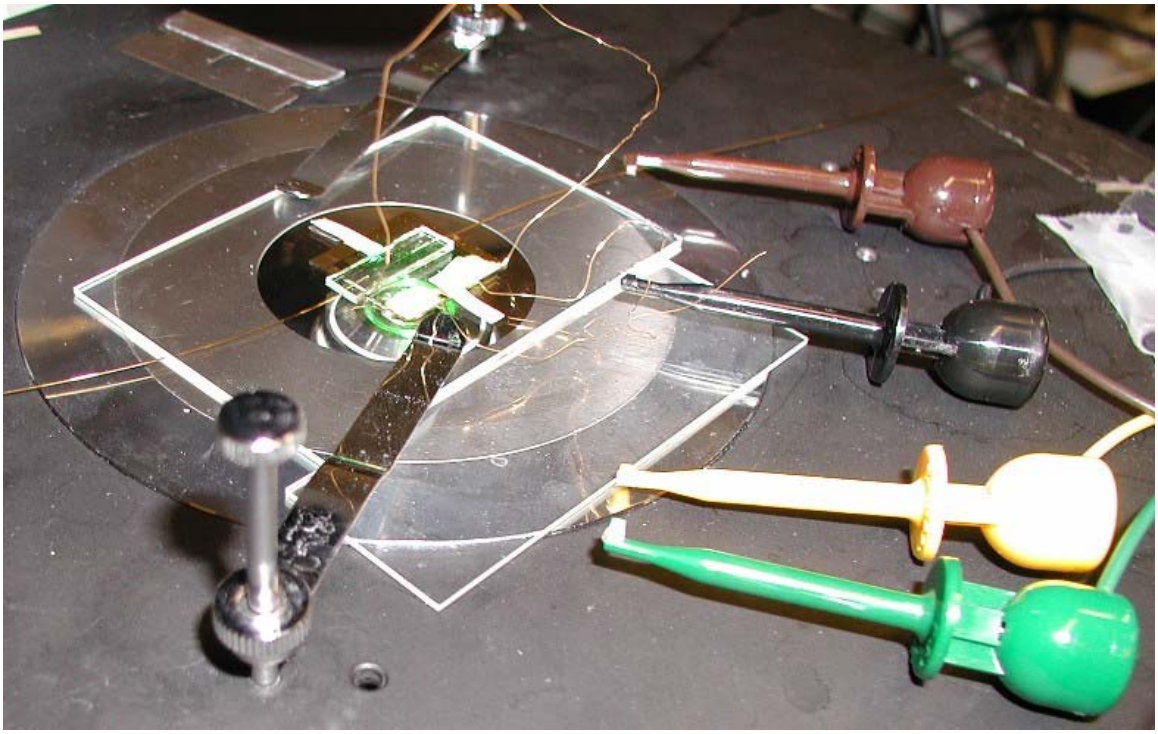

Figure 4.11 Experimental setup for studying the detailed motion of the nanobelts induced by DEP forces, seen on top of the inverted microscope platform.

The electric field inside the channel was generated by applying AC signal between the electrodes to induce DEP forces. A Synthesized Function Generator (*Stanford Research Systems Inc.*, Sunnyvale, CA, USA) in combination with a transformer was used for the low frequency range (5 Hz - 100 kHz), and model AG 1006 LF power amplifier/generator (*T&C Power Conversion, Inc*., Rochester, NY, USA) was

used as a source of RF signals for the high frequency range (1 MHz - 10 MHz). Since DEP force depends on the volume of the particle [20], and nanobelts are quite small [1] (typical widths of 30 - 300 nm, width-to-thickness ratios of 5 to 10), high voltages (~ 70 V_{peak}) were required to observe the nanobelt motion clearly.

Motion of the single nanobelts in the channel was observed using a Nikon Eclipse TE2000-S (*Nikon Instruments Inc.*, Melville, NY, USA) inverted optical microscope coupled with a digital CCD camera for image acquisition. Digital images and movies were acquired using a computer controlled imaging software, MetaMorph® Imaging System (*Universal Imaging Corporation*, Downingtown, PA, USA), which enabled automated image capture and analysis from the digital CCD camera attached to the microscope.

The brightness and contrast settings in the software were found very useful in visualization of the nanobelts. Proper adjustments of the settings of the digital image enabled good contrast. In fact, nanobelts of width as narrow as 100 nm could be detected using brightness and contrast settings and Köhler illumination [67] with the condenser. Köhler illumination helps in achieving the best optical resolution on a light microscope. A model TE-C ELWD condenser with 0.3 N.A. (*Nikon Instruments Inc.*, Lewisville, TX, USA) was used with the microscope for illumination of the DEP electrode chip for improved imaging. Proper lighting is critical for good imaging of the nanobelts. By adjusting the size of the imaging regions in the software, movies with frame rates in the 15 - 25 fps range could be acquired. With full frame image acquisition the frame rate was on the order of 10 fps.

The shallow PDMS channel (~ 10 μm) used over the DEP electrodes made sure that the nanobelts do not go out of focus, and they remained constrained near the electrode region. This is also beneficial because this allowed the nanobelts to be close to the electrodes where DEP forces are higher.

Figure 4.12 Experimental setup showing the inverted microscope and computer data acquisition system.

4.2 Results and Discussion

4.2.1 Positive Dielectrophoresis

In the MHz frequency range, positive DEP of the nanobelts was observed. Figure 4.13 shows a sample from the measurements, which shows a nanobelt gradually getting attracted towards the top electrode. However, the attractive forces were much weaker compared to the repulsive forces, as can be observed from the longer time intervals for successive nanobelt positions in the figure.

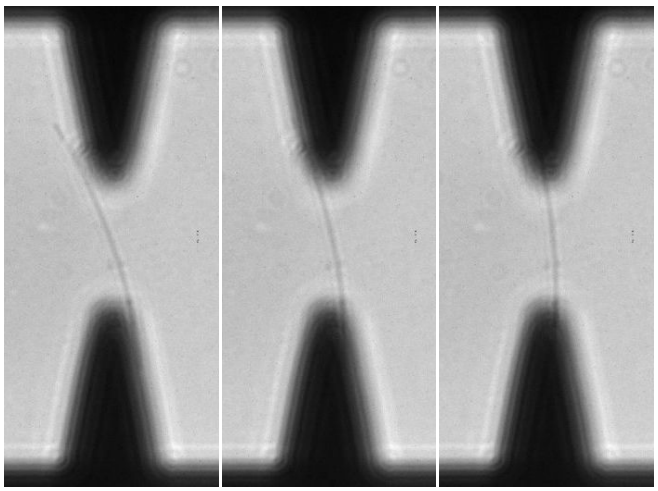

7.708 s 9.048 s 10.120 s

Figure 4.13. Time snapshot (from 15 fps movie) showing nanobelt attraction at a high frequency signal (70 V_{peak}, 10 MHz). Nanobelt size was not determined.

4.2.2 Negative Dielectrophoresis

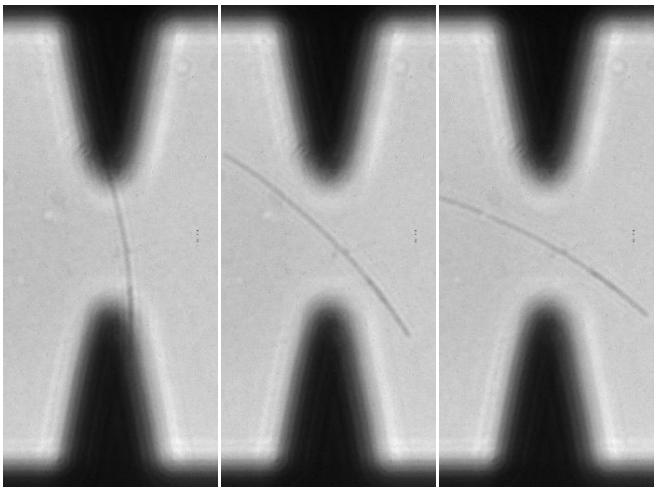

3.416 s 3.765 s 4.096 s

Figure 4.14. Time snapshot (from a 15 fps movie) showing nanobelt repulsion at a low frequency signal (70 V_{peak}, 50 kHz). Nanobelt size was not determined.

Strong negative DEP (repulsion) of the nanobelts was observed in the low frequency range (< 100 kHz). Figure 4.14 is a sample from the measurements, which shows the nanobelt getting repelled from the top electrode as a function of time. The

strong force can be appreciated from the short time intervals for the successive nanobelt positions in the figure. The nanobelt shown in Figure 4.13 and Figure 4.14 are identical. It was first attracted and then repelled using different frequency signals.

4.2.3 Nanobelt Deformation

For low frequency (< 100 kHz) signals, the DEP forces caused deformation of the nanobelts. Figure 4.15 is a sample from the measurements, which shows the change in position as well as deformation of a long nanobelt due to the strong repulsive forces. In this figure the two ends of the nanobelt are fixed. For cases where the ends are not fixed, the repulsive forces caused the nanobelts to change position (rigid body motion). Some deformation was still seen in addition to the rigid body motions, although it was not as strong as in the case where the ends are fixed.

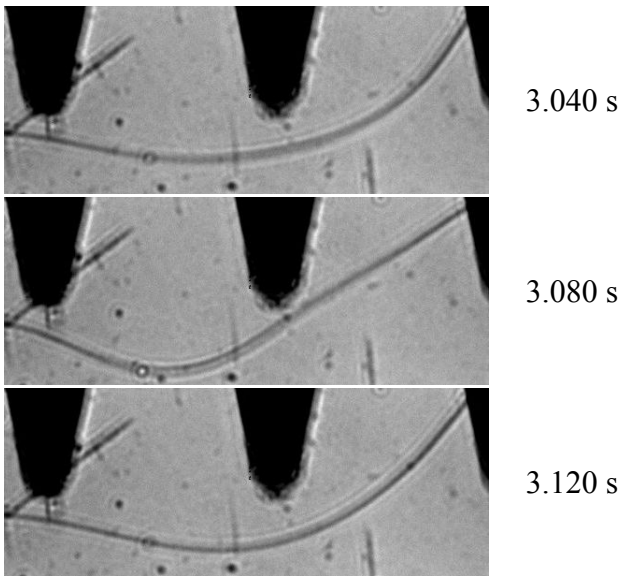

Figure 4.15. Time snapshot (from a 25 fps movie) showing nanobelt position change and deformation at a low frequency signal (87 V_{peak}, 50 kHz). AFM measurement on this nanobelt after the experiment showed the thickness to be ~ 60 nm and width to be ~ 500 nm.

4.2.4 Pearl Chain Formation

For short nanobelts and particles, pearl chain [20] formation was observed in the low frequency (< 100 kHz) range signals. In this phenomenon the particles combine into a long single entity. Figure 4.16 shows a sample from the measurements. Because of negative DEP in this frequency range, the combination oscillated between the electrodes with time.

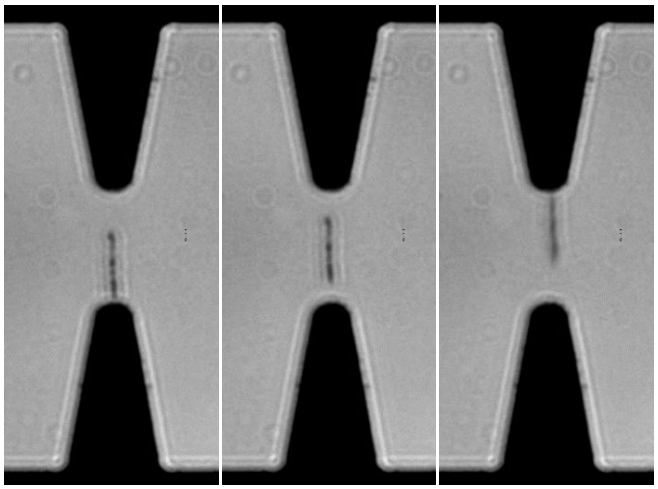

0.767 s 0.836 s 0.974 s

Figure 4.16. Time snapshot (from a 15 fps movie) showing pearl chain formation of short nanobelts and particles, which oscillated between the electrodes as a single entity due to negative DEP at 70 V_{peak}, 50 kHz signal.

4.2.5 Frequency Dependence of Force and Torque Magnitudes

In contrast to particles, nanobelts are not point objects. Since different electric field gradients can affect the different points along the length of a nanobelt, making a comparison of the DEP force as a function of frequency from experimental data is quite difficult. It requires that the motion of a particular nanobelt be observed at approximately the same location, while signals of different frequencies are applied. Since the long nanobelts deform due to the strong repulsive forces, and the very short nanobelts are

difficult to observe, medium length nanobelts may be used for such a measurement. Such favorable conditions occur when one of the ends of the nanobelt is fixed, while the other end is free to move. It was observed that the nanobelt makes a circular motion under repulsive forces generated by the electrical fields. In such a situation, the relative repulsive forces can be compared by measuring the angular velocity of the free end of the nanobelt, in the absence of deformation. Because, the circular motion may not be very uniform at all angular positions, RMS angular velocity may be computed and used for this comparison.

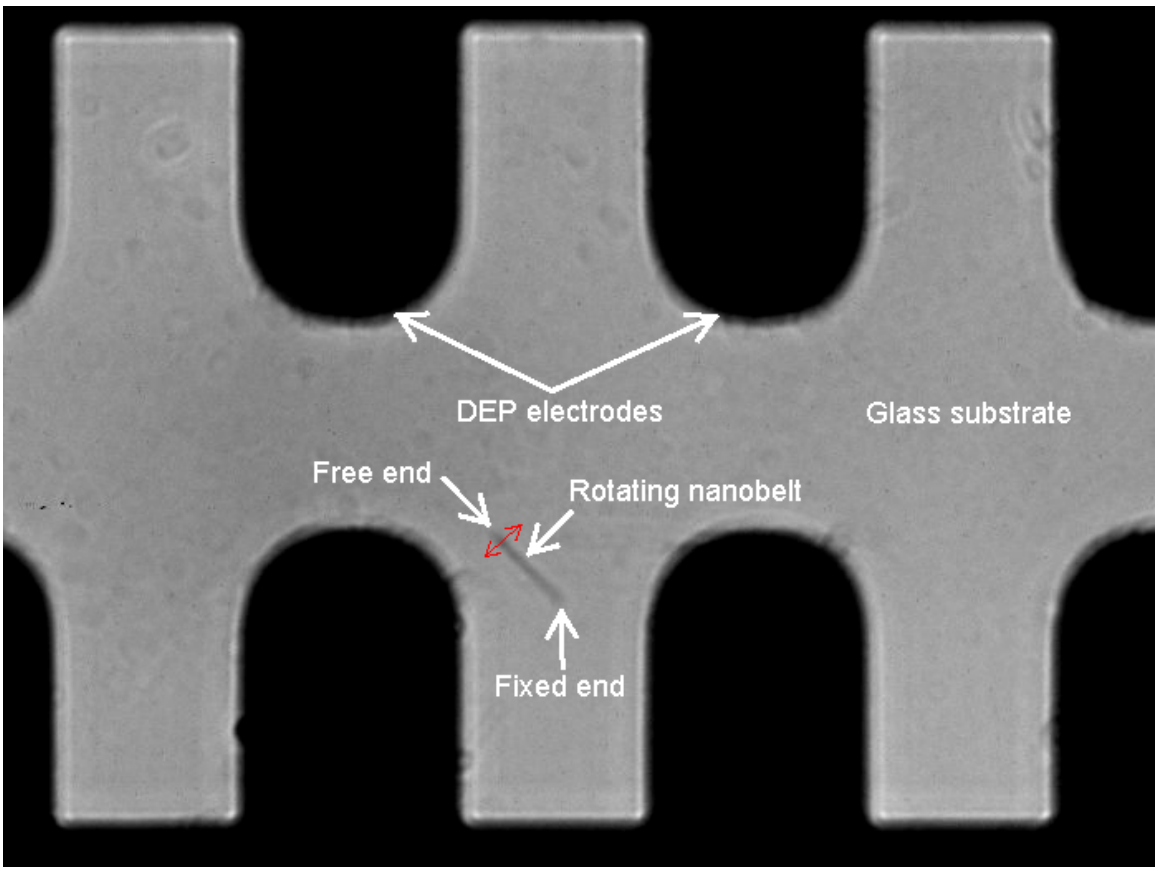

Figure 4.17. One of the frames (from a 15 fps movie) showing an SnO_2 nanobelt undergoing angular rotation due to electrical forces at ~ 32 V_{peak}, 10 kHz signal. The application of a constant voltage with varying frequency allowed an approximate comparison of the electrical field induced forces as a function of the signal frequency. The electrode gaps are ~ 20 μm.

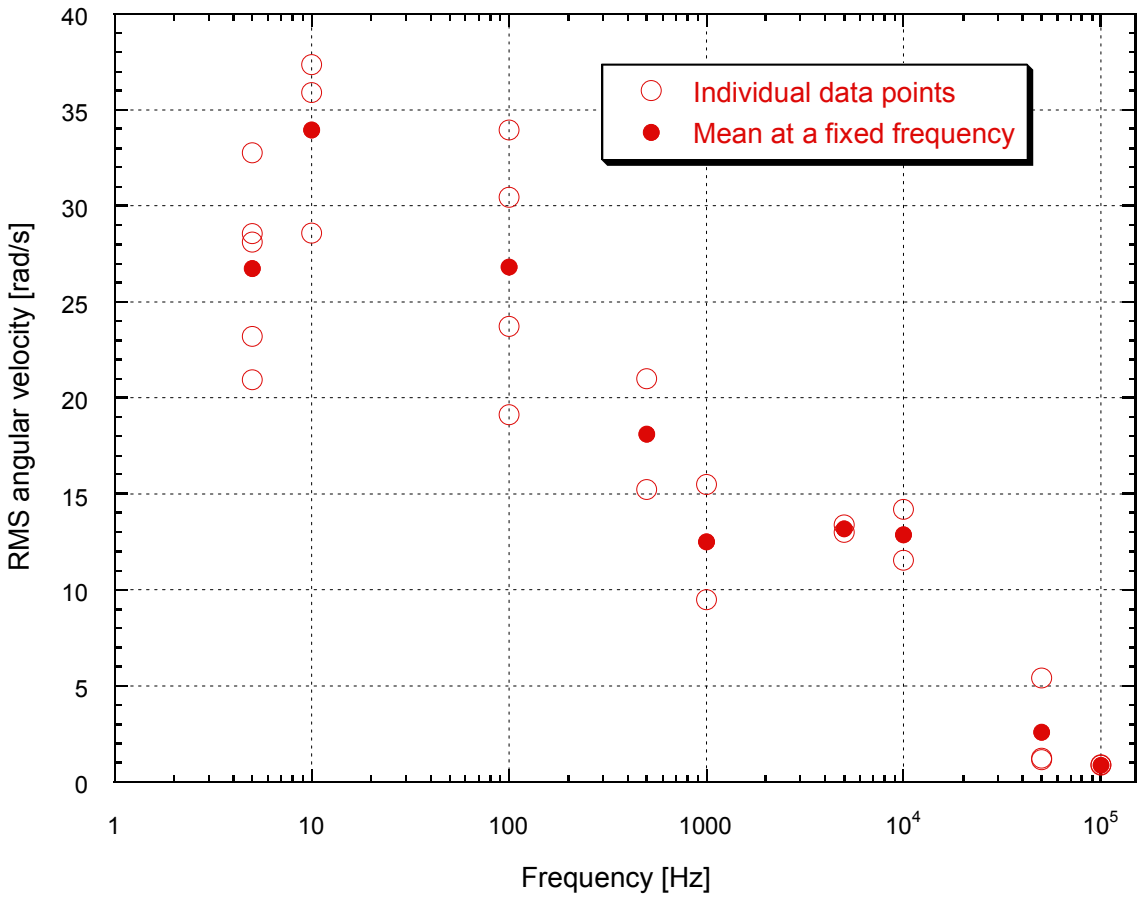

Figure 4.18 Angular velocity of the free end of a nanobelt as a function of the applied signal frequency at a fixed voltage of ~ 32 V_{peak}.

Such a measurement was performed in the frequency range 5 Hz - 100 kHz while keeping the applied voltage approximately fixed at ~ 32 V_{peak}. Figure 4.17 shows a typical situation where the nanobelt is rotating in a circular path, with one of the ends fixed. In the positive DEP regime (frequencies greater than approximately 100 kHz), it is difficult to perform a similar measurement for force comparison, since the nanobelts stick to the electrodes due to the attractive forces. For the low frequency range measurement, the RMS angular velocity of the nanobelt was computed from the recorded movies corresponding to the different frequencies (Figure 4.18). It can be observed from the figure that the "crossover frequency" [20] is about 100 kHz. The angular velocities are

larger for lower signal frequencies. A later chapter (Chapter 7) describes the presence of charge on the nanobelts. Hence, in addition to negative DEP forces, some electrophoretic forces are also expected to contribute to the nanobelt angular motion at very low frequencies (~ Hz).

The movies were acquired at a frame rate of 15 fps. According to the Nyquist criterion, the recorded observations are reliable if the sampling rate is at least 2 times the frequency of the oscillating force causing the nanobelt motion. The forcing motion is due to the electrical forces generated by the application of voltage signals. The oscillating force frequency and the signal frequency do not have a direct relationship. Strictly speaking, using the Nyquist criterion, it can be concluded that up to a forcing frequency of $15/2 = 7.5$ Hz, the angular velocity is being resolved well. This corresponds to an angular rotation frequency of $\sim 2\pi \times 7.5 = 47$ rad/s. For forcing frequencies higher (corresponding to lower signal frequencies) than 7.5 Hz, it is possible that the angular motion is not sufficiently resolved and hence the rotation rate of the nanobelt is not very accurate. In such a situation the use of a camera with a faster frame rate will become necessary. For forcing frequencies lower (corresponding to higher signal frequencies) than 7.5 Hz, the wire is expected to move slowly compared to the frame rate, and hence the nanobelt angular rotation rates are accurate. In summary one can say that for lower forcing frequencies the recorded angular velocities have a direct correlation with the electrically generated forces. For high forcing frequencies this correlation cannot be drawn because of the slow frame rates, since the angular positions will not be recorded accurately as a function of time. From Figure 4.18 one can observe that the maximum rotation rate is less than but close to the 47 rad/s number. So it may not be very accurate

to correlate this angular rotation in the low frequency signal range to the electrically generated forces. A higher frame rate is desirable.

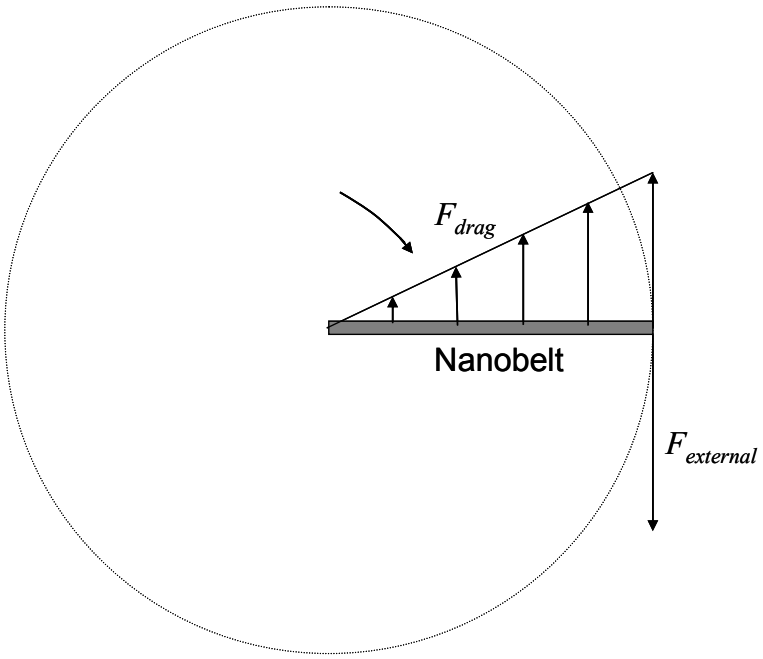

Figure 4.19 Schematic showing the balance between the externally imposed forces and the fluid drag force on a rotating nanobelt in liquid.

Assuming that the frame rate is not a limiting factor, the angular velocity shown in Figure 4.18 represents the relative magnitude of the repulsive torque experienced by the nanobelt under the electrically induced forces, since these two quantities are related to each other. As mentioned in section 2.1, the particle velocity in microsystems is proportional to the externally applied force acting on it. In the literature no analytical solution for the drag coefficient is available for a long object (e.g., cylinder) rotating about a point on it, because velocity changes along the length of the object. Keshoju et al. [68] developed a method to estimate the angular drag coefficient for a cylinder rotating about its midpoint, based on translational motion. Here, a similar procedure is used to derive expressions relating the angular velocity of the nanobelt to the force and

torque due to the fluid drag. In this simple analysis the nanobelt has to be considered as a cylinder of certain hydrodynamic radius. This should provide an approximate method to obtain an estimate of the force acting on the nanobelt.

The situation of the nanobelt rotating in a circular motion, with one of its ends fixed, in a liquid medium is shown in the schematic in Figure 4.19. The predominant force acting on the nanobelt is the DEP force, with the possibility of some electrophoretic force also being present at the very low frequencies. The drag force and the electrical forces ($\sim F_{external}$) are approximately equal.

Let us approximate the nanobelt as a long prolate spheroid. For low Reynolds number flow, it has been shown that the drag coefficient for such a structure moving perpendicular to its long axis can be expressed as [68]

$$D = \frac{4\pi\eta L}{\ln(L/r) + 0.5} \qquad \text{for } L >> r \tag{4-1}$$

where η is the dynamic viscosity of the fluid, and L and r are the length and radius of the spheroid, respectively. To calculate the drag force and torque acting on the nanobelt when it is rotating in a circular motion, the nanobelt is divided into N segments with individual lengths of $\Delta l = L/N$.[68] The total drag force (F_{drag}) and torque (T_{drag}) are calculated by summing the individual translational drag forces and torques on the segments, which are at different velocities. The individual drag force on a segment is obtained by multiplying the local velocity with the local drag coefficient. Hence,

$$F_{drag} = \sum_{n=1}^{N} \frac{\omega_{rot} l_n 4\pi\eta\Delta l}{[\ln(\Delta l/r) + 0.5]} = \frac{4\omega_{rot}\pi\eta L^2}{N^2[\ln(L/Nr) + 0.5]} \sum_{n=1}^{N} (n - 1/2)$$

$$= 2\omega_{rot}\pi\eta L^2 \frac{1}{[\ln(L/Nr) + 0.5]} = 2\omega_{rot}\pi\eta L^2 C_f \tag{4-2}$$

$$T_{drag} = \sum_{n=1}^{N} \frac{\omega_{rot} l_n 4\pi\eta\Delta l}{[\ln(\Delta l / r) + 0.5]} l_n = \frac{4\omega_{rot}\pi\eta L^3}{N^3[\ln(L/Nr) + 0.5]} \sum_{n=1}^{N} (n - 1/2)^2$$

$$= \frac{1}{3}\omega_{rot}\pi\eta L^3 \frac{4N^3 - N}{N^3[\ln(L/Nr) + 0.5]} = \frac{1}{3}\omega_{rot}\pi\eta L^3 C_t \qquad (4\text{-}3)$$

where ω_{rot} is the angular velocity of the rotating nanobelt, and $l_n = (n - 1/2)\Delta l$. The summation formulas, $\sum_{n=1}^{N} n = \frac{N(N+1)}{2}$, and $\sum_{n=1}^{N} n^2 = \frac{N(N+1)(2N+1)}{6}$, have been used in obtaining the expressions. It is clear from the expressions that the drag force and the torque on the nanobelt are directly related to the angular velocity. For calculating the drag force and the torque one has to select *N* such that $L >> r$.

For converting the nanobelt angular velocity data into the approximate electrically induced force and torque data, the above expressions can be used in combination with the liquid properties and the nanobelt dimensions. The nanobelt length (*L*) is found to be ~ 10 μm. Let us assume the hydrodynamic radius (*r*) of the nanobelt to be ~ 50 nm, and select *N* = 10. At room temperatures, the viscosity of ethanol (η) is ~ 1.2×10^{-3} Pa·s. Using these numbers it is found that,

$$F_{drag} = 2.16\times10^{-13}\omega_{rot} \text{ (N)} \qquad (4\text{-}4)$$

$$T_{drag} = 1.43\times10^{-18}\omega_{rot} \text{ (Nm)} \qquad (4\text{-}5)$$

Applying these expressions, the nanobelt angular velocity data is converted into drag force and torque data as shown in Figure 4.20. These numbers should give an order of magnitude of the electrically generated forces in the experiments.

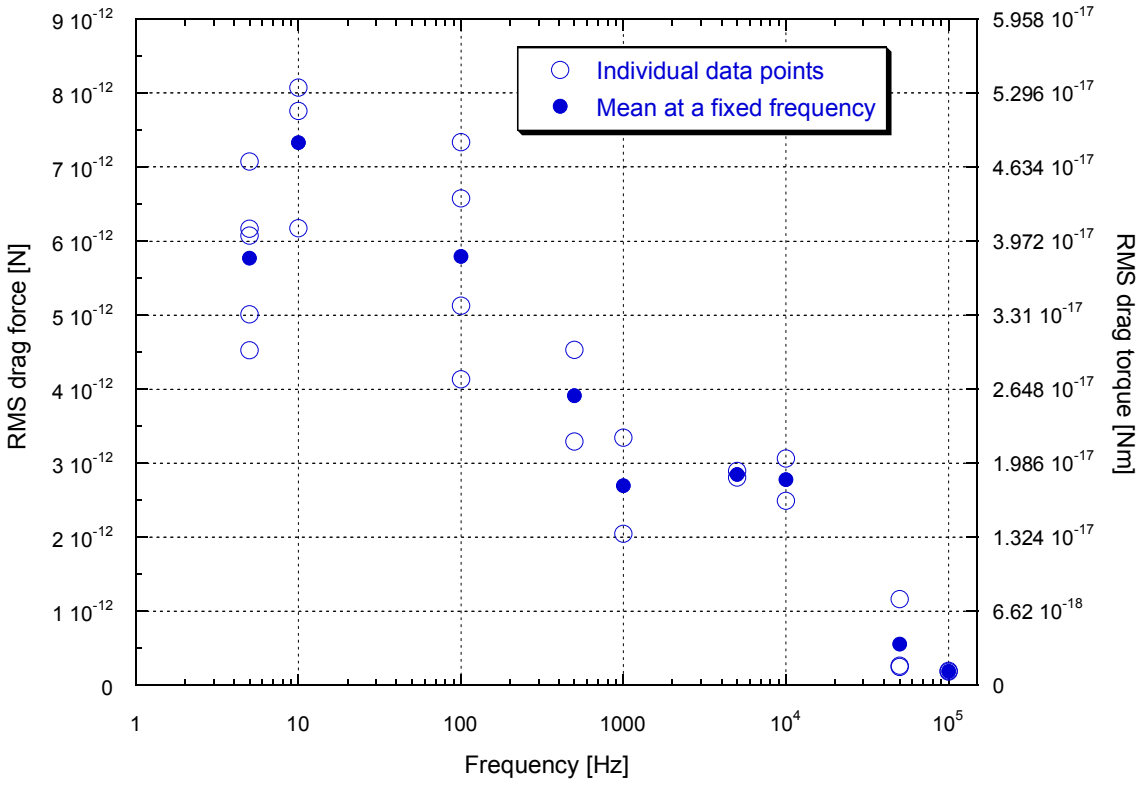

Figure 4.20 Estimated drag force and torque on the rotating nanobelt in ethanol liquid as a function of the applied signal frequency at a fixed voltage of ~ 32 V_{peak}.

4.3 CONCLUDING REMARKS

The experiments performed on single nanobelts revealed different types of motion under electrically generated forces, and the presence of negative DEP for electric fields in the low frequency range. The existence of negative DEP effect is unusual considering the fact that if bulk SnO_2 conductivity and permittivity values are used in combination with ethanol properties, and the Clausius Mossotti factor [20] is calculated using the simple dipole approximation (valid for particles, but not for nanobelts), it predicts positive DEP for the frequency range studied. The probable reasons for the negative DEP are investigated in the subsequent chapters.

CHAPTER 5

FLUID FLOW ALIGNMENT OF TIN OXIDE NANOBELTS

Fluid flow alignment was used to study the alignment of nanobelts and also to make devices to study their electrical properties. PDMS was used to fabricate the microchannel used in the experiments. The SnO_2 nanobelts aligned over linear electrodes were found useful in impedance measurements on the nanobelts, and in obtaining an estimate of the conductivity of the nanobelts. This was the major application of the nanobelt device. The impedance measurements are reported in Chapter 6.

5.1 EXPERIMENTAL

5.1.1 Microchannel Mold Fabrication Using Stereolithography

Microchannels were made using replica molding of PDMS exploiting its ease of fabrication. For fabricating the molds, stereolithography (SLA) was employed. The minimum feasible feature size of SLA is ~ 50 μm on the lateral plane. The designed microchannel had a width of 500 μm and a height of 300 μm.

Pro/Engineer software (*Parametric Technology Corporation*, Needham, MA, USA) was used to design 3D models of the microchannel mold parts with exact dimensions. For easier separation of the PDMS microchannel from the mold, the mold was designed to have 3 parts. The Pro/Engineer mold models were saved in STL file format so that the stereolithography (SLA) machine can recognize the format for fabrication. The STL file is loaded into the program 3D Lightyear (*3D Systems*, Rock

Hill, SC, USA), which controls the SLA machine. 3D Lightyear allows the user to orient and layout the part on a 3D platform that represents the actual platform of the SLA machine. The support for the designed structure is automatically created by the program. SLA-Viper (*3D Systems*, Valencia, CA) machine was used to fabricate the mold pieces in a high resolution mode.

An Nd:YV04 laser cured the photopolymer resin, Vantico SL 5510 (*Huntsman Advanced Materials,* Salt Lake City, UT, USA) in a bath using a layer by layer process to make the mold structure. The tensile strength of the resin is 77 MPa (listed in the datasheet), which is sufficient to provide durability of the molds for microchannel fabrication. After the completion of the laser curing process, the resin was drained from the bath and the parts were rinsed with Tripropylene Glycol Monomethyl Ether (TPM). To aide the cleaning process, the parts with residual TPM were placed in an ultrasonic bath for 30 minutes. After that step, the parts were rinsed with iso-propyl alcohol. The left over resin in narrow structures was removed by blowing air. Once the parts are clean, they were cured in an UV oven for 90 minutes. Figure 5.1 shows the fabricated SLA molds.

5.1.2 PDMS Replica Molding

First, the SLA mold parts (a), (b), and (c) shown in Figure 5.1 were assembled to create the microchannel mold for PDMS replica molding (Figure 5.1 (d)). Then the PDMS (polydimethylsiloxane) pre-polymer components were weighed in a 10:1 ratio with 10 parts elastomer and 1 part curing agent. The pre-polymer components are Sylgard® 184 Silicone elastomer base and Sylgard® 184 Silicone curing agent (*Dow Corning Corporation*, Midland, MI). The polymer was prepared by adding the curing

agent to the base. After mixing carefully, the mixture was degassed in a vacuum chamber for 30 minutes to remove bubbles. PDMS was then poured into the microchannel mold. Finally, the PDMS was thermally cured by placing the SLA mold with the PDMS in an oven at 80 °C for 2 hours. The cured PDMS microchannels were then released from the mold by disassembling the SLA mold parts. The flexibility of the molding process enabled multiple replications of the SLA molds easily.

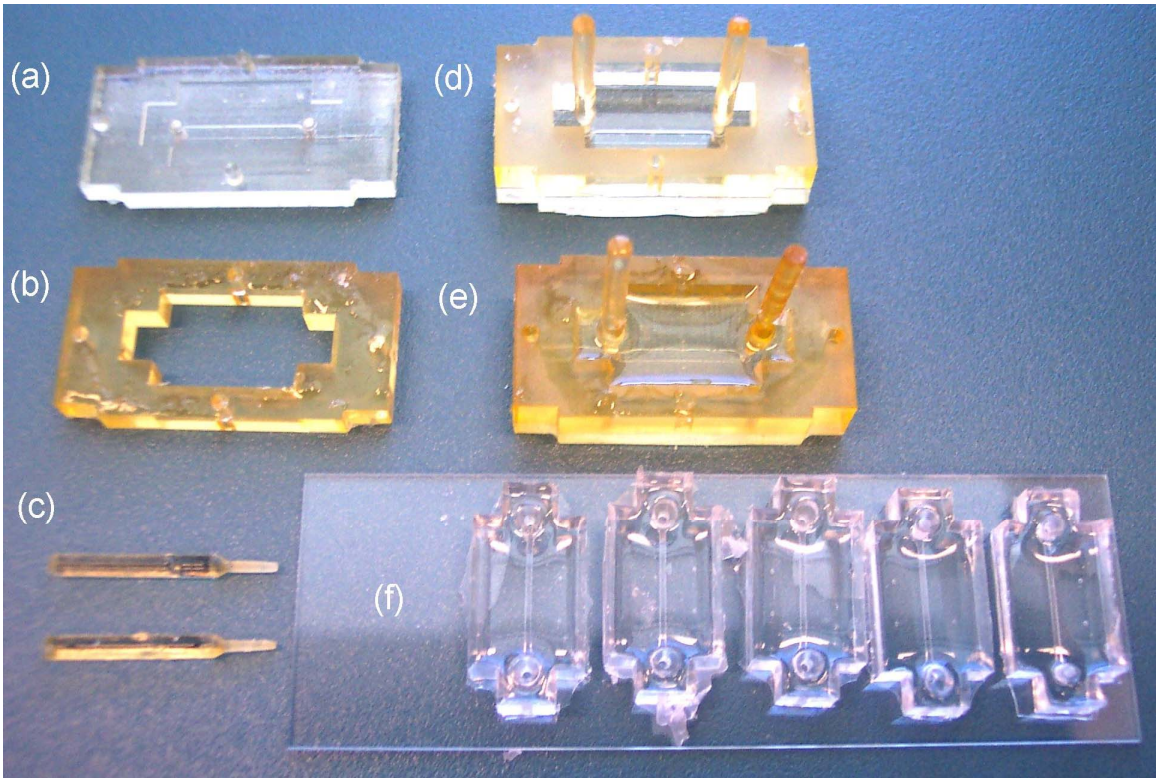

Figure 5.1 Photograph showing (a), (b), and (c) the SLA mold parts, (d) the assembled mold, (e) the mold filled with PDMS, and (f) the released PDMS channels sticking on a glass slide.

5.1.3 Microfabrication

Nanobelt alignment tests were performed on 5 different types of substrates:

Substrate (a): Si substrates

Substrate (b): Si substrate with Au (300 nm) layer deposited on it

Substrate (c): Au lines patterned on Si substrates using a photomask

1. Ti/Au (20 nm/200 nm) deposited on Si wafer,
2. Photolithography performed to pattern the wafer,
3. Au dissolved in patterned areas using wet etching with aqua regia.

Substrate (d): Au electrodes patterned on Si/SiO_2 substrate using a photomask

1. SiO_2 (~ 1 μm thick) grown on Si wafer,
2. Photolithography performed to pattern the wafer,
3. Ti/Au (20 nm/200 nm) or Cr/Au (15 nm/200 nm), deposited and the resist lifted-off using solvents (RR2 and acetone).

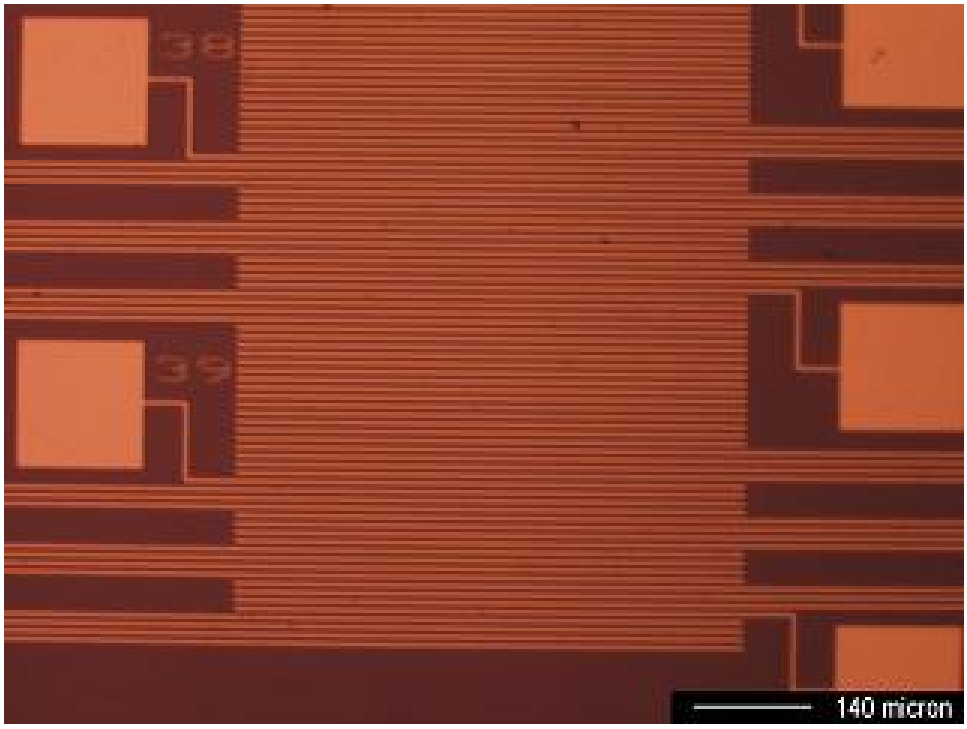

Figure 5.2 Magnified view of the linear electrode pattern and bond pad layout.

Substrate (e): Au lines patterned on Pyrex glass substrate using a photomask

1. Photolithography performed to pattern the glass wafer,

2. Ti/Au (20 nm/200 nm) or Cr/Au (15 nm/200 nm), deposited and the resist lifted-off using solvents (RR2 and acetone).

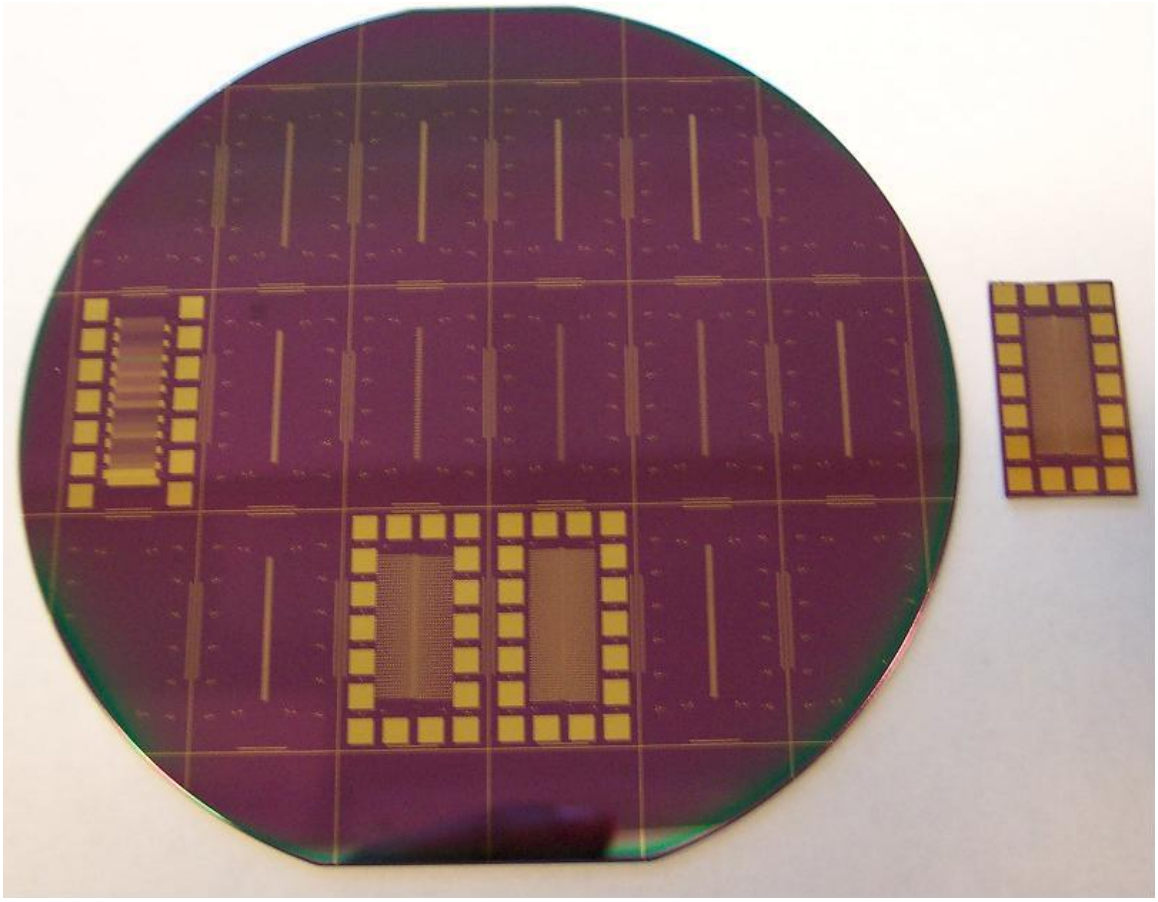

Figure 5.3 Si/SiO_2 wafer with electrode patterns and a diced electrode chip (right).

5.1.4 SnO_2 Nanobelt Sample

SnO_2 nanobelt samples were made and suspended in ethanol as described in section 3.1.5 of Chapter 3.

5.1.5 Alignment Tests

The PDMS channel was visually aligned over the linear electrode array (Figure 5.2 and Figure 5.3) which is located in the central area and along the length of the chip.

Figure 5.4 shows a schematic of the PDMS microchannel which makes a leak-free binding of the PDMS structure with the substrate/electrode chip. The testing process is quite simple. Initial alignment tests were performed on the substrates (a), (b) and (c) by flowing SnO_2 nanobelt suspension at the flow rate of about 0.05 - 0.15 ml/min (5.5 - 16.7 mm/s average velocity) through the PDMS microchannel of 500 μm × 300 μm cross section, attached over the substrate. A PHD 2000 Programmable Syringe pump (*Harvard Apparatus*, Holliston, MS, USA) was used for pumping the suspension at the controlled flow rates. After a certain amount of flow time, the liquid in the channel was withdrawn and the sample was allowed to dry. The PDMS channel was then removed from the substrate and the sample was observed under an optical microscope. Good alignment was observed.

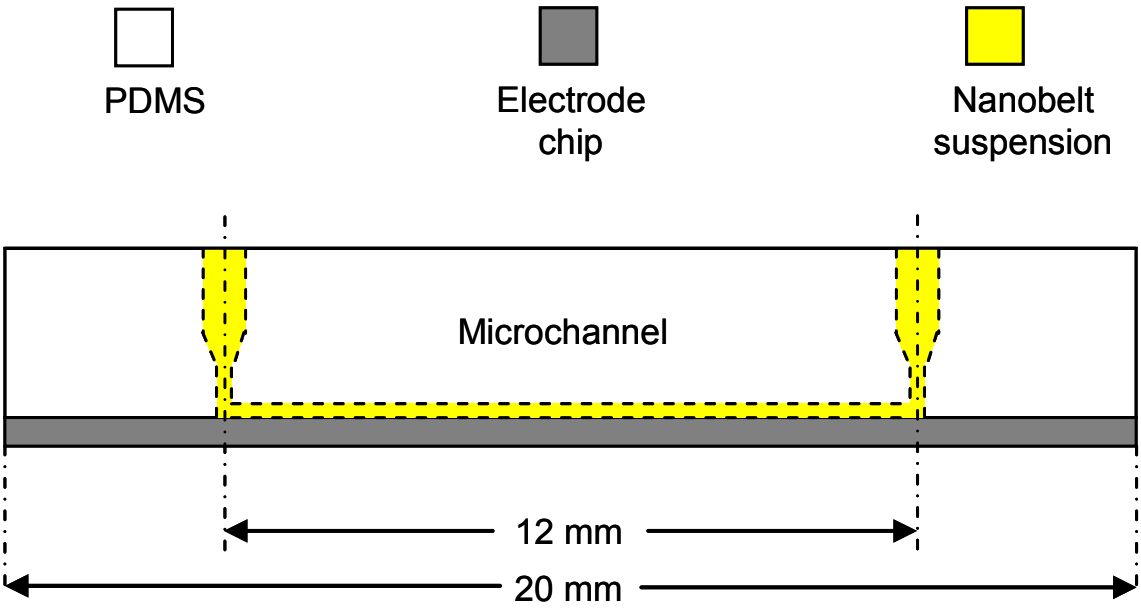

Figure 5.4 Schematic of the PDMS microchannel attached on the electrode chip for fluidic alignment of nanobelts.

Following the success of the alignment tests on the Si surface (substrate (a)), Au surface (substrate (b)), and alternate Au lines (substrate (c)), a photomask was designed for fabricating electrodes (substrate (d) and (e)) and making a nanobelt device. The photomask was used to produce many linear electrodes with bond pads connected to it. The electrodes were fabricated on Si/SiO_2 substrate and Pyrex glass substrates as described in the fabrication process in section 5.1.3. Electrodes with different widths and gaps (2, 3, 4, and 5 μm) in groups of four were made on the Si and Pyrex glass substrates. The alignment of SnO_2 nanobelts was performed on the electrode lines as in the alignment tests for substrate (a), (b), and (c). If the concentration of nanobelts in the suspension is high, multiple nanobelts can deposit between the linear electrodes. One way to control this is to use a lower concentration of nanobelts in the suspension, and also to decrease the time of the fluid flow during the alignment process. Since each chip has many electrodes, not every electrode pair has multiple aligned nanobelts. If necessary, focused ion beam (FIB) milling can be used to break some of the nanobelts after the samples have been dried.

Sometimes it was observed that many large particles were also deposited between the electrodes, because those are present in the nanobelt suspension. One way to get rid of the particles is to use a sticky object such as a piece of PDMS after the samples have been dried. The PDMS piece is allowed to gently make contact with the electrode areas where the nanobelts have been aligned, and then move it away. Because of the sticky nature of the PDMS, it picks up the particles from the electrode areas, reducing the contaminants, and cleaning up the substrate. It is anticipated that a more complete

cleanup will be possible if a stage with precise position resolution is used in combination with, for example, a probe tip which has a sticky object attached on its tip.

The other method that was used to minimize the particles and nanobelts on the electrode surface is to pump out the suspension while the microchannel was filled with it, using a syringe with a needle or microtube connected to it. When pumping out, the bigger particles move easily, while not affecting the nanobelts sticking to the surface of the electrodes. The nanobelts which are suspended in the liquid and not sticking to the linear electrodes are also removed from the channel. This increases the probability of single nanobelts being aligned and deposited on the linear electrodes.

Some alignment tests were also performed using the shallow (~ 10 μm deep) microchannels used in the DEP experiments (described in a Chapter 4). It was found that the number of nanobelts deposited between the linear electrodes was very low, apparently because the velocity of the liquid was quite high (since the channel cross section is very small). However, one difference that was observed with the shallow channel experiments was that fewer particles were deposited or even seen under the real time observation using an inverted microscope. It is probable that this is due to the filtering action of the shallow channel. The particles can enter the ~ 250 μm cross section of the channel entrance, but cannot get inside the ~ 10 μm tall shallow channel.

Following the alignment, there were 3 options for making electrical measurements on the nanobelts:

1. Anneal the aligned nanobelts without any metal deposition on the contacts,
2. Deposit metal over the nanobelt contacts using a 2nd layer of metal using photolithography, or

3. Deposit metal over the nanobelt contacts using focused ion beam (FIB).

   The details are described in the following sections.

5.1.6 Annealing

In some cases electrical measurements were performed on the nanobelts deposited on the electrodes without a second layer of metal on top of it. For these, it was hoped that heating will improve the Au/nanobelt electrical contacts. In one procedure, wafers were put in an oven and the sample was heated for about 12 hours in N_2 atmosphere at elevated temperatures (~ 350 °C).

In another procedure, the electrode chips with the aligned nanobelts were heated in a tube furnace with Argon flowing (~ 20 SCCM) in it. The annealing can change the conductivity of SnO_2.[69] The temperature in the heating process was selected to be ~ 400 °C in the Argon atmosphere. This was decided because, for annealing temperatures of around 450 °C, Ti and Au start to form intermetallic compounds [70], and oxygen is removed from the ZnO surface causing decomposition of ZnO. Similar effects are also anticipated in the case of the electrode chips with the SnO_2 nanobelts. Annealing SnO_2 in contact with the metal electrodes at high temperatures for too long may cause Sn to dissociate and diffuse into the Au contact and even cause a break in the nanobelt near the Au electrode edge.

5.1.7 Metal Deposition Using Photomask

For some samples, photolithography was performed over the substrates with aligned nanobelts on linear electrodes. A lift-off procedure was used to deposit an Au top

layer (~ 100 nm thickness) over the first Au electrode layer so that the nanobelt ends get sandwiched between the top and bottom gold layers (see Figure 5.9).

5.1.8 FIB Deposition

Some of the samples were used for measuring the electrical conductivity of SnO_2 nanobelts when its oxygen vacancy has been unaffected by any type of annealing process. Annealing SnO_2 can change its oxygen vacancy concentration, and hence its electrical conductivity. The room temperature conductivity is required for the analysis of the DEP characteristics of the nanobelts, since the DEP experiments were performed at room temperatures. For that purpose, FIB metal deposition was carried out using Quanta 3D 200 (*FEI Company*, Hillsboro, OR, USA) and Nova Nanolab 200 (*FEI Company*, Hillsboro, OR, USA) systems for improving the nanobelt/electrode contact properties. FIB deposition was successful for the nanobelts aligned on Si/SiO_2 substrates. For the nanobelts aligned on Pyrex glass substrates, FIB deposition was not successful because of strong charging effects preventing correct alignment of the ion beam with the sample. Similar FIB deposition of metal has been reported in the literature [71, 72] for making contacts on nanowires.

Figure 5.5 shows a typical example of a 100 nm thick Pt metal pad deposited using FIB. On the top left area of the image one can observe a rectangular mark. This is due to the ion beam bombarding the sample. It may affect the nanobelt properties if the ions are allowed to interact with the sample for significant times. It is one of the disadvantages of the FIB deposition.

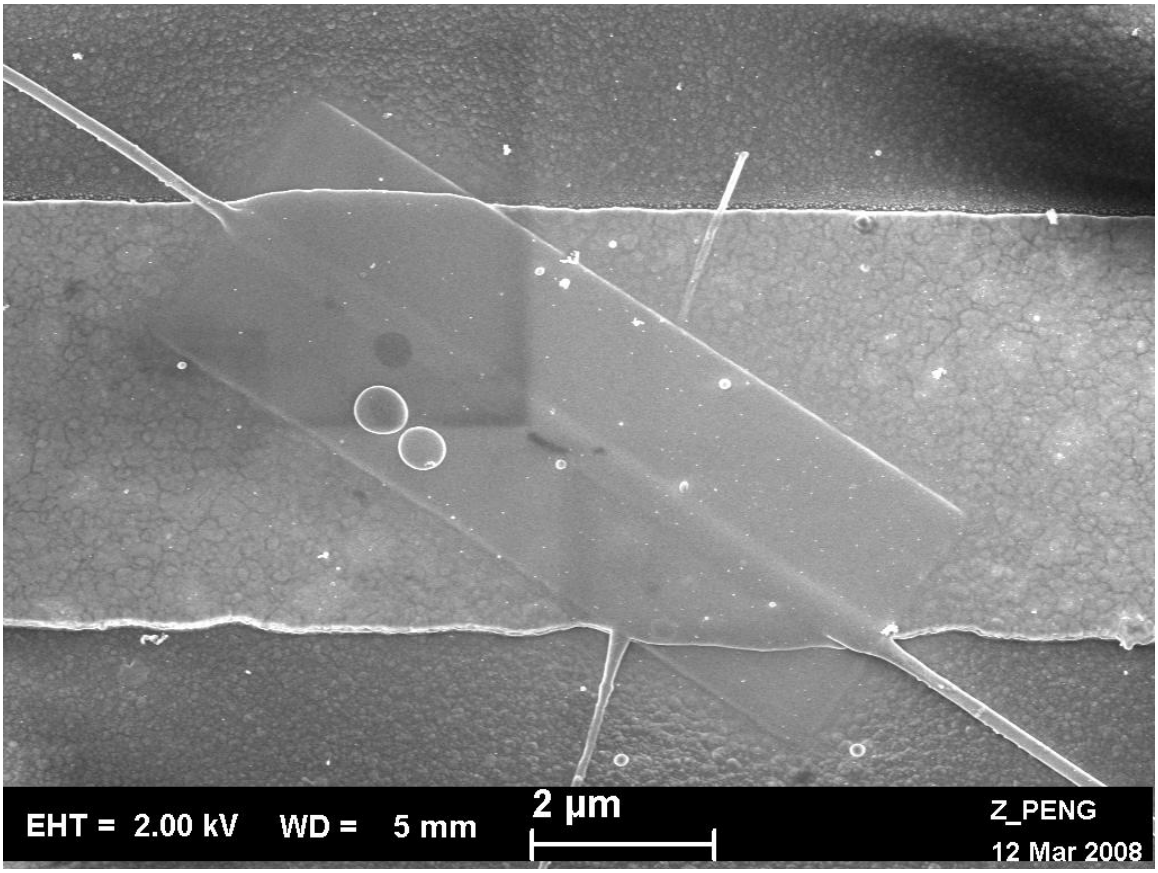

Figure 5.5 SEM image showing 100 nm thick Pt deposited using FIB over an SnO_2 nanobelt lying over Au electrode. Electrode width is ~ 5 µm.

5.2 RESULTS AND DISCUSSION

5.2.1 Nanobelt Alignment Tests

Figure 5.6 (a) and (b) show the good alignment of SnO_2 nanobelts using the fluid flow alignment process, both along and perpendicular to gold lines defined on silicon substrate. Chemical patterning [51] was not necessary in the alignment process.

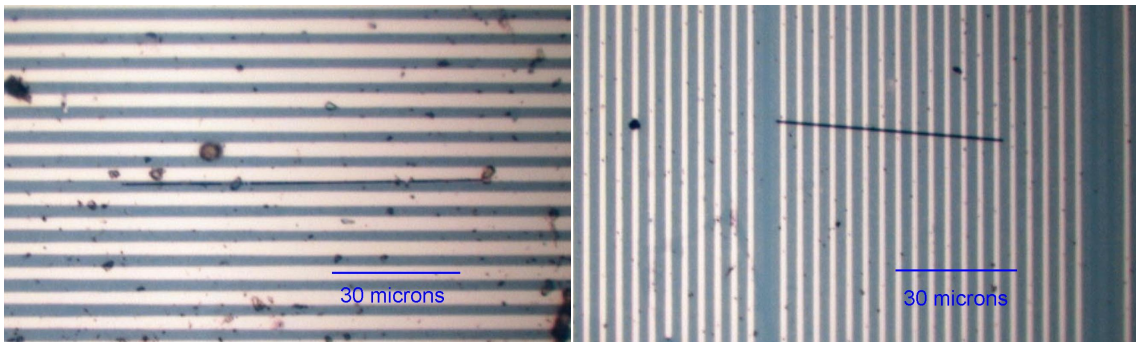

(a) (b)

Figure 5.6 (a) An SnO_2 nanobelt aligned along the Au/Si alternate lines, and (b) an SnO_2 nanobelt aligned perpendicular to the Au/Si alternate lines. Fluid flow direction is horizontal.

The number of nanobelts deposited on the substrate depends on the flow time. Higher flow times caused larger number of nanobelts to deposit on the surface. Higher flow rates improved the degree of alignment. One interesting observation that was made is that the SnO_2 nanobelts have a strong propensity of sticking to the Au surfaces. Even the application of a fluid jet of acetone or ethanol, using a spray bottle, could not detach them from the surface. In contrast, the SnO_2 nanobelts did not like to stick to Si surfaces. Very few nanobelts were found on the surface after the alignment tests on Si surfaces. Obviously there are differences between Si and Au surface interactions with the nanobelts. Figure 5.7 shows aligned nanobelts on Au linear electrodes, which indicate that the alignment process worked well on the Si/SiO_2 substrates. The degree of alignment is very good.

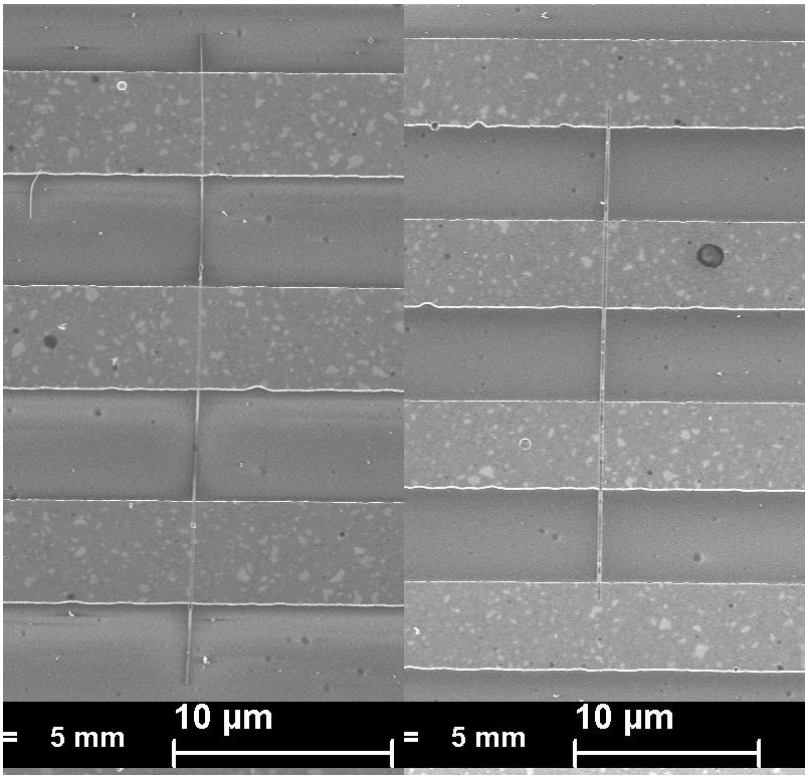

(a) (b)

Figure 5.7 SEM image of SnO_2 nanobelts aligned perpendicular to the Au electrodes on Si/SiO_2 substrate. Fluid flow direction is vertical.

5.2.2 Nanodevice

Figure 5.8 shows an optical image of a nanobelt aligned over linear Au electrodes. No metal deposition was performed on the nanobelt contacts. Figure 5.9 shows an SEM image of a nanobelt device with both top and bottom layers of Au. The SnO_2 nanobelt ends are in contact with the Au electrodes. Figure 5.10 shows a nanobelt with Pt deposited over its contacts. Figure 5.11 and Figure 5.12 shows additional details of the bond pad and wedge wire bonding used for connecting the nanobelt device to wire bonding packages for convenience of electrical measurements.

Figure 5.8 Optical image showing an SnO_2 nanobelt (dark) aligned over multiple Au electrodes (see left). The electrode width and gap are ~ 3 μm for the electrodes on which the nanobelt is aligned.

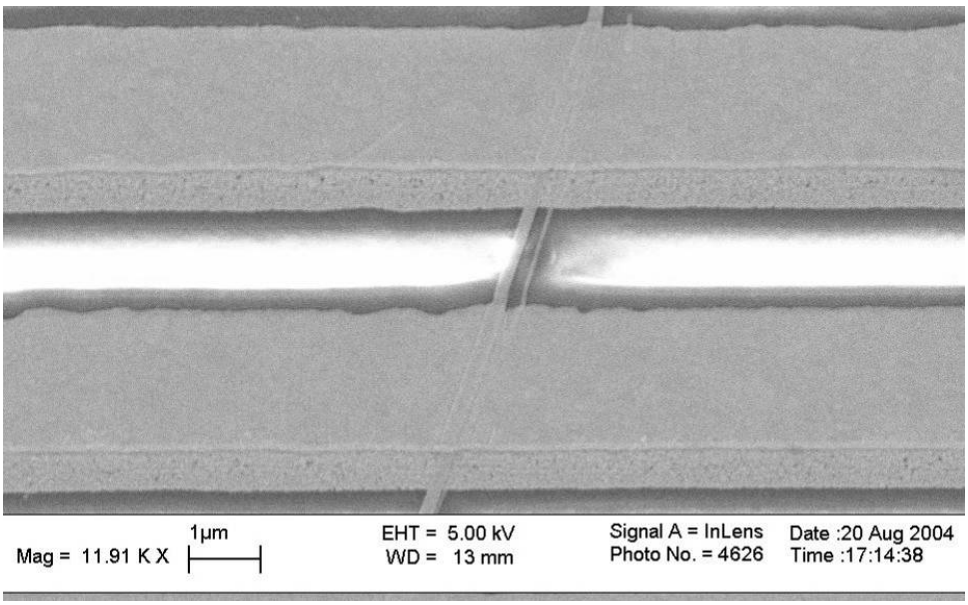

Figure 5.9 SEM image showing an SnO_2 nanobelt sandwiched between Au layers to form a two terminal device. The electrode width and gap are ~ 2 μm.

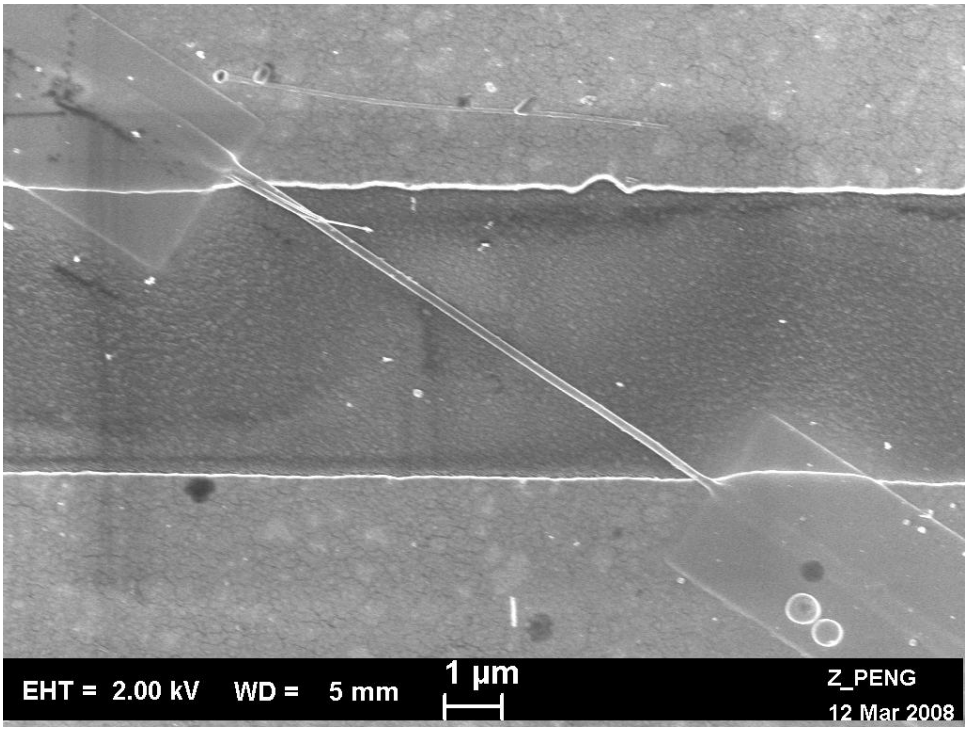

Figure 5.10 SEM image showing an SnO_2 nanobelt between two electrodes, with Pt deposited using FIB over its contacts. The electrode width and gap are ~ 5 µm.

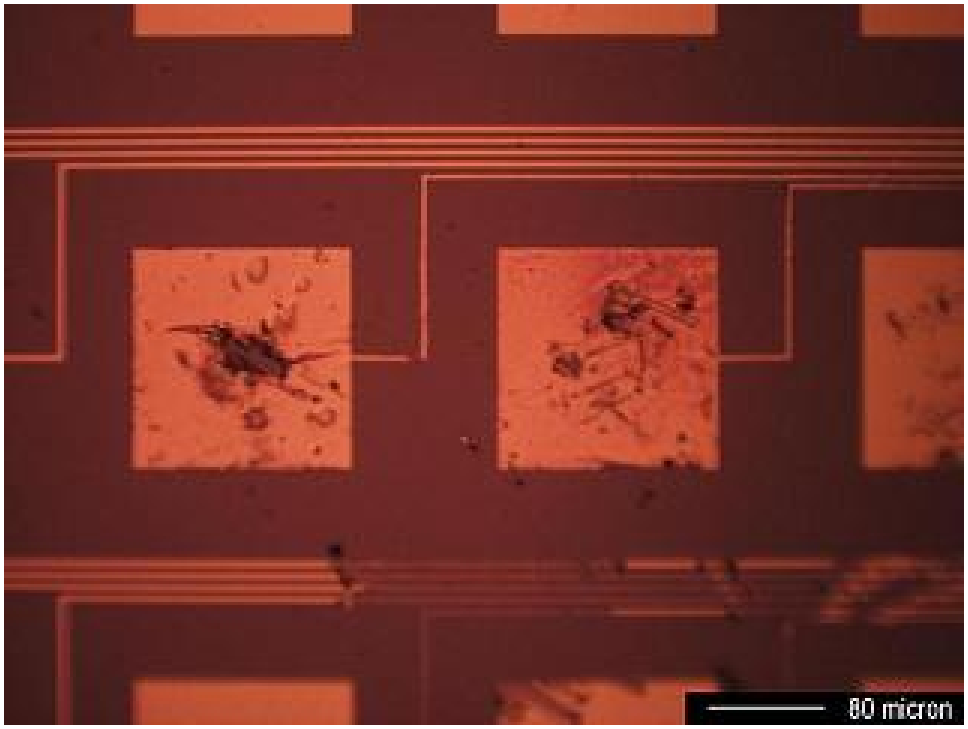

Figure 5.11 Optical image showing bond pads used for electrical measurements with probe tips. The marks on the Au pads are damages caused by the probe tips.

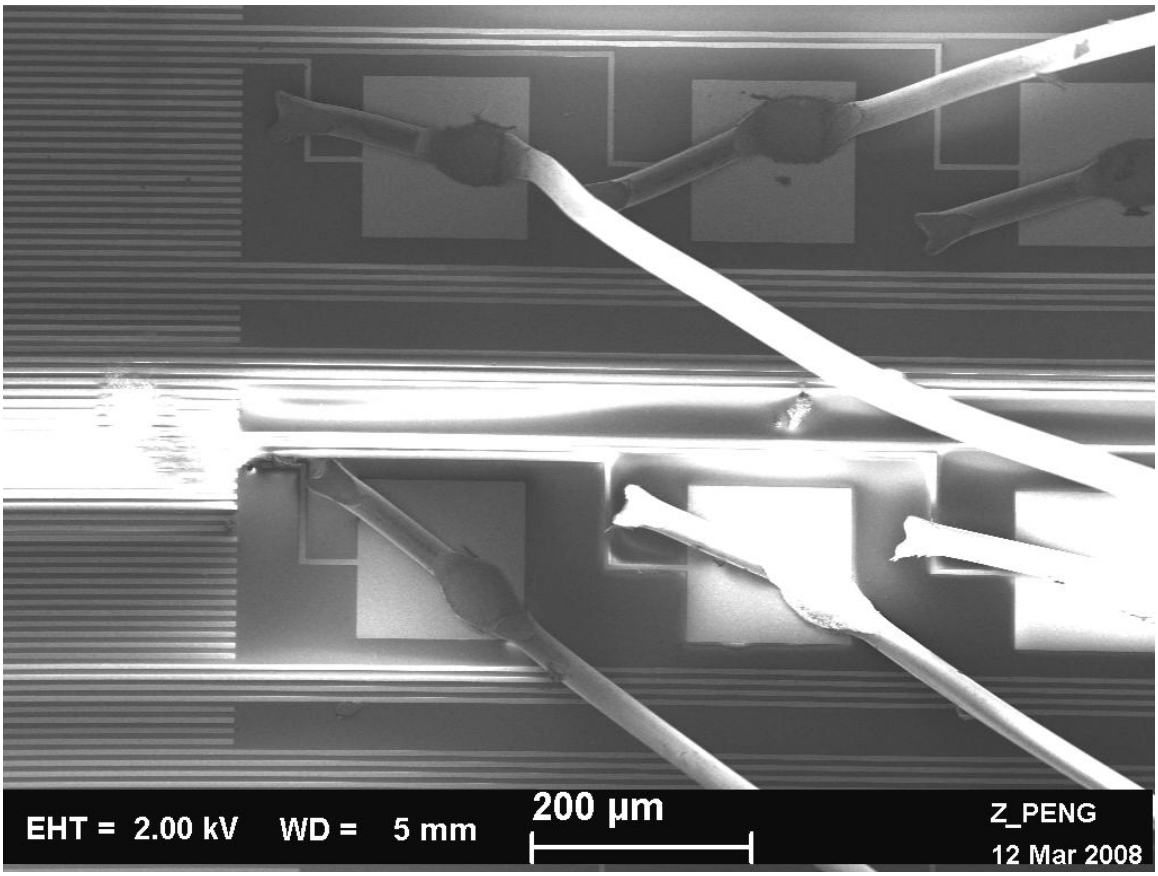

Figure 5.12 SEM image showing the wedge wire bonding of the bond pads, which allowed electrical measurements on the nanobelts using a wire bonding package.

5.2.3 Electrical Measurements

Figure 5.13 shows the condition of a nanobelt when potential was applied between the electrodes on which the nanobelt was aligned. There is no metal deposition over the nanobelt and the sample was not annealed either. When the current at low voltages (~ 5 V DC) was not measureable with the ammeter, higher voltages were applied (10 - 30 V DC). This resulted in the nanobelt breaking, probably due to high current flow and overheating. Hence, it can be inferred that even without metal deposition over the nanobelt contacts after its alignment, there is a reasonably good electrical contact between the Au electrode and the SnO_2 nanobelt. It is thought that the

sharp and flat surface of the nanobelt helps in providing a uniform contact with the electrodes.

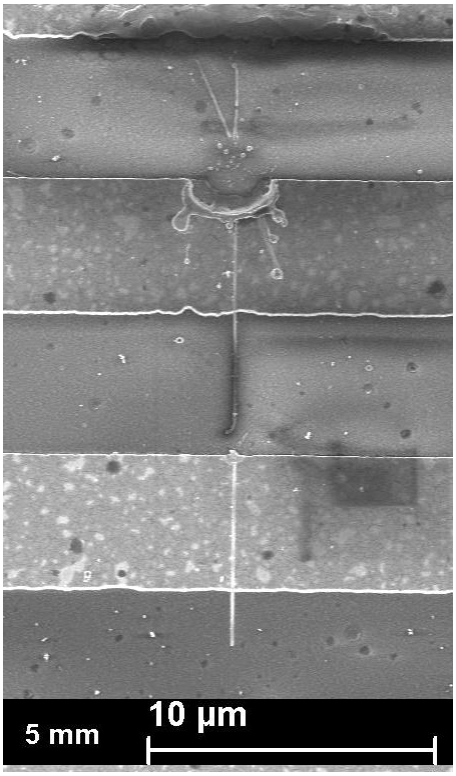

Figure 5.13 An aligned SnO_2 nanobelt between electrodes, broken due to current flow. The electrode width and gap are ~ 5 µm. No metal deposition or annealing was performed.

In many cases, current flowing through the nanobelts could be measured even without metal deposition over the contacts. Figure 5.14 shows the I-V relationship of a nanobelt device with the SnO_2 nanobelt aligned over Au electrodes. The sample was annealed at 300 °C, but no metal deposition was performed. For I-V measurements, potential was applied between the bond pads connected to the electrodes, and current flow was recorded. It is difficult to conclude that the annealing process improved the electrical contact between the nanobelt and the electrode material, because the heating process in an oxygen deficient environment affects the oxygen vacancy in SnO_2 and

increases its conductivity. In any case the measured current through the single nanobelt device was significant.

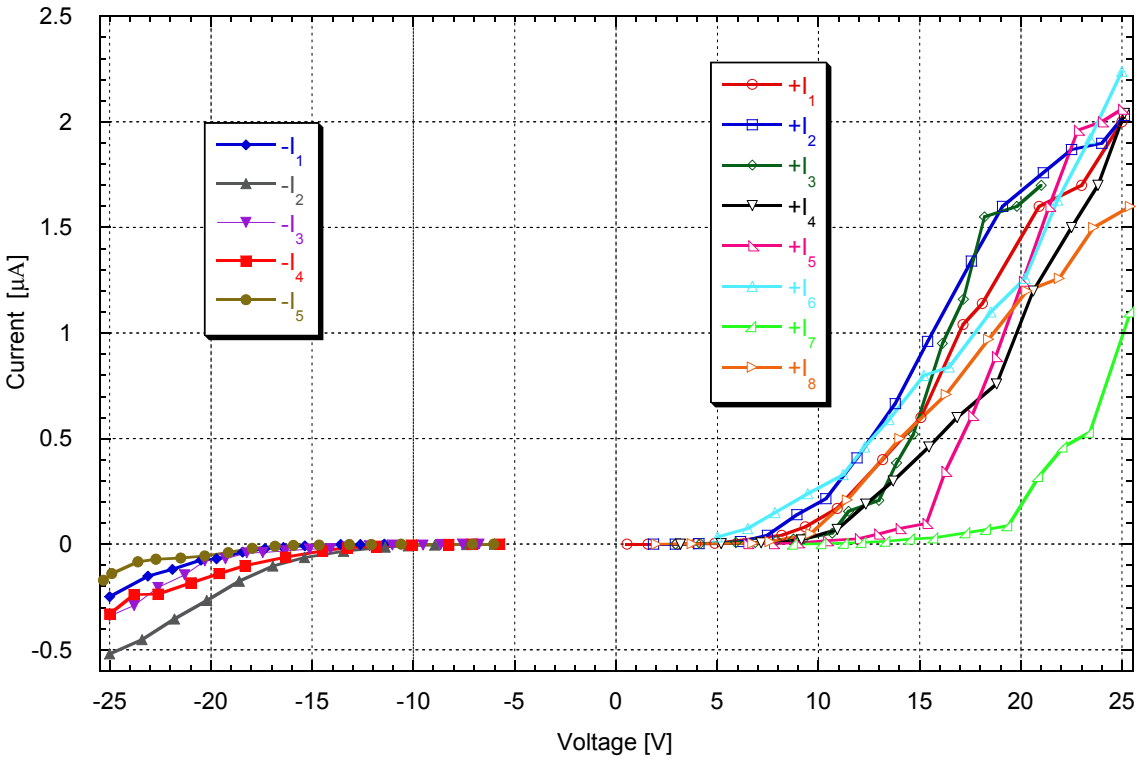

Figure 5.14 Current voltage relationship of a two terminal SnO_2 nanobelt device. Annealing was performed, but no metal was deposited on the nanobelt contacts.

The I-V curves in the forward and reverse biases show exponential character in the low voltages, which then transition to become linear at higher voltages. The current levels are different in the forward and reverse biases. This indicates non-ohmic contact with different contact resistances at the two contacts. In the literature, it has been stated that this nonlinear behavior observed in nanowires is due to the existence of back-to-back Schottky barriers arising from the two metal-semiconductor contacts.[72] However, recently a research group demonstrated that the nonlinear behavior originates instead from space-charge limited current.[73] According to them this behavior is common, and

occurs whenever diffusive transport dominates and the effective carrier concentration is low.

The I-V traces for the same device changed somewhat for each scan. It is believed that this is due to the Joule heating effect which makes the contact properties change after each scan.[74] Moreover, some amount of temperature rise in the nanobelts is anticipated because of the large current (μA) flowing through it, which can also affect the conductivity of semiconducting materials.

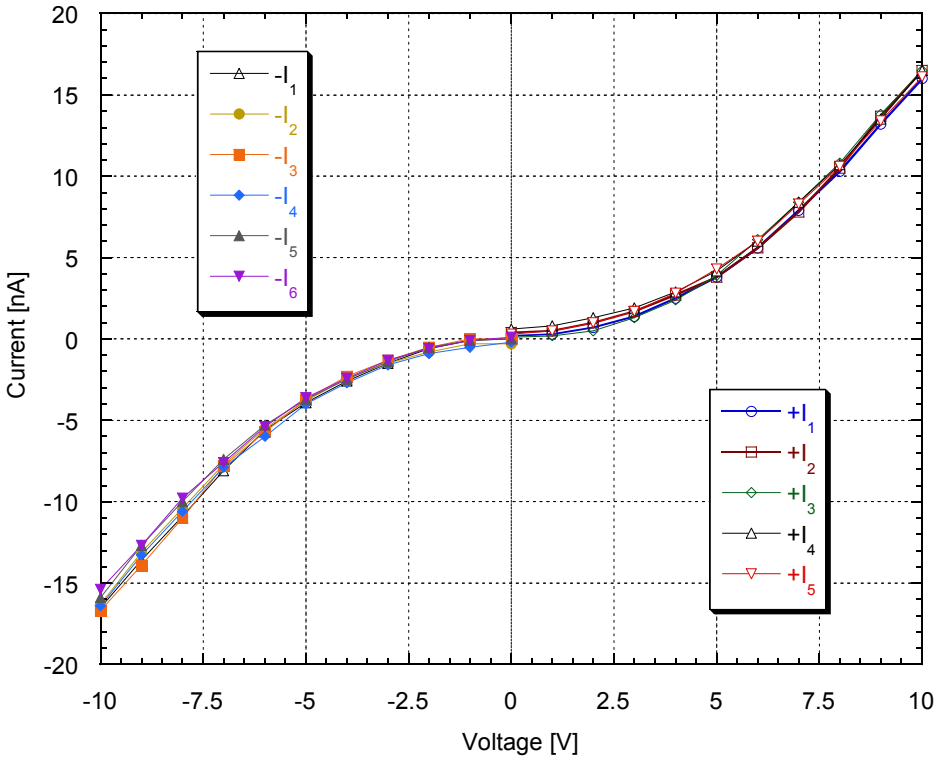

Figure 5.15 Current voltage relationship of a two terminal SnO_2 nanobelt device with FIB deposited Pt on the nanobelt contacts, but no annealing.

Figure 5.15 shows the I-V relationship of a nanobelt device with the SnO_2 nanobelt aligned over Au electrodes. Instead of annealing the sample, Pt metal of about 100 nm thickness was deposited over the nanobelt contacts. From the figure it can be

observed that the I-V scans are much more repeatable, and the forward and reverse bias characteristics are quite symmetric. This implied that the contacts are stable. However, non-ohmic behavior is still present, which is expected because of the metal-semiconductor junctions formed at the contacts.

5.3 SIGNIFICANCE

The fluid flow alignment method of making nanobelt devices will be found useful in studying electrical and other properties of nanowires and similar long nanostructures. While it may not be a good method for manufacturing devices, the method is significant for conducting nanotechnology research. One of the advantages of this method is that multiple nanowire-like structures can be aligned on separate electrodes on the same electrode chip. Hence, one can study the properties of the nanostructures easily. The method of aligning and studying nanostructures using nanomanipulators, such as Zyvex S100 Nanomanipulator (*Zyvex Instruments*, Richardson, TX, USA), is a time consuming process because one has to apply and repeat the process on the individual nanostructures, one at a time.

CHAPTER 6

IMPEDANCE MEASUREMENTS

This chapter presents the results of impedance measurements carried out to determine the electrical conductivity of the suspending liquid used in the DEP experiments, and to investigate the electrical properties of the SnO_2 nanobelts. Analysis of the impedance data provided the conductivity range of the ethanol and the nanobelts. This information is required for carrying out the parametric COMSOL simulations for calculating DEP force, torque, etc. The details of the simulations are the subject of Chapter 9.

6.1 EXPERIMENTAL SETUP

For the impedance measurements Solartron SI 1260 Impedance/Gain-Phase Analyzer (*Solartron Analytical*, Farnborough, UK) was used in combination with Solartron 1296 Dielectric Interface. The Dielectric Interface is required for high impedance measurements. The experimental setup is shown in Figure 6.1.

To measure the conductivity of ethanol used in the DEP experiments, impedance measurements were performed using the 12962A room temperature sample holder (*Solartron Analytical*, Farnborough, UK) shown in Figure 6.2 (a) in combination with the 12964A liquid sample holder (*Solartron Analytical*, Farnborough, UK) shown in Figure 6.2(b). The standard electrode provided has a diameter (d) of 20 mm. Both anhydrous ethanol and absolute ethanol were tested by filling the liquid sample holder and using it

with the 12962A sample holder. The thickness (l) of the liquid from the bottom electrode to the top electrode surface was found to be ~ 9.5 mm.

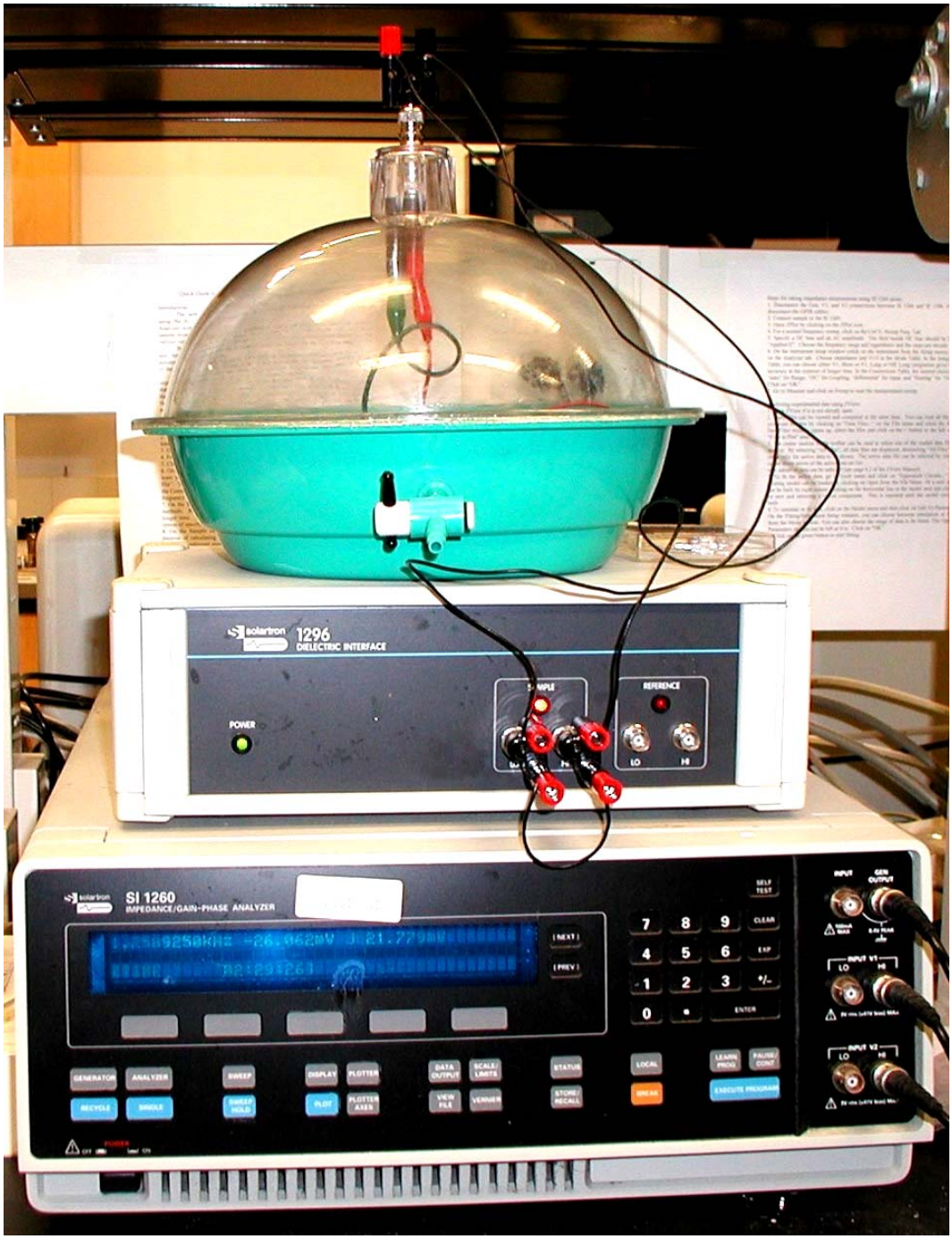

Figure 6.1 Photograph showing Solartron SI 1260 Impedance/Gain-Phase Analyzer (bottom), Solartron 1296 Dielectric Interface (middle), and a closed plastic chamber to control the environment around the sample for performing measurements.

(a) (b)

Figure 6.2 Photograph of (a) the 12962A sample holder, and (b) the liquid cup and top electrode (right). The diameter of the circular electrode in the cup is 20 mm.

Impedance measurements were performed on single nanobelt devices in ambient conditions as well as in the presence of ethanol vapor at room temperatures. The fabrication of the single nanobelt device, by the alignment of SnO_2 nanobelts over Au electrodes using the fluid flow alignment method has already been discussed in Chapter

5. After the alignment, Pt metal was deposited over the nanobelt/electrode contact areas using focused ion beam (FIB) as described in Chapter 5 to improve the contact properties. Figure 6.3 shows a typical example.

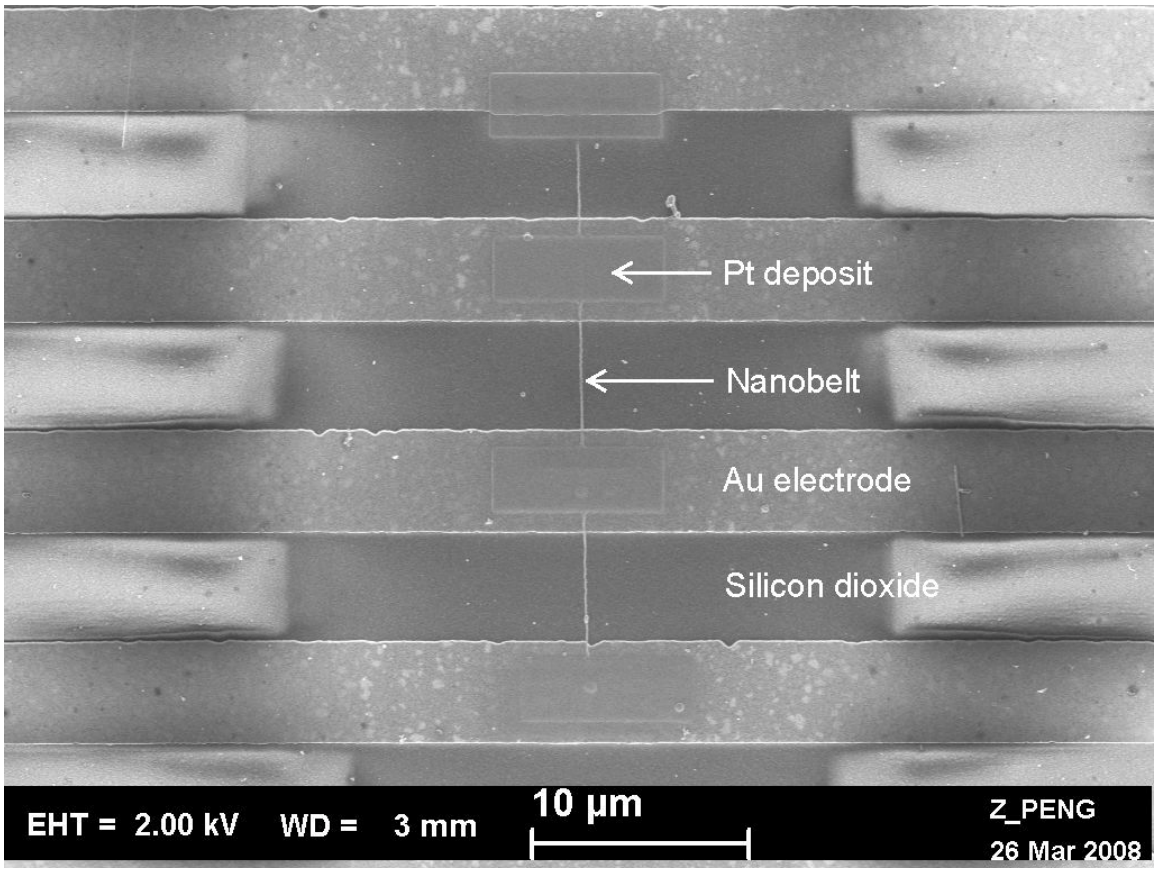

Figure 6.3 SEM image of an aligned SnO_2 nanobelt over Au electrodes, with Pt metal deposited on the contacts using FIB. The electrode width and gap are ~ 5 µm.

Measurements on longer single SnO_2 nanobelts, trapped using DEP, were also performed. Pt metal was deposited using FIB on the electrode/nanobelt contacts after the DEP trapping. Figure 6.4 shows a typical example. However, because of the long length of the nanobelt on such a sample, the value of the resistance obtained from the measurements was found to be very high. Some measurements were also performed on multiple nanobelts trapped using DEP on castellated electrodes. But there was no metal

deposition on the contacts. Hence, it was not convenient to extract quantitative information from such measurements.

In the impedance measurements usually frequency sweeps from 0.001 Hz to 10 MHz were performed. To save time sometimes the lower frequency limit was chosen to be 0.01 Hz or 0.1 Hz. The typical AC signal amplitude used in these measurements was 0.1 V_{rms}. Sometimes somewhat higher amplitudes were also used.

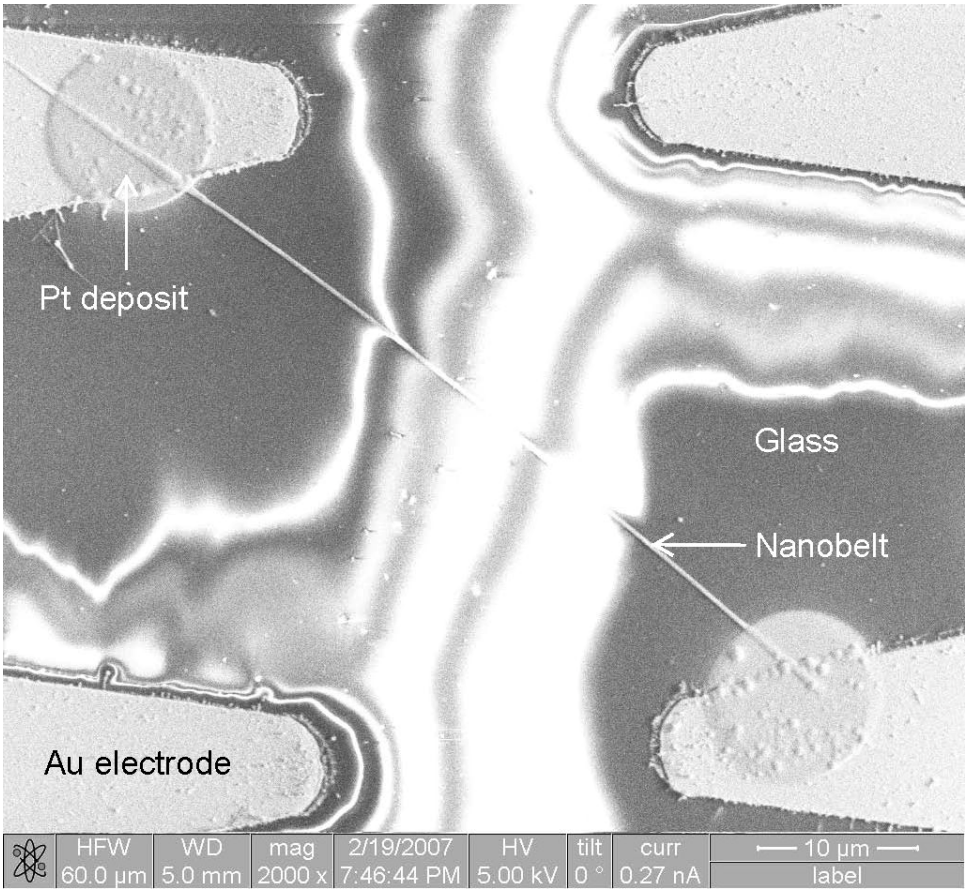

Figure 6.4 SEM image of a long SnO_2 nanobelt trapped using DEP and Pt metal deposited over the nanobelt contacts using FIB. The length of the nanobelt from metal edge to metal edge is ~ 45 µm, and the width is ~ 350 nm. The white fringes between the electrodes are due to charging of the glass substrate during SEM imaging.

6.2 RESULTS AND DISCUSSION

6.2.1 Measurements on Ethanol

Using one of the frequency sweeps from the measurement, the impedance data is plotted as Bode (Figure 6.5 (a)) and Complex (Figure 6.5 (b)) plots. The Complex plot shows that there are 2 semicircles, implying 2 dielectric relaxations. The high frequency relaxation is the one that is of interest. The low frequency relaxation is most probably due to relaxation of the space charge at the interface between the solid electrode and the liquid. A circle was fitted with the data representing the smaller semicircle using the ZView2 program (*Scribner Associates, Inc.*, Southern Pines, NC, USA). The fitting parameters for the circle were found to be

Estimated Resistance: 1.7386×10^{5} ohms

Estimated Capacitance: 6.3677×10^{12} farads

So, the resistance of the liquid between the electrodes can be taken as $R = 1.7386\times10^{5}$ ohms. The expression relating conductivity σ, resistance R, and the area of cross section A, is

$$R = \rho\frac{l}{A} = \frac{1}{\sigma}\frac{l}{A} = \frac{1}{\sigma}\frac{l}{\left(\pi d^{2}/4\right)} \tag{6-1}$$

where ρ is the resistivity of the liquid. The conductivity is given by

$$\sigma = \frac{1}{R}\frac{l}{\left(\pi d^{2}/4\right)} \tag{6-2}$$

Substituting the appropriate numbers, the value of conductivity is found to be $\sigma = 1.739\times10^{-4}$ S/m ~ 1.74×10^{-4} S/m.

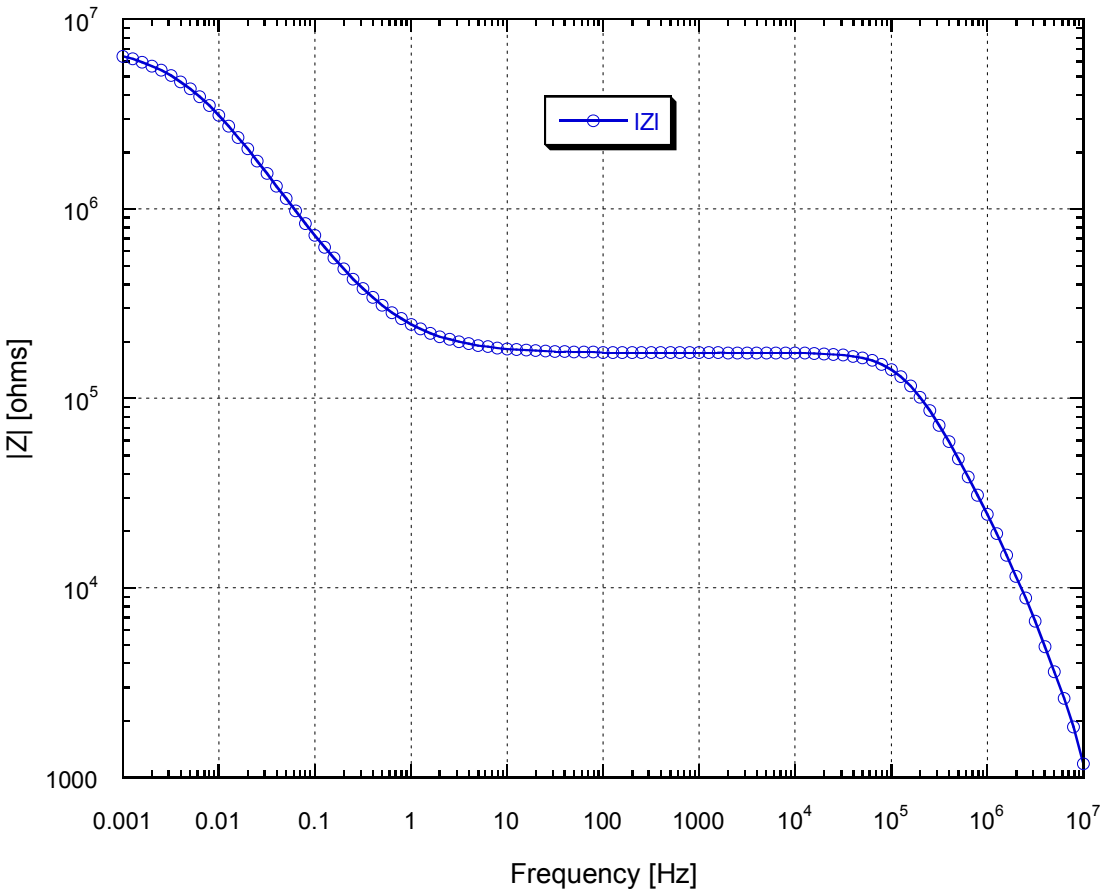

(a)

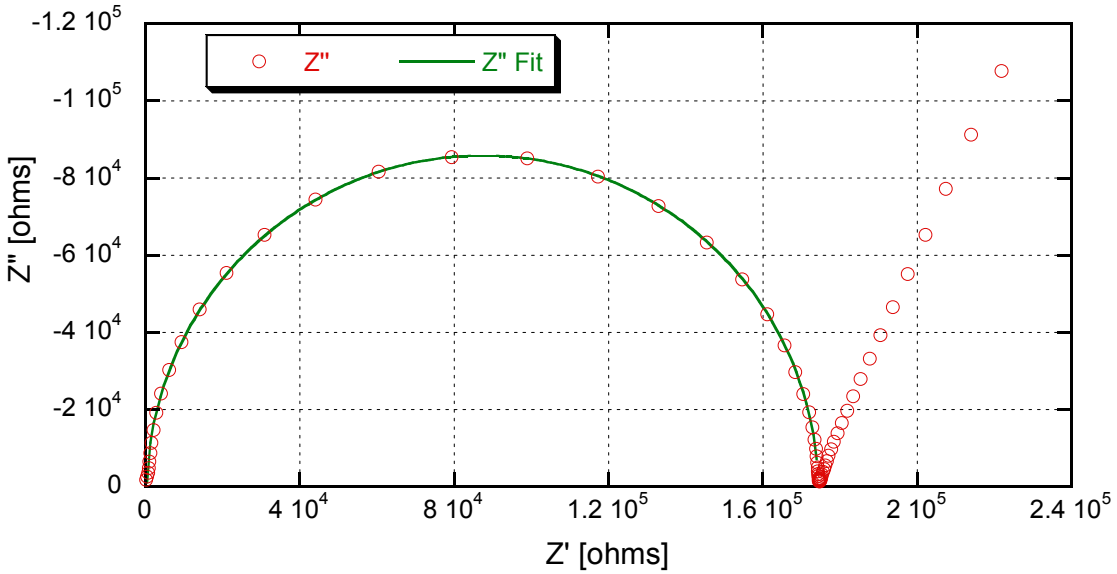

(b)

Figure 6.5 Impedance measurement of anhydrous ethanol using a liquid cup, (a) Bode plot showing two dielectric relaxations, and (b) Complex impedance plot. The diameter of the semicircle represents the ethanol resistance.

Measurements with absolute ethanol also showed similar trends. Absolute ethanol is likely to have a greater percentage of water compared to anhydrous ethanol. Interestingly the resistance value was actually higher than that of anhydrous ethanol. The resistance was ~ 4×10^{5} ohms. That corresponds to a conductivity value of $\sigma \sim 7.56\times10^{-5}$ S/m. In all these measurements the impedance scans show some fluctuation in values with each frequency sweep. Hence, for all practical purposes the conductivity value of ethanol can be taken to be on the order of 10^{-4} S/m - 10^{-5} S/m.

Impedance measurement on the liquid cup was also performed when just air was inside, and no liquid was present. The Bode plot showed a linear characteristic with very high impedance values (10^{13} - 10^{14} ohms) in the low frequencies and ~ 10^{4} - 10^{5} ohms in the high frequencies. There was noisy data below 1 Hz frequency, which was quite repeatable.

6.2.2 Measurements on Fluid Flow Aligned SnO_2 Nanobelts

To measure the approximate conductivity of the nanobelts, impedance measurements were performed on some nanobelt devices made using the fluid flow alignment method, and which had FIB deposited Pt metal on the electrode contacts. The measured data is plotted as Bode (Figure 6.6(a)) and Complex (Figure 6.6 (b)) plots. There is only 1 semicircle in the Complex plot, implying a single relaxation process. A circle is fitted with the data representing the semicircle using ZView2 program (*Scribner Associates, Inc.*, Southern Pines, NC, USA). The fitting parameters for the circle were found to be:

Estimated Resistance: 1.7577×10^{9} ohms

Estimated Capacitance: 1.5832×10^{-12} farads

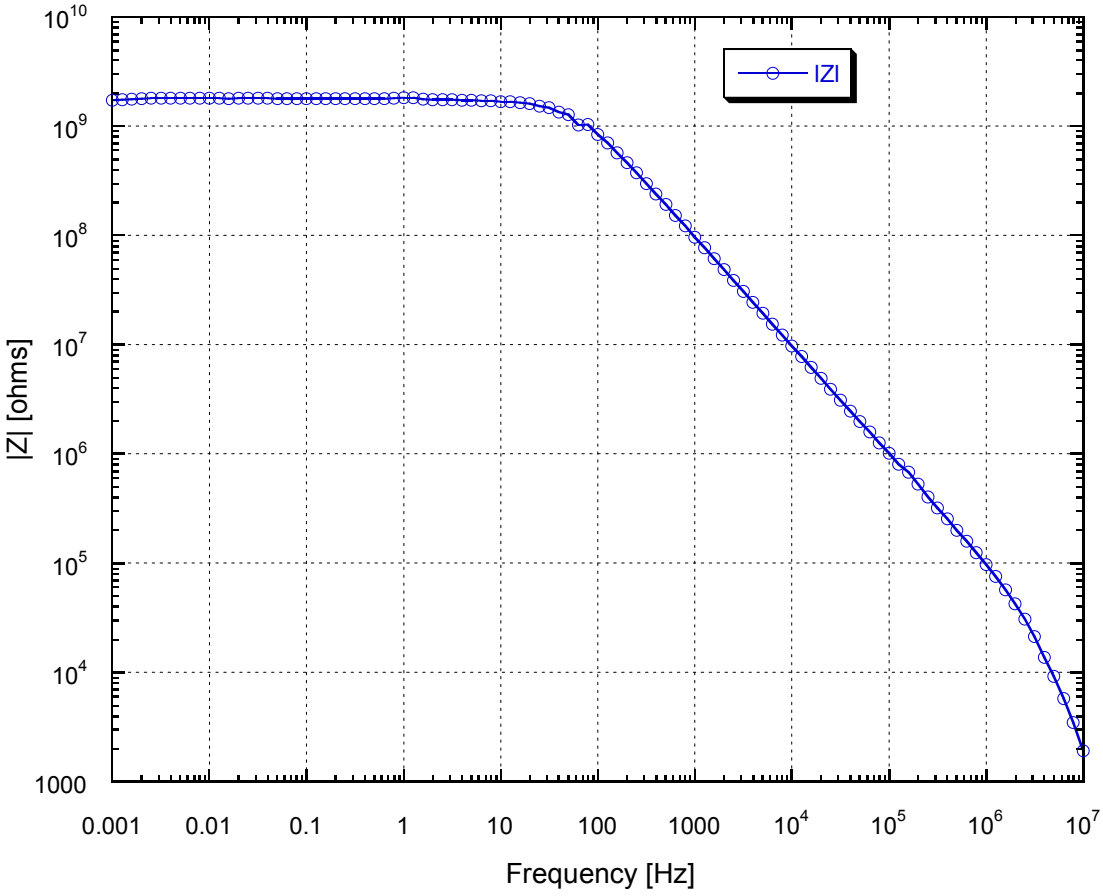

(a)

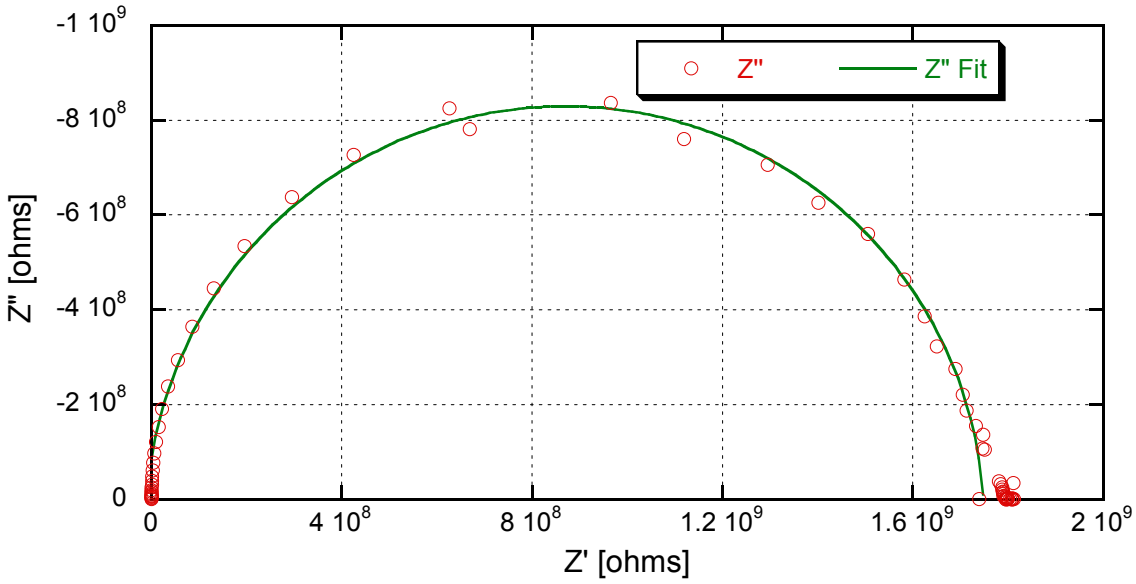

(b)

Figure 6.6 Impedance measurement on single SnO_2 nanobelt in ambient conditions, (a) Bode plot showing a single dielectric relaxation, and (b) Complex impedance plot. The diameter of the semicircle represents the nanobelt resistance.

So, the resistance of the nanobelt between the electrodes is $R = 1.7577\times10^{9}$ ohms. The expression relating conductivity σ, resistance R, and the area of cross section A, where w is the width, and t is the thickness of the nanobelt is given by

$$R = \rho\frac{l}{A} = \frac{1}{\sigma}\frac{l}{A} = \frac{1}{\sigma}\frac{l}{(wt)} \tag{6-3}$$

where ρ is the resistivity of the nanobelt. The conductivity is given by

$$\sigma = \frac{1}{R}\frac{l}{(wt)} \tag{6-4}$$

The electrode width was $l \sim 3$ μm. If it is assumed that the nanobelt thickness $t \sim 50$ nm and the width $w \sim 300$ nm, after substituting the numbers, the value of conductivity is obtained to be $\sigma \sim 0.1138$ S/m. In another measurement the resistance value was found to be on the order of 10^{9} ohms. So the conductivity will be somewhat higher. The I-V curves for the nanobelt device were shown in Figure 5.15 of Chapter 5. It indicates a linear region for higher voltages. The conductivity obtained from the linear part of this curve give a value of $\sigma \sim 0.4$ S/m.

Some measurements were also performed on the sample after it was dried by heating at 110 °C for about 4 hours in an oven. During the heating process, air was inside the oven. After drying, impedance measurements were performed inside the plastic chamber in a dry condition. The dry environment inside the chamber was maintained during the measurement by using desiccants. From the measurements the resistance was found to be $R = 3\times10^{10}$ ohms. This corresponds to a conductivity value of $\sigma \sim 6.66\times10^{-3}$ S/m. The higher resistance after drying the sample is due to desorption of moisture from the nanobelt surface and possibly the substrate. The chip substrate has

large surface area and can adsorb some water. The oxygen adsorption on the nanobelt surface during the drying process can also reduce the conductivity.

Hence, the simple calculations show the conductivity of the nanobelts to be on the order of 0.001 - 0.4 Sm^{-1}. These values are more representative of a cross sectional area averaged quantity, since there can be a depletion layer on the outer regions of the SnO_2 nanobelt. The possibility of a depletion layer is discussed in Chapter 8. Because of various factors, such as contact properties and surface interactions of the nanobelt with the environment (water, air, etc.), variation of the electrical conductivity can be anticipated. Therefore, an order of magnitude value of the conductivity is quite sufficient for studying the DEP characteristics through finite element simulations.

6.2.3 Measurements on Single SnO_2 Nanobelt Trapped Using Dielectrophoresis

Figure 6.7 shows the Bode plot of the impedance measurement on the DEP trapped nanobelt shown in Figure 6.4. Pt metal was deposited on the contacts using FIB. The measurement was performed in the plastic chamber with desiccants inside it to keep the environment dry. The low frequency impedance value did not plateau completely. The values are very high (~ 10^{11} ohms) because the nanobelt is very long (~ 45 μm). From the low frequency value of the impedance one can approximate that the resistance will be on the order of 10^{11} ohms. So, the resistance of the nanobelt between the electrodes is $R \sim 10^{11}$ ohms. $l \sim 45$ μm, $w \sim 350$ nm, which were estimated from the SEM image. If it is assumed that the nanobelt thickness $t \sim 50$ nm, and the numbers are substituted into the expression for conductivity in section 6.2.2, the value of conductivity is found to be $\sigma \sim 0.0257$ S/m. This is within the range of values obtained in section 6.2.2.

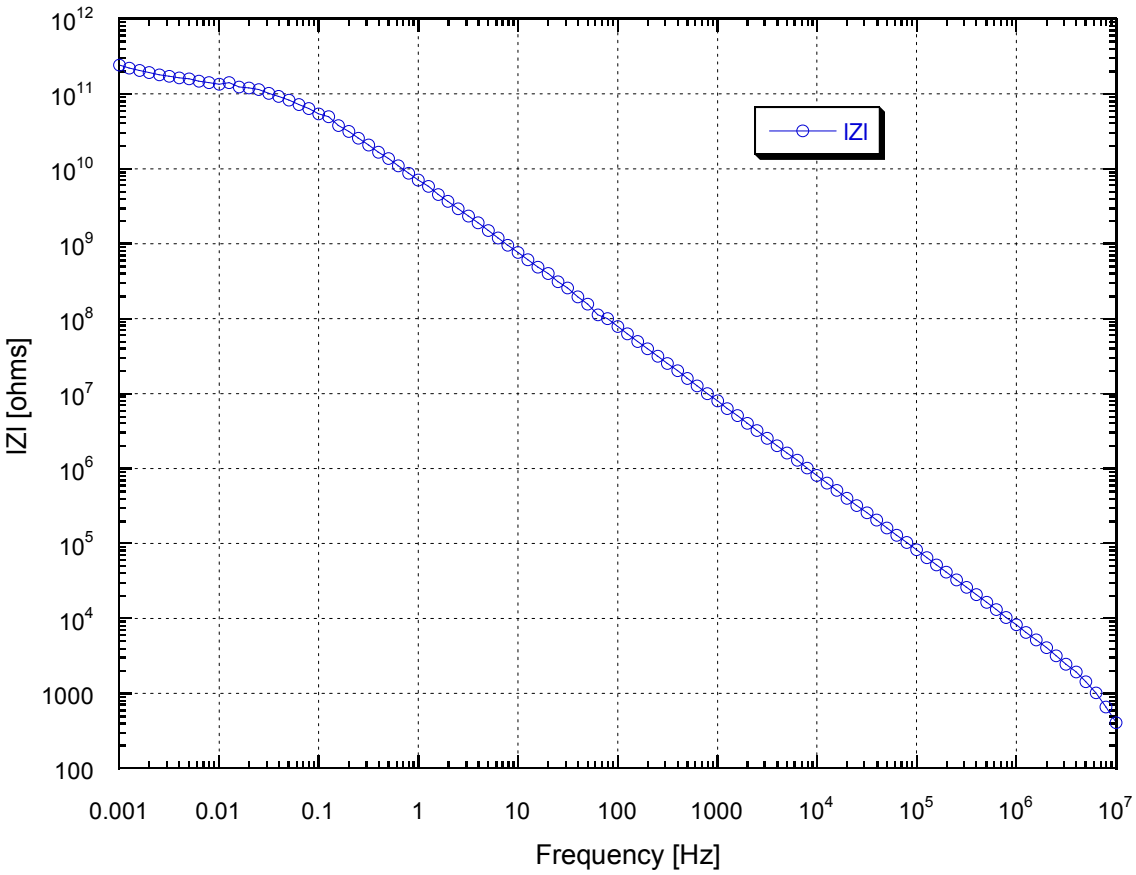

Figure 6.7 Bode plot of the measured impedance of a single SnO_2 nanobelt in a dry environment.

6.2.4 Measurements to Study the Effect of Ethanol on SnO_2 Nanobelts

Effort was made to find out if the nanobelt impedance changed under the influence of an ethanol vapor environment. To perform this measurement an open bottle of ethanol was kept along with the nanobelt sample inside the plastic chamber. After making the electrical connections to the fluid flow aligned nanobelt device, the chamber was closed. Because of the high vapor pressure of ethanol, the molecules started depositing on the sample surface and probably formed a layer. With repeated frequency scans of impedance with time, it was observed that for frequencies above 1 Hz there was a change in the impedance. Initially, it was though that this was a manifestation of the

ethanol vapor affecting the electrical properties of the nanobelt. However, experiments with blank samples (bare electrodes, no nanobelt) also revealed similar changes. Hence, the change in the impedance of the sample with nanobelts between electrodes cannot be assigned to the change in the nanobelt conductivity. The reason for this is that the surface area of the nanobelt is much smaller compared to the total surface area of SiO_2 and Au on the measured sample. The conductance of the ethanol layer condensing on the sample dominates the measurements. Therefore, it is not possible to observe the change in the nanobelt conductance, if any, using the samples in an ethanol vapor environment. During DEP the nanobelt is suspended in liquid ethanol. This condition cannot be experimentally simulated by the ethanol vapor experiments.

6.3 Significance of the Conductivity Values

The conductivity of the anhydrous ethanol and absolute ethanol used for suspending SnO_2 nanobelts is found to be on the order of 10^{-5} - 10^{-4} Sm^{-1}. The nanobelt cross sectional area averaged conductivity is found to be on the order of 0.001 - 0.4 Sm^{-1}. The significant fact is that the conductivity of the nanobelt is always greater than that of ethanol. But, negative DEP can only occur when the nanobelt conductivity is lower than that of the suspending fluid (ethanol in the current research). Hence, it is very likely that either the condition of the nanobelt changes significantly after being suspended in the nanobelt, or that a depletion layer is already present before suspension. If a layer of the nanobelt surface has low conductivity, it can cause negative DEP. Simulations with varying values of nanobelt conductivity will provide important insights. In the simulations the permittivity values of ethanol and SnO_2 from the literature are used.

CHAPTER 7

NANOBELT SURFACE CHARGE

Experiments were performed to find out if there is charge on the SnO_2 nanobelts using a parallel plate electrode experimental arrangement and applying DC and low frequency electric fields.

7.1 EXPERIMENTAL

7.1.1 Parallel Plate Electrode Arrangement

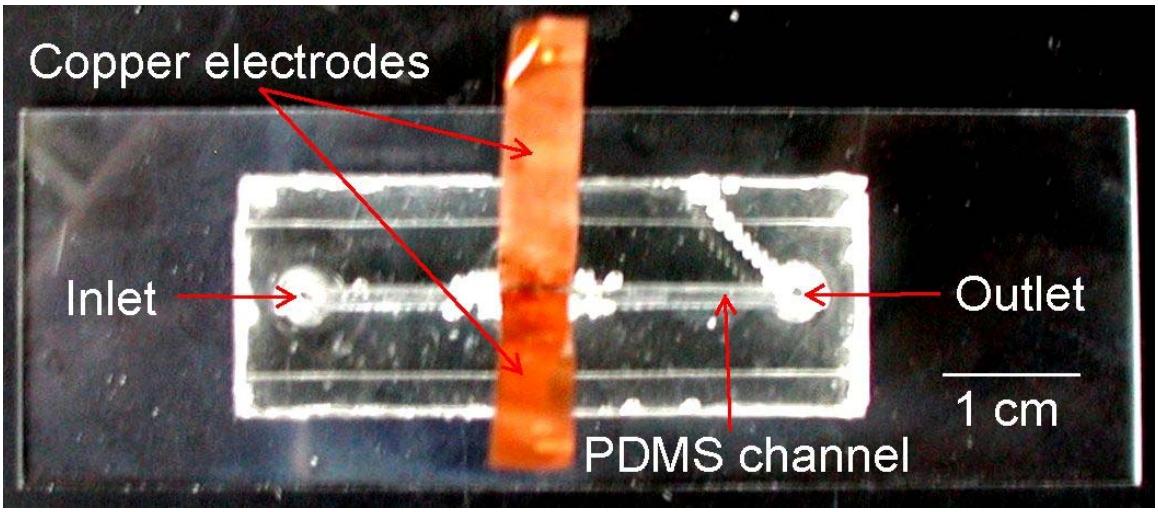

Figure 7.1 The experimental setup used to investigate the electrophoretic effect in SnO_2 nanobelts. The PDMS piece is 4 cm long and 1.5 cm wide.

To find out if electrophoresis effects exist in the SnO_2 oxide nanobelts, a parallel plate configuration was used to produce approximately uniform electric fields. A PDMS channel of about 1000 μm width, and 5 mm height was made using the procedure

described in sections 5.1.1 and 5.1.2 of Chapter 5. The only difference is that during the PDMS molding process, two copper strips were inserted on the sides of the channel mold in a vertical position. The copper strips function as a pair of parallel plate electrodes. The gap between the electrodes was ~ 800 μm. After curing, the PDMS channel with the electrodes was placed on a glass slide, resulting in a flow conduit. Figure 7.1 shows the experimental setup.

7.1.2 Testing

Nikon Eclipse TE2000-S (*Nikon Instruments Inc.*, Melville, NY, USA) inverted microscope was used for the observation of the nanobelts. Digital images and time lapse movies were acquired using a computer controlled imaging software, MetaMorph® Imaging System (*Universal Imaging Corporation*, Downingtown, PA, USA), which enabled automated image capture and analysis from a digital CCD camera attached to the microscope.

During the experiments SnO_2 nanobelts, suspended in ethanol liquid, were introduced at one of the channel inlets using a thin glass pipette. The microscope was focused so that observation of nanobelts and particles, freely suspended in the liquid medium in the PDMS channel, could be performed. Some observations were also made by focusing on the surface of the glass, but the surface forces made movement of the nanobelts and the particles difficult. Hence, focusing on the nanobelts which were freely suspended in the liquid was the better option. In some tests, the field was applied after the movement of the fluid and the suspended particles and nanobelts in the channel stopped. But, in this case the nanobelts and particles rapidly went out of focus, because of the effect of gravity. In other cases, the movement of the fluid and particle was

deliberately induced, and then the electric field was applied. The field was either purely DC or low frequency AC, so that electrophoretic effects can manifest, if any. Because the electrodes are parallel and the electrode gap is quite large (~ 800 μm), the field gradients are likely to be negligible, and hence DEP effects can be neglected.

7.2 Results and Discussion

The nanobelt motion was apparent on the application of uniform DC fields. Changing the polarity of the electrodes also changed the direction of movement of the nanobelts and particles (present in the SnO_2 nanobelt sample). This is indicative of electrophoresis. The nanobelts tended to move towards one of the electrodes. On the application of a DC field, the nanobelts moved towards the electrode with positive polarity, indicating presence of a negative charge on the nanobelts. Sometimes bouncing motion of some of the particles between the two electrodes was observed in the DC field experiments. As described in section 2.4 this type of phenomenon occurs with metallic particles subjected to uniform DC electric fields.[12, 13] Hence, the presence of such motions could indicate that some of the particles in the nanobelt samples are metallic in nature.

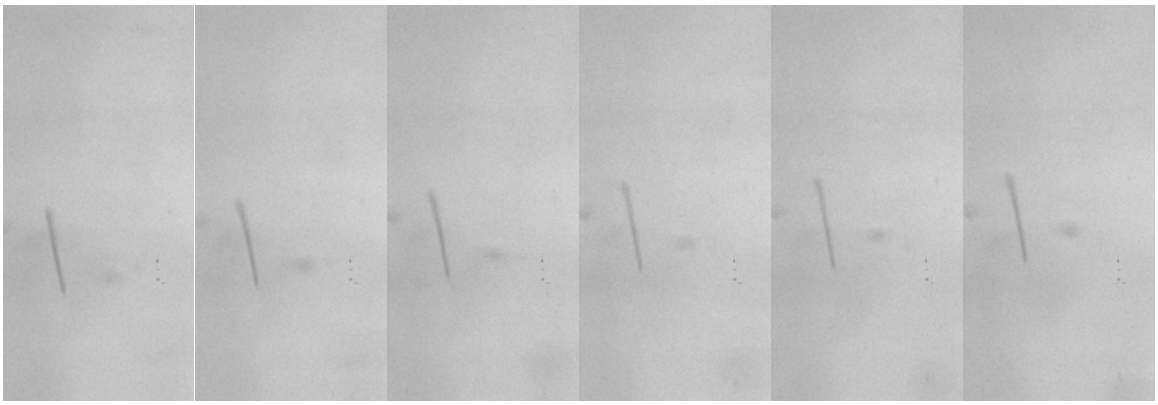

(a)

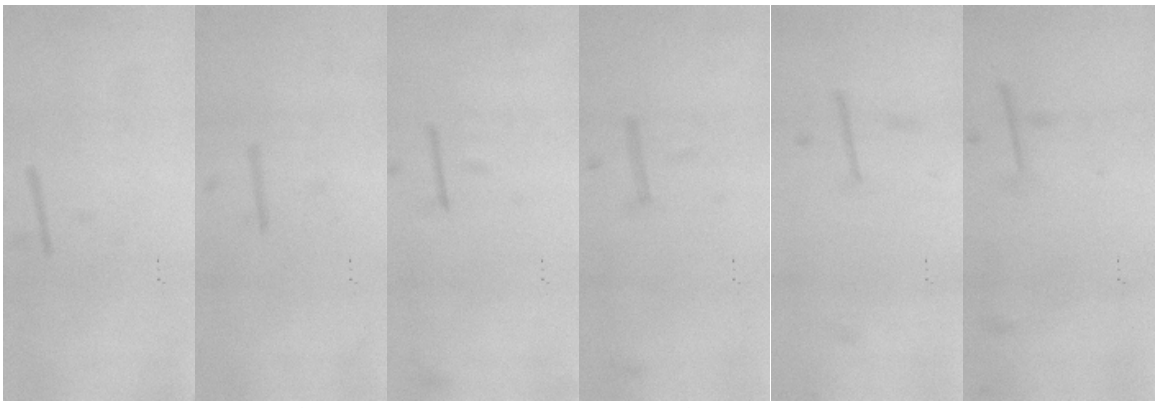

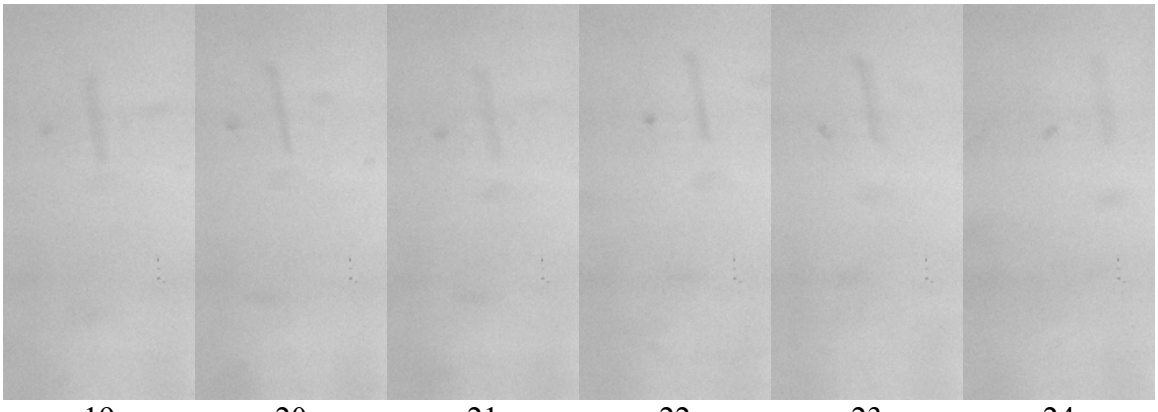

(b)

Figure 7.2 Images showing time snapshot (~ 0.4 s between each frame) of the nanobelt position as it flowed through the microchannel, (a) without any applied field, and (b) under the influence of a low frequency electric field (10 V_{peak}, 1 Hz AC sine wave). The field was turned on between snapshot no. 12 and 13. Each image is about 65 μm wide and 130 μm tall.

Figure 7.2 shows the time snapshots of a typical experiment. Figure 7.2 (a) shows the nanobelt moving in the liquid channel, when there is no applied field. The nanobelt is moving up as a whole along the channel direction (vertical), without lateral motion (left or right). Figure 7.2 (b) shows the situation when a 10 V_{peak}, 1 Hz AC Sine wave signal was applied using a Synthesized Function Generator (*Stanford Research Systems Inc.*, Sunnyvale, CA, USA). The two parallel plate electrodes are on the left and the right of the image. On the application of the sinusoidal signal, the nanobelt oscillates left and right. This is due to the electrophoretic effect. The later snapshots (after no. 13) show the image of the nanobelt to be blurred. This is because the nanobelt was moving slowly downwards due to the effect of gravity, and therefore was going out of focus.

To make the oscillatory motion shown in Figure 7.2 (b) clearer, the lateral positions (along the same direction as the applied electric field) of the nanobelt center in the microfluidic channel are plotted as a function of time in Figure 7.3. A sine wave of 1 Hz frequency is also superimposed on the data points. Most of the points follow this curve closely. Considering the errors in manually extracting the pixel positions of the nanobelt center from the images, this is quite a good fit. Hence, it shows that the nanobelt is oscillating with almost the same frequency as the applied signal frequency.

On the application of somewhat higher frequency signals (e.g., 10 Hz), the nanobelts were still oscillating, although the amplitudes became smaller. For very high frequencies (e. g., 1 MHz), there was no response to the field and the nanobelt simply moved along the channel following the flow of the fluid.

The experiments were found useful for observing the presence of electrophoretic effects in the nanobelts suspended in ethanol. However, it is difficult to deduce

quantitative information on the nanobelt charge using these experimental results. One major problem is that, it is virtually impossible to recover and identify the nanobelts that were under observation during the experiments, later on to obtain specific size information. However, it may be possible to deduce an estimate using typical order of magnitude numbers for the nanobelt size, etc.

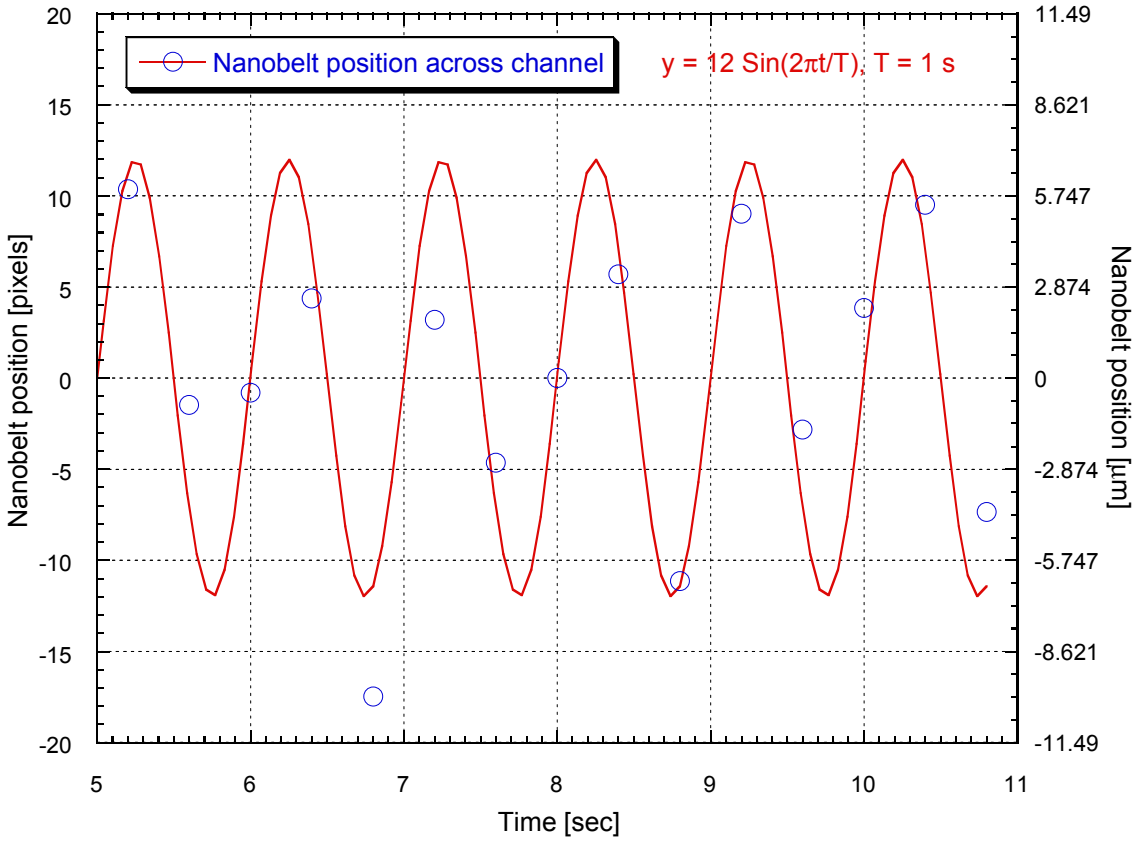

Figure 7.3 Figure showing a 1 Hz sinusoidal function of time superimposed on the nanobelt center position data across the channel.

The electrophoretic response can be due to induced charge on the SnO_2 nanobelts. It is difficult to reach a conclusion on the origin of this charge. But it does have significance in electrokinetic effects like DEP. The presence of electrophoresis on the

nanobelts implies that it may make some contribution to the low frequency response observed in the DEP experiments.

The evidence of charge on SnO_2 nanobelts suspended in ethanol has some similarity with the experimental observations of Ploscaru et al. [10], that $Mo_6S_3I_6$ nanowire bundles are charged when they are dispersed in polar liquids like ethanol and isopropanol. So, it may be that the use of polar liquid is a contributing factor for the presence of surface charge on SnO_2 nanobelts. The major factors are discussed in Chapter 8.

The current experiments provided qualitative information on the presence of surface charge. To obtain quantitative information, equipments for electrophoretic mobility measurements [75] might be found useful. However, these equipments are used for the mobility determination of colloidal particles [75], not nanowires. The uniformity of the particles is important. One of the major challenges, in the case of nanobelts, is that the suspended nanobelts do not have uniform lengths, widths, or thicknesses.

CHAPTER 8

ORIGIN OF NEGATIVE DIELECTROPHORESIS IN TIN OXIDE NANOBELTS

8.1 REVIEW OF TIN OXIDE ELECTRICAL PROPERTIES

In search of the reasons for the negative DEP observed in the SnO_2 nanobelts suspended in ethanol, it is instructive to review and understand the current literature on the electrical properties of SnO_2 in general, and SnO_2 nanostructures in particular. SnO_2 is a wide band gap (E_g = 3.6 eV) n-type semiconductor, which crystallizes in the rutile structure. At room temperatures it has a low conductivity.

In SnO_2 the electrical conductivity primarily results from the presence of oxygen vacancies, which generate electrons for conduction. The loss of oxygen from the bulk lattice of a non-stoichiometric oxide like SnO_2 causes the generation of oxygen lattice defects (vacancies) and electron donor states.[76] The electrons left behind in the oxide structure by the oxygen atoms constitute the carriers for electrical conduction. The published literature on SnO_2 electrical transport properties primarily concentrates on its behavior as a sensing material.[77] A conductance model of SnO_2 sensor has been described by Bârsan et al.[77] SnO_2 interacts with atmospheric oxygen and ionosorption of molecular (O_2^-) and atomic (O^-, O^{2-}) oxygen occurs.[77] The adsorbate captures electrons from the interior of the material and holds them at the surface by electrostatic attraction. This leads to the formation of depletion layers on the surfaces of SnO_2 structures. Oprea et al. [78] used Hall and four point conductance measurements on 70

nm thick thin films of porous SnO_2 with grain size between 10 and 30 nm. Figure 8.1 shows the SnO_2 conductance and charge carrier concentration as a function of O_2 concentration in dry N_2 for different temperatures. It is interesting to note that the values corresponding to room temperature (20 °C) lies above the values corresponding to 365 °C and 418 °C. The maximum conductance in the conductance plot is less than a decade higher compared to the conductance values corresponding to room temperatures. Because of the surface interactions, oxide semiconductors like SnO_2 behave differently compared to normal semiconductors like silicon. Usually, for semiconductors, with a temperature increase there is a monotonic increase in its conductance. That is not necessarily the case with oxide semiconductors as can be observed from the figure.

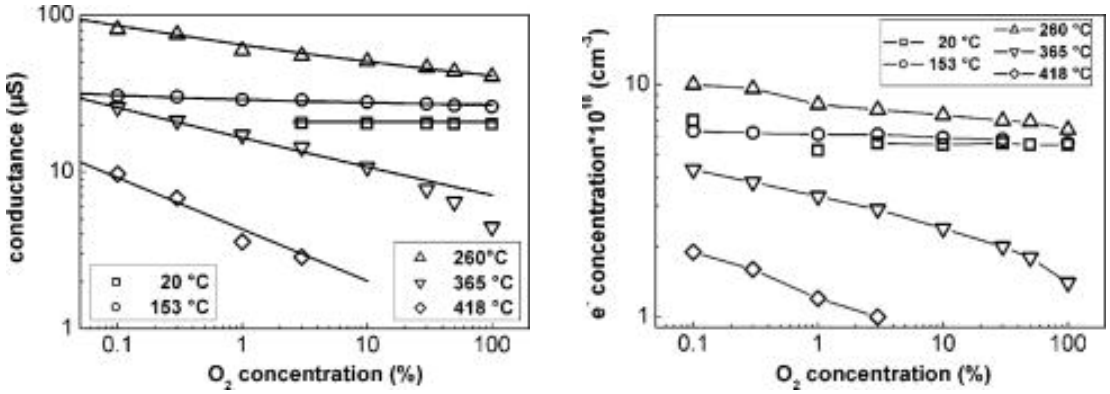

(a) (b)

Figure 8.1 (a) SnO_2 conductance, and (b) charge carrier concentration, versus O_2 concentration in dry N_2 for different fixed temperatures.[78]

One of the issues to keep in mind is that in polycrystalline films the current passing through it faces multiple barriers of depletion layers [79] because the film is composed of multiple grains. The situation is explained in Figure 8.2 (a). Band bending due to the adsorption of the negatively charged oxygen species on the grain surface causes a depletion layer to form.[79] Because of this a Schottky-like barrier exists across

the grain boundaries.[79] In the case of an individual nanobelt, because it is a single crystal, it can be visualized as consisting of a continuous depleted shell with a region of bulk properties inside it, as shown in Figure 8.2 (b).

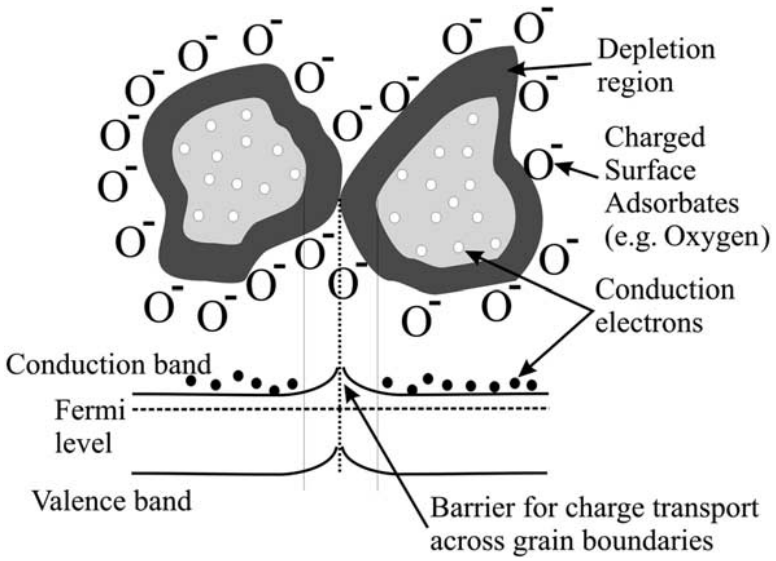

(a)

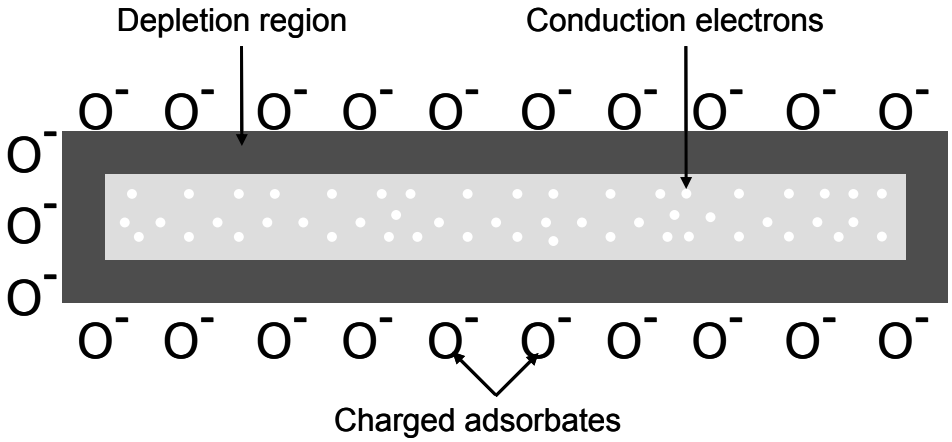

(b)

Figure 8.2 Schematic showing (a) depletion in SnO_2 grains of a polycrystalline film [79], and (b) a single SnO_2 nanobelt.

The properties of metal oxide surfaces have been reviewed by Henrich et al.[80, 81] The depletion widths in SnO_2 nanosized polycrystalline films used for sensing

application, have been calculated by solving Poisson's equation in spherical grains.[82, 83]. A more detailed calculation of the potential profile, trapped charge density, and carrier concentration as a function of the surface state density for different sizes of spherical grains of SnO_2 has been performed by Rothschild et al.[84]

Raman studies on SnO_2 nanobelts at room temperatures have revealed that the nanobelts are oxygen deficient.[85]. Bulk properties could be recovered only after annealing at 900 °C in pure oxygen for 1 hr. The depletion widths for an SnO_2 layered structure, a cylindrical structure, and a spherical particle were calculated and compared for the case when the depletion width is less that the crystal dimensions.[59] The depletion width was found to be on the order of 13 - 15 nm, for gas sensing applications. In such a situation the nanobelt has a depleted layer surrounding a central core with bulk conductivity. If the crystal dimension is smaller than the potential extinction region or depletion region, the crystal interior does not contain areas with bulk electrical conductivity. The whole crystal is depleted.

Some studies on the effect of oxygen vacancies on the dielectric properties of oxide materials have been reported in the literature. Yokota et al. [86, 87] reported the increase in the dielectric constant of TiO_2 films on the introduction of O deficient TiO_2 cells. Liu et al. [88] demonstrated that increasing the concentration of oxygen vacancies in homo-epitaxially grown $SrTiO_3$ thin films increases its dielectric constant and reduces the dielectric loss.

There are very few reports on dielectric constant measurements on nanostructured SnO_2. In a recent paper Dutta et al. [89] reported the dielectric properties of tin dioxide SnO_2 - polyaniline hybrid nanocomposites, made using polymerization of aniline in

colloidal SnO_2 nanoparticle (diameter ~ 40 nm) solution. Impedance measurements showed the nanocomposites to have a high dielectric constant, which is due to the difference in the conductivities of the electrically semiconducting grains and the more resistive grain boundaries of the nanoparticles.[89] At low frequencies Maxwell-Wagner relaxation is the dominant dielectric relaxation mechanism. At high frequencies the dielectric relaxation was attributed to the thermally activated motion of charges among the potential minima generated by lattice distortions.[89] The lattice distortions are due to the oxygen vacancies and mixed valence states of Sn in nanosized SnO_2.[89]

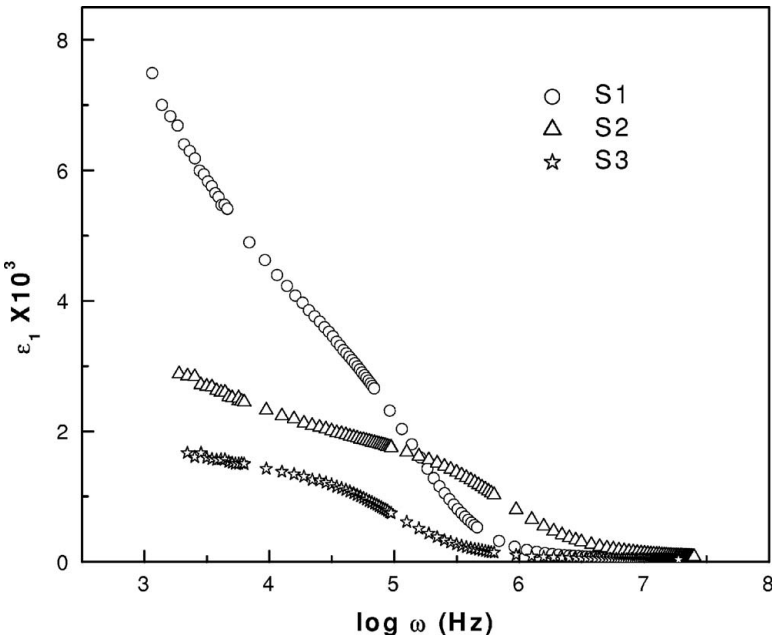

Figure 8.3 The real part of the relative dielectric constant of nanocomposites as a function of frequency at room temperatures for three samples with decreasing (S1-S3) SnO_2 content.[89]

8.2 TIN OXIDE NANOBELTS IN LIQUID MEDIUM

Since the dielectrophoresis experiments are performed at room temperatures, it is of interest to understand the different aspects that may affect its dielectric properties at

room temperatures. While it is well known that depletion of SnO_2 surface takes place in O_2 atmosphere, and is affected by the presence of other gases, for temperatures above 100 °C [77], fewer reports exist in the literature indicating the importance of the depletion layer on SnO_2 and similar metal oxide material surfaces at room temperatures. Mathur et al. [61] explained the increase in the SnO_2 nanowire conductance on UV illumination at room temperatures as due to the release of electrons into the depletion layer of the nanowire. This occurs because the UV illumination removes the adsorbed oxygen species (O^{2-}, O_2^-, and O_2) from the nanowire surface.[61] In the absence of UV illumination or heating, the adsorbed species cause the electrons from the nanowires to be surface-bound and hence, the formation of the depletion layer. Similarly, Luo et al. [90] explained the oxygen sensing properties of ZnO nanowires at room temperatures with and without UV illumination on the basis of the presence of the depletion layer on the oxide surface. In the case of dielectrophoresis of SnO_2 nanobelts, the nanobelts are suspended in a liquid (e.g., ethanol). So, the situation is somewhat different compared to that of a nanobelt in ambient environment. There are several factors that might potentially affect the electrical properties of the nanobelt, in addition to initial depletion due to O_2 adsorption. One cannot easily study directly what the electrical properties of the nanobelt are, while suspended in the liquid media. Hence, it is important to consider and visualize some of the factors that might affect the nanobelt in such a situation, using the available literature.

The nanobelt sample is initially in the ambient environment, and hence water adsorption on the surface from the humidity of air is possible. It is known that most oxide surfaces interact with H_2O. There is a strong bond between the oxide surface and

hydroxyl radicals, OH^-, frequently in monolayers.[80] The interaction is quite strong. Complete removal of the OH^- groups from the surface requires heating to several hundred °C.[80] It has been found that for SnO_2 surfaces the hydroxyl groups exist even up to 500 °C.[91] Although the effect of water on SnO_2 nanowires at high temperatures was studied by Hernandez-Ramirez et al. [92], the effect can be different at room temperature conditions, because at high temperatures chemical reactions take place.

Evidence of OH^- groups at room temperatures was found by Barreca et al. [93] on SnO_2 thin films of nanocrystalline layers prepared using MOCVD with diethylaminodimethylstannane (IV) (I) as precursor. XPS surface analysis showed, in addition to the normal peaks observed for SnO_2, a peak located around 531.7 eV which was assigned to OH^- and CO_3^{2-} groups. These groups form on the SnO_2 surface due to its interactions with the atmosphere.[93] This peak disappeared after a mild sputtering, which confirms its surface origin. Another consequence of the presence of the adsorbed OH^- groups on the outermost layer of the film is the appreciable change in the dielectric response of the SnO_2 surface layer with respect to the inner one.[94]

The nanobelt sample is suspended in a medium (ethanol). The liquid may affect the surface properties [95], although the impedance measurements on the nanobelts with ethanol vapor at room temperatures did not indicate measureable change due to technical difficulties. It may be reasonable to assume that the hydroxyl groups are present on the nanobelt surface even after their suspension in a liquid medium. Evidence of charge on the nanobelts has also been found experimentally, which may be due to these groups.

The presence of surface charge on semiconducting nanowires can strongly affect the conductance of the nanowire. In fact this principle has been used to demonstrate

chemical and biological sensing using boron-doped silicon nanowires (SiNWs) by Cui et al.[96] The silicon oxide layer on the nanowire was surface-functionalized with 3-aminopropyltriethoxysilane (APTES) so that the surface could protonate and deprotonate. When a solution with high pH came in contact with the functionalized nanowire, –SiOH deprotonated to $–SiO^-$.[96] This caused an increase in conductance in the p-type SiNW.[96] At low pH, the $–NH_2$ groups protonated to $–NH_3^+$.[96] The positive surface charge depleted hole carriers in the p-type SiNW to decrease the conductance.[96] So, a change in the surface charge can chemically gate the SiNW, affecting the conductance.[96] This change could be measured. Using the same principle, but with different surface functionalizations, streptavidin binding at picomolar concentrations, and antigen-antibody binding were also demonstrated.

The effect of screening of surface charge by ions on nanowire sensors in ionic liquids has been studied by Sørensen et al.[97] Measurements on SnO_2 nanowire based FET's showed that field-induced surface charge on the nanostructure by the gate strongly affected DC measurements.[98]

The effect of acidic and basic solution on indium tin oxide (ITO) was studied by Swint et al. [99] they and noticed changes in the in-plane resistance. This was explained in terms of the reaction of the aqueous acids and bases at the ITO surface to cause surface protonation-deprotonation reactions. Both surface charge and dipole layers contribute to change the depletion layer depth in the ITO, which explains the resistance change.

In addition to change in electrical conductivity, change in electrical permittivity can take place in metal oxides due to the effect of water. A semi-analytical model for the depletion region width and permittivity of polycrystalline WO_3 has been described by

Malagù et al.[100] It mentions that impedance measurement of the sample in humid air environment showed higher capacitance and hence higher electrical permittivity compared to dry air environment. They theorize that it is due to the high dielectric constant of OH^- groups.

Bose et al. [101] studied the grain size dependent electrical properties of nanocrystalline SnO_2 with grains in the size range 5 - 20 nm. They found that at low temperatures (25 - 300 °C), both the grains and the grain boundaries contribute to the DC conductivity, but at higher temperatures (above 300 °C), the contribution from the grain boundaries dominates. The activation energies for the conduction process increased with the decrease in grain size.

In an interesting study on surface cleaning of indium tin oxide (ITO)/glass substrates with different solvents (acetone, isopropanol, methanol, and chloroform), Abderrahmen et al. [102] found that treatment of the ITO substrate with methanol gives the most hydrophilic (lowest water contact angle) ITO surface and the highest surface energy. The dehydration of all the treated plates decreased the surface energy values of the ITO substrates, making them hydrophobic. It is believed that this methanol discards the ionic impurities on the ITO surface. This cleaning action was attributed to the highest dielectric constant and the strong polarity of methanol, among the different solvents used.

8.3 Possible Scenarios to Explain Negative Dielectrophoresis in Tin Oxide Nanobelts

While quantitative analysis of the DEP force in nanobelts requires a full 3D simulation, in this section an analysis using the Clausius Mossotti (CM) factor for a

spherical particle is used to get a feel for the variation of the CM factor as a function of the dielectric parameters of the nanobelts. This will provide guidance as to what type of configuration and parameter values will give DEP characteristics similar to that observed in the experiments. This is required because one cannot study the electrical properties of the nanobelt while it is suspended in a medium (ethanol). This exercise will also help in deciding the model and parameters to be simulated for the finite-element 3D calculation described in Chapter 9.

8.3.1 Using Nanobelt Bulk Properties ($\sigma_{nanobelt} > \sigma_{ethanol}$)

The CM factor is plotted using the following numbers.

$\varepsilon_0 = 8.854\times10^{-12}$ F/m (permittivity of free space)

$\varepsilon_{nanobelt} = 12\,\varepsilon_0$ (SnO_2 dielectric constant)

$\sigma_{nanobelt} = 0.001$ to 0.1 S/m (measured SnO_2 conductivity range)

$\varepsilon_{ethanol} = 24\,\varepsilon_0$ (ethanol dielectric constant)

$\sigma_{ethanol} = 1.74\times10^{-4}$ S/m (measured ethanol conductivity)

From Figure 8.4 it can be observed that the CM factor is positive for most of the frequency range, except at some values of high frequencies. Hence, it predicts positive DEP for most of the frequency range. This is contrary to what is observed in the DEP experiments. To see the experimental character, some changes in the parameters can be anticipated (see the following sections).

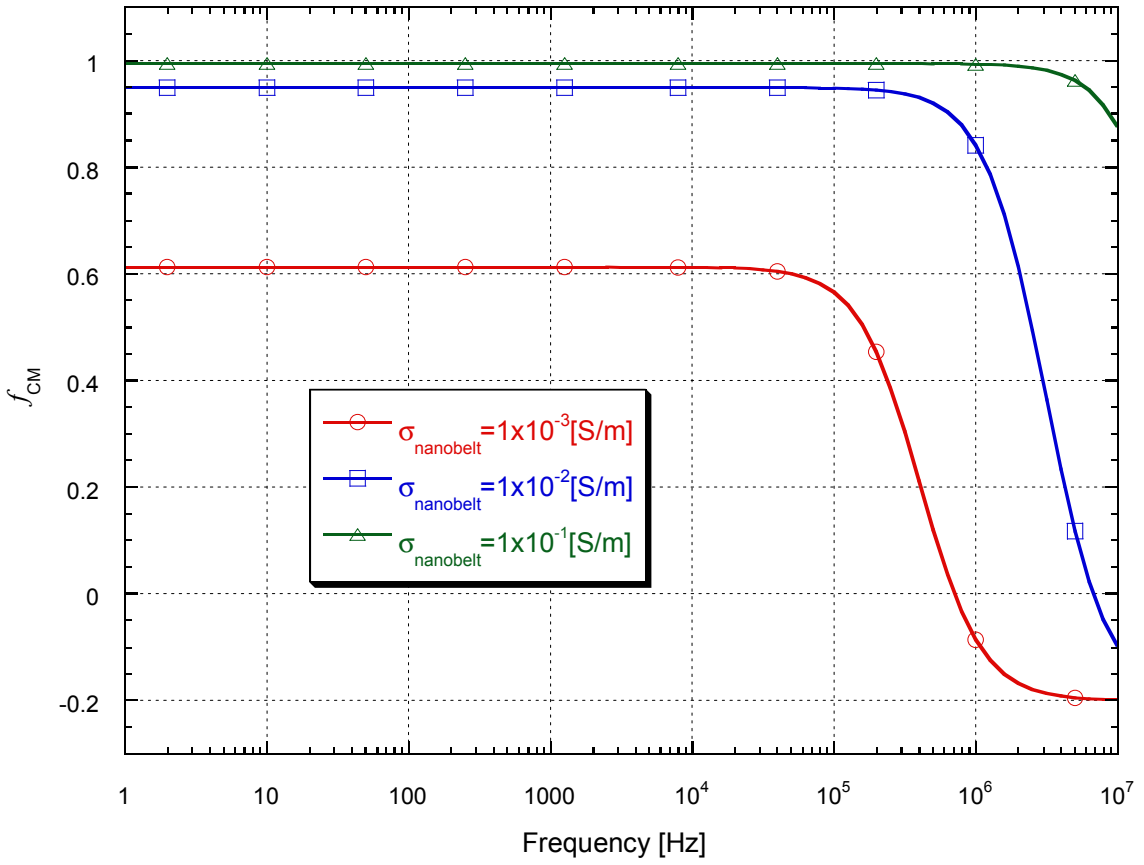

Figure 8.4 CM factor plot for different nanobelt bulk conductivities ($\sigma_{nanobelt} > \sigma_{ethanol}$).

8.3.2 Assuming $\sigma_{nanobelt} \leq \sigma_{ethanol}$

The CM factor is plotted using the following numbers.

$\varepsilon_{nanobelt} = 12\,\varepsilon_0$ (SnO_2 dielectric constant)

$\sigma_{nanobelt} = 0$ to1.74×10^{-4} S/m (assumed less than or equal to ethanol conductivity)

$\varepsilon_{ethanol} = 24\,\varepsilon_0$ (ethanol dielectric constant)

$\sigma_{ethanol} = 1.74\times10^{-4}$ S/m (measured ethanol conductivity)

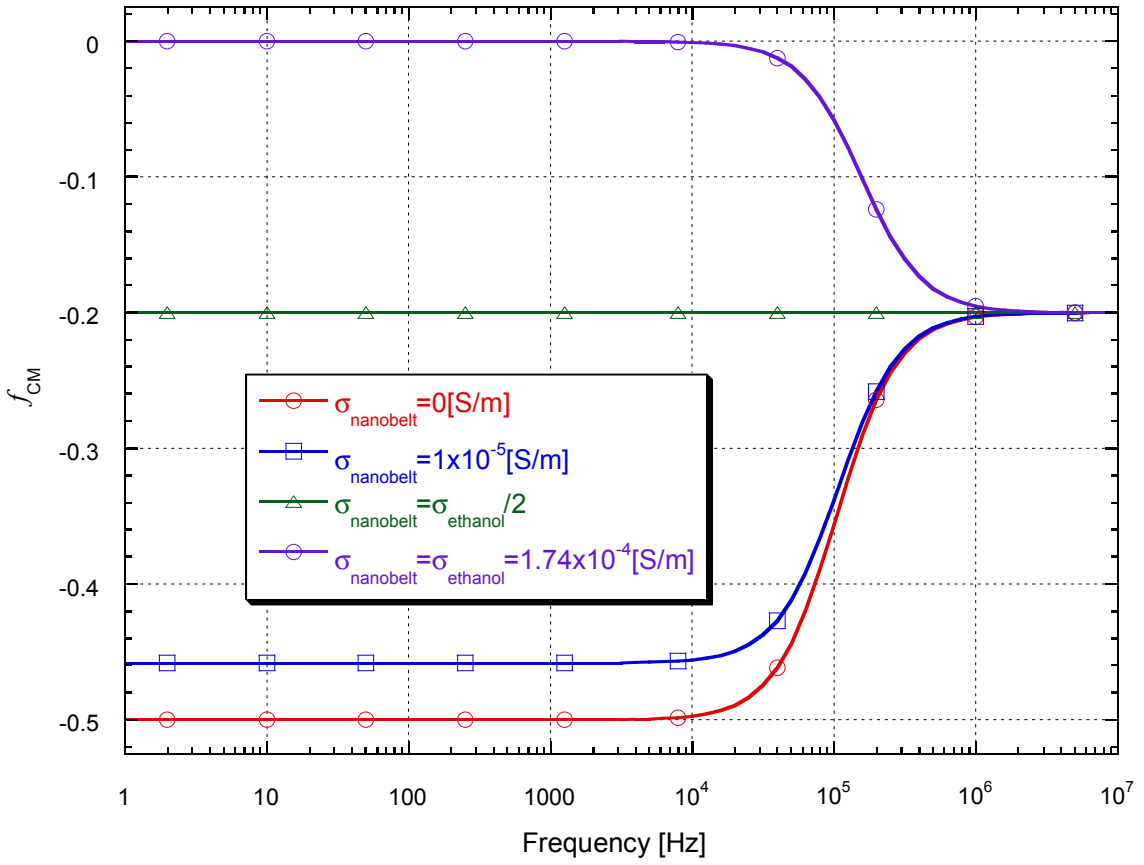

Figure 8.5 CM factor plot for nanobelt conductivity values less than or equal to that of ethanol.

From Figure 8.5 it can be observed that the CM factor is negative or zero for the entire frequency range plotted. So, negative DEP is expected for most of the cases. This trend is similar to the low frequency behavior observed in the experiments. However, the high frequency behavior of positive DEP is not seen here.

8.3.3 Assuming Completely Depleted Nanobelt and Permittivity Change

The CM factor is plotted using the following numbers.

$\varepsilon_{nanobelt} = 12\,\varepsilon_0$ to $30\,\varepsilon_0$ (assumed greater than bulk values)

$\sigma_{nanobelt} = 0$ S/m (nanobelt is assumed to be completely depleted)

$\varepsilon_{ethanol} = 24\,\varepsilon_0$ (ethanol dielectric constant)

$\sigma_{ethanol} = 1.74\times10^{-4}$ S/m (measured ethanol conductivity)

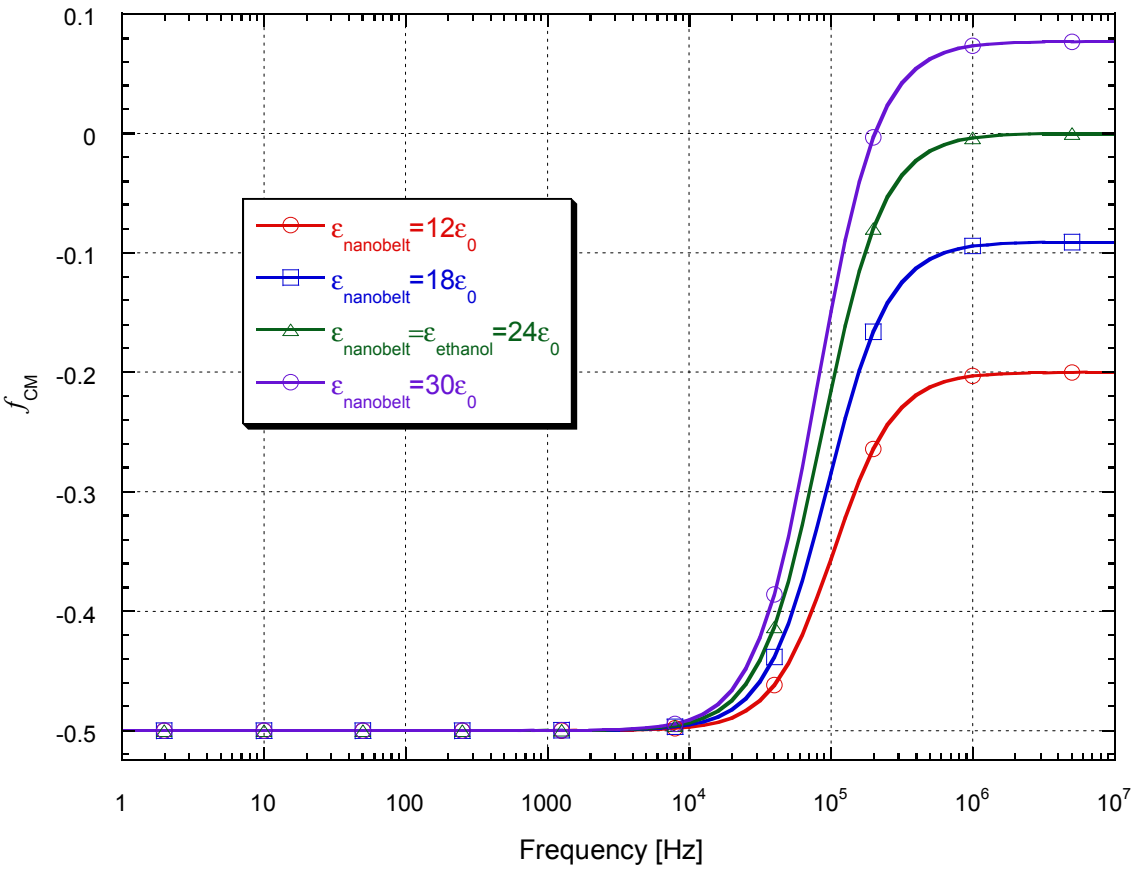

Figure 8.6 CM factor plot for completely depleted nanobelt with permittivity values greater than that of bulk SnO_2 permittivity value.

Figure 8.6 shows that the low frequency DEP characteristics match with the experimental observations, for all the permittivities. For higher frequencies the characteristics match for nanobelt permittivities somewhat greater than that of ethanol ($24\,\varepsilon_0$). In such a case, there are small positive values of the CM factor in the high frequency range, implying weak positive DEP.

8.3.4 Assuming Depleted Nanobelt Surface Layer

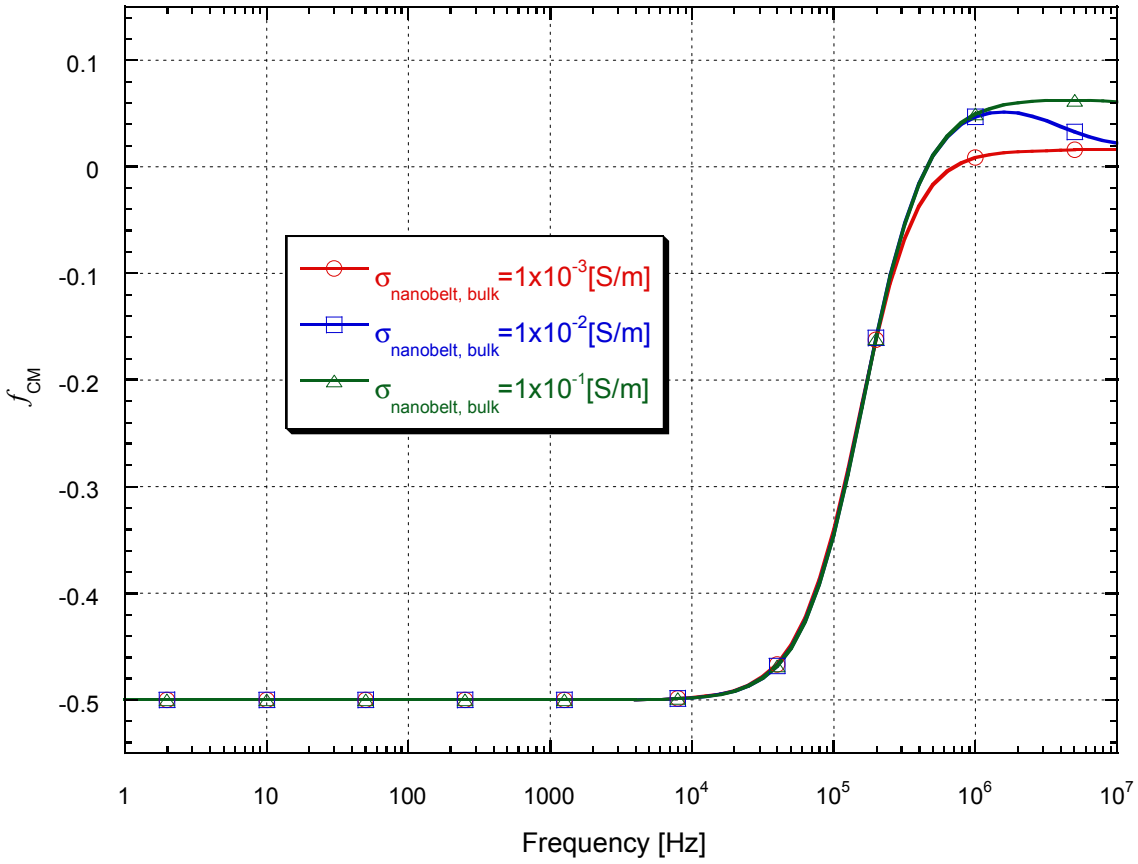

Figure 8.7 CM factor plot for a nanobelt with depleted surface layer and different bulk conductivities.

In this case the spherical shell model for DEP CM factor described in section 2.7 is applied to plot the CM factor using the following numbers.

$\varepsilon_3 = \varepsilon_{nanobelt,bulk} = 12\,\varepsilon_0$ (bulk SnO_2 dielectric constant)

$\sigma_3 = \sigma_{nanobelt,bulk} = 0.001$ to 0.1 S/m
(bulk SnO_2 conductivity values)

$\varepsilon_2 = \varepsilon_{nanobelt,layer} = 12\,\varepsilon_0$ (depleted SnO_2 dielectric constant is assumed equal to the bulk value)

$\sigma_2 = \sigma_{nanobelt,layer} = 0$ S/m (nanobelt surface layer is assumed to be completely depleted)

$\varepsilon_1 = \varepsilon_{ethanol} = 24\,\varepsilon_0$ (ethanol dielectric constant)

$\sigma_1 = \sigma_{ethanol} = 1.74\times10^{-4}$ S/m (measured ethanol conductivity)

$\gamma = \frac{R_o}{R_i} = 2.5$ (assumed value of outer/inner radius)

Figure 8.7 shows that the low and high frequency DEP characteristics match with the experimental observations for all the bulk conductivities used in the calculation. In this situation, there are small positive values of the CM factor at high frequencies, implying positive DEP. One difference, compared to the case of a completely depleted nanobelt and permittivity change, is that the cross over frequency does not change much with a shell model. So, at high frequencies a permittivity change can affect the CM factor and the cross over frequency much more strongly compared to a nanobelt bulk conductivity change.

8.3.5 Assuming Depleted Nanobelt Surface Layer and Permittivity Change

The spherical shell model for DEP CM factor described in section 2.7 is applied to plot the CM factor using the following numbers.

$\varepsilon_3 = \varepsilon_{nanobelt,bulk} = 12\,\varepsilon_0$ (bulk SnO_2 dielectric constant)

$\sigma_3 = \sigma_{nanobelt,bulk} = 0.001$ S/m (bulk SnO_2 conductivity, greater than ethanol conductivity)

$\varepsilon_2 = \varepsilon_{nanobelt,layer} = 12\,\varepsilon_0$ to $30\,\varepsilon_0$ (depleted SnO_2 dielectric constant assumed greater than the bulk value)

$\sigma_2 = \sigma_{nanobelt,layer} = 0$ S/m (nanobelt surface layer is assumed to be completely depleted)

$\varepsilon_1 = \varepsilon_{ethanol} = 24\,\varepsilon_0$ (ethanol dielectric constant)

$\sigma_1 = \sigma_{ethanol} = 1.74\times10^{-4}$ S/m (measured ethanol conductivity)

$\gamma = \frac{R_o}{R_i} = 2.5$ (assumed value of outer/inner radius)

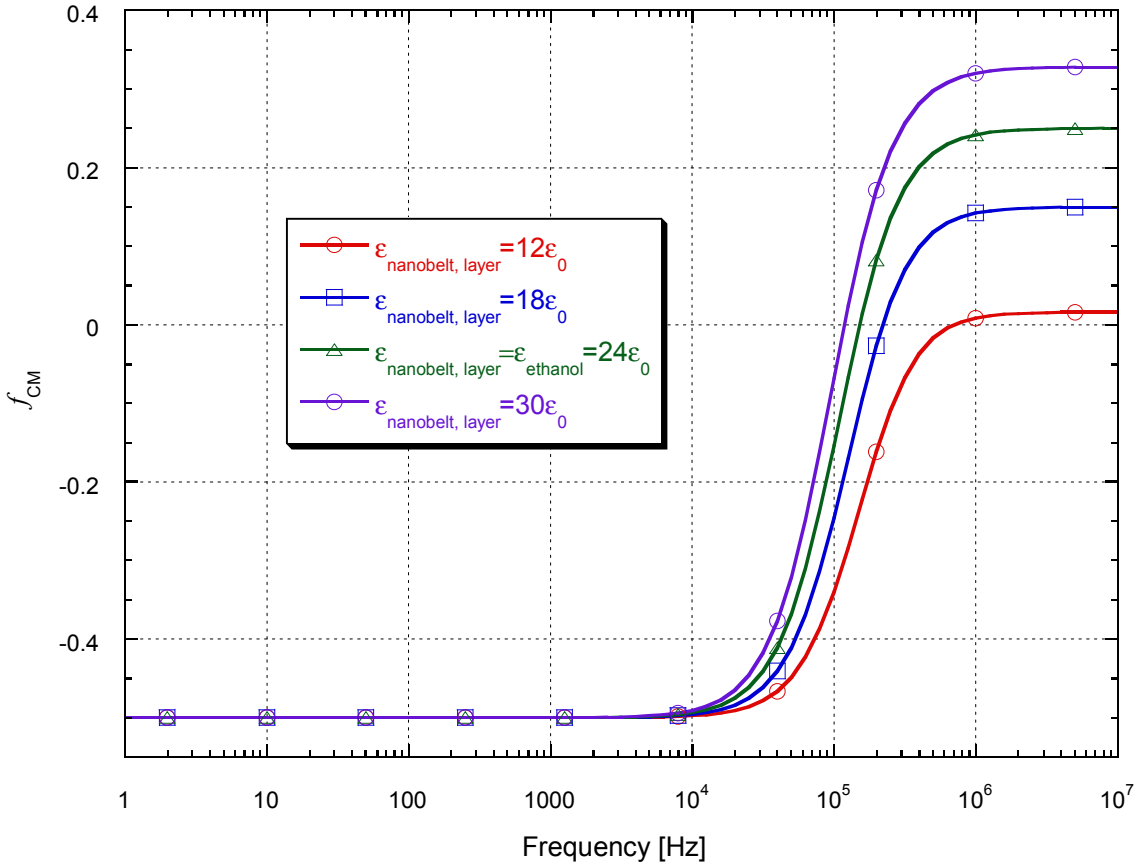

Figure 8.8 CM factor plot for a nanobelt with depleted surface layer and different nanobelt layer permittivities.

Figure 8.8 shows that the DEP characteristics are similar to that shown in Figure 8.6, except that in the present case even a slight increase in $\varepsilon_{nanobelt,\,layer}$ with respect to the bulk permittivity value of SnO_2 ($12\,\varepsilon_0$) can give appreciable positive values of the CM factor, resulting in positive DEP forces in the high frequency range. In Figure 8.6, to get

even weak DEP forces, the nanobelt permittivity had to be greater than $24\varepsilon_0$, which is a very large change from the bulk permittivity value of SnO_2 ($12\varepsilon_0$). It means that the nanobelt depletion model with a shell structure is more likely to explain the experimentally observed DEP characteristics, irrespective of whether permittivity change is incorporated or not. Slight permittivity changes can be expected, for example, due to the presence of hydroxyl groups on the nanobelts. Large permittivity changes are less likely. Hence, a fully depleted nanobelt model is not going to explain the weak positive DEP forces in the high frequencies, since it requires large changes in permittivities.

8.4 DISCUSSION

Because nanostructures have small sizes and hence large surface areas, the physical properties of nanomaterials can be affected significantly by the surface dominant properties. SnO_2 is an n-type semiconductor. Since nanobelts are very thin (10's of nm), surface induced properties can affect the properties of the nanobelt as a whole easily. The anomalous results observed in the dielectrophoresis experiments may be assigned to surface dominant electrical properties. It is known that metal oxide semiconductors like SnO_2, ZnO, etc., possess surface depletion layers due to adsorption of oxygen molecules.

In addition, evidence of charge on the nanobelts has been found through the electrophoresis effects observed in DC and low frequency field experiments in parallel plate electrodes, as reported in Chapter 7. It is anticipated that the presence of the negative charge on the nanobelt surface can also contribute to the depletion of the electrons from the surface regions. From the literature review, one can make an educated guess that the probable reason for the charge is the OH^- groups on its surface, generated

during the interaction of the nanobelts with the atmosphere, before it is suspended in the ethanol. The suspending liquid might affect the nanobelts as well, although that seems to be a lesser effect. Some of the factors that can cause surface charge, depletion, and change in the permittivity of a nanostructure are

1) Adsorption or reaction of molecules on the nanostructure surface before it is suspended in a liquid medium.
2) While being suspended in the liquid, the dipoles of the liquid molecules may interact with the surface.
3) The surface may react with the suspending liquid.

The above factors can affect the DEP forces on nanostructures, suspended in a liquid medium. In addition to reviewing some of these factors, in the current chapter, some semi-empirical calculations were performed by varying the electrical properties of the material, to study the trends of the DEP forces likely to be seen in SnO_2 nanobelt dielectrophoresis.

CHAPTER 9

FINITE ELEMENT SIMULATIONS

In this chapter numerical simulations are performed in an effort to understand and expand the possible explanations for the unusual experimental results observed in the AC dielectrophoresis (DEP) experiments performed on SnO_2 nanobelts suspended in ethanol. To recall, in a previous chapter (Chapter 4) detailed and direct experimental observations of the wide variety of nanobelt motions induced by the DEP forces were reported. Negative DEP (repulsion) of the nanobelts was observed on the application of voltages in the low frequency range (< 100 kHz) and positive DEP (attraction) was found in the high frequency range (1 MHz - 10 MHz). The existence of negative DEP effect is unusual considering the fact that if bulk SnO_2 conductivity and permittivity values are used in combination with the ethanol properties to calculate the Clausius Mossotti factor [20], using the simple dipole approximation, it predicts positive DEP for most of the frequency range studied. As mentioned in Chapter 2, the low frequency behavior of DEP is determined by the conductivity mismatch of the particle and the suspending liquid medium. Hence, the negative DEP at low frequencies, in the case of nanobelts suspended in ethanol, can take place only if the conductivity of the nanobelt is less than that of ethanol. It is hypothesized that the lower conductivity of the SnO_2 nanobelts is due to depletion of the charge carriers from the surface regions. The presence of depletion layers on oxide semiconductors such as SnO_2, ZnO, etc. is well known. In addition, evidence of negative charge on the nanobelt surface has also been found experimentally.

The presence of surface charge on the nanobelt can also contribute to the depletion of the charge carriers from the nanobelt surface regions [96], effectively decreasing the conductivity of the nanobelt. Because of the small dimensions of the nanobelts, the surface properties are likely to dominate its overall properties. After considering some simple models, a more sophisticated model of the nanobelt is proposed and verified to explain qualitatively the experimentally observed DEP characteristics.

9.1 THEORY

Dielectrophoresis results from the polarization of dielectric materials under an applied electric field. Hence, for calculating the DEP forces and torques, it naturally requires the solution of the electric fields under an applied electric potential. In the case of AC dielectrophoresis the potential is time varying and possibly harmonic. So, it is necessary to start from the generalized Maxwell's equations. The differential form of Maxwell's equations for general time varying fields can be written as

$$\nabla \times \boldsymbol{H} = J + \frac{\partial \boldsymbol{D}}{\partial t} \qquad \text{Maxwell-Ampere's law} \qquad (9\text{-}1)$$

$$\nabla \times \boldsymbol{E} = -\frac{\partial \boldsymbol{B}}{\partial t} \qquad \text{Faraday's law} \qquad (9\text{-}2)$$

$$\nabla \cdot \boldsymbol{D} = \rho \qquad \text{Gauss's law (electric form)} \qquad (9\text{-}3)$$

$$\nabla \cdot \boldsymbol{B} = 0 \qquad \text{Gauss's law (magnetic form)} \qquad (9\text{-}4)$$

where,

$\boldsymbol{E}$ is the electric field intensity,

$\boldsymbol{D}$ is the electric displacement or electric flux density,

$\boldsymbol{H}$ is the magnetic field intensity,

$\boldsymbol{B}$ is the magnetic flux density,

$\boldsymbol{J}$ is the current density, and

ρ is the electric charge density.

In addition to the Maxwell's equations, another useful equation is

$$\nabla \cdot \boldsymbol{J} = -\frac{\partial \rho}{\partial t} \qquad \text{Equation of continuity} \tag{9-5}$$

Of the five equations, only three are independent.

In the case of dielectrophoresis calculations, quasi-static approximation can be used. This approximation is valid when currents and the electromagnetic fields are slowly varying. This also implies that the dimensions of the structure in the problem are small compared to the wavelength of the electromagnetic field. The frequency of the electric fields used in the DEP experiments varies from 1Hz to 10 MHz. This corresponds to a wavelength of 3×10^8 m to 3×10 m, which are quite large compared to the electrode gap size (~ 20 μm) used. Hence, this approximation is valid for the current DEP study.

One can neglect the coupling between the electric and magnetic fields if the skin depth in all the domains is much larger than the geometry. This effectively ignores the induced current $\left(\frac{\partial \boldsymbol{B}}{\partial t} = 0\right)$. This approximation is valid for the DEP simulations. So the equations simplify to

$$\nabla \times \boldsymbol{H} = \boldsymbol{J} + \frac{\partial \boldsymbol{D}}{\partial t} \tag{9-6}$$

$$\nabla \times \boldsymbol{E} = 0 \tag{9-7}$$

$$\nabla \cdot \boldsymbol{D} = \rho \tag{9-8}$$

$$\nabla \cdot \boldsymbol{B} = 0 \tag{9-9}$$

$$\nabla \cdot \boldsymbol{J} = -\frac{\partial \rho}{\partial t} \tag{9-10}$$

The equation $\nabla \times \boldsymbol{E} = 0$ implies that one can express the electric field as a function of the electric potential only, i.e. $\boldsymbol{E} = -\nabla V$. Because of the uncoupling, the relevant equations for obtaining the electric field are

$$\nabla \cdot \boldsymbol{D} = \rho \tag{9-11}$$

$$\nabla \cdot \boldsymbol{J} = -\frac{\partial \rho}{\partial t} \tag{9-12}$$

$$\boldsymbol{E} = -\nabla V \tag{9-13}$$

Using the following two equations in the above three equations,

$$\boldsymbol{D} = \varepsilon \boldsymbol{E} \qquad \text{Constitutive relation} \tag{9-14}$$

$$\boldsymbol{J} = \sigma \boldsymbol{E} + \boldsymbol{J}^e \qquad \text{Ohm's law} \tag{9-15}$$

and simplifying, the equation in terms of the electric potential is obtained as

$$-\nabla \cdot \left[\left(\sigma + \varepsilon \frac{\partial}{\partial t} \right) \nabla V - \boldsymbol{J}^e \right] = 0 \tag{9-16}$$

where,

ε is the permittivity of the medium,

σ is the electrical conductivity of the medium, and

$\boldsymbol{J}^e$ is the externally generated current density.

If there is no externally generated current, the above equation reduces to

$$\nabla \cdot \left(\sigma + \varepsilon \frac{\partial}{\partial t} \right) \nabla V = 0 \tag{9-17}$$

In the case of AC dielectrophoresis, time-harmonic analysis is appropriate. For such a situation, the time derivative can be replaced by the ($j\omega$) operator, and the potential can be replaced by the phasor amplitude $\widetilde{V}$. So, the equation becomes

$$\nabla \cdot \left(\varepsilon - j\frac{\sigma}{\omega} \right) \nabla \widetilde{V} = \nabla \cdot \left(\widetilde{\varepsilon} \nabla \widetilde{V} \right) = 0 \tag{9-18}$$

where $\widetilde{\varepsilon}$ is the complex permittivity.

Hence, the problem effectively reduces to solving the electric potential in the simulation domain, and then obtaining the electric field and DEP force through post-processing of the solution.

9.2 SIMULATION METHODOLOGY

The numerical simulations were performed using COMSOL Multiphysics (*Comsol Inc.*, Burlington, MA). COMSOL Multiphysics is a software package that implements a finite element method to solve partial differential equations. COMSOL Multiphysics is one of the few software packages commercially available that was originally made just for solving partial differential equations, in general. There are other packages in the market, but they are specialized for certain areas of study. It is possible to solve the common PDE's of importance found in engineering and physics using this package. It also has the capabilities to solve generic forms of PDE's. An interesting aspect if of this package is its multiphysics capabilities. It is possible to couple and solve different types of equations, such as, mechanical, electrical, thermal, fluid, chemical, magnetic, etc.

Computations were performed using the Time Harmonic-Electric Currents solver in the AC/DC Module of COMSOL Multiphysics Version 3.3. The objective was to solve the Maxwell's equations for the time harmonic electric potential phasor $\tilde{V}$ described in section 9.1 in full 3D. In the literature, 3D simulations of dielectrophoresis phenomenon are very rare because of the large computational resources required for it, compared to 2D simulations. For the computations a dedicated Dell Precision 490 Workstation with an Intel® Xeon 5130® CPU of 2.00 GHz speed, and 4 GB RAM, running Windows XP Professional x64 Edition, Version 2003, Service Pack 2, was used.

The electric field is simply the negative gradient of the electric potential. Direchlet boundary conditions for the applied potentials are used on the electrodes, and Neumann boundary conditions are used for most other exterior boundaries, to model either electrical insulation or symmetry. Interior boundaries were generally modeled with continuity in the electric field displacements.

The domain was meshed with a free mesh of unstructured tetrahedral elements. Very fine mesh elements were defined near the particle (nanobelt), and near the sharp edges of the electrodes. Appropriate element sizes were selected for these small dimensions, and at locations near interfaces where permittivity and conductivity changes are encountered. The maximum dimensions of the elements on the particle (nanobelt) as a whole, the particle (nanobelt) surface, and the sharp edges of the nanobelts were defined independently. The mesh elements were allowed to grow larger, away from the particle (nanobelt), as the electric fields became nearly uniform in the bulk liquid surrounding the particle (nanobelt).

Due to the electric fields generated around the particle (nanobelt), the fluid surrounding it exerts a surface stress (Maxwell Stress Tensor) on the particle (nanobelt) surface. The different components of the force and the torque exerted on the particle (nanobelt) by the fluid were calculated by integrating the Maxwell Stress Tensor over the particle (nanobelt) surface. This integration was performed using a built in function in COMSOL Multiphysics.

9.2.1 Microparticle Dielectrophoresis Simulation

For the comparison of the dipole approximation and the Maxwell Stress Tensor (MST) methods, a spherical microparticle was selected because the dipole approximation is valid for spherical particles. COMSOL Multiphysics simulations using a full 3D model were used to make this comparison, and also to get an idea of the mesh element sizes required for accurate solutions. Time-harmonic analysis was performed to obtain the electric potential in the simulation domain. The objective was to do a parametric study with different particle conductivities and frequencies. The general steps for these simulations were,

1) Create model,
2) Mesh model,
3) Apply boundary conditions,
4) Perform parametric solution (with particle conductivity as parameter) to solve for the electric potential using quasi-static time harmonic analysis, with a selected frequency,
5) Post process field gradients to obtain DEP force using dipole approximation.
6) Post process and integrate MST to obtain DEP force,

7) Repeat step (4) to (6) for a different frequency, and finally,
8) Plot and compare the DEP force calculated using the dipole approximation and MST methods for the different conductivity and frequency values used.

The details of the model and results are discussed in the results and discussion section. Because of the large mesh size the iterative solver GMRES, with the pre-conditioner SSOR, was used for solving the electric potential.

9.2.2 Nanobelt Dielectrophoresis Simulation

COMSOL Multiphysics simulations, for comparison with the DEP characteristics observed in the experiments, were performed using full 3D models. There are many unknowns. The electrical properties of the nanobelt while being suspended in the liquid medium, is not known. The height at which the nanobelt is located above the substrate and electrodes is also not known for the experimental conditions. Hence, the calculations had to be performed with some assumed numbers. Parametric studies with varying nanobelt conductivity and frequency values were conducted. The time-harmonic analysis was performed by solving the electric potential in the simulation domain, assuming quasi-static conditions. The DEP forces and torques on the nanobelt were calculated using the Maxwell Stress Tensor (MST) method. The dipole approximation method cannot be used in the case of nanobelts. The general steps for these simulations were,

1) Create model (different types depending on the nanobelt length and mesh size),
2) Mesh model,
3) Perform parametric solution to solve for the electric potential using quasi-static time harmonic analysis, with

a) frequency as a parameter, and selected nanobelt conductivity and permittivity,

b) nanobelt conductivity or permittivity as a parameter, and selected frequency,

4) Post process and integrate MST to obtain DEP force and torque

5) Repeat step (3a) or (3b), depending on the computational stability issues, and (4), and finally,

6) Plot and analyze the results.

There are variations to this general approach. The general objective was to plot the force and torque quantities as a function of frequency. Hence, a frequency sweep (3a) was ideally desired. But in some cases, because of computational instabilities, frequency sweeps could not be performed. In such a situation, one had to perform calculations at a fixed frequency and do a parametric solution using electrical conductivity or permittivity as a parameter from low values to the final high values. The details of the model and results are discussed in the results and discussion section. In many cases, a shell structure was created around the nanobelt to control the mesh element size near it, so that appropriate resolutions for the calculated quantities such as electric potential and field could be obtained.

9.3 RESULTS AND DISCUSSION

9.3.1 Comparison of Dipole Approximation and MST Method

A spherical particle of 1 μm diameter suspended in a liquid medium was placed at the coordinates, x = - 5 μm, y = 0 μm, z = 1 μm, between triangular electrodes with an

electrode gap of 20 μm. The following material properties were used in the simulation: $\varepsilon_p = 12\,\varepsilon_0$, $\sigma_p = 0$ - 0.1 S/m in steps of 0.01 S/m, $\varepsilon_m = 24\,\varepsilon_0$, $\sigma_m = 0$ S/m. The applied voltage between the electrodes was V = 70 V_{peak}, with a frequency sweep from 100 Hz to 10 MHz and 2 points per decade. The model is similar to the one used for the nanobelt simulation shown in Figure 9.2, except that instead of the nanobelt, a sphere is located between the electrodes.

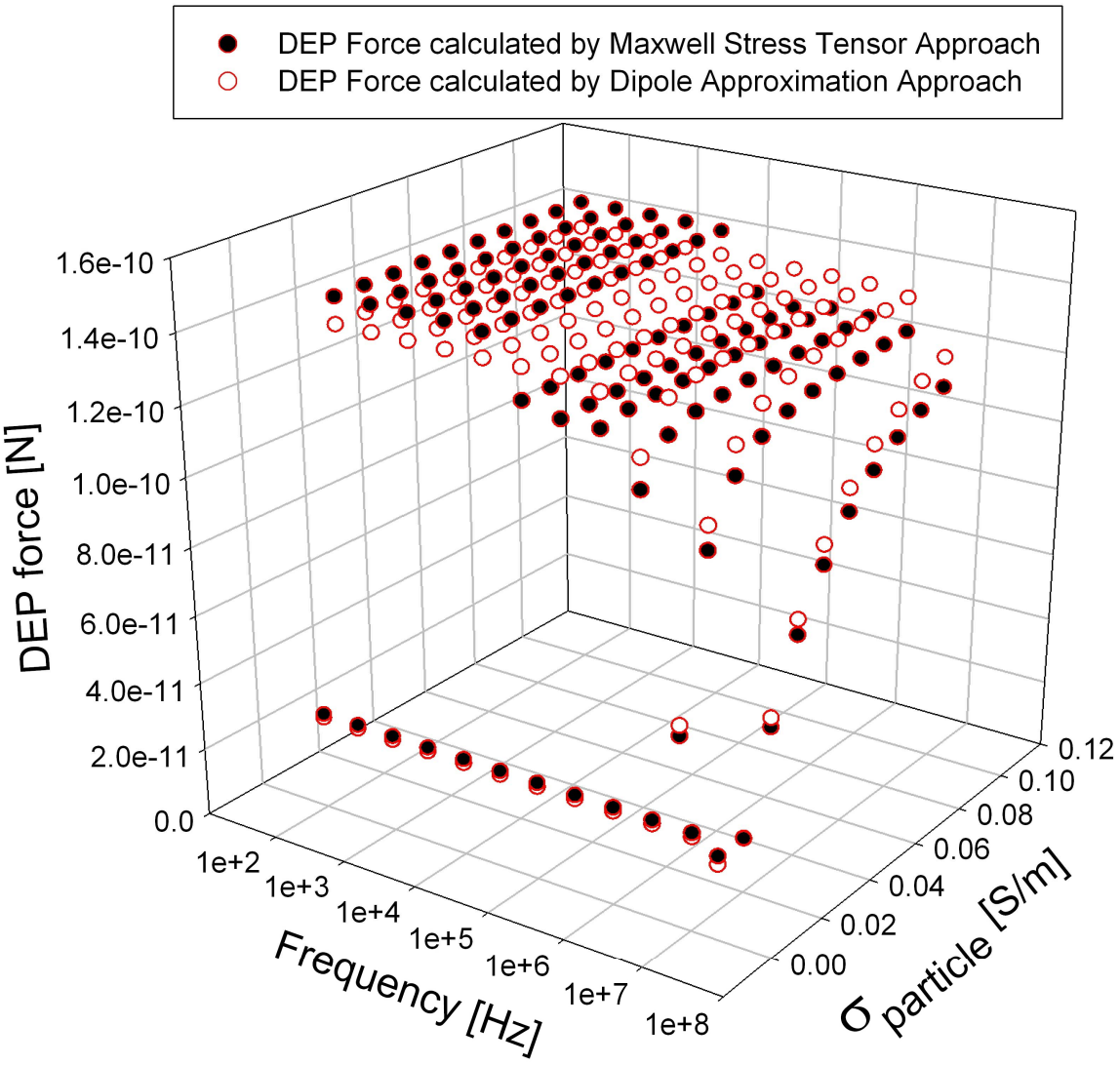

Figure 9.1 Comparison of DEP force on a 1 μm diameter spherical particle calculated using dipole approximation and MST methodologies.

The DEP force on the microparticle was calculated using the Maxwell Stress Tensor method compares well with the dipole approximation calculations as shown in Figure 9.1 for most of the frequency range. Some deviations are observed for points corresponding to high frequency values.

9.3.2 Illustration of Negative Dielectrophoresis Due to Conductivity Decrease

Because, the electrical condition of the nanobelt while being suspended in the liquid ethanol cannot be studied easily, numerical simulations were performed for a range of nanobelt conductivity values. Simulations using COMSOL Multiphysics were performed to obtain the electrical fields and the DEP forces and torques using the Maxwell Stress Tensor (MST) approach.[32] The DEP force on the nanobelt was calculated for the cases when the nanobelt conductivity is assumed to be equal to (Figure 9.3), greater than (Figure 9.4), and smaller than (Figure 9.5) the conductivity of ethanol.

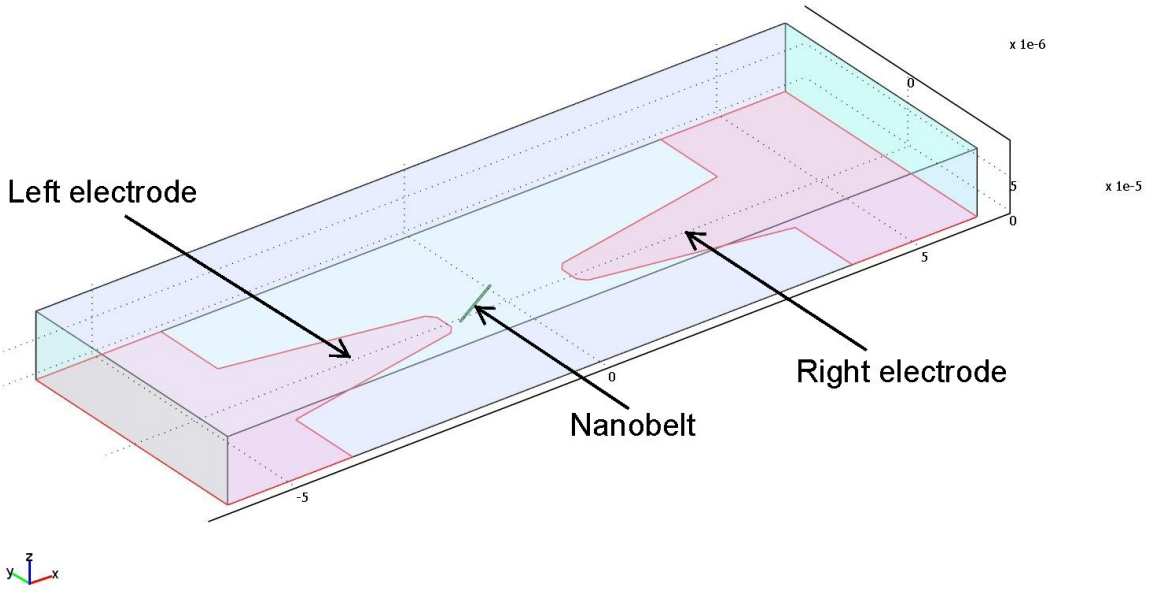

Figure 9.2 COMSOL model for calculation of nanobelt DEP force. The triangular microelectrodes have a gap of 20 μm. The length of the domain is 120 μm, the width is 40 μm, and the height is 10 μm.

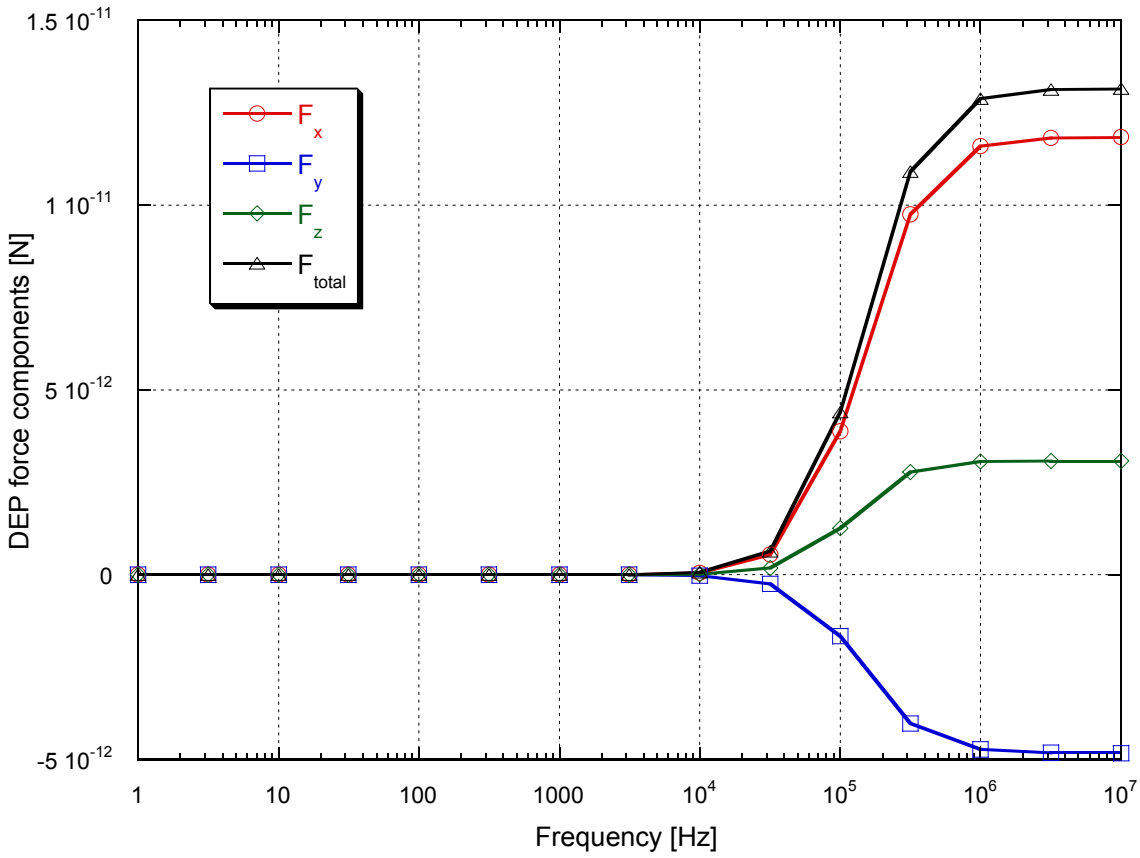

Figure 9.3 Calculated DEP force components when the nanobelt conductivity is equal to that of ethanol (1.74×10^{-4} S/m). Positive F_x means the nanobelt is moving away from the left electrodes and vice-versa, since the nanobelt is located on the negative region of the x-axis.

The simulation to demonstrate negative DEP in nanobelt as a result of a decrease in its conductivity is illustrated using the following parameters: $\varepsilon_{nanobelt} = 12\,\varepsilon_0$, $\sigma_{nanobelt} = 2\times10^{-5}$ S/m, 1.74×10^{-4} S/m, and 1.0×10^{-2} S/m, $\varepsilon_{ethanol} = 24\,\varepsilon_0$, $\sigma_{ethanol} = 1.74\times10^{-4}$ S/m. The nanobelt dimensions were chosen to be 10 µm long, 300 nm wide, and 50 nm thick. The center of the nanobelt is located at x = - 5 µm, y = 0 µm, z = 0.5 µm, and it made an angle about x-axis of 30° (see Figure 9.2). Time harmonic analysis was performed with 70 V_{peak} signal applied between the electrodes and a frequency sweep from 1 Hz to 10 MHz. 1.7 million mesh elements were used in the simulation. Except for the two

electrodes, which were assigned a potential, all the rest of the exterior boundaries of the domain were assigned electric insulation boundary conditions. The electrodes were defined as a conductive surface without any thickness, i.e., a fixed potential. In later models, the electrodes were assigned a thickness of 200 nm.

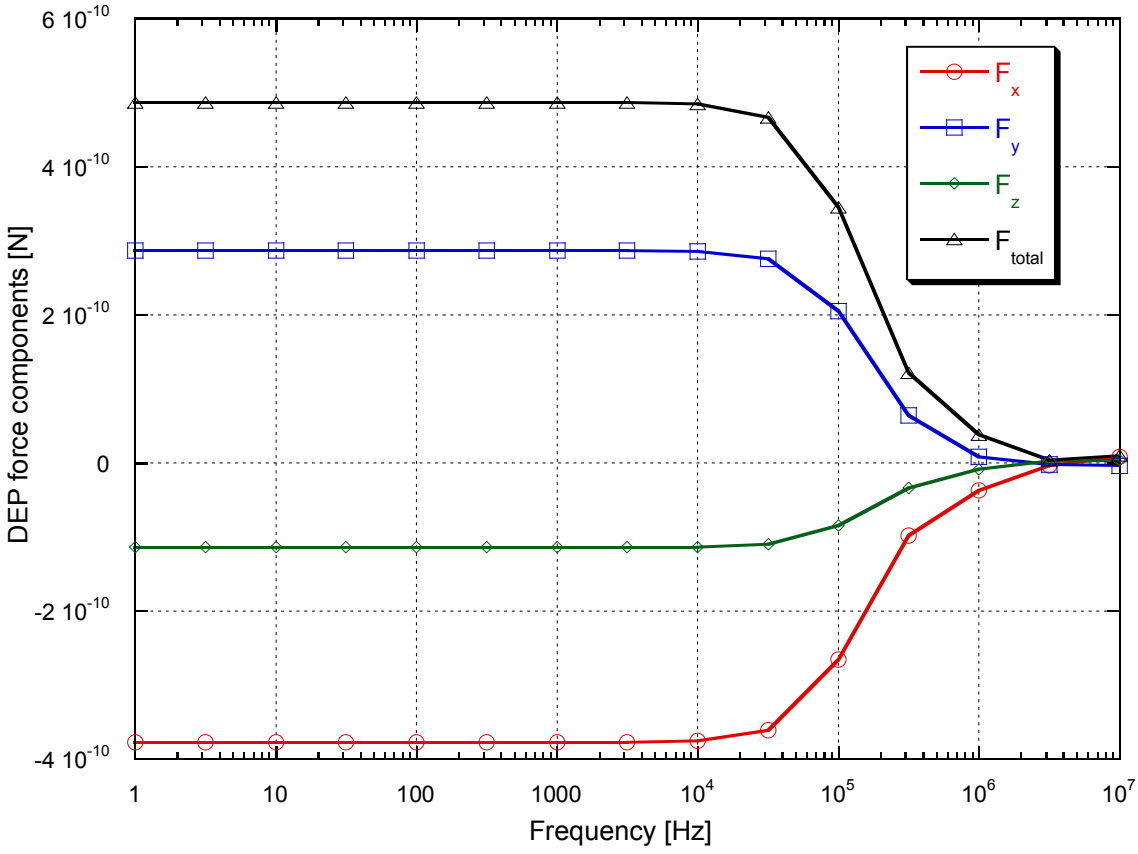

Figure 9.4 Calculated DEP force components when the nanobelt conductivity is assumed (1.0×10^{-2} S/m) to be greater than that of ethanol.

Out of the three cases considered, the results shown in Figure 9.5 show some similarity with the experimental observations. For signal frequencies of up to 100 kHz, the x component of the DEP force is a positive number, implying that the nanobelt is getting repelled from the left electrode (Figure 9.2) towards low field regions. Please refer to the sign convention described in the caption of Figure 9.3. This means there is a

negative DEP effect. This is also verified by the z component of the DEP induced torque (Figure 9.6), which shows positive values, implying counterclockwise rotation away from the left electrode. In the other two calculations either no force or attractive forces are found up to 100 kHz. However, even in Figure 9.5, the force direction does not change in the high frequency range, contrary to experimental observations. Hence, a more sophisticated model is required to predict negative DEP in the low frequency range and positive DEP at high frequencies. Such a model was studied, and the details are discussed in later sections.

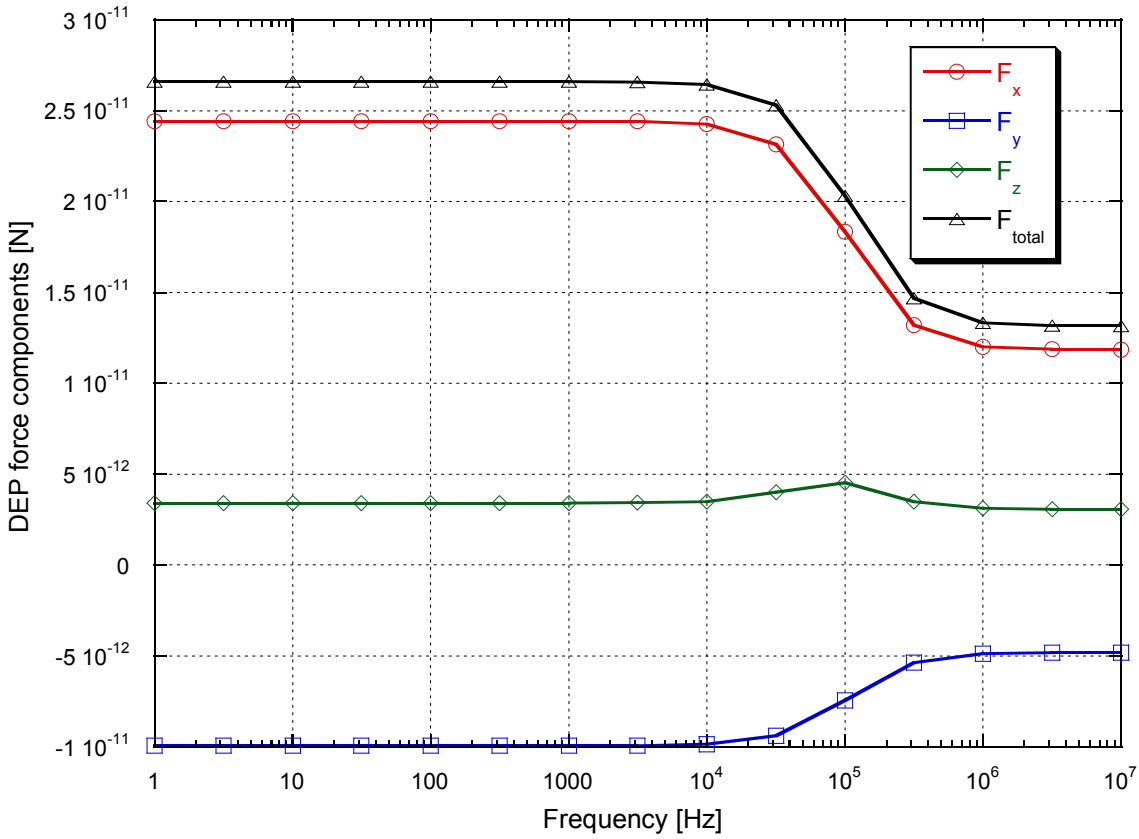

Figure 9.5 Calculated DEP force components when the nanobelt conductivity is assumed (2.0×10^{-5} S/m) to be less than that of ethanol.

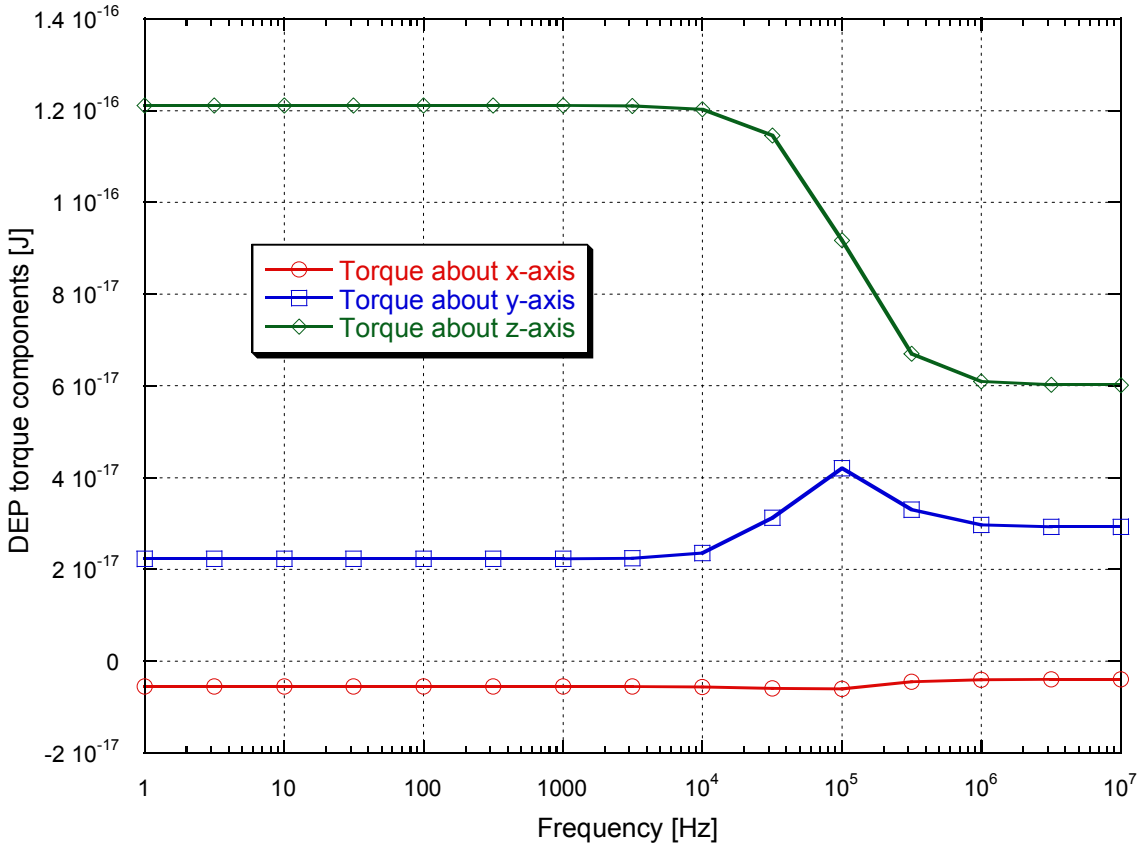

Figure 9.6 Calculated components of torque generated due to DEP, when nanobelt conductivity is assumed (2.0×10^{-5} S/m) to be less than that of ethanol. Positive torque about z axis means counterclockwise rotation, if seen from the top of the model.

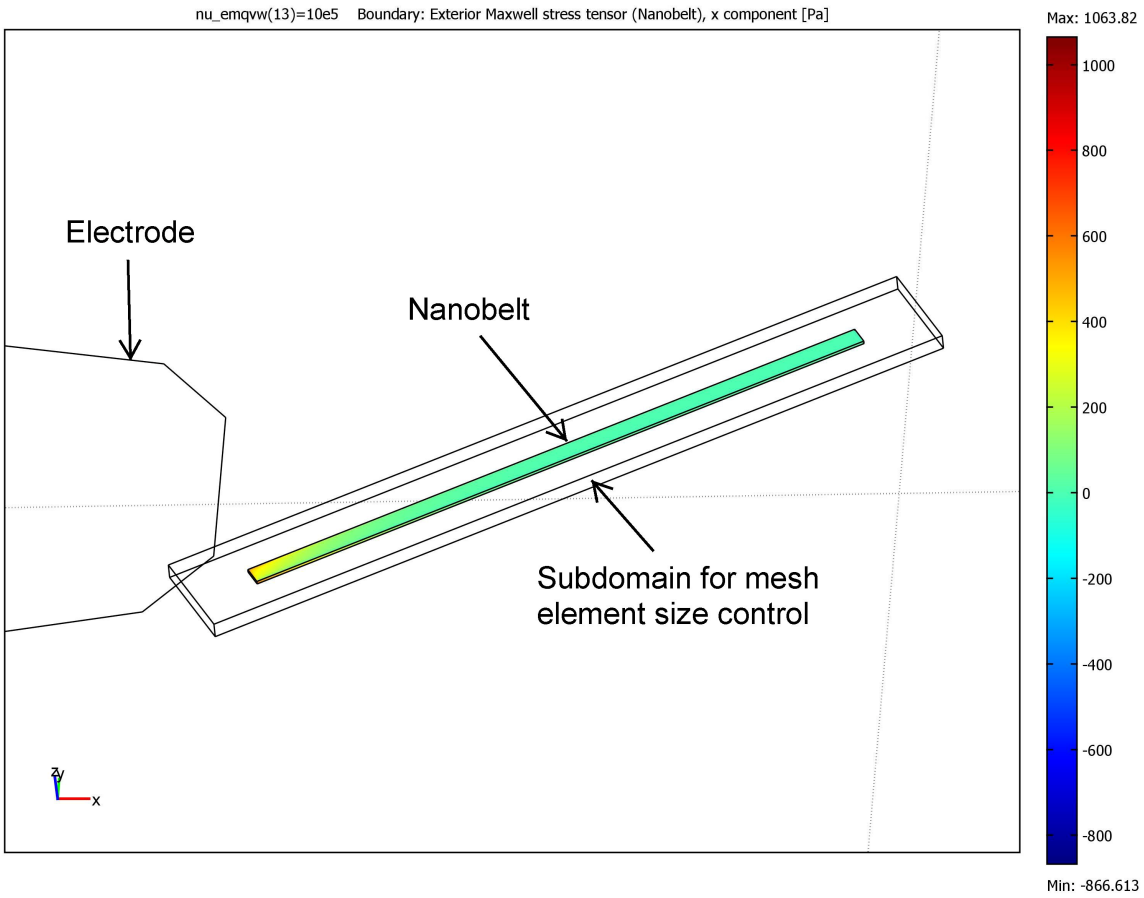

Figure 9.7 Figure showing the x component of the Maxwell Stress Tensor on the nanobelt surface at a frequency of 1 MHz. Nanobelt conductivity used in the simulation is 2.0×10^{-5} S/m. The white structure around the colored nanobelt is a shell to control the mesh element size.

9.3.3 DEP Force Variation with Height

The change of the DEP force on the nanobelt as a function of height change was studied using the following parameters: $\varepsilon_{nanobelt} = 12\,\varepsilon_0$, $\sigma_{nanobelt} = 2\times10^{-5}$ S/m, $\varepsilon_{ethanol} = 24\,\varepsilon_0$, $\sigma_{ethanol} = 1.74\times10^{-4}$ S/m. The nanobelt dimensions were chosen to be 5 µm long, 300 nm wide, and 50 µm thick. The center of the nanobelt is located at x = 7 µm, y = 0 µm, z = 0.5 µm, and it made an angle about the x-axis of 0°. A voltage V = 70 V_{peak} was applied between the electrodes with a frequency of 1 kHz and 10 MHz. The model used

for this study is shown in Figure 9.8. This model is similar to the model shown in Figure 9.2, except that the electrodes are assigned a height of 200 nm to be closer to reality corresponding to the electrodes used for the DEP experiments. One minor difference is that in this model the nanobelt is located on the positive region of the x-axis, as opposed to the negative region in the case of the model shown in Figure 9.2. The height of the nanobelt above the substrate was varied and the model was solved for each height to calculate the DEP force components. The force components are plotted as a function of height in Figure 9.9, which shows the rapid decrease of force as the nanobelt moves away from the electrodes. The z component of the DEP force shows a non-monotonic trend near the electrode. This is due to the complicated nature of the electric fields at small heights (~ 0.5 μm) as a result of the finite electrode thickness (~ 0.2 μm).

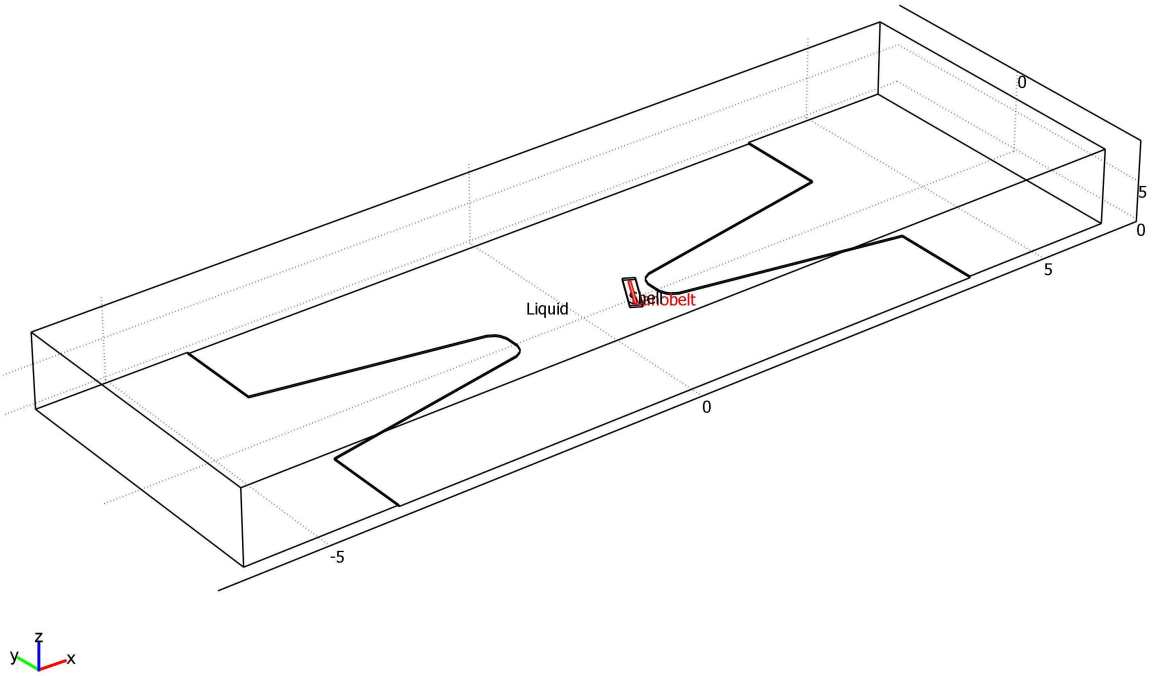

Figure 9.8 COMSOL model to study the DEP force change with height and angle. The triangular microelectrodes have a gap of 20 μm. The electrode thickness is set at 200 nm. The nanobelt length is chosen to be 5 μm.

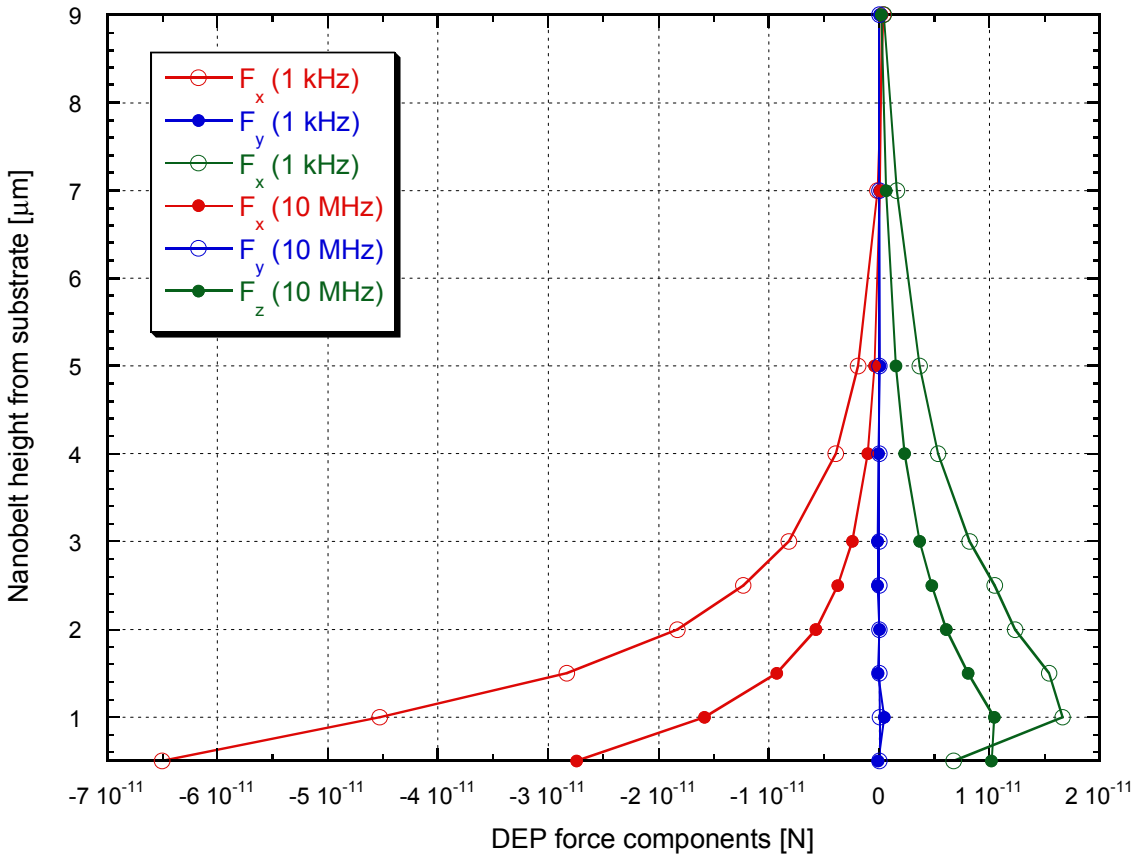

Figure 9.9 The components of DEP force on a nanobelt shown as a function of height from the substrate, for two frequencies.

9.3.4 DEP Force Variation with Angle

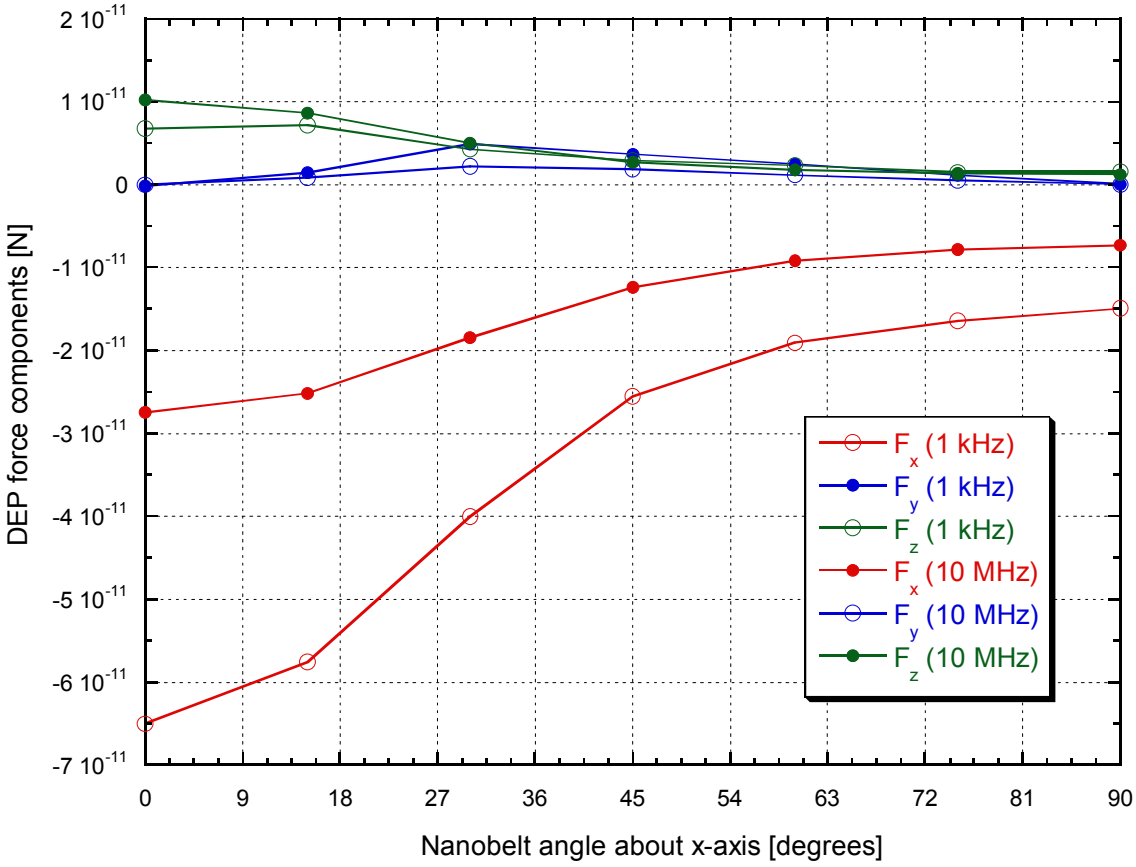

Figure 9.10 The components of DEP force on nanobelt shown as a function of the angle it makes about the x-axis, for two frequencies. Refer to Figure 9.8 for the location and orientation of the nanobelt.

The change of the DEP force on the nanobelt as a function of the angle it makes about the x-axis was studied using the following parameters: $\varepsilon_{nanobelt} = 12\,\varepsilon_0$, $\sigma_{nanobelt} = 2\times10^{-5}$ S/m, $\varepsilon_{ethanol} = 24\,\varepsilon_0$, $\sigma_{ethanol} = 1.74\times10^{-4}$ S/m. The nanobelt dimensions were chosen to be 5 μm long, 300 nm wide, and 50 nm thick. The center of the nanobelt is located at x = 7 μm, y = 0 μm, z = 0.5 μm, and it made a variable angle about the x-axis, between 0° and 90°. A voltage V = 70 V_{peak} was applied between the electrodes with a frequency of 1 kHz and 10 MHz. The model used for this study is shown in Figure 9.8.

The angle of the nanobelt about the x-axis was changed, and the model was solved for each angle to calculate the DEP force components. The force components are plotted as a function of the angle in Figure 9.10, which shows the gradual decrease of force as the nanobelt angle increased, and one of the ends of the nanobelt moved farther away from the electrode.

9.3.5 Comparison of Shell Model and MST Method for a Sphere

Since the use of a single bulk conductivity value for the nanobelt could not explain the positive DEP observed in the experiments, it was decided that a shell structure for the nanobelt will be investigated. In this nanobelt model a depleted layer surrounds a more conductive interior. However, before that calculation, two sample calculations on a sphere with a shell structure were performed using the following parameters: $\varepsilon_3 = \varepsilon_{nanobelt,bulk} = 12\varepsilon_0$, $\sigma_3 = \sigma_{nanobelt,bulk} = 0.01$ S/m, $\varepsilon_2 = \varepsilon_{nanobelt,layer} = 12\varepsilon_0$, $\sigma_2 = \sigma_{nanobelt,layer} = 0$ S/m, $\varepsilon_1 = \varepsilon_{ethanol} = 24\varepsilon_0$, $\sigma_1 = \sigma_{ethanol} = 1.74\times10^{-4}$ S/m, and $R_o/R_i =$ 500 nm/200 nm, and 500 nm/300 nm. Please refer to sections 8.3.4 and 8.3.5 for the terminology, and section 2.7 for the dipole approximation method for spherical shell models. The center of the sphere was located at x = 5 μm, y = 0 μm, z = 2 μm, and a voltage V = 70 V_{peak} was applied between the electrodes, with a frequency sweep from 1 Hz to 10 MHz. The model used for this study is shown in Figure 9.11. The original model was reduced in half by truncating in the symmetry plane between the two triangular electrodes in Figure 9.8. Some extra volume was also reduced near the far end of the triangular electrode. So, the current domain size is 50 μm long, 40 μm wide, and 10 μm high. The potential on the horizontal right electrode was set at 70 V_{peak}, and the

left vertical plane is set at 70/2 = 35 V_{peak}. This is effectively the same situation as setting the two electrodes in the original full model at 70 V_{peak} and 0 V_{peak}, respectively.

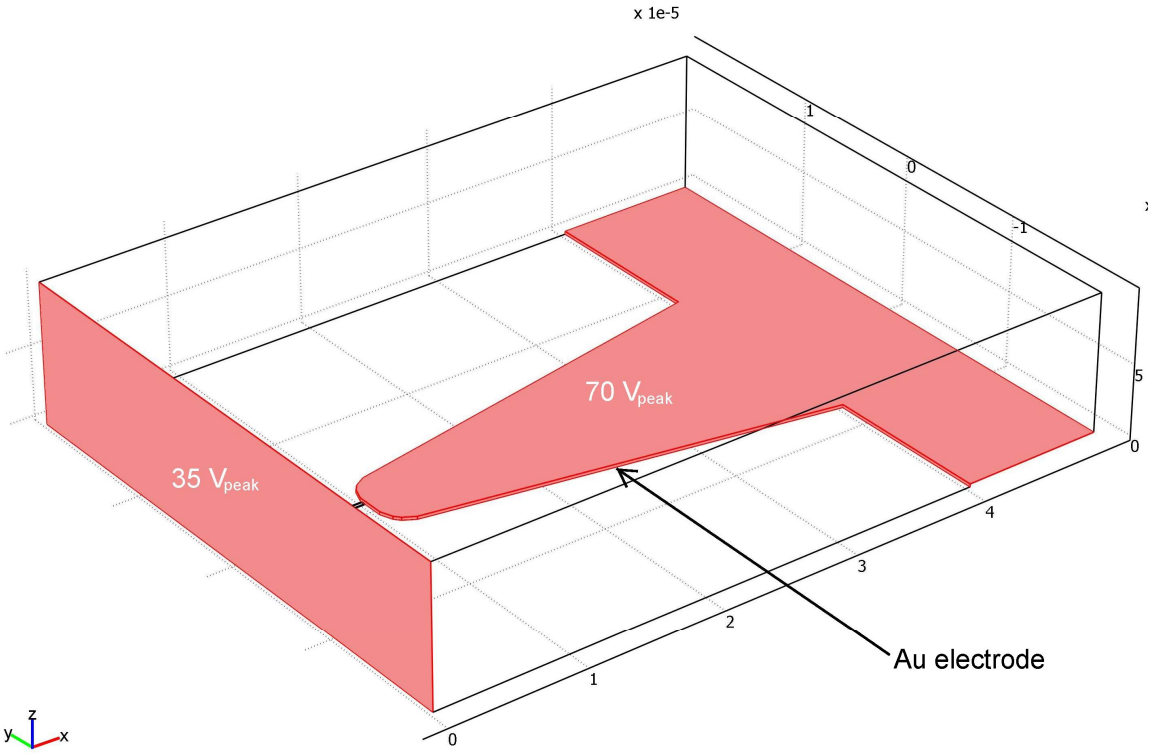

Figure 9.11 COMSOL model to study the DEP force in a sphere with a shell structure. The pink colored areas are the surfaces where potential is applied.

The comparison of the calculated DEP force using the MST and the dipole approximation methods are plotted in Figure 9.12 and Figure 9.13 for the two radius ratios simulated. It is observed that for the high frequency range there is some discrepancy in the values calculated using the two methods. The dipole approximation is not accurate in this range. MST values can be considered the correct ones, since it fully solves the electric fields in each point on the sphere surface and there is no approximation involved. Calculations with a refined mesh did not show any significant difference in the DEP force values. So, the deviation is not due to lack of mesh resolution.

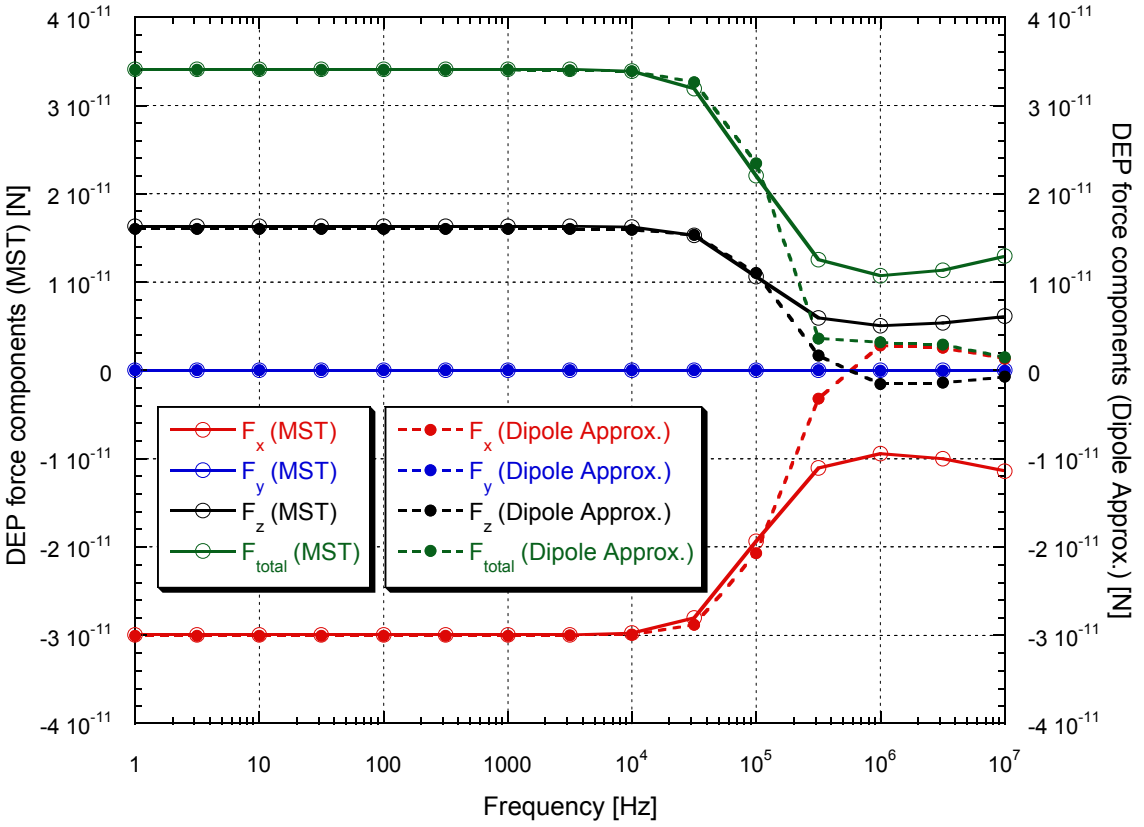

Figure 9.12 Comparison of the different DEP force components for a microparticle with a shell structure (R_o = 500 nm, R_i = 200 nm) using the full MST method and the dipole approximation method.

Comparing Figure 9.12 and Figure 9.13, one can observe that when the inner sphere radius, which has a higher conductivity compared to the outer shell, is increased, the MST force (the correct values) components start getting closer to the zero line in the high frequency range. This is an interesting observation. If the inner sphere radius keeps increasing, or the conductivity of the inner sphere is increased, it can be expected that the force components will cross the zero line. In such as situation, the DEP force directions in the low frequency and high frequency range will become opposite, implying positive DEP in high frequencies and negative DEP in low frequencies. This DEP characteristic is similar to the experimental observations. For observing the zero line crossing, thinner

shells will have to be simulated. Thinner shells require large number of mesh elements. Hence, such a calculation was not performed. In any case, one is interested in the simulation of the nanobelt, not the sphere. The present calculations were performed to observe the trends for a few cases, as shown by the figures.

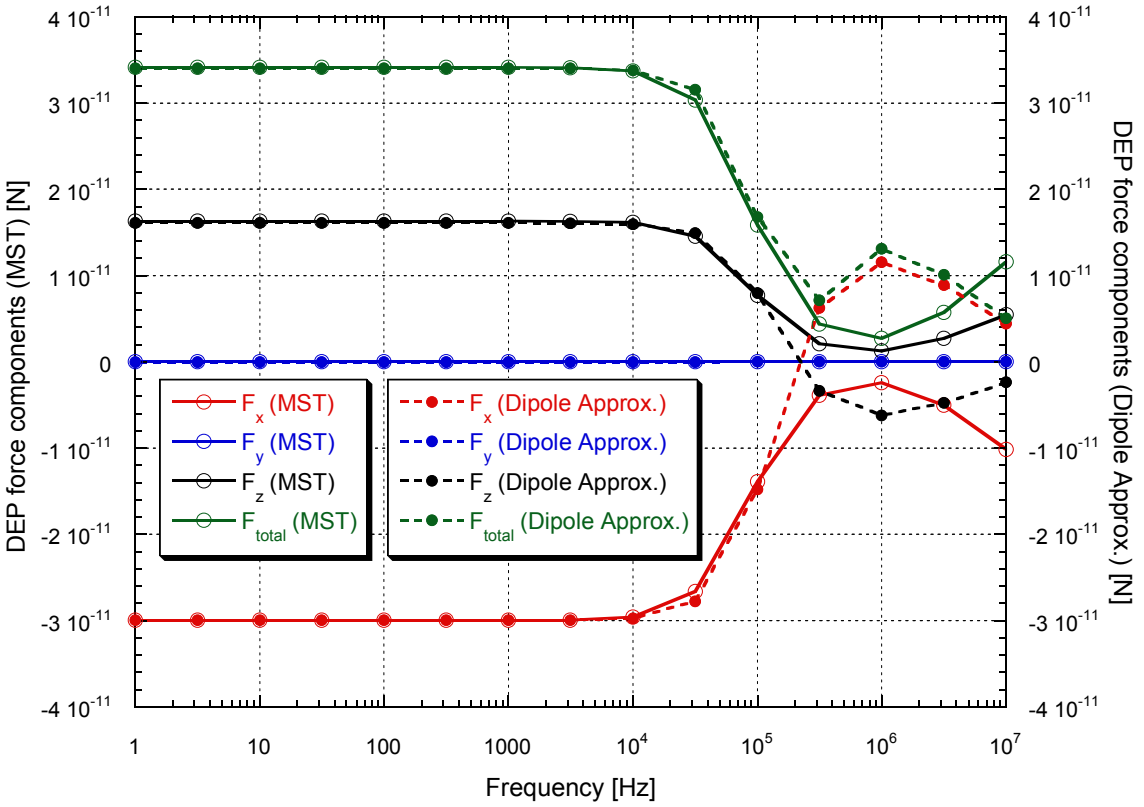

Figure 9.13 Comparison of the different DEP force components for a microparticle with a shell structure (R_o = 500 nm, R_i = 300 nm) using the full MST method and the dipole approximation method.

The use of the dipole approximation allows the calculation of the DEP force in the whole domain of the simulation, since it requires only the field gradients. Figure 9.14 shows the color plot of the electric potential in the x-z symmetry plane (y = 0) for the model shown in Figure 9.11, which is independent of frequency. This plane is actually the vertical plane passing through the triangular electrode and bisecting the model. Since

it passes through the electrode gap, points near the electrodes on this plane have the highest field gradients and hence, the highest DEP forces. Similarly, Figure 9.15 shows the electric field magnitude (independent of frequency), and Figure 9.16 shows the log (base 10) of the DEP force (for 1 kHz frequency) in that particular plane. The DEP force is very strong near the electrode edge which is shown by the red colored areas in Figure 9.16. The DEP force falls rapidly for positions far away from the electrode edge. This is understandable because the field gradients fall rapidly away from the electrode edge.

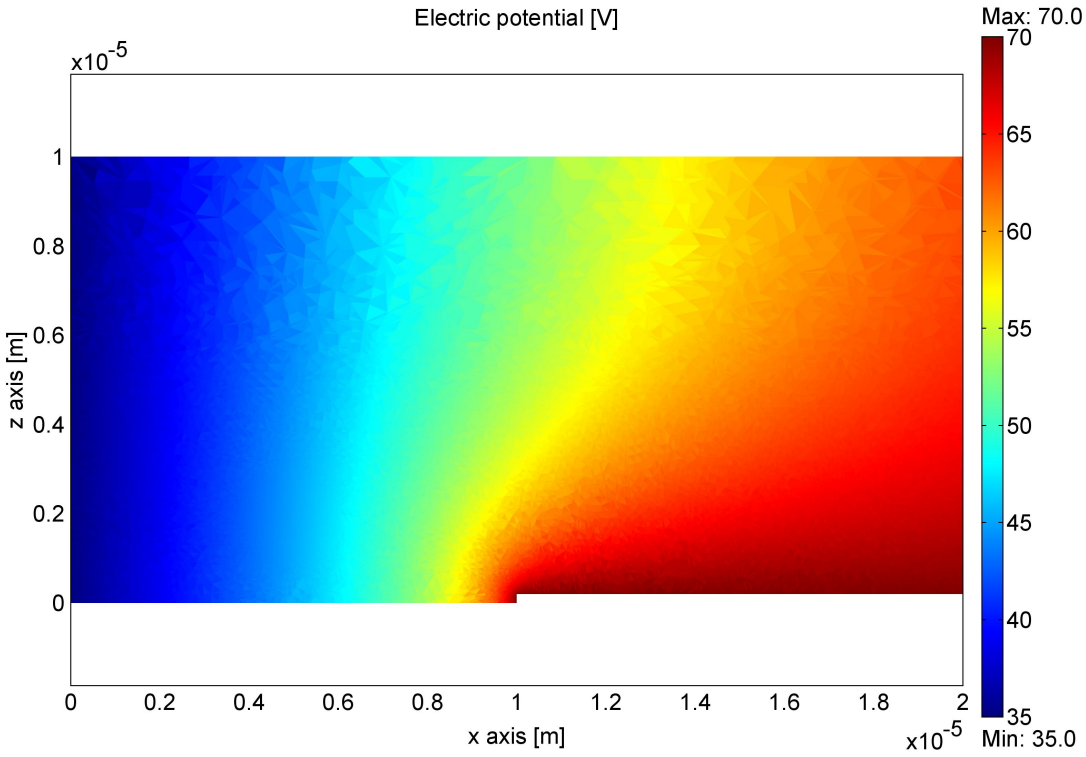

Figure 9.14 Color plot of electric potential in the x-z symmetry plane (y = 0).

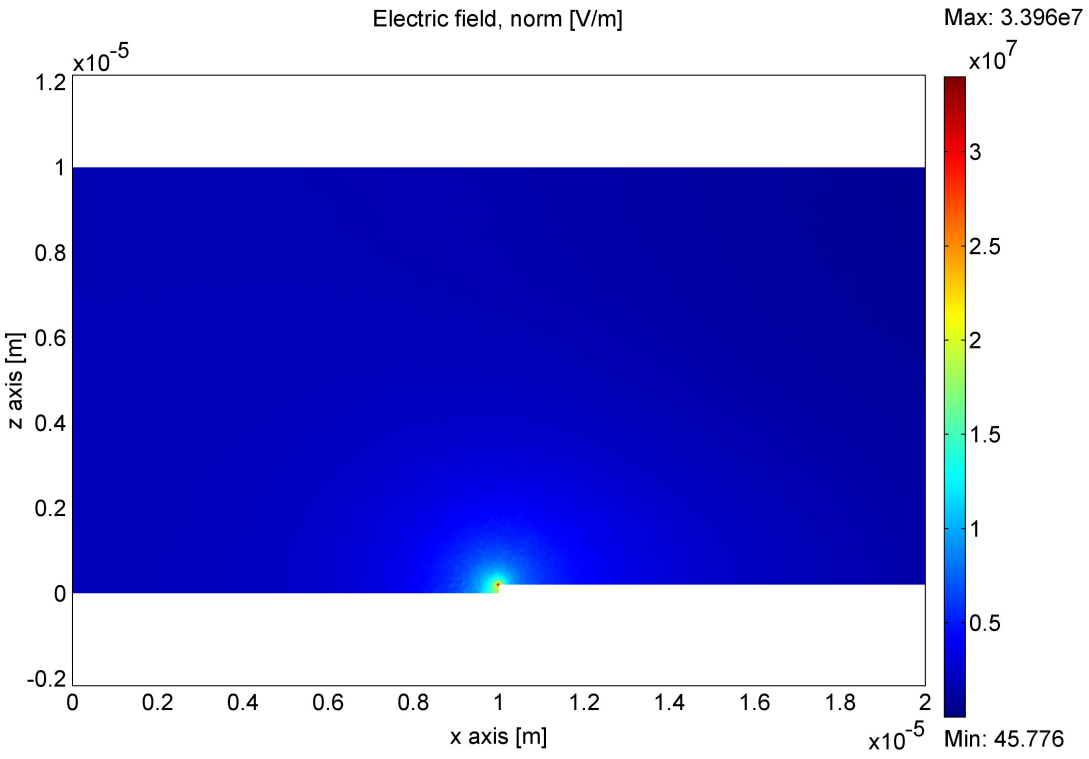

Figure 9.15 Color plot of electric field magnitude in the x-z symmetry plane (y = 0).

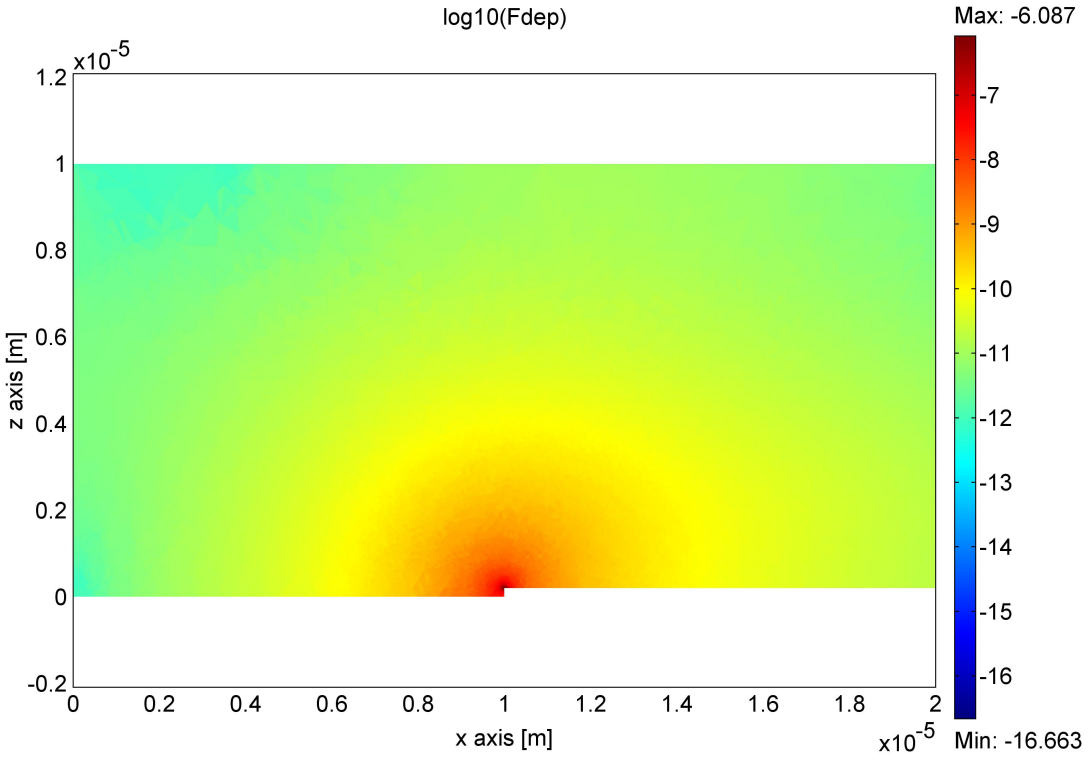

Figure 9.16 Color plot of $\log_{10}$ of DEP force in the x-z symmetry plane (y = 0).

9.3.6 Shell Model for Nanobelt

In section 9.3.2 it was found that assuming a lower conductivity for the nanobelt compared to that of the suspending liquid (ethanol) predicts negative DEP in the low frequency range. This is similar to the experimentally observed DEP behavior. However, using a lower conductivity for the nanobelt as a whole, does not predict positive DEP in the high frequencies. In an effort to resolve this situation, a shell type nanobelt model was studied numerically. Figure 9.17 shows a schematic of the nanobelt shell structure. In this simplified model, the thickness of the depletion layer is assumed to be constant for all the surfaces of the nanobelt. In reality however, the actual thickness of the depletion layer can be different in the differently oriented surfaces of the nanobelt, and the interface between the depletion and the conductive regions is likely to be curved near the edges and corners.

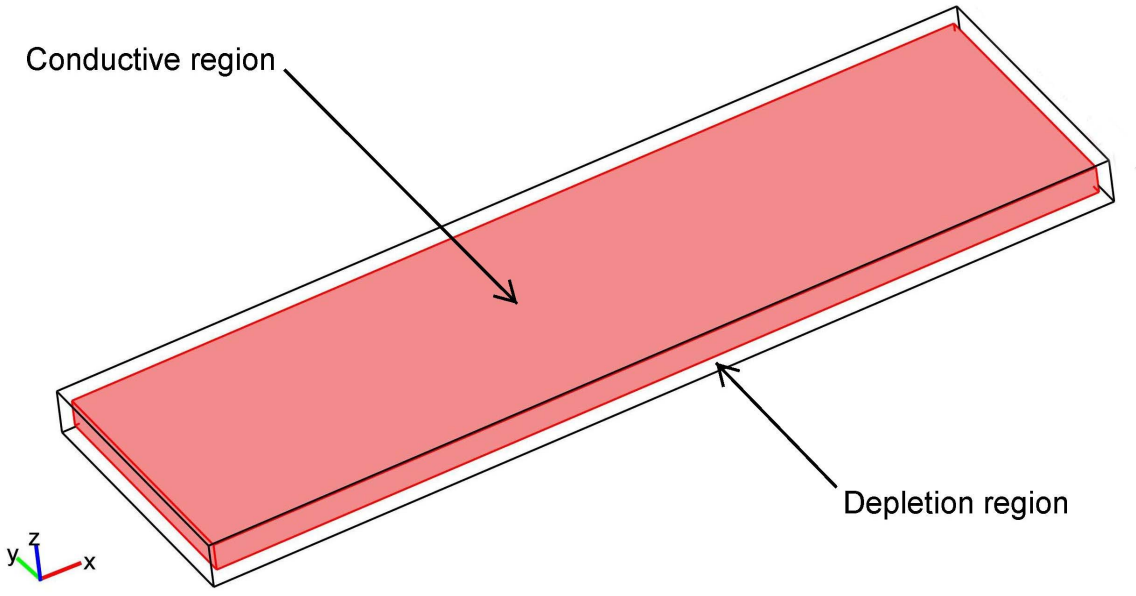

Figure 9.17 Schematic showing the nanobelt shell structure.

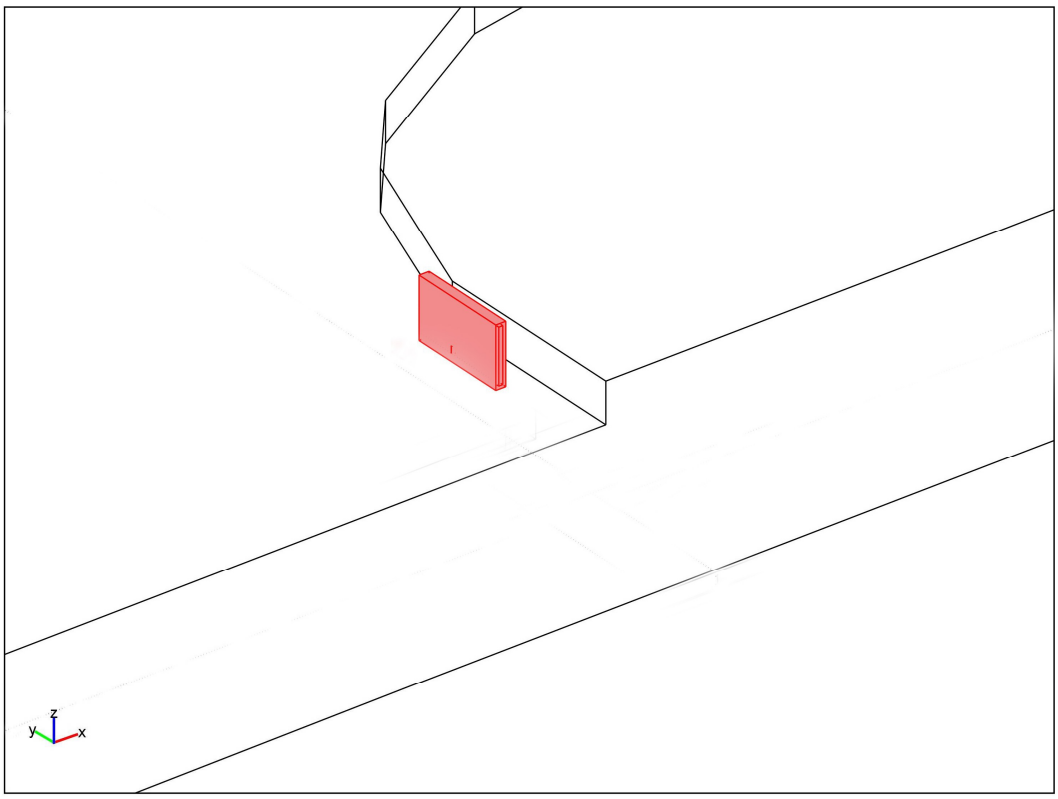

Figure 9.18 Picture showing the orientation of a nanobelt (pink color) with shell structure near a 200 nm thick electrode.

The computation was performed using the following parameters: $\varepsilon_3 = \varepsilon_{nanobelt,bulk} = 12\varepsilon_0$, $\sigma_3 = \sigma_{nanobelt,bulk} = 0.001$ to 1.0 S/m, $\varepsilon_2 = \varepsilon_{nanobelt,layer} = 12\varepsilon_0$, $\sigma_2 = \sigma_{nanobelt,layer} = 0$ S/m, $\varepsilon_1 = \varepsilon_{ethanol} = 24\varepsilon_0$, $\sigma_1 = \sigma_{ethanol} = 1.74\times10^{-4}$ S/m. The nanobelt dimensions were chosen to be 1 µm long, 300 nm wide, and 50 nm thick. The shell was assumed to be 15 nm thick, so that the interior of the nanobelt with bulk conductivity had dimensions of 0.970 µm length, 270 nm width, and 20 nm thickness. The center of the nanobelt was located at $x \approx 9.5$ µm, $y = 0$ µm, $z = 0.5$ µm. The minimum distance from one of the vertical sided of the nanobelt to the electrode edge was 0.5 µm. Effectively, a voltage V = 70 V_{peak} was applied between the DEP electrodes, although a quarter model was used for this calculation. A parametric solution with a frequency sweep from 1 Hz to 10 MHz

was performed. Some details about the model are relevant here. Because of the depletion layer thickness of 15 nm (very small number compared to the domain size), the number of elements in the mesh became very large for the half model shown in Figure 9.11. To handle this situation the model was halved again along the x-z symmetry plane (y = 0). Also, for solving the model in a reasonable amount of computational time, nanobelt lengths longer than 1 μm was difficult to handle. The 1 μm long nanobelt in Figure 9.11 corresponds to a 0.5 μm long nanobelt in Figure 9.18 because of the model symmetry.

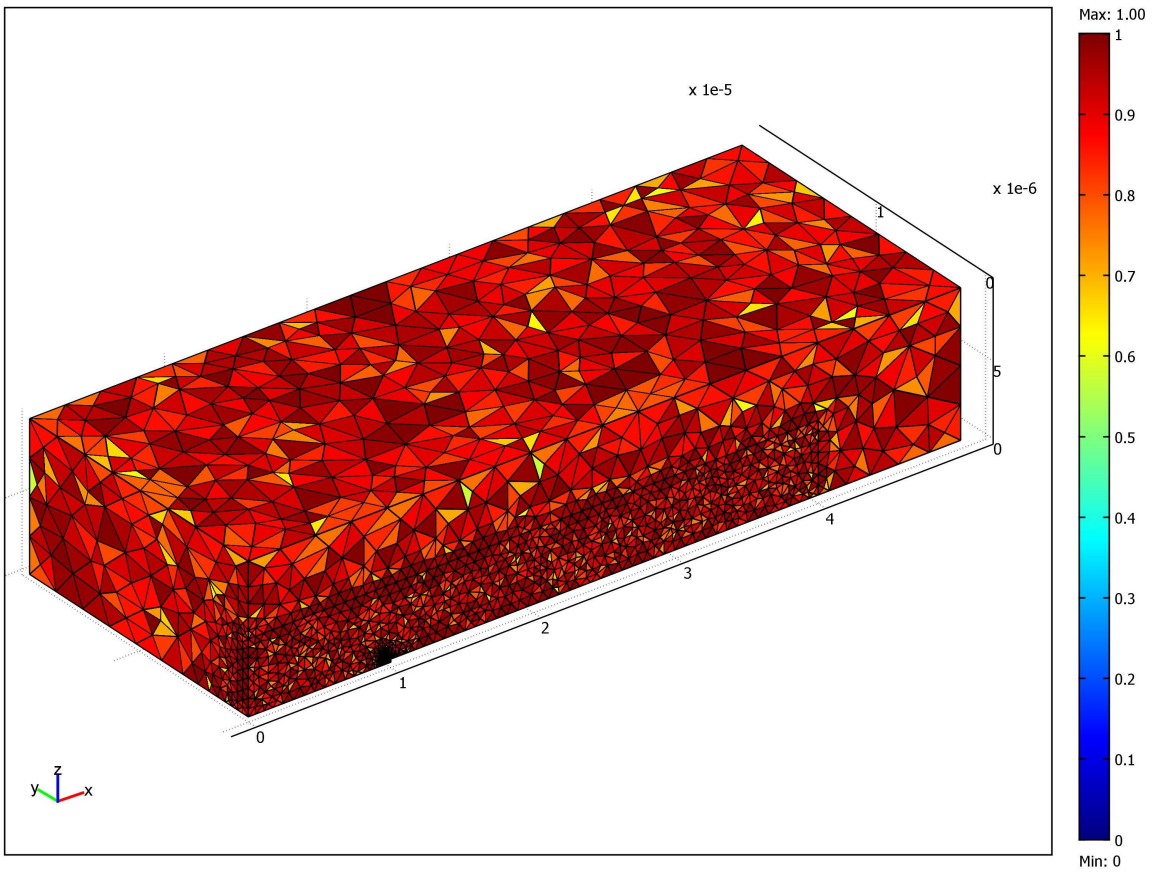

Figure 9.19 Picture showing the mesh of the model used for the DEP simulation with a nanobelt shell structure. The color bar corresponds to mesh element quality. The computational domain is 50 μm long, 20 μm wide, and 10 μm tall.

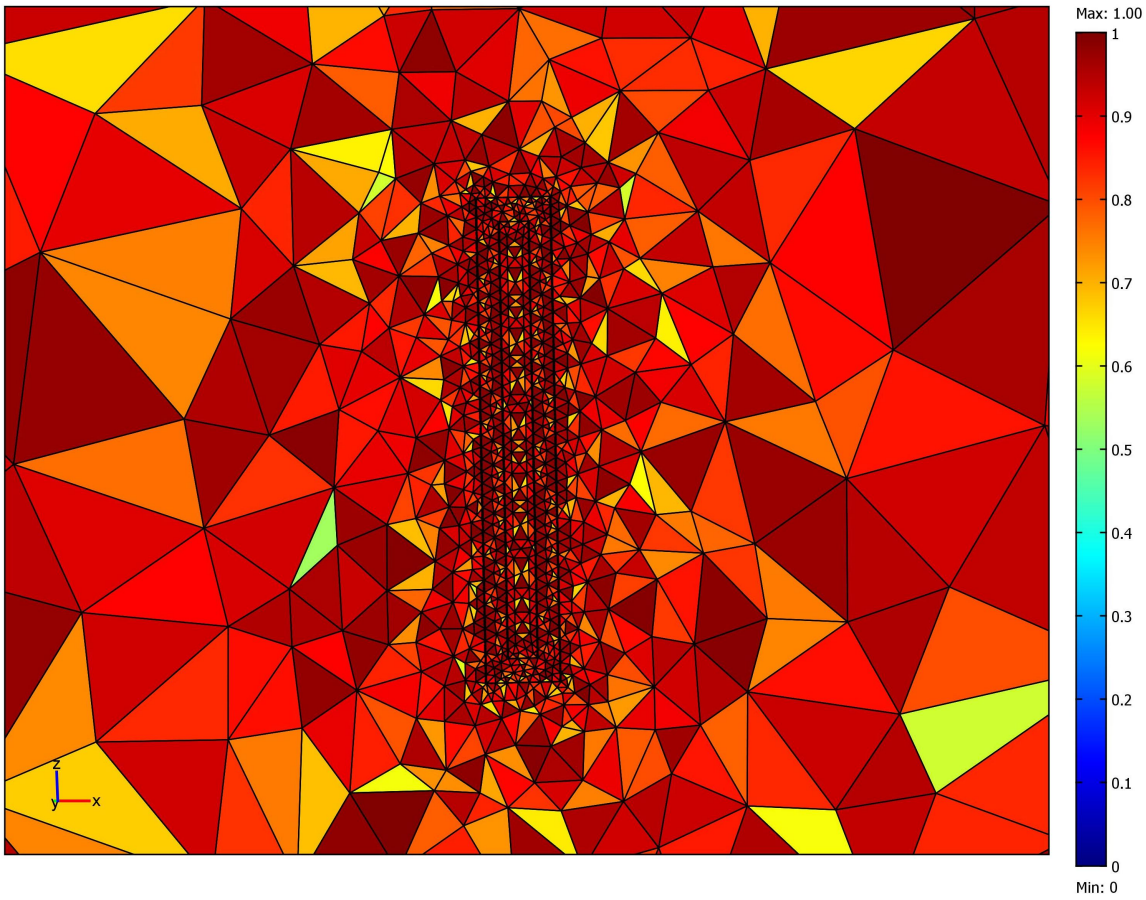

Figure 9.20 A magnified view near the nanobelt showing the fine mesh. The color bar corresponds to mesh element quality. The shell structure is clearly seen.

Figure 9.19 shows the mesh used for the computation. For better control of the mesh size, the domain outside the nanobelt is divided into two parts. The outermost part is meshed with a maximum mesh element length of 2.5 μm and the inner part is meshed with a maximum mesh element length of 0.75 μm. The nanobelt is meshed with a mesh element length of about 5 nm. Figure 9.20 shows a magnified view of the mesh element size distribution near the nanobelt. The thickness (horizontal) of the nanobelt is 50 nm and the width (vertical) is 300 nm.

Figure 9.21 shows an isometric view of the 3D mesh elements of the nanobelt and its adjoining areas. Because of the small mesh element size required to resolve the small

nanobelt, the number of elements in the model can go up rapidly. This is a limiting factor on whether a realistic simulation can be performed with a certain computer system. Also, for performing simulations with higher electrical conductivities in the interior of the nanobelt, a finer mesh is required. Same is the case with low frequency simulations. These are some of the additional factors that can put constraints on the number of elements in the mesh, and hence the simulation that can performed.

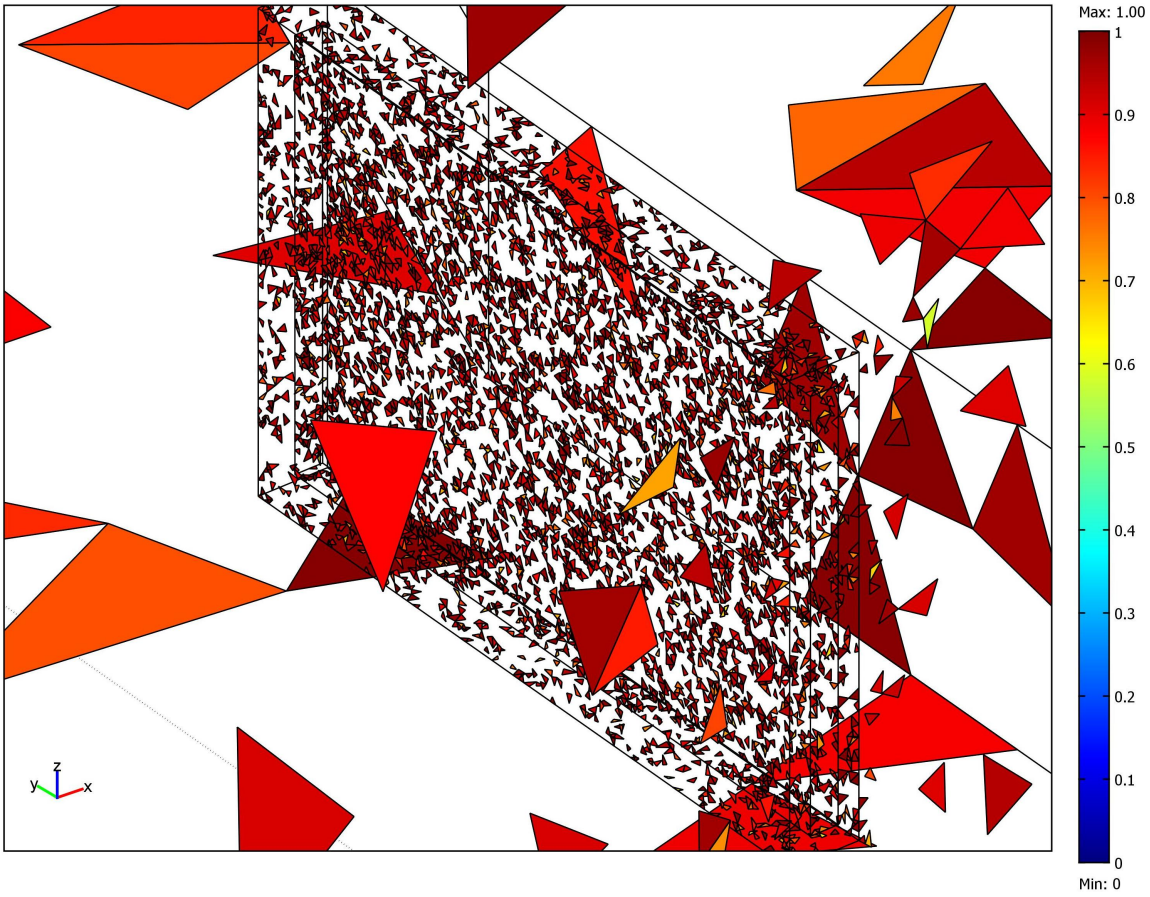

Figure 9.21 A magnified view of the mesh near the nanobelt showing the 3D elements. Only 10 % of the total elements are shown for transparency reasons. The color bar corresponds to mesh element quality.

For a better appreciation of the potential, and the electric field lines, a few sample plots are shown displaying these quantities for $\sigma_3 = \sigma_{nanobelt,bulk} = 0.1$ S/m, at a frequency

of 1 kHz. The other parameters are as mentioned at the beginning of this section. Figure 9.22 shows the color plot of the electric potential in one of the slices, along with 3D electric field lines. Figure 9.23 shows the electric field lines as seen from the top of the model. Figure 9.24 shows the electric field lines passing around and through the nanobelt. Because of the higher electrical conductivity, the fields in the nanobelt interior is quite low, as can be appreciated from the blue color of the lines. In contrast, the field is very high in the outer depleted layer, seen as brown colored lines. In fact, there are discontinuities at the interfaces.

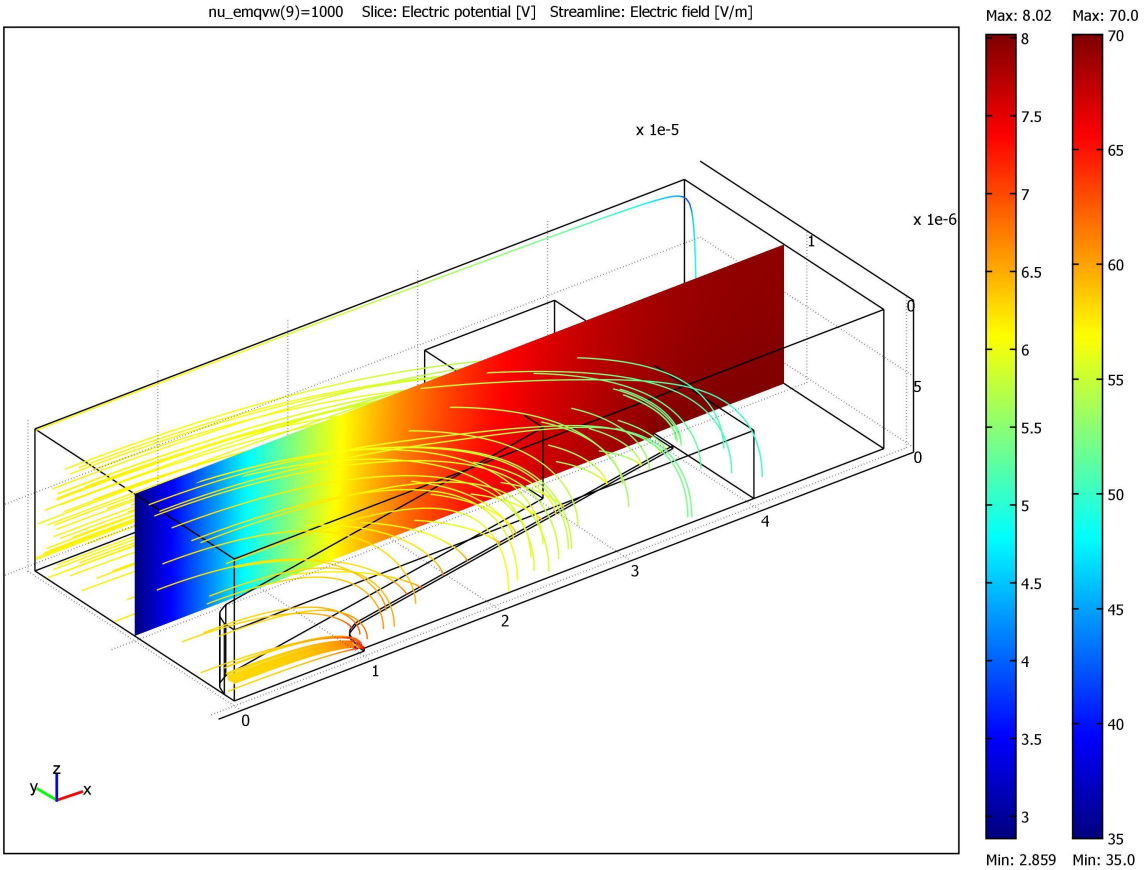

Figure 9.22 Plot showing the electric field (magnitude) lines in the DEP model. The color (left color bar) of the line is determined by the $\log_{10}$ of the electric field magnitude at a particular location through which the line is passing. The vertical color (right color bar) plot shows the electric potential in one of the slices in the model.

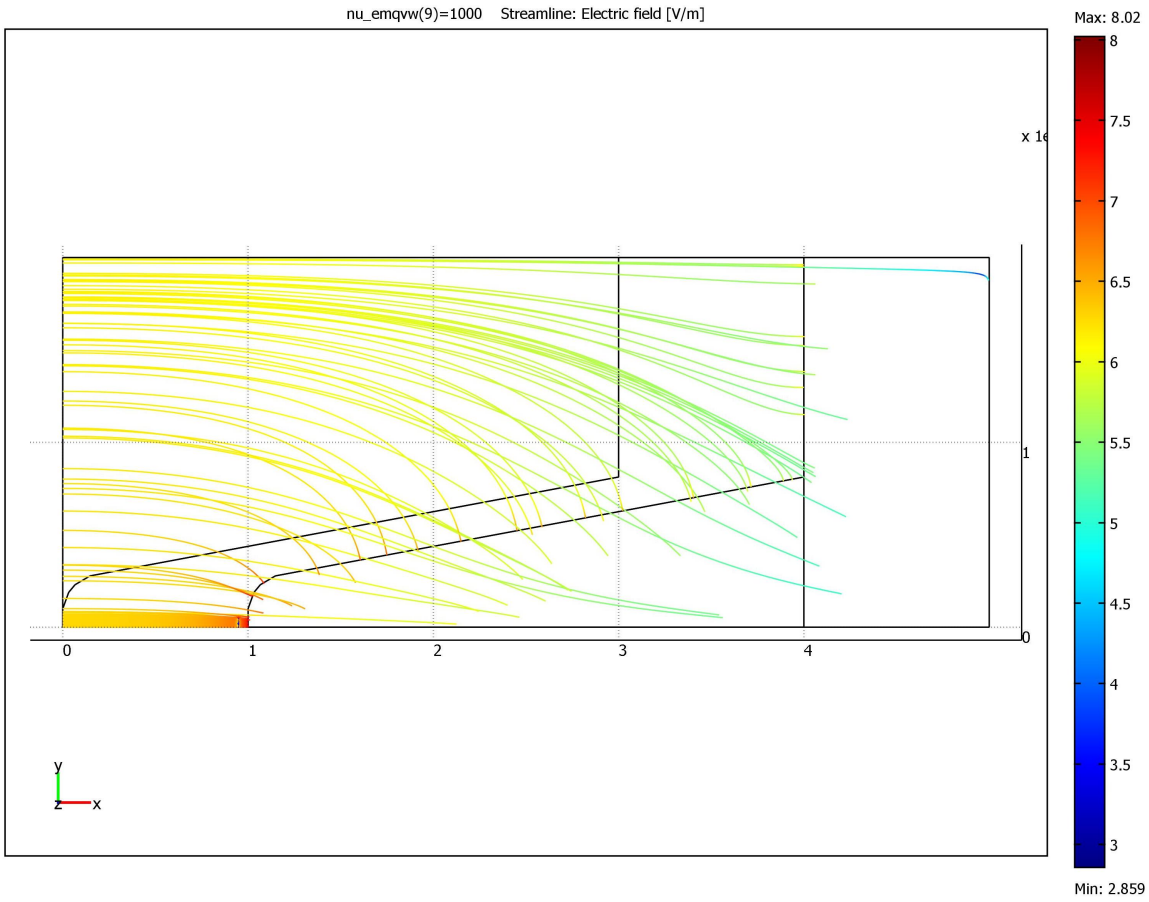

Figure 9.23 Plot showing the electric field (magnitude) lines (top view of model). The color of the line is determined by the $\log_{10}$ of the electric field magnitude at the particular location through which the line is passing. The triangular (bottom) and rectangular (right) area correspond to the electrode. The area in the central region is not an electrode but the domain defined for better mesh size control.

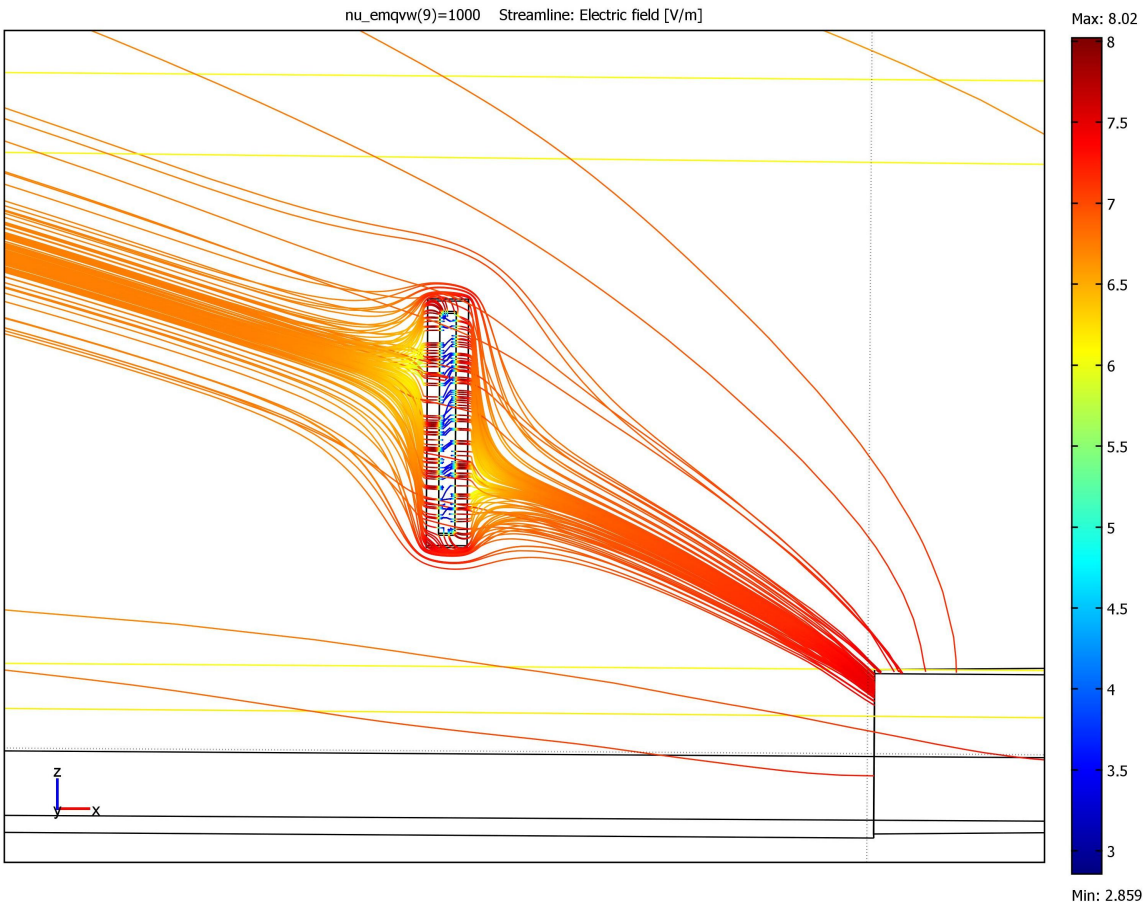

Figure 9.24 Plot showing the electric field (magnitude) lines (side view of model) near the nanobelt and the electrode (right corner). The color of the line is determined by the $\log_{10}$ of the electric field magnitude at the particular location through which the line is passing.

Figure 9.25 shows a line extrusion plot of the electric field magnitude along a straight line in the x direction passing through the nanobelt thickness. This was computed for $\sigma_3 = \sigma_{nanobelt,bulk} = 0.1$ S/m, at a frequency of 10 MHz. The other parameters are as mentioned at the beginning of this section. As mentioned before, there are discontinuities at the interfaces of the conductive nanobelt interior and the outer depleted layer, as well as the interface with the liquid. The depleted regions have high field magnitudes, while the conductive interiors have low fields. For lower frequencies, the electric field peaks are found to be much higher (not shown).

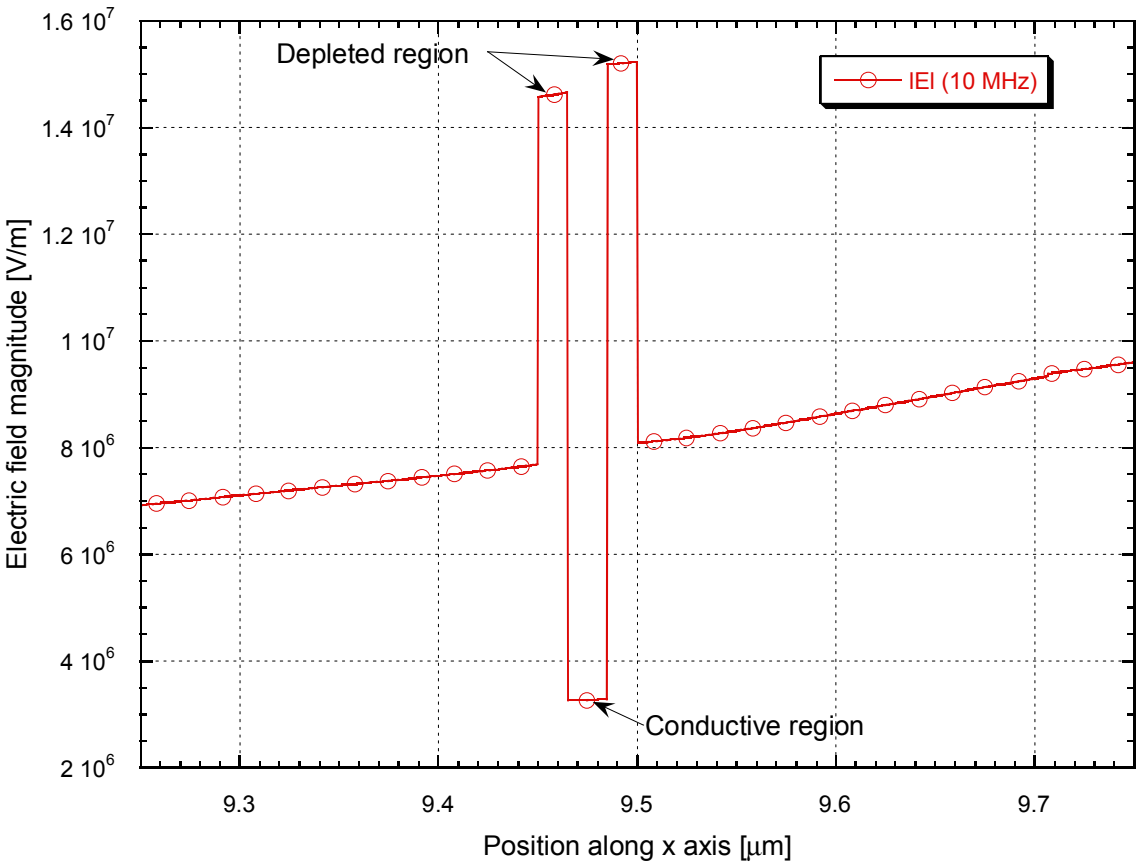

Figure 9.25 A plot of the electric field magnitude along the line y = 0 μm, z = 0.5 μm (x axis direction) showing sudden changes in its value near the nanobelt-liquid medium interfaces, and the nanobelt conductive/depleted region interfaces.

Once the model was solved for its electric potential, electric fields could be computed easily. Using the electric fields on the outer surface of the nanobelt, the DEP force was computed by applying the MST methodology. Figure 9.26 shows the x component of the DEP force (F_x) on the nanobelt as a function of frequency for 4 different interior bulk conductivities of the nanobelt. It is observed that for low conductivity values, F_x is always negative. But as the conductivity value increases, F_x changes sign in the high frequency range and becomes positive. This explains the experimentally observed DEP results qualitatively. Hence, it is possible to have both positive and negative DEP in a shell type nanobelt model for certain conductivities. For a

different orientation of the nanobelt, similar results are observed, but with subtle differences. It turns out that the orientation of the nanobelt with respect to the electrode is very important in determining what type of DEP characteristics will be observed. Figure 9.27 shows all the three components and the total magnitude of the DEP force on the nanobelt for a nanobelt interior conductivity value of 0.1 S/m.

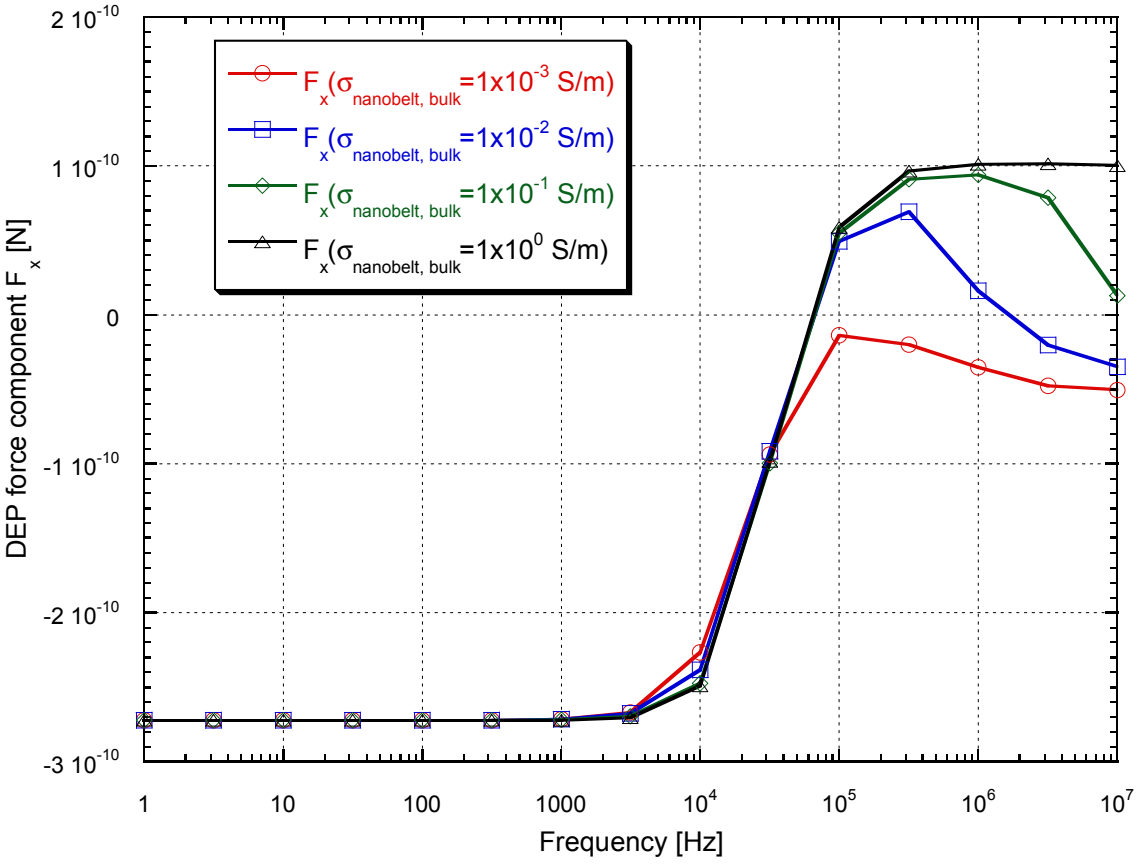

Figure 9.26 Plot showing the x component of the DEP force for a nanobelt with a 15 nm depletion layer and different interior conductivities.

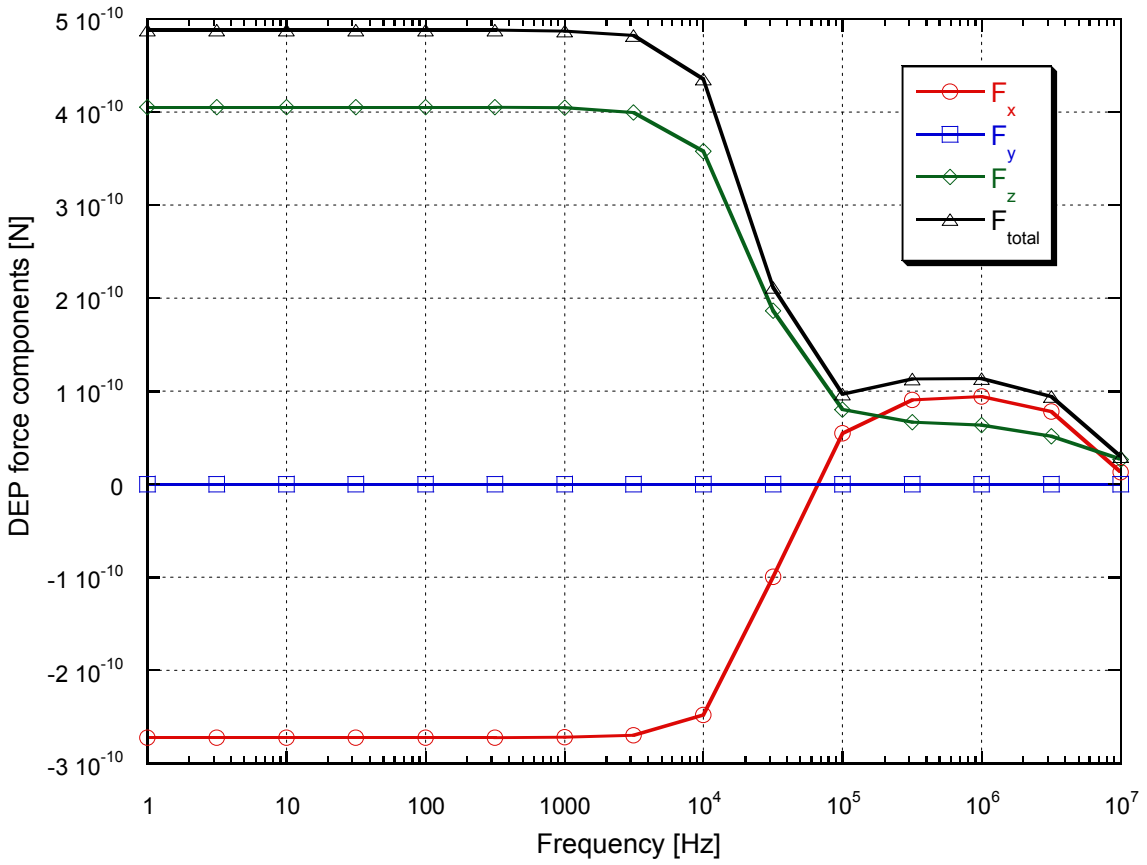

Figure 9.27 Plot showing the DEP force components for a nanobelt with a 15 nm depletion layer and interior conductivity of 0.1 S/m.

9.3.7 Order of Magnitude Calculation for Nanobelt Deflection

In the DEP experiments on single nanobelts discussed in Chapter 4, deformation of the nanobelts was observed. To check if the computed DEP forces are reasonable, and can cause those deflections, performing an order of magnitude calculation will be found useful. For that, one has to estimate the possible deflection that a nanobelt can undergo under typical DEP force magnitudes (~ 10^{-10} N), that were predicted by the simulations. Let us consider a cantilever with three different types of loadings, as shown in Figure 9.28.

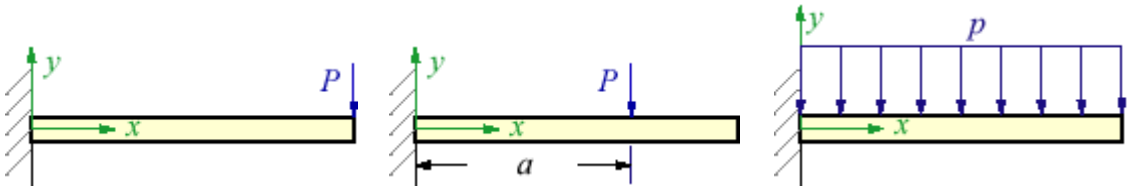

Figure 9.28 Schematics showing three different types of loading on a cantilever.

The expressions for the displacement (w) of the cantilever subjected to the different loading conditions are as follows.

Cantilever with end loading of force P

$$w(x) = -\frac{Px^2(3L - x)}{6EI} \tag{9-19}$$

$$w_{\max} = w(L) = -\frac{PL^3}{3EI} \tag{9-20}$$

Cantilever with intermediate load at $x = a$ of force P

$$w(x) = \begin{cases} -\dfrac{Px^2(3a - x)}{6EI}, & 0 \le x \le a \\ -\dfrac{Pa^2(3x - a)}{6EI}, & a \le x \le L \end{cases} \tag{9-21}$$

$$w_{\max} = w(L) = -\frac{Pa^2}{6EI}(3L - a) \tag{9-22}$$

Cantilever with uniform distribution of force per unit length p

$$w(x) = -\frac{px^2(6L^2 - 4xL + x^2)}{24EI} \tag{9-23}$$

$$w_{\max} = w(L) = -\frac{pL^4}{8EI} \tag{9-24}$$

The moment of inertia for a rectangular cross section with thickness t, and breadth b, is given by

$$I = \frac{bt^3}{12} \tag{9-25}$$

The above expressions can be used for finding an order of magnitude number for the deflection of a nanobelt. Let us consider a nanobelt, with the applied force perpendicular to the wide flat surface. Let the dimensions of the nanobelt be, length L = 50 μm, breadth b = 300 nm, and thickness t = 50 nm.

The indentation modulus of $(10\bar{1})$ oriented SnO_2 nanobelts have been measured and found to be 66 ± 10 GPa.[103, 104] If this number (66 GPa) is used in the expression for the displacement of a cantilever with end loading of force $P = 1.0\times10^{-10}$ N, the maximum displacement is found to be $w_{\max} \approx 20$ μm. This is a quite large deformation. So, the forces calculated from the simulations are quite reasonable to produce nanobelt deformations observed in the experiments (Figure 4.15 of Chapter 4).

9.4 SUMMARY OF RESULTS

The following table summarizes the major simulations performed by varying the different parameters, and the observations that were made from the exercise.

Table 9-1 Summary of the DEP simulations.

DEP simulations with different parameters	Observations
DEP of a spherical particle calculated using dipole approximation method and MST method, with the following parameters: $\varepsilon_p = 12\varepsilon_0$, $\sigma_p = 0$ to 0.1 S/m in steps of 0.01 S/m, $\varepsilon_m = 24\varepsilon_0$, $\sigma_m = 0$ S/m, V = 70 V_{peak}.	Both methods predicted comparable DEP forces for wide range of conductivities and frequencies. At higher frequencies there is some deviation.
DEP simulation of nanobelt conducted using the following parameters: $\varepsilon_{nanobelt} = 12\varepsilon_0$, $\sigma_{nanobelt} =$	Demonstrated that negative DEP in the nanobelt is possible if there is a

2×10^{-5} S/m, 1.74×10^{-4} S/m, and 1.0×10^{-2} S/m, $\varepsilon_{ethanol} = 24\varepsilon_0$, $\sigma_{ethanol} = 1.74\times10^{-4}$ S/m, V = 70 V_{peak}.	decrease in the nanobelt conductivity as a whole. However, positive DEP was not observed at high frequencies.
The change of the DEP force on the nanobelt as a function of height change was studied using the following parameters: $\varepsilon_{nanobelt} = 12\varepsilon_0$, $\sigma_{nanobelt} = 2\times10^{-5}$ S/m, $\varepsilon_{ethanol} = 24\varepsilon_0$, $\sigma_{ethanol} = 1.74\times10^{-4}$ S/m, V = 70 V_{peak}.	The DEP force falls rapidly with height from the electrode surface.
The change of the DEP force on the nanobelt as a function of angle (about x axis) change was studied using the following parameters: $\varepsilon_{nanobelt} = 12\varepsilon_0$, $\sigma_{nanobelt} = 2\times10^{-5}$ S/m, $\varepsilon_{ethanol} = 24\varepsilon_0$, $\sigma_{ethanol} = 1.74\times10^{-4}$ S/m, V = 70 V_{peak}.	The DEP force falls gradually as the angle increased, since one of the nanobelt ends started moving farther away from the electrode edge.
Comparison of shell model and MST was performed for a spherical particle with the following parameters: $\varepsilon_3 = \varepsilon_{nanobelt,bulk} = 12\varepsilon_0$, $\sigma_3 = \sigma_{nanobelt,bulk} = 0.01$ S/m, $\varepsilon_2 = \varepsilon_{nanobelt,layer} = 12\varepsilon_0$, $\sigma_2 = \sigma_{nanobelt,layer} = 0$ S/m, $\varepsilon_1 = \varepsilon_{ethanol} = 24\varepsilon_0$, $\sigma_1 = \sigma_{ethanol} = 1.74\times10^{-4}$ S/m, and R_o/R_i = 500 nm/200 nm, and 500 nm/300 nm, V = 70 V_{peak}.	The approximate shell model and the MST method provided good agreement. Some deviation was observed in the high frequency range. From this calculation it was found that if the inner conductive sphere size is gradually increased, the high frequency range DEP force will ultimately become positive.
Simulation with the nanobelt as a shell structure was performed using the following parameters: $\varepsilon_3 = \varepsilon_{nanobelt,bulk} = 12\varepsilon_0$, $\sigma_3 = \sigma_{nanobelt,bulk} = 0.001$ to 1.0 S/m, $\varepsilon_2 = \varepsilon_{nanobelt,layer} = 12\varepsilon_0$, $\sigma_2 = \sigma_{nanobelt,layer} = 0$ S/m, $\varepsilon_1 = \varepsilon_{ethanol} = 24\varepsilon_0$, $\sigma_1 = \sigma_{ethanol} = 1.74\times10^{-4}$ S/m, depletion thickness of 15 nm, V = 70 V_{peak}.	It was found that as the conductivity of the nanobelt interior was increased, the DEP force changed from negative to positive in the high frequency range. In the low frequency range, the force is always negative. This situation is similar to the experimental observations.

From the simulation results one can make a reasonable argument that the presence of a depletion (non-conductive) layer on the nanobelt outer surface can explain the unusual negative DEP effect observed with SnO_2 nanobelts suspended in ethanol. While many parameters are not accurately know, order of magnitude and assumed numbers

were used in the simulations to obtain a qualitative understanding of the factors that can influence the DEP forces on the nanobelts. The simulation results are consistent with the hypothesis for explaining negative DEP in SnO_2 nanobelts. The DEP force on a nanobelt depends strongly on the position and orientation, e.g., whether the flat side is horizontal or vertical or in some intermediate angle. In conclusion, this work will develop a fundamental understanding of the importance of surface dominant properties on AC dielectrophoresis applied to nanostructures. Finally, using bulk properties in nanostructures can give misleading results.

CHAPTER 10

CONCLUSIONS

10.1 SUMMARY

The goal of this research was to study fluidic and electric manipulation techniques applied to SnO_2 nanobelts suspended in a liquid medium, and to understand the different aspects affecting this process. In summary, the following are the major accomplishments achieved in this research.

1) Demonstrated manipulation of semiconducting metal oxide nanobelts using AC dielectrophoresis (DEP), for the first time. DEP trapping of SnO_2 nanobelts between microelectrodes resulted in the fabrication of single and multiple nanobelt based devices.
2) Characterized the nanobelt devices, which may be used as nanosensors for detection of gases, such as NO_2, NH_3, etc.
3) Devised an innovative experimental setup, and conducted detailed investigation of the DEP phenomenon in SnO_2 nanobelts (suspended in ethanol) under AC electric fields (produced using microelectrodes in microchannels) of wide frequency range (Hz to MHz). Direct observations with a high magnification inverted microscope revealed a wide variety of nanobelt motions. An approximate estimate of the relative DEP force and torque magnitudes in the low frequency range (< 100 kHz) was also obtained.

4) Studies with DC and low frequency AC fields in a parallel plate electrode configuration indicated the presence of electrophoretic effects in the nanobelts. Hence, the low frequency (~ Hz) response observed in the DEP electrodes could have an electrophoretic component in addition to the DEP induced forces.
5) Investigated microfluidic alignment technique on SnO_2 nanobelts, which allowed the fabrication of single nanobelt devices. SnO_2 nanobelts were suspended in ethanol and introduced into a microchannel placed over an electrode array.
6) Performed impedance spectroscopy measurements on the nanobelt devices to estimate the nanobelt electrical properties, and also to measure the electrical conductivity of the suspending liquid.
7) Proposed explanations for the experimentally observed DEP characteristics.
8) Performed full 3D DEP simulations using COMSOL Multiphysics software package to verify qualitatively the proposed explanation for the experimentally observed DEP characteristics, complement the experimental observations, and gain additional insights on the DEP phenomenon in SnO_2 nanobelts.

The important understanding that has been realized as a result of this research is the following. In DEP, the orientation of the nanobelt near the electrode has a strong effect on the electric polarization and hence the generated DEP forces and torques. Also, because of the "thin" nature of the nanobelts, to generate large electric field gradients in the medium large potentials on the electrodes are required. Only then significant DEP forces can be induced, and motion of the nanobelts in real-time can be observed. Another aspect is that, because nanostructures have large surface area, using bulk properties to understand the DEP phenomenon will not be accurate. Surface dominant properties have

to be considered. Finally, because of the peculiar shape and aspect ratios of nanobelts, their nanomanipulation has more complexity and more aspects to it than say cylindrical nanowires.

10.2 Recommendations for Future Work

The literature on dielectrophoresis and manipulation techniques on long nanostructures are limited. There is future scope for study and research in this direction. While dielectrophoretic manipulation of nanostructures has potential for automation in the future, to use it for precise alignment and placement of nano-objects on predefined locations, and fabrication of nanodevices, a lot of work still needs to be done. Some of the aspects for future work are listed below.

1) Other techniques such as traveling wave dielectrophoresis [6], electrorotation [6], etc., will be found useful in nanomanipulation of semiconducting nanowires/nanobelts in addition to the AC dielectrophoresis that has been demonstrated in the present work. Building single nanobelt/nanowire devices will require improved electrode design to obtain optimum field distribution and better manipulation. In addition, control of the concentration of the nano-objects in the suspending fluid (so that a fewer number of nano-objects come near the electrodes) will also be found useful in achieving this goal.
2) Investigation of the origin of the surface charge on the nanobelts, while suspended in a liquid medium, and the role of the medium, if any, is an important aspect. In the current research the possible reasons for the surface charge have been discussed. The contribution to depletion caused by adsorption of oxygen and

other molecules/ions on the nanobelt surface at room temperatures, before the nanobelt is suspended in a liquid medium needs to be estimated, as well.

3) Investigation of the dielectric properties of nano-objects as a function of frequency, while being suspended in a liquid medium, will be an interesting study.

4) While direct visualization of the nanobelts using an optical microscope was possible in this research, it has limitations. For more effective visualization, other schemes of visualization would be of interest, such as fluorescence based. There are many challenges in this area, the chemical functionalization of metal oxide surfaces with fluorescent molecules or quantum dots being one of them. Studies in this area will be of great interest.

5) Brownian motion was not observed in the experiments with the current setup. The reason may be that the CCD camera used in the experiments is not fast enough. Study of the Brownian motion using a much faster camera will be useful in obtaining data on its effects on long nanostructures. There are very limited data on such structures, since the current literature on Brownian motion is mostly concentrated on particles.

6) In the current work, the 3D simulations of the nanobelt DEP was limited by the necessity of a very large number of mesh elements in the mesh, because the nanobelt is so small compared to the other domains in the simulation space. A more powerful computer system with faster processor and larger memories will be required for performing a more complete simulation study. That will allow the computation of the trajectory of the nanobelt with time, which requires

calculation of the DEP force according to position and time, and inclusion of the effect of fluid drag, gravity, and possibly also Brownian motions. The deformation of the nanobelt can also be studied. It is desirable to use direct solvers instead of the currently used iterative solvers, because iterative solvers do not converge for all parameter values selected for a particular simulation. However, direct solvers require larger memories.

REFERENCES

[1] Z. W. Pan, Z. R. Dai, and Z. L. Wang, "Nanobelts of semiconducting oxides", *Science*, vol. 291, no. 5510, pp. 1947-1949, 2001.

[2] E. Comini, G. Faglia, G. Sberveglieri, Z. Pan, and Z. L. Wang, "Stable and highly sensitive gas sensors based on semiconducting oxide nanobelts", *Applied Physics Letters*, vol. 81, no. 10, pp. 1869-1872, 2002.

[3] E. Comini, G. Faglia, G. Sberveglieri, D. Calestani, L. Zanotti, and M. Zha, "Tin oxide nanobelts electrical and sensing properties", *Sensors and Actuators B: Chemical*, vol. 111-112, pp. 2-6, 2005.

[4] M. Arnold, P. Avouris, Z.W. Pan, and Z.L. Wang, "Field-effect transistors based on single semiconducting oxide nanobelts", *Journal of Physical Chemistry B*, vol. 107, no. 3, pp. 659-663, 2003.

[5] H. A. Pohl, *Dielectrophoresis*, Cambridge University Press, Cambridge, UK, 1978.

[6] H. Morgan, and N. G. Green, *AC Electrokinetic: Colloids and Nanoparticles* (Microtechnologies and Microsystems Series), Research Studies Press, Baldock, Hertfordshire, UK, 2003.

[7] O. O. Biest, and L. J. Vandeperre, "Electrophoretic deposition of materials", *Annual Review of Materials Science*, vol. 29, pp. 327-352, 1999.

[8] P. Feng, Q. Wan, X. Q. Fu, T. H. Wang, and Y. Tian, "Anomalous electrorheological behavior of ZnO nanowires", *Applied Physics Letters*, vol. 87, iss. 3, pp. 33114-1-3, 2005.

[9] M. S. Kumar, S. H. Lee, T. Y., Kim, T. H. Kim, S. M. Song, J. W. Yang, K. S. Nahm, and E. K, Suh, "DC electric field assisted alignment of carbon nanotubes on metal electrodes", *Solid State Electronics*, vol. 47, pp. 2075-2080, 2003.

[10] M. Ploscaru, A. Mrzel, D. Vrbanic, P. Umek, M. Uplaznik, B. Podobnik, D. Mihailovic, D. Vengust, V. Nemanic, M. Zumer, and B. Zajec, "Isolation, positioning and manipulation of $Mo_6S_3I_6$ by (di)electrophoresis", *AIP Conference Proceedings*, vol. 723, iss. 1, pp. 435-438, 2004.

[11] B. Brown, D. Hess, V. Desai, and M. J. Deen, "Dielectric science and technology", The Electrochemical Society *Interface*, vol. 15, no. 1, pp. 28-31, 2006.

[12] R. Tobazéon, "Electrohydrodynamic behaviour of single spherical or cylindrical conducting particles in an insulating liquid subjected to a uniform DC field", *Journal of Physics D: Applied Physics*, vol. 29, iss. 10, pp. 2595-2608, 1996.

[13] C. Choi, K. Yatsuzuka, and K. Asano, "Dynamic motion of a conductive particle in viscous fluid under DC electric field", *IEEE Transactions on Industry Applications*, vol. 37, iss. 3, pp. 785-791, 2001.

[14] T. Itoh, S. Masuda, and F. Gomi, "Electrostatic orientation of ceramic short fibers in liquid", *Journal of Electrostatics*, vol. 32, iss. 1, pp. 71-89, 1994.

[15] G. Molinari, and A. Viviani, "Experimental results and computer simulation of impurity particles motion in n-hexane under DC and AC conditions", *Journal of Electrostatics*, vol. 5, pp. 355-367, 1978.

[16] R. Bozzo, P. Girdinio, F. Lazzeri, and A. Viviani, "Parameter identification for a model of impurity particle motion in a dielectric fluid", *IEEE Transactions on Electrical Insulation*, vol. 20, iss. 2, pp. 389-393, 1985.

[17] S. Masuda, and T. Itoh, "Electrostatic means for fabrication of fiber-reinforced metals", *IEEE Transactions on Industry Applications*, vol. 25, iss. 3, pp. 552-557, 1989.

[18] A. Hozumi, T. Itoh, Y. Yokogawa, and T. Kameyama, "Preparation of unidirectionally aligned hollow TiO_2 fibers using electrostatically assembled short organic fibers", *Journal of Materials Science Letters*, vol. 21, no. 11, pp. 897-900, 2002.

[19] J. C. Lin, M. Z. Yates, A. T. Petkoska, and S. Jacobs, "Electric-field-driven assembly of oriented molecular-sieve films", *Advanced Materials*, vol. 16, no. 21, pp. 1944-1948, 2004.

[20] R. Pethig, *Dielectric and Electronic Properties of Biological Materials*, John Wiley & Sons, Chichester, UK, 1979.

[21] P. J. Burke, "Nanodielectrophoresis: electronic nanotweezers", in *Encyclopedia of Nanoscience and Nanotechnology*, Ed. H. S. Nalwa, vol. 6, pp. 623-641, American Scientific Publishers, Stevenson Ranch, CA, USA, 2004.

[22] K. H, Kang, Y. Kang, X. Xuan, and D. Li, "Continuous separation of microparticles by size with direct current-dielectrophoresis", *Electrophoresis*, vol. 27, iss. 3, pp. 694-702, 2006.

[23] Y. Huang, X. B. Wang, J. A. Tame, and R. Pethig, "Electrokinetic behaviour of colloidal particles in travelling electric fields: studies using yeast cells", *Journal of Physics D: Applied Physics*, vol. 26, pp. 1528-1535, 1993.

[24] H. Morgan, N. G. Green, M. P. Hughes, W. Monaghan, and T. C. Tan, "Large-area travelling-wave dielectrophoresis particle separator", *Journal of Micromechanics and Microengineering*, vol. 7, pp. 65-70, 1997.

[25] M. S. Talary, J. P. H. Burt, J. A. Tame, and R. Pethig, "Electromanipulation and separation of cells using travelling electric fields", *Journal of Physics D: Applied Physics* , vol. 29, iss. 8, pp. 2198-2203, 1996.

[26] A. T. Kadaksham, P. Singh, and N. Aubry, "Dielectrophoresis of nanoparticles", *Electrophoresis*, vol. 25, iss. 21-22, pp. 3625-3632, 2004.

[27] R. Kretschmer, and W. Fritzsche, "Pearl chain formation of nanoparticles in microelectrode gaps by dielectrophoresis", *Langmuir*, vol. 20, iss. 26, pp. 11797-11801, 2004.

[28] H. Morgan, and N. G. Green, "Dielectrophoretic manipulation of rod-shaped viral particles", *Journal of Electrostatics*, vol. 42, iss. 3, pp. 279-293, 1997.

[29] T. B. Jones, *Electromechanics of Particles*, Cambridge University Press, Cambridge, UK, 1995.

[30] J. J. Boote, and S. D. Evans, "Dielectrophoretic manipulation and electrical characterization of gold nanowires", *Nanotechnology*, vol. 16, pp. 1500-1505, 2005.

[31] A. Motayed, M. He, A. V. Davydov, J. Melngailis, and S. N. Mohammad, "Simple model for dielectrophoretic alignment of gallium nitride nanowires", *Journal of Vacuum Science and Technology B: Microelectronics and Nanometer Structures*, vol. 25, iss. 1, pp. 120-123, 2007.

[32] W. Xujing, X. B. Wang, and P. R. C. Gascoyne, "General expressions for dielectrophoretic force and electrorotational torque derived using the Maxwell stress tensor method", *Journal of Electrostatics*, vol. 39, iss., pp. 277-295, 1997.

[33] J. Voldman, "Electrical forces for microscale cell manipulation", *Annual Review of Biomedical Engineering*, vol. 8, pp. 425-454, 2006.

[34] P. A. Smith, C. D. Nordquist, T. N. Jackson, T. S. Mayer, B. R. Martin, J. Mbindyo, and T. E. Mallouk, "Electric-field assisted assembly and alignment of metallic nanowires", *Applied Physics Letters*, vol. 77, iss. 9, pp. 1399-1401, 2000.

[35] K. Yamamoto, S. Akita, and Y. Nakayama, "Orientation and purification of carbon nanotubes using AC electrophoresis," *Journal of Physics D: Applied Physics*, vol. 31, no. 8, pp. L34-L36, 1998.

[36] K. Yamamoto, S. Akita, and Y. Nakayama, "Orientation of carbon nanotubes using electrophoresis", *Japanese Journal of Applied Physics*, vol. 35, part 2, no. 7B, pp. L917-L918, 1996.

[37] X. Q. Chen, T. Saito, H. Yamada, and K. Matsushige, "Aligning single-wall carbon nanotubes with an alternating-current electric field", *Applied Physics Letters*, vol. 78, no. 23, pp. 3714-3716, 2001.

[38] R. Krupke, F. Hennrich, H. B. Beckmann, O. Hampe, S. Malik, M. M. Kappes, and H. V. Lohneysen "Contacting single bundles of carbon nanotubes with alternating electric fields", *Applied Physics A: Materials Science and Processing*, vol. 76, pp. 397-400, 2003.

[39] J. Chung, and J. Lee, "Nanoscale gap fabrication and integration of carbon nanotubes by micromachining", *Sensors and Actuators A: Physical*, vol. 104, pp. 229-235, 2003.

[40] L. A. Nagahara, I. Amlani, J. Lewenstein, and R. K. Tsui, "Directed placement of suspended carbon nanotubes for nanometer-scale assembly", *Applied Physics Letters*, vol. 80, no. 20, pp. 3826-3828, 2002.

[41] J. Suehiro, G. Zhou, and M. Hara, "Fabrication of a carbon nanotubes-based gas sensor using dielectrophoresis and its application for ammonia detection by impedance spectroscopy", *Journal of Physics D: Applied Physics*, vol. 36, no. 21, pp. L109-L114, 2003.

[42] X. Duan, Y. Huang, Y. Cui, J. Wang, and C. M. Lieber, "Indium phosphide nanowires as building blocks for nanoscale electronic and optoelectronic devices", *Nature*, vol. 409, pp. 66-69, 2001.

[43] S. Kumar, S. Rajaraman, R. A. Gerhardt, Z. L. Wang, and P. J. Hesketh, "Tin oxide nanosensor fabrication using AC dielectrophoretic manipulation of nanobelts", *Electrochimica Acta*, vol. 51, pp. 943-951, 2005.

[44] D. Wang, R. Zhu, Z. Zhou, and X. Ye, "Controlled assembly of zinc oxide nanowires using dielectrophoresis", *Applied Physics Letters*, vol. 90, iss. 10, pp. 103110-1-3, 2007.

[45] L. F. Dong, J. Bush, V. Chirayos, R. Solanki, and J. Jiao, "Dielectrophoretically controlled fabrication of single-crystal nickel silicide nanowire interconnects", *Nano Letters*, vol. 5, no. 10, pp. 2112-2115, 2005.

[46] D. L. Fan, F. Q. Zhu, R. C. Cammarata, and C. L. Chien, "Manipulation of nanowires in suspension by AC electric fields", *Applied Physics Letters*, vol. 85, no. 18, pp. 4175-4177, 2004.

[47] A. D. Wissner-Gross, "Dielectrophoretic reconfiguration of nanowire interconnects", *Nanotechnology*, vol. 17, iss. 19, pp. 4986-4990, 2006.

[48] S. J. Papadakis, Z. Gu, and D. H. Gracias, "Dielectrophoretic assembly of reversible and irreversible metal nanowire networks and vertically aligned arrays", *Applied Physics Letters*, vol. 88, 233118-1-3, 2006.

[49] R. J. Hamers, J. D. Beck, M. A. Eriksson, B. Li, M. S. Marcus, L. Shang, J. Simmons, and J. A. Streifer, "Electrically directed assembly and detection of nanowire bridges in aqueous media", *Nanotechnology*, vol. 17, iss. 11, pp. S280-S286, 2006.

[50] M. S., Marcus, L. Shang, B. Li, J. A. Streifer, J. D. Beck, E. Perkins, M. A. Eriksson, and R. J. Hamers, "Dielectrophoretic manipulation and real-time electrical detection of single-nanowire bridges in aqueous saline solutions, *Small*, vol. 3, no. 9, pp. 1610-1617, 2007.

[51] Y. Huang, X. Duan, Q. Wei, and C. M. Lieber, "Directed assembly of one-dimensional nanostructures into functional networks", *Science*, vol. 291, pp. 630-633, 2001.

[52] Y. H. Yan, S. Li, L. Q. Chen, M. B. Chan-Park, and Q. Zhang, "Large-scale submicron horizontally aligned single-walled carbon nanotube surface arrays on various substrates produced by a fluidic assembly method", *Nanotechnology*, vol. 17, iss. 22, pp. 5696-5701, 2006.

[53] S. Li, N. Liu, M. B. Chan-Park, Y. Yan, and Q. Zhang, "Aligned single-walled carbon nanotube patterns with nanoscale width, micron-scale length and controllable pitch", *Nanotechnology*, vol. 18, iss. 45, pp. 455302-1-7, 2007.

[54] J. Q. Li, Q. Zhang, Y. H. Yan, S. Li, and L. Q. Chen, "Fabrication of carbon nanotube field-effect transistors by fluidic alignment technique", *IEEE Transactions on Nanotechnology*, vol. 6, no. 4, pp. 481-484, 2007.

[55] J. Im, M. Lee, S. Myung, L. Huang, S. G. Rao, D. J. Lee, J. Koh, and S. Hong, "Directed-assembly of single-walled carbon nanotubes using self-assembled monolayer patterns comprising conjugated molecular wires", *Nanotechnology*, vol. 17, iss. 14, pp. 3569-3573, 2006.

[56] N. Mahajan, and J. Y. Fang, "Two-dimensional ordered arrays of aligned lipid tubules on substrates with microfluidic networks", *Langmuir*, vol. 21, iss. 7, pp. 3153-3157, 2005.

[57] P. F. Jacobs, *Stereolithography and Other RP&M Technologies: From Rapid Prototyping to Rapid Tooling*, ASME Press, New York, NY, USA, 1996.

[58] Z. R. Dai, Z. W. Pan, and Z. L. Wang, "Novel nanostructures of functional oxides synthesized by thermal evaporation", *Advanced Functional Materials*, vol. 13, iss. 1, pp. 9-24, 2003.

[59] E. Comini, V. Guidi, C. Malagù, G. Martinelli, Z. Pan, G. Sberveglieri, and Z. L. Wang, "Electrical properties of tin dioxide two-dimensional nanostructures", *Journal of Physical Chemistry B*, vol. 108, iss. 6, pp. 1882-1887, 2004.

[60] G. Martinelli, and M. C. Carotta, "Thick-film gas sensors", *Sensors and Actuators B: Chemical*, vol. 23, no. 2, pp. 157-161, 1995.

[61] S. Mathur, S. Barth, H. Shen, J. C. Pyun, and U. Werner, "Size-dependent photoconductance in SnO_2 nanowires", *Small*, vol. 1, iss. 7, pp. 713-717, 2005.

[62] S. Luo, J. Fan, W. Liu, M. Zhang, Z. Song, C. Lin, X. Wu, and P. K. Chu, "Synthesis and low-temperature photoluminescence properties of SnO_2 nanowires and nanobelts", *Nanotechnology*, vol. 17, pp. 1695-1699, 2006.

[63] N. Kroger, M. B. Dickerson, G. Ahmad, Y. Cai, M. S. Haluska, K. H. Sandhage, N. Poulsen, and V. C. Sheppard, "Bio-enabled synthesis of rutile (TiO_2) at ambient temperature and neutral pH," *Angewandte Chemie International Edition*, vol. 45, pp. 7239-7243, 2006.

[64] T. C. Pearce, S. S. Schiffman, H. T. Nagle, and J. W. Gardner, *Handbook of Machine Olfaction-Electronic Nose Technology,* Wiley-VCH, Weinheim, Germany, 2003.

[65] S. R. Morrison, *The Chemical Physics of Surfaces*, Plenum Press, New York, NY, USA, 1978.

[66] S. C. Chang, and D. B. Hicks, "Tin oxide microsensors," *Digest of Technical Papers, TRANSDUCERS'85: The 3rd IEEE International Conference on Solid State Sensors and Actuators*, pp. 381-384, 1985.

[67] A. Köhler, "A new system of illumination for photomicrographic purposes", in *Köhler Illumination Centenary*, Royal Microscopical Society, Oxford, United Kingdom, pp. 1-5, 1994, translation of the original paper in German (A. Köhler, "Gedanken zu einem neuen Beleuchtungsverfahren für mikrophotographische Zwecke", *Zeitschrift für wissenschaftliche Mikroskopie*, vol. 10, pp. 433-440, 1893).

[68] K. Keshoju, H. Xing, and L. Sun, "Magnetic field driven nanowire rotation in suspension", *Applied Physics Letters*, vol. 91, iss. 12, pp. 123114-1-3, 2007.

[69] K. B. Sundaram, and G. K. Bhagavat, "High-temperature annealing effects on tin oxide films", *Journal of Physics D: Applied. Physics*, vol. 16, pp. 69-76, 1983.

[70] B. S. Kang, J. J. Chen, F. Ren, Y. Li, H.-S. Kim, D. P. Norton, and S. J. Pearton, "ITO/Ti/Au ohmic contacts on n-type ZnO", *Applied Physics Letters*, vol. 88, iss. 18, pp. 182101-1-3, 2006.

[71] A. Romano-Rodríguez, and F. Hernández-Ramírez, "Dual-beam focused ion beam (FIB): A prototyping tool for micro and nanofabrication", *Microelectronic Engineering*, vol. 84 , iss. 5-8, pp. 789-792, 2007.

[72] F. Hernandez-Ramirez, A. Tarancon, O. Casals, J. Rodriguez, A. Romano-Rodriguez; J. R. Morante, S. Barth, S. Mathur, T. Y. Choi, D. Poulikakos, V. Callegari, and P. M. Nellen, "Fabrication and electrical characterization of circuits based on individual tin oxide nanowires", *Nanotechnology*, vol. 17, no. 22, pp. 5577-5583, 2006.

[73] A. A. Talin, F. L´eonard, B. Swartzentruber, X. Wang, and S. D. Hersee, "Origin of nonlinear current-voltage characteristics in nanowires", *submitted to Physical Review Letters for publication.*

[74] L. Dong, S. Youkey, J. Bush, J. Jiao, V. M. Dubin, and R. V. Chebiam, "Effects of local Joule heating on the reduction of contact resistance between carbon nanotubes and metal electrodes", *Journal of Applied Physics*, vol. 101, iss. 2, pp. 024320-1-7, 2007.

[75] L. R. B. Santos, T. Chartier, C. Pagnoux, J. F. Baumard, C. V. Santillii, S. H. Pulcinelli, and A. Larbot, "Tin oxide nanoparticle formation using a surface modifying agent", *Journal of the European Ceramic Society*, vol. 24, pp. 3713-3721, 2004.

[76] J. F. McAleer, P. T. Moseley, J. O. W. Norris, and D. E. Williams, "Tin dioxide gas sensors: Part 1-Aspects of the surface chemistry revealed by electrical conductance variations", *Journal of the Chemical Society, Faraday Transactions 1: Physical Chemistry in Condensed Phases*, vol. 83, pp. 1323-1346, 1987.

[77] N. Bârsan, and U. Weimar, "Conduction model of metal oxide gas sensors", *Journal of Electroceramics*, vol. 7, no. 3, pp. 143-167, 2001.

[78] A. Oprea , E. Moretton, N. Bârsan, W. J. Becker, J. Wöllenstein, and U. Weimar, Conduction model of SnO_2 thin films based on conductance and Hall effect measurements, *Journal of Applied Physics*, vol. 100, iss. 3, pp. 033716-1-10, 2006.

[79] M. Batzill, and U. Diebold, "The surface and materials science of tin oxide", *Progress in Surface Science*, vol. 79, iss. 2-4, pp. 47-154, 2005.

[80] V. E. Henrich, "The surfaces of metal oxides", *Reports in Progress in Physics*, vol. 48, pp. 1481-1541, 1985.

[81] V. E. Henrich, "Metal-oxide surfaces", *Progress in Surface Science*, vol. 50, iss. 1-4, pp. 77-90, 1995.

[82] C. Malagù, V. Guidi, M. Stefancich, M. C. Carotta, and G. Martinelli, "Model for Schottky barrier and surface states in nanostructured *n*-type semiconductors", *Journal of Applied Physics*, vol. 91, pp. 808-814, 2002.

[83] P. Romppainen, and V. Lantto, "The effect of microstructure on the height of potential energy barriers in porous tin dioxide gas sensors", *Journal of Applied Physics*, vol. 63, iss. 10, pp. 5159-5165, 1988.

[84] A. Rothschild, and Y. Komen, "The effect of grain size on the sensitivity of nanocrystalline metal-oxide gas sensors", *Journal of Applied Physics*, vol. 95, no. 11, pp. 6374-6380, 2004.

[85] K. McGuire, Z. W. Pan, Z. L. Wang, D. Milkie, J. Menéndez, and A. M. Rao, "Raman studies of semiconducting oxide nanobelts", *Journal of Nanoscience and Nanotechnology*, vol. 2, no. 5, pp. 499-502, 2002.

[86] K. Yokota, K. Nakamura, T. Sasagawa, T. Kamatani, and F. Miyashita, "An oxygen ion dose dependence of dielectric constant and surface roughness of titanium oxide films deposited on silicon by an ion beam assisted deposition technique", *Proceedings of the 2000 IEEE International Conference on Ion Implantation Technology*, pp. 350-353, 2000

[87] K. Yokota, K. Nakamura, T. Sasagawa, and T. Kamatani, "Deposition of titanium oxide films with high dielectric constants on silicon by an ion beam assist deposition technique", *Japanese Journal of Applied Physics*, vol. 40, Part 1, no. 2A, pp. 718-723, 2001.

[88] X. Z. Liu, and Y. R. Li, "Effect of oxygen vacancies on nonlinear dielectric properties of $SrTiO_3$ thin films", *Journal of Materials Science*, vol. 42, no. 1, pp. 389-392, 2007.

[89] K. Dutta, and S. K. De, "Double dielectric relaxations in SnO_2 nanoparticles dispersed in conducting polymer", *Journal of Applied Physics*, vol. 102, iss. 8, pp. 084110-1-7, 2007.

[90] L. Luo, B. D. Sosnowchik, and L. Lin, "UV-enhanced oxygen sensing of zinc oxide nanowires", *Proceedings of MEMS 2008: The 21st IEEE International Conference on Micro Electro Mechanical Systems*, pp. 216-219, 2008.

[91] E. W. Thornton, and P. G. Harrison, "Tin oxide surfaces. Part 1.- Surface hydroxyl groups and the chemisorption of carbon dioxide and carbon monoxide on tin (IV) oxide", *Journal of the Chemical Society, Faraday Transactions 1: Physical Chemistry in Condensed Phases*, vol. 71, pp. 461-472, 1975.

[92] F. Hernandez-Ramirez, S. Barth, A. Tarancon, O. Casals, E. Pellicer, J. Rodriguez, A. Romano-Rodriguez, J. R. Morante, and S. Mathur, "Water vapor detection with individual tin oxide nanowires", *Nanotechnology*, vol. 18, pp. 424016-1-6, 2007.

[93] D. Barreca, S. Garon, P. Zanella, and E. Tondello, "MOCVD of SnO_2 thin films from a new organometallic precursor", *Journal de Physique*, vol. 9, pp. 667-673, 1999.

[94] M. Losurdo, D. Barreca, P. Capezzuto, G. Bruno, and E. Tondello, "Interrelation between nanostructure and optical properties of oxide thin films by spectroscopic ellipsometry", *Surface and Coatings Technology*, vol. 151-152, pp. 2-8, 2002.

[95] M. A. Barteau, "Organic reactions at well-defined oxide surfaces", *Chemical Reviews*, vol. 96, iss. 4, pp. 1413-1430, 1996.

[96] Y. Cui, Q. Wei, H. Park, and C. M. Lieber, "Nanowire nanosensors for highly sensitive and selective detection of biological and chemical species", *Science*, vol. 293, no. 5533, pp. 1289-1292, 2001.

[97] M. H. Sørensen, N. A. Mortensen, and M. Brandbyge, "Screening model for nanowire surface-charge sensors in liquid", *Applied Physics Letters*, vol. 91, pp. 102105-1-3, 2007.

[98] S. V. Kalinin, J. Shin, S. Jesse, D. Geohegan, A. P. Baddorf, Y. Lilach, M. Moskovits, and A. Kolmakov, "Electronic transport imaging in a multiwire SnO_2 chemical field-effect transistor device", *Journal of Applied Physics*, vol. 98, no. 4, pp. 44503-1-8, 2005.

[99] A. L. Swint, and P. W. Bohn, "Effect of acidic and basic surface dipoles on the depletion layer of indium tin oxide as measured by in-plane conductance", *Applied Physics Letters*, vol. 84, iss. 1, pp. 61-63, 2004.

[100] C. Malagù, M. C. Carotta, S. Gherardi, V. Guidi, B. Vendemiati, and G. Martinelli, "AC measurements and modeling of WO_3 thick film gas sensors", *Sensors and Actuators B: Chemical*, vol. 108, iss. 1-2, pp. 70-74, 2005.

[101] A. C. Bose, P. Thangadurai, and S. Ramasamy, "Grain size dependent electrical studies on nanocrystalline SnO_2", *Materials Chemistry and Physics*, vol. 95, iss. 1, pp. 72-78, 2006.

[102] A. Abderrahmen, F. F. Romdhane, H. B. Ouada, and A. Gharbi, "Indium-tin oxide surface treatments: Effects on the performance of liquid crystal devices", *Materials Science and Engineering C: Biomimetic and Supramolecular Systems*, vol. 26, no. 2-3, pp. 538-541, 2006.

[103] M. Zhao, C. Jiang, S. Li, and S. X. Mao, "Probing nano-scale mechanical characteristics of individual semi-conducting nanobelts", *Materials Science and Engineering A: Structural Materials*, vol. 409, iss. 1-2, pp. 223-226, 2005.

[104] Y. Zheng, R. E. Geer, K. Dovidenko, M. Kopycinska-Müller, and D. C. Hurley, "Quantitative nanoscale modulus measurements and elastic imaging of SnO_2 nanobelts", *Journal of Applied Physics*, vol. 100, no. 12, pp. 124308-1-6, 2006.